Electrosynthesis of nanocomposite thin films at immiscible liquid|liquid interfaces

By

Reza Moshrefi

A thesis submitted to the

School of Graduate Studies

in partial fulfillment of the requirement for the degree of

Doctor of Philosophy in Chemistry

Department of Chemistry | Faculty of Science

Memorial University of Newfoundland

August 2023

St. John's Newfoundland and Labrador

To my family, Shiva and Sepehr

Abstract

Contemporary research on conductive thin film materials has expanded beyond its applications in solar cells, semiconductor devices, and optical coatings to include the development of biocompatible electrode materials and organic thin film transistors. This study focuses on the use of immiscible micro liquid|liquid interfaces between water|oil (w|o) or water|ionic liquid (w|IL) to generate free-standing thin films that incorporate metal nanoparticles (NPs) electrogenerated in situ by reducing a metal salt in the aqueous phase and a hydrophobic electron donor dissolved in the organic/ionic liquid phase. Following an exploration of recent advancements in electropolymerization at an electrified interface, which encompassed the synthesis of polymeric base networks, metal nanoparticles, and nanocomposite film formation, as well as the electrochemical processes at the interface between immiscible electrolyte solutions, four electron donors were examined: ferrocene, IL-modified ferrocene, 2,2′:5′,2″-terthiophene (TT), and a specialized dithiafulvenyl-substituted pyrene (bis(dithiafulvenyl)pyrene). The research first focused on TT polymerization and the reduction of $AuCl_4^-$ to Au NPs to generate a flexible electrocatalytic composite thin film. The results showed that high aqueous phase pH facilitated the polymerization reaction and the half-wave potential of the electron transfer wave shifted to lower potentials, indicating improved thermodynamics. Furthermore, the study found that the capacitive nature of the interface increased, and the resistance towards simple ion transfer increased with increasing [TT], pH, and potential cycling.

Later the metal salt was replaced with copper sulfate to study the formation of Cu NP/poly-TT nanocomposite thin films at different interfacial sizes. The data revealed that the film formed quickly, but the interfacial reaction did not proceed without an applied potential. Preliminary electrocatalysis results showed that the nanocomposite-modified large glassy carbon electrode had

a >2× increase in CO_2 reduction currents compared to an unmodified electrode. Finally, the electropolymerization of bis(dithiafulvenyl)pyrene with $KAuCl_4$(aq) was studied.

The study found that miniaturization of the immiscible micro liquid|liquid interface facilitated external potential control and limited the reaction pathway to heterogeneous electron transfer across the interface. This method of nanocomposite film generation provides a low overpotential, controlled alternative to large-scale film generation, making it an attractive option for materials chemistry, electrocatalysis, and as soft electrodes for bioimplantation. The chapter dedicated to conclusions and future work provides a comprehensive analysis of the findings and identifies potential avenues for future research in this field.

Acknowledgements

I would like to express my deep gratitude to Dr. Jane Stockmann, for her invaluable guidance, patience, and support throughout my research. Her unwavering commitment to excellence and passion for the subject have inspired me and helped me grow both as a scholar and as an individual.

I would like to thank my committee members, Dr. Kerton and Dr. Reader, for their valuable feedback and support throughout my thesis journey.

I would like to thank members of Dr. Stockmann's research group, Qi, Abhishek, Siamak, Nazanin, Mona, Oforbuike, Hanna, Katelyn, Bradley, Leila, and Bahareh, for their support, and encouragement throughout the course of my research.

I am grateful to Stephanie Tucker, Dr. Wanda Aylward, Dr. Céline Schneider, Dr. Zhao, Dr. Merschrod, Dr. Bodwell, Maryam, Evan, and Josh who generously shared their time, experiences, and perspectives, and made this research possible.

I would like to extend my appreciation to Debbie Hickey, and Nathalie Vanasse, for their kind assistance and their support during my studies.

I would like to express my heartfelt gratitude to my wife, Shiva, for her unwavering support and understanding throughout this journey. To my son Sepehr, your constant love kept me going during the challenging times, and for that, I am eternally grateful. Your sacrifice and support made all the differences.

Table of Contents

List of Figures

List of Tables

List of Abbreviations

AFM	Atomic force microscopy
BT	2,2′-bithiophene
CE	Counter electrode
CPE	Constant phase element
CV	Cyclic voltammograms
CVD	Chemical vapor deposition
DCE	Dichloroethane
DTF	Dithiafulvenyl
EC	Electrochemical chemical
ECSOW	Electron conductor separating an oil|water phase
EDL	Electric double layer
EDX	Dispersive x-ray
EEC	Equivalent electric circuits
EIS	Electrochemical impedance spectroscopy
ET	Electron transfer
Fc	Ferrocene
FcIL	Trioctyl(ferrocenylheptanoyl)phosphonium tetrakis(pentafluorophenyl)borate
FIT	Facilitated ion transfer
GC	Glassy carbon electrode
HET	Heterogeneous electron transfer
IL	Ionic liquid
IT	Simple ion transfer

ITIES	Interface between Two Immiscible Electrolyte Solutions
KPFM	Kelvin probe force microscopy
MOF	Metal organic framework
NPs	Nanoparticles
OCP	Open circuit potential
$P_{8888}TB$	Tetraoctylphosphonium tetrakispentafluorophenyl)borate
PEDOT	Poly(3,4-ethylenedioxythiophene
PPW	Polarizable potential window
PVD	Physical vapor deposition
RAIL	Redox active ionic liquid
RE	Reference electrode
RMS	Root-mean-square
SCE	Standard calomel electrode
SECM	Scanning electrochemical miscroscopy
SEM	Scanning electron microscopy
SHE	Standard hydrogen electrode
SWCNT	Single-walled carbon nanotubes
TEM	Transmission electron microscopy
TFT	*α*,*α*,*α*-trifluorotoluene
TPAs	Tetraphenylarsonium
TPB	Tetraphenylborate
TT	2,2′:5′,2″-terthiophene
UME	Ultramicroelectrodes

WE	Working electrode
XAF	X-ray absorption fine structure
XPS	X-ray photoelectron spectroscopy

List of Symbols

V_{AC}	AC voltage
$a_{a,i}$	Activity of ion *i* in phase *α*
A	Ampere
ω	Angular frequency
K_0	Apparent rate of charge transfer
C_j	Bulk concentration of species j
C_d	Capacitance of the double layer
Q	Charge transferred
z_i	Charges of species i
μ_i	Chemical potential of species *i* in phase *α*
C	Concentration
I	Current
V_{DC}	DC voltage
ρ	Density
$D_{i,\alpha}$	Diffusion coefficient of i in phase α
D	Electron donor
A	Electrode surface area
F_{es}	Electrostatic force
e_0	Elementary electronic charge
γ	Factor of speciation
F	Faraday constant
Z_f	Faraday impedance

f	Frequency
C_{geo}	Geometric capacitance
$\Delta_o^w G_{el}$	Gibbs energy of heterogeneous electron transfer from water to organic
$\Delta G^{\circ}_{\mathrm{i,tr\ w\rightarrow o}}$	Gibbs energy of ion transfer of i from water to organic phase
ϕ_α, ϕ_β	Inner potential of α and β phases
σ	Interfacial charge density
K	Kelvin
L	Litre
MΩ	Megaohm
µC	Microcolumb
µm	Micrometer
mM	Millimolar
mm	Millimolar
nm	Nanometer
nA	Nanometer
r_{NP}	NP radius
n	Number of electrons transferred
R	Number of electrons transferred
$R_{i,\alpha}$	Oxidizing agent in the phase
i_p	Peak current
pF	Picofarad
E	Potential
$O_{i,\alpha}$	Reducing agent in the phase

ν	Scan rate
s	Second
Rs	Solution resistance
ΔG	Standard Gibbs energy
R_c	Stray resistance
ΔG_s	Supersaturation Gibbs energy
S	Surface tension
T	Temperature in degrees Kelvin
t	Time
τ	Time constant
R_{CT}	Transfer resistance
V	Voltage
Z_w	Warburg impedance
w|DCE	water|Dichloroethane
w|IL	water|Ionic liquid
w|o	water|oil

Chapter 1

1. Introduction

Recent advances in electronic medical devices have paved the way for affordable treatments that were previously inaccessible, particularly in cases such as Parkinson's disease.[1] However, there is still a remaining leap in creating a good electrical connection between neural tissues and electronic instruments, *i.e.*, brain-machine interface devices. Most of the current biocompatible electrode technologies are based on thin films.[2,3] Moreover, the growing demand for flexible conductive thin films with tailored properties has extended to other domains such as organic thin film transistors[4], flexible electronics[5], and molecular electronics.[6] Current thin film production methods are based on gas phase techniques, *e.g.*, physical vapor deposition (PVD), chemical vapor deposition (CVD), and liquid phase techniques, *e.g.*, bulk[7] and interfacial polymerization.[5,8] However, the conventional fabrication techniques are inadequate for generating multicomponent and complex flexible nanocomposite thin films due to material properties or the constraints of the fabrication process.[9]

Among liquid phase techniques, bulk polymerization is the most straightforward approach[10], where reactants are mixed more efficiently.[5] However, removing the reaction heat or the product from the reactor are issues that have limited the commercialization of bulk polymerization processes.[10] Conversely, interfacial polymerization is better suited for large-scale thin film production, *e.g.*, Nylon 66[11] (polyamide) and polyester membranes.[5] Liquid-liquid interfacial polymerization and electropolymerization are widely recognized as the two most predominant

interfacial polymerization methodologies. Liquid-liquid interfacial polymerization and electropolymerization hinge on the unique features of the interfacial region, alongside a slew of other benefits. In the former, the interface is instrumental in the formation of a defect free, uniform, and free-standing film. By contrast, electropolymerization capitalizes on the interface as a potential template, heterogeneous catalysis, and stabilizer for intermediate species.[12]

To overcome the disadvantages of the developed methods, researchers have focused on using various stimuli[11,13], *e.g.*, external electrical field, light, and temperature, at a liquid-liquid interface to include spatial, temporal, and chemical controls over the polymerization reactions. Using an external electrical field to control liquid-liquid interfacial polymerization reactions is an intermediate method between single-phase bulk synthesis and electrosynthesis on a solid electrode surface.[14,15] There are four main benefits to using an electrified liquid-liquid interface to synthesize a polymeric film; firstly, it allows activation of reactants (*e.g.*, monomer or electron acceptor) under mild conditions. Secondly, the formed polymers neither float in pieces in a bulk solution nor attach to a solid surface but are localized on a soft interface.[16] Third, applying electrochemical control makes it possible to modulate polymerization kinetics[14,16], reduce side reactions[17], and obtain a polymer with low dispersity.[11] Fourth, liquid-liquid electrochemical control is a promising technique for reducing the consumption of chemical reagents, particularly oxidants and catalysts, during the processing of nanocomposite thin films. This approach aligns well with the principles of greener chemistry, which aim to develop chemical processes that are more environmentally sustainable by reducing the use of hazardous substances and minimizing waste generation.[13,18]

This chapter delves into the recent advancements in electropolymerization at an electrified interface, focusing specifically on the simultaneous synthesis of polymeric base networks and metal nanoparticles. The findings are presented in a structured manner, beginning with an

exploration of the polymerization process at a liquid-liquid interface, followed by a discussion of nanocomposite film formation at the same interface. The chapter then delves into electropolymerization and the production of nanocomposite films at an electrified liquid-liquid interface. Finally, the electrochemistry at the interface between two immiscible electrolyte solutions (ITIES) is explored, as are the charge transfer mechanisms at a liquid-liquid interface.

1.1. Liquid-liquid Interface

Exploiting the liquid-liquid interface as an interfacial platform for polymerization goes back to 1898 when Alfred Einhorn carried out polymerization at a water|toluene interface between pyrocatechol and phosgene.[5] Later, the successful commercialization of nylon 66[11,19] in the 1930s led to the expansion of studies on the process and mechanism of liquid-liquid interfacial polymerization.[5] The utilization of the interface between two immiscible liquids holds significant promise for film synthesis, owing to several key advantages. Firstly, the interface serves as a conducive platform for the interaction between immiscible reactants.[19] Secondly, water molecules play a significant role in accelerating reactions in organic synthesis "on water" systems, while also facilitating ion transport across the two phases. "On water" organic synthesis[20] is applicable to various chemical reactions and relies on a hydrophobic effect that induces the aggregation of organic molecules in water, leading to increased reaction kinetics. The efficiency of the reaction is impacted by factors such as the nature of the interface, ease of hydrogen bonding, and presence of competing molecules.[19] Lastly, it allows for the efficient synthesis of conjugated polymers with desirable electronic and optical properties through the formation of carbon-carbon bonds under mild reaction conditions, *e.g.*, Suzuki polymerization.[21] The liquid-liquid interfacial polymerization technique has been used to fabricate polymeric thin films[21], nanofibers[22], organic nanoparticles[23], and core-shell particles.

1.1.1. Polymerization

Polymerization reactions can occur at the interface between two liquids that are not miscible by dissolving monomers and an oxidizer/catalyst in separate liquid phases. This technique allows the reactants to react solely at the interface[5], leading to the self-assembly of a polymer film.[9] There are three techniques for preparing polymeric films at a liquid-liquid interface. The first method involves the non-perturbative placement of two immiscible liquids in contact. Formation of porphyrin- and triphenylamine-based conjugated polymers[21], poly(aniline), poly(pyrrole), poly(thiophene), poly(indole), and poly(3,4-ethylenedioxythiophene) films has been studied extensively in the last three decades using this method. Initially, the reaction is controlled by kinetics until a thin polymer layer forms between the two phases, which slows down the reaction due to transfer and termination reactions.[19] The concentration and solubility of monomers, solvents, additives, temperature, the permeability of monomers through the generated film, the solubility of polymers, ionic strength[24], and pH of the aqueous phase have a significant impact on the polymerization process and its final morphological properties.

The second method entails the dispersion of an organic phase into an aqueous phase, *i.e.*, an oil-in-water emulsion. Polymerization reactions at a liquid-liquid interface such as dispersed-phase polymerization and emulsion polymerization[10] can be utilized to synthesize polymeric micro- and nanoparticles. Using disperse systems, in this case, increases the efficiency, and the reaction rate can be adjusted by controlling the size of the interface.[19] In dispersed-phase polymerization, dispersed liquid monomers in the aqueous phase react with an initiator to start the polymerization reaction. The initiator dissolves only in the monomer's phase and does not partition into the aqueous phase. Each droplet reaction proceeds independently following the kinetics of bulk polymerization. Based on the technique used to form the droplets, the size of the forming beads

can be adjusted[19] and reach 0.1-2 mm.[10] Adding a surfactant to the system would decrease the size of the beads to about 10-40 μm. In emulsion polymerization[10], the initiator is water-soluble, and the size of the beads is in the range of 50-500 nm.[10] The same principles used to form the beads can be applied to creating core-shell particles, nanoencapsulation of organic compounds, and hollow particles. The main applications for polymeric nanoparticles are nanoengineering and biomedicine[13] as smart nanocarriers.[19] In the last approach, the formation of beads is interrupted after a certain period, resulting in the self-organization of a film at the interface between two immiscible liquids.[9]

1.1.2. Nanocomposite Films

Unlike polymerization, forming a nanocomposite film with an orderly structure with certain organic and inorganic entities at a liquid-liquid interface does not necessarily include a chemical reaction.[9] This method utilizes self-organization at the interface to assemble solid particles dispersed in two separate phases once the stirring is interrupted. The balance between repulsive and attractive forces, which depends on the composition, shape, and size of the solid constituents, leads to the formation of a nanocomposite layer at the interface.[9] This approach has been used to prepare films of various carbon nanostructures, such as a transparent graphene sheet film with a thickness of 4 nm and a resistance of 100 Ω/cm, by Biswas and Drzal[25], as well as, a 2-D fullerene-based film consisting of macropores and mesopores was synthesized by Shrestha *et al.*[23] Multicomponent nanocomposite films, like Graphene-$Ni(OH)_2$[9], CNT/TiO_2[9], PVP-Ag[9], Ag-NP/Au-NP[26] in addition to uniform films of MOF (metal organic framework) precursors[27], organic crystals (*e.g.*, polydiacetylene[28]), metal nanoparticles (*e.g.*, Au[29], Pt[30], Ag[31], Cu), have been prepared at the liquid-liquid interfaces with the same procedure. The properties of the resulting films are influenced by several factors, including the volume of both phases, temperature, stirring condition, stirring velocity, and the amount of dispersed solid material.[9] Another approach

involves the evaporation of an organic solvent in an immiscible liquid-liquid system, resulting in the self-organization of dissolved monomers in the organic phase and dopants in the aqueous phase to form a nanocomposite film at the aqueous-air interface.[9]

When a chemical or electrochemical reaction is involved, more complex films, including semiconducting or conductive polymer-based nanocomposite films, can be synthesized at a liquid-liquid interface. For example, a semiconductive CdS film was prepared by Sathaye *et al.*[32] by inducing a reaction between Cd^{2+} ions in the aqueous phase and CS_2 in an organic solution at the interface of water and carbon tetrachloride. Similarly, conductive polymer-based nanocomposites can be formed by chemically oxidizing conductive polymers at a liquid-liquid interface in the presence of metal nanoparticles.[9]

1.2. Electropolymerization

Electrochemically controlled polymerization is a relatively low cost[33] and facile synthetic procedure[34] that occurs at the solid electrode/electrolyte interface through either a chain-growth or condensative chain-growth mechanism.[11] The unique reactivity and selectivity of electro-organic synthesis chemistry under cell potential control, which in turn modulates the reaction kinetics/thermodynamics, has gained massive popularity in the last five decades.[35] Applied potential can be used for generating transient species[11], oxidizing the monomer[11], or activating a catalyst to initiate the polymerization process.[11,13] In 1949, Wilson et al[11] used electrochemistry to directly control the polymerization of acrylic acid, ethyl acrylate, and methyl methacrylate, marking a significant milestone in the field. Since then, electropolymerization of various monomers, including vinyl chloride, vinyl acetate, acrylonitrile, acrylamide, and conductive polymers such as carbazole, thiophene, pyrrole, and aniline, on a solid electrode has been extensively studied.[11,36] For conductive polymers, electropolymerization produces smooth and

robust conductive films, whose molecular weight, dispersity, morphology, and thickness can be adjusted by changing the reaction time and applied potential or current.[36] As the understanding in this area grew, controlled synthesis of polymer films found interesting applications[33,34], while strategies like co-polymerization[11], doping[37], template synthesis[36], chemical modification, and dipole orientation have been employed to improve and tune polymers properties such as stability[33], flexibility[37], conductivity, as well as chemical and physical durability.[11,38]

Electropolymerization occurs on the solid electrode/electrolyte interface through either a chain-growth or condensative chain-growth, with two main mechanisms being radical cation-radical cation coupling and radical cation-substrate coupling.[11] The influential parameters in electropolymerization include the concentration of the monomer, the applied potential regime, temperature, solvent, and supporting electrolyte. These parameters have a significant impact on the electropolymerization process and the properties of the resulting polymer films.[11]

1.3. Nanocomposite Film at an Electrified Liquid-liquid Interface

An electrified interface has been used for polymer composite synthesis by adding particles into one phase or preparing them *in situ* during polymerization.[39] The first method exploits dispersed particles' tendency to adsorb on the interface to minimize surface energy.[39,40] Particles get trapped in the polymer's network by diffusion toward the interface and entering the reaction zone. In the second approach, a dopant, mostly metal nanoparticles (NPs), forms simultaneously during polymerization at the interface.[41,42] The polymer acts as a linker and capping agent for dopant/metallic nanoparticles in both cases. Over the past thirty years, electropolymerization at the liquid-liquid interface has witnessed increasing advancements based on the chemistry of the monomer and the properties of the of dopant/metal nanoparticles.[43–45] The simplicity of this approach is its most intriguing aspect. In reported studies, scanning toward positive potentials at

an ITIES results in a heterogeneous electron transfer (HET) wave due to the oxidation of the monomer and the simultaneous reduction of the electron acceptor. For example, in the case of terthiophene, polymerization happens through a bidirectional C-C coupling at α and α′ positions after the anodic oxidation of monomers.[46] The HET reaction is followed by a series of chemical and physical steps, culminating in the deposition of oligomers and NPs at the interface through a one-step and one-pot reaction – a straightforward yet robust process.

The initial demonstration of an EC-type (electrochemical, chemical) reaction leading to electropolymerization at a water|DCE (1,2-dichloroethane) interface was introduced by Cunnane and colleagues.[47] This was achieved by inducing a HET reaction through the application of an external electrical field between methyl- or phenyl-pyrrole in the organic phase and ferri-/ferrocyanide in the aqueous phase. The group's primary objective was to understand the underlying mechanisms of this phenomenon, but they also explored the electrodeposition of metal nanoparticles combined with electrosynthesis of polymers at an interface to develop nanocomposite films. By considering possible scenarios, several attempts have been made to understand electropolymerization at an ITIES in terms of monomers/metal precursors' redox potential and the techniques employed for polarizing the interface. The systems reported to date are listed in Table 1-1.

The mechanism of polymerization at an ITIES has yet to be fully explained since it is a complex multistep reaction.[15,48] However, some areas have been well investigated. It was found that the reactants' bulk concentration[45]; diffusion coefficient[48]; the solubility of reactants in the opposite phase[48]; aqueous phase pH[49]; concentration and nature of supporting electrolyte[37,50]; and solubility of the forming oligomers[50] impact the morphology and the structure of films produced at the ITIES. It also has been reported that the concentration of the metal precursor, the pH of the

aqueous phase, the chemistry of the monomer, and the potential of the applied external electrical field[49,51] play a crucial role in determining the size and the shape of the embedded nanoparticles. Table 1-1 lists relevant electron donor/acceptor combinations along with the polarization technique and associated reference.

Table 1-1 *Reported interfacial electropolymerization at water|DCE electrified interface.*

Aqueous phase	Organic phase	Interface polarization technique	Interface size (mm^2)	Ref.
ferric(III)/ferrous(II) sulfate	methyl -pyrrole	Potentiodynamic	125	47
	phenyl-pyrrole			
ceric(IV)/cerous(III) sulfate	2,2′:5′,2″ terthiophene	Galvanostatic	126	52
Silver(I) sulfate	N-phenylpyrrole		--	53
ceric(IV)/cerous(III) sulfate	2,2′:5′,2″ terthiophene	Potentiodynamic	--	50
		Common ion partitioning	1962	
tyramine	tetraoctylammonium tetrachloroaurate		200	43
ceric(IV)/cerous(III) sulfate	2,2′:5′,2″ terthiophene	Potentiodynamic	19.64	48
			1964	
tyramine	tetraoctylammonium tetrachloroaurate	Potentiodynamic	--	49
resorcinol		Common ion partitioning		
tetrachloroaurate	2,2′:5′,2″ terthiophene	Potentiodynamic	314×10^{-6}	54
			452	
hexachloroiridate (IV)	pyrrole	Potentiodynamic	--	55
ferric(III) sulfate	[bis(pyrrol-1-yl)methyl]-phenyloxyacetic acid	Potentiodynamic	200	56
ferric(III) sulfate	4-{4-[bis(pyrrol-1-yl)me-thyl]-phenyloxy}-butanoic acid	Potentiodynamic	200	56
ceric(IV) sulfate	4-(pyrrol-1-yl)phenyloxyacetic acid	Potentiodynamic	235	57
	4-(pyrrol-1-yl)-1-propoxybenzene			
	4-(pyrrol-1-yl)-1-dodecyloxybenzene			
ceric(IV)/cerous(III) sulfate	3,4-ethylenedioxythiophen	Multi-step-potentiostatic	78.5	15
tetrachloroaurate	2,2′:5′,2″ terthiophene	Potentiodynamic	49×10^{-6}	58
copper(II) sulfate	2,2′:5′,2″ terthiophene	Potentiodynamic	49×10^{-6}	59
			78.5	
tetrachloroaurate	dithiafulvenyl functionalized pyrene	Potentiodynamic	49×10^{-6}	60

The concentration of the reactants involved in the reaction at an electrified liquid-liquid interface plays a crucial role in determining the Galvani potential difference and the overall behavior of the system, as described by equations 1-13 and 1-11, see below. By controlling the concentration of the reactants, it is possible to regulate the type of electrochemical reaction, the potential of the HET, as well as the mechanism and kinetics of the reaction. For instance, Evans-Kennedy *et al.*[50] demonstrated reversible and irreversible HET between ceric(IV)/cerous(III) sulfate in the aqueous phase and 2,2′:5′,2″ terthiophene (TT) in DCE in low and high concentrations of the monomer.[50] Similarly, Cunnane *et al.*[47] showed that increasing the ferric(III)/ferrous(II) ratio in the aqueous phase, as an electron acceptor, shifted the HET peak to more positive potentials. Our group corroborated these findings and observed that increasing the monomer concentration decreased the HET half-wave potential.[60] Additionally, Ivan *et al.*[61] reported that a higher monomer concentration favored a kinetically fast reaction pathway over a thermodynamically stable one. We also observed that the reactants' concentration in both phases strongly influenced the reaction mechanism in our studies.[58–60] Notably, we did not observe any HET between aqueous copper sulfate and TT in DCE when the monomer concentration was 5 and 10 mM. However, increasing the monomer concentration to 20 mM resulted in the appearance of a HET peak at positive potentials.[59] Electrochemical impedance spectroscopy confirmed that a deposition formed at the interface at high monomer concentrations, altering the interface's properties, whereas minimal changes were observed at low monomer concentrations.[59] Evans-Kennedy *et al.*[50] utilized UV-Visible absorption studies to investigate the TT polymerization process. They found that at low concentrations of TT, no deposition occurred at the interface, and the oligomers formed had a maximum chain length of six monomers, corresponding to a hexamer in solution. However, at higher concentrations of monomer, a highly dispersed polymeric structure was deposited over the interface.

The selection of solvents is a crucial factor that significantly impacts polymerization kinetics and the mechanism at an interface between two immiscible electrolyte solutions (ITIES), in addition to the concentration. A solvent is the dominant chemical species in a liquid phase, and the characteristics of the solvent exert a significant influence on various aspects of a reaction, such as redox potentials, diffusion coefficients, solubility of the forming oligomers, and the reaction rate and selectivity. The diffusion rate of reactants is further influenced by multiple factors, including temperature, convection, bulk concentration, solubility of reactants, and micro-convections resulting from the creation of a porous liquid-solid-liquid junction.[62] One of the primary goals of polymerization at an electrified liquid-liquid interface is to modulate the film's properties electrochemically. To achieve this objective, it is imperative to restrict the reaction strictly to the interface, *i.e.*, a HET reaction. To this end, the design of the system must take into account two critical factors: limited solubility of reactants in the opposite phase and negligible miscibility of solvents.[35,62] Although the solvent effect on the polymerization reaction at an electrified interface has not been thoroughly explored, studies by Lepkova *et al.*[49,51] and Knake *et al.*[43] have shown that altering the phases in which the monomer and metal precursor are delivered at a water|DCE interface can impact the reaction mechanism. A HET peak was observed when the monomer was dissolved in DCE and the metal precursor in water[47,48,50,52], but a facilitated ion transfer reaction leading to a homogeneous electrochemical reaction was detected when the metal precursor, such as tetraoctylammonium tetrachloroaurate ($TOAAuCl_4$), was dissolved in DCE.[43,49,63] Recently, alternative solvents such as TFT (α,α,α-trifluorotoluene) and hydrophobic ionic liquids have been utilized by Suarez-Herrera *et al.*[64], Lehane *et al.*[15], and Nishi *et al.*[65] due to their lower toxicity compared to DCE, but no comparison between these systems has been made.

Evans-Kennedy *et al.* showed that the HET reaction is a potential dependant phenomenon. They used UV-Visible absorption spectroscopy to monitor the reaction progress at an ITIES that was polarized at varying Galvani potential differences.[50] Later studies by Gorgyet *et al.*, Knake *et al.*, Vignali *et al.*, and Lepkova *et al.* using different approaches for polarizing the interface, including potentiodynamic[43,47–49,53], galvanostatic[52], and common ion partitioning[49–51], confirmed Evans-Kennedy *et al.*'s results. As evident in Table 1-1 and considering equations 1-13 (see below), various research groups have investigated systems with positive[52], negative[47,53] and zero[15] theoretical $\Delta_o^w G_{el}$. Although the HET reaction is thermodynamically favored in systems with negative $\Delta_o^w G_{el}$, film formation has been reported in all three cases. Based on the current-time graphs reported by Gorgy, the initial film layers consisting of 2,2′:5′,2″ terthiophene (TT) coupled with ceric(IV)/cerous(III) sulfate at the water|DCE interface formed within 10 s with an applied current density of 50 μA/cm^2.[2] Hence with an electrochemically controlled system with a positive theoretical $\Delta_o^w G_{el}$ the polymerization can be carried out rapidly.[52] On the other hand, having a negative $\Delta_o^w G_{el}$ does not guarantee appreciable HET kinetics, even under an applied external electrical field.[56]

The nucleation of polymer/metal NPs is the onset of a phase transition at both interfacial sides. From a thermodynamics point of view, a nanocomposite/polymer deposition over fresh ITIES is complicated because a solid phase starts to appear and grow at a clean and defect-free interface where the interaction between the two phases is just repulsive.[66] Despite the complexity, the properties of an ITIES make it an ideal framework for synthesizing a free-standing thin film. Firstly, surface tension between two phases and surface charges of the particles at ITIES can be manipulated by an applied external electric field, explained below. Second, the driving force of the deposition and, consequently, the film deposition rate can be adjusted by adjusting the Galvani

potential difference that forms across the interface.[44] Lastly, the HET reaction is limited to a single plane (the interface), making it simpler to manage compared to the complexities that arise in bulk-phase polymerization.[44] The driving force for the formation and growth of a new phase, *i.e.*, supersaturation Gibbs energy (ΔG_s), can be expressed as in eq. 1-1:[67,68]

$$\Delta G_s = -n\mathrm{F}\eta + SA \qquad 1\text{-}1$$

Where the overpotential (η) and surface tension (S) are described by the in eq. 1-2 and in eq. 1-3:

$$\eta = \Delta_o^w\phi - \Delta_o^w\phi_e \qquad 1\text{-}2$$

$$S = S_{p/w} - S_{p/o} - S_{w/o} \qquad 1\text{-}3$$

while, n is the number of electrons; A is the surface area of the formed particles or cluster of metal atoms; $S_{p/w}$ and $S_{p/o}$ are surface tension between particles and solution phases; $S_{w/o}$is the surface tension at the ITIES, and $\Delta_o^w\phi_e$ is the equilibrium Galvani potential difference for the HET reaction. According to Lippmann's equation (eq. 1-4), the surface tension between water and oil, $S_{w/o}$, is a function of the Galvani potential difference. [44]

$$\frac{\partial^2 S_{w/o}}{\partial\phi^2} = \frac{-\partial\sigma}{\partial\phi} = -C_d \qquad 1\text{-}4$$

C_d is the capacitance of the back-to-back electric double layers that form at the ITIES, and σ is the interfacial charge density. Consequently, both terms that describe ΔG_s, η and S, are a functions of the Galvani potential difference across the interface. Due to the lack of nucleation sites at a liquid-liquid interface, the energy required during the initial formation of the first nuclei at the ITIES is relatively high. In such a condition, if $S_{w/o}$ is higher than $S_{p/w}$ and $S_{p/o}$, the decrease in surface tension at the w|o interface due to particle formation and adsorption would help

compensate for the energy needed to overcome the lack of nucleation sites. Such compensation can occur spontaneously or be externally induced. The balance between the electrostatic repulsion among the same material[66,69], attraction between polymeric components and metal NPs, and capillary forces[66,69] leads to the first deposition of a nanocomposite layer. Any change in the chemistry of the monomer and material of the NPs will change interspecies forces and, consequently the whole nucleation mechanism.[70] Here the applied external potential plays an important role in screening the surface charges of the particles at ITIES.[69]

The mechanism behind the deposition of the film over the interface and whether it occurs gradually or instantaneously has been a topic of research. In this regard, Gründer *et al.*[71] reported a stepwise nucleation process, where particles land around the initial nuclei in electrodeposition[39], and the new phase grows. On the other hand, Dryfe *et al.*[44] reported an instantaneous nucleation process. The polymer's deposition mechanism can explain this discrepancy at the interface. If formed, monomer/oligomer cations are surface active and get adsorbed at the interface[57], the polymerization would proceed via stepwise nucleation. However, in cases where oligomers are soluble in the organic/aqueous phase or get stabilized by anions of supporting electrolyte[15], only reaching a certain concentration threshold would trigger the coupling between floating oligomers leading to a rapid deposition at the interface. [50]

As the polymerization proceeds, the oligomers formed carry a positive charge in the organic phase. To gain stability, these charged oligomers form weak coordination with the anions present in the organic phase.[15] In this way, they drag these anions into the growing polymeric structure at the interface. However, at the interface, they are exposed to aqueous phase anions, which are smaller and have less shielded negative charges.[15] In addition, any metal nanoparticles formed simultaneously, *e.g.*, Au, carry a negative charge[54], which would help stabilize the depositing film.

Doping the deposited oligomers at the interface with aqueous anions would be more efficient in stabilizing and neutralizing the forming film. Doping and de-doping is a slow process[72] and happens at different Galvani potential differences than HET and electropolymerization.[15] Hence potentiodynamic or multistep-potentiostatic electrochemical techniques are more effective in electropolymerization at an ITIES[15] than potentiostatic ones. As the film grows, the selected potential range must support the doping and de-doping process since more negative charge is needed to compensate the positive charge on the growing polymeric network.[48]

It has been reported that polymerization at ITIES is diffusion controlled in all applied current densities[50,52], mainly because the diffusion field expands in two phases, and reactants must diffuse to get to the interface to react. As the film forms, it acts as a physical barrier, blocking ion transfer across the ITIES [48,56,57], rather than an electrostatic one.[57] Research by Maeda *et al.*[57] and Mareček *et al.*[56] has shown that when a compact film covers the interface, even small ions such as potassium and protons cannot transfer across the film. Consequently, the reaction continues in a spatially separated manner with aqueous and organic side components, leading to the development of a mixed potential at the interface and resulting in 3D Janus-type film growth.[54] The reactions on the nanocomposite film can be described as oxidation and reduction half-cell reactions occurring at the liquid|solid|liquid interface, as summarized in eq. 1-5 and 1-6.

$$O_{1,w} + n_1 e \leftrightharpoons R_{1,w} \qquad 1\text{-}5$$

$$R_{2,org} \leftrightharpoons O_{2,org} + n_2 e \qquad 1\text{-}6$$

Where $O_{1,w}$, $R_{1,w}$, $O_{2,org}$ and $R_{2,org}$ refer to oxidized and reduced forms of redox couples in phase 1, and 2 respectively; In this way, the film at the interface acts as a bipolar electrode, facilitating the HET reaction across the interface.[15] Hence the autocatalytic effect[15] of floating pieces of the film at ITIES and longer chain oligomers[50] (see below) would lower the required

overpotential for HET/electropolymerization. In the scenario of a single monomer unit entering the reaction zone from the organic phase, the likelihood of encountering a growing polymer chain is higher than encountering other individual monomers.[62] As a result of this phenomenon, the formation of high molecular weight polymers is expected. Consequently, there is a period of rapid polymerization, which leads to the appearance of a compact 2D film at the interface, followed by a spatially separated electrochemical reaction leading to further extension of the polymer chains towards the organic side and deposition of a metal-rich layer on the aqueous side of the film, generating a 3D Janus-type film. That is why film growth at ITIES does not fit classical growth mechanisms as seen at a solid electrode/electrolyte interface.[52] Vignali *et al.*'s[48] calculations showed that the electronic resistance of the film at the interface is not a significant portion of the overall resistance at a macro-interface, so the interface can still be effectively polarized. However, by depositing a polymer layer at an ITIES, surface tension is no longer potentially dependent.[48,57]

By adding large, charged complexes into the system, the permeability of the forming film at the interface can be modified as reported by Mareček.[56] Controlled adsorption and desorption of these ions at the ITIES can form channels that facilitate ion transfer through the film. This finding suggests that electropolymerization at the ITIES can enable in-situ deposition of size, charge, and even shape-selective membranes.

Through the chemical modification of the basic monomer, Mareček *et al.*[56] was able to polymerize a molecule containing two pyrrole units at a lower potential than the monomers with a single pyrrole unit at the w|DCE interface. Furthermore, the addition of an electron donating moiety to the monomer would also lower the monomer oxidation potential. As polymerization proceeds, the chain length of oligomers grows at the interface, leading to a lower oxidation potential due to increased conjugated structure that can effectively stabilize a radical cation.[50,73]

As a result, the magnitude of the applied potentials during polymerization at an ITIES has been a focus, since applying large overpotentials could lead to over-oxidation of the film.[48]

1.4. Electrochemistry at an interface between two immiscible electrolyte solutions (ITIES)

The investigation of liquid-liquid interfaces at the junction of two immiscible phases[74] has attracted considerable interest in scientific research. This includes interfaces between water|organic solvent[75–78] (w|o), water|ionic liquids[79–83] (w|IL), and organic solvent/ionic liquid[84] (o|IL). It is an easily reproducible[66,85], molecularly sharp[86,87], defect free[88,89], and mechanically flexible[88,90] framework in all its forms that can be interrogated by applying external electrical potential. A polarizable ITIES provides a platform for studying a wide variety of phenomena, such as simple ion transfer (IT)[75,91], facilitated ion transfer (FIT)[76,77,91–95], heterogeneous electron transfer (HET)[47,48,63,91,96], interfacial redox catalysis[29,88], and adsorption.[97] Developing an understanding of phenomena happening at a polarizable liquid|liquid interface as well as functionalizing the soft interface with promising applications in a biphasic electrocatalysis[39,88–90,92], optics[29,90,98], electrodeposition[39,53,99,100], synthesis[47,52,101], extraction[82,93,102–104], and sensors[77,94,105,106] has driven numerous studies around the world.

1.4.1. Polarizable Liquid-liquid Interface Structure

Our understanding of charge concentration profile at a polarizable liquid-liquid interface has been based on surface tension measurements[85], surface capacitance measurements[85], surface second harmonic generation technique[85,107], X-ray reflectivity[87,91], neutron reflectivity[87], and molecular dynamics simulations.[86,107] An ITIES is a discontinuity between two phases, and polarization around it is carried out by ionic species.[107] The nature, viscosity, and miscibility of solvents, in addition to dissolved species in two phases, affect the structure of the ITIES.[62,85] By

getting close, ~ 1 nm, to an electrified interface, solvent molecules take a preferred orientation and their permittivity changes accordingly to transit from one phase to another.[87,107] Recent studies suggest that charged species get arranged in two monolayers of opposite charge back-to-back on either side of the interface to balance the overall charge. In other words, there is no significant charge screening effect from the bulk electrolyte at a liquid-liquid interface, as proposed by Gschwend *et al.*[85,107]

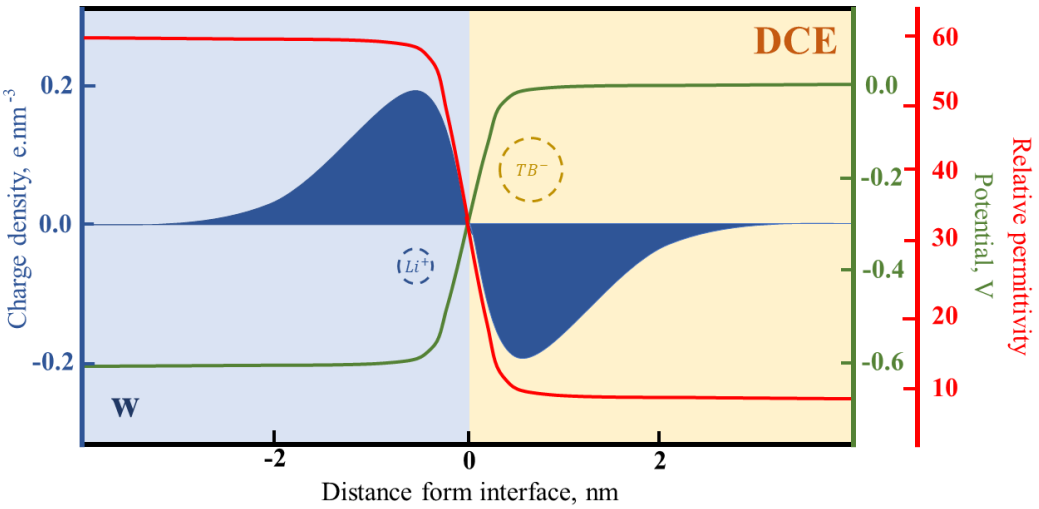

Figure 1-1 Charge density profile and potential profile at a w|DCE interface[107]

Moreover, bulk concentration does not have much influence on the surface charge, and there is a linear relationship between applied potential and observed surface charges.[85,107] The potential drop across the ITIES is localized to within +/–1 nm on either side, Figure 1-1.[85] Such outcomes are important because those results support the Helmholtz model for ITIES structure in a long-running dispute. Thus, Gschwend *et al.*[85,107] refer to this model as the 'discrete Helmholtz model' following early models of electrolyte structure during electrode polarization.

1.4.2. Galvani potential difference Scale

Galvani potential difference, or inner potential of a phase, is the potential difference between the bulk and vacuum.[108] Galvani potential difference rises at the interface of two phases, so in the case of an ITIES, Galvani potential difference forms due to the differences in ions solvation in either of the two phases. By considering $\Delta G^{o}_{t,\, w\rightarrow o}$ as the difference in standard Gibbs energy of solvation for ions between the aqueous and organic phase, eq. 1-7:[109]

$$\Delta G^{o}_{t,\, w\rightarrow o} = \mu^{o}_{org} - \mu^{o}_{w} \qquad \textit{1-7}$$

where μ^{o}_{org} and μ^{o}_{w} represents standard chemical potentials; for an established equilibrium for an ion dissolved at an aqueous and organic phase $\Delta G^{o}_{t,\, w\rightarrow o}$ can be written as:[110]

$$\mu^{o}_{i,w} + RT\ln(a_{i,w}) + z_i F\phi_{w} = \mu^{o}_{i,org} + RT\ln(a_{i,org}) + z_i F\phi_{org} \qquad \textit{1-8}$$

and by rearranging eq. 1-8, Galvani potential difference can be obtained as:

$$\Delta^{w}_{o}\phi = \phi_{org} - \phi_{w} = \Delta^{w}_{o}\phi^{o}_{i} + \frac{RT}{z_i F}\ln\frac{a_{i,org}}{a_{i,w}} \qquad \textit{1-9}$$

which is known as Nernst-Donnan equation[50,51] or transfer potential.[109] In eq. 1-9, $\Delta^{w}_{o}\phi^{o}_{i}$ is the standard transfer potential of the ion, z is the ion's charge, and a is the activity of the ion in both phase in phase *w* or *org*.

The accepted potential scale in liquid-liquid electrochemistry for referring to charge transfer potential differs from traditional electrochemistry. An extra thermodynamic assumption, called the TATB (tetraphenylarsonium tetraphenylborate) assumption has been used in liquid-liquid electrochemistry. In the TATB assumption, standard Gibbs free energy of ion transfer for $TPAs^{+}$ and TPB^{-} are considered to be of the same magnitude but opposite sign, *i.e.*, $\Delta G^{0,\, w\rightarrow o}_{tr}\left(TPAs^{+}\right) = -\Delta G^{0,\, w\rightarrow o}_{tr}(TPB^{+})$[51,111]; indeed, experimentally the ion transfer of $TPAs^{+}$ and TPB^{+} appear at either ends of the polarizable potential window. This is because both ions are similar in size with similar

charge shielding. In this assumption, the midpoint between the half-wave transfer potentials of $TPAs^+$ and TPB^- is considered zero on the Galvani potential difference scale, $\Delta_o^w\phi$. [111]

1.5. Charge Transfer Mechanisms at a Liquid-liquid Interface

In 1968 Gavach *et al.*[87] observed simple ion transfer under an externally applied potential for the first time. In 1978, Samec *et al.*[112] recorded the first current signal corresponding to a heterogeneous electron transfer across an ITIES. Current at the liquid-liquid interface is measured through charge transfer reactions similar to those at solid/solution interfaces. However, a solid/solution interface is limited to electron transfer and non-faradaic reactions. While at a liquid-liquid interface, ions can also be transferred.[113] This has attracted great attention towards the liquid-liquid interface in electrochemistry, particularly due to its biomimetic nature.[76]

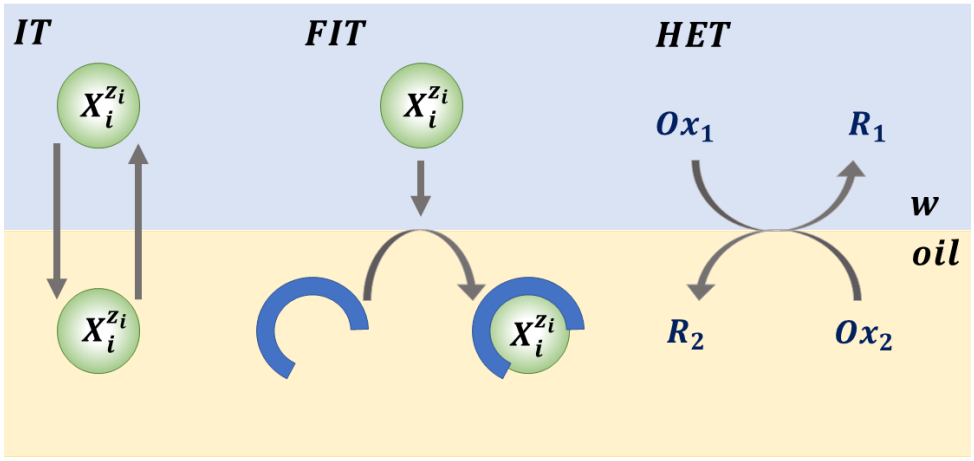

Figure 1-2 Simple ion transfer (IT), facilitated ion transfer (FIT), and heterogeneous electron transfer (HET), through an ITIES.

Charge transfer reactions, both ion and electron transfer, at an ITIES are potential dependant.[87,90,91] Ions move inside a solvent by continuous displacement of solvent molecules[87], and adjusted Galvani potential difference at the interface dictates the direction of ions' movement. The measured current is directly related to charge transfer across the ITIES, $i = \frac{dQ}{dt}$, and occurs by

three main mechanisms; simple ion transfer (IT), facilitated ion transfer (FIT), and HET, Figure 1-2.

1.5.1. Simple Ion Transfer (IT)

When an ion receives enough energy to overcome the activation barrier to cross the ITIES, a simple ion transfer reaction happens.[87] The main proposed mechanisms for ion transfer through the interface are solvent fingers[87], shuttling of ions[87], aqueous clusters,[87,114] and ionosome formation.[113] Despite the complexity of the proposed mechanisms, due to solvation dynamics[114], a simple ion transfer phenomenon at an ITIES has been treated as a first-order chemical reaction, eq. 1-10,[115]

$$X_{aq}^{z_i} \rightleftarrows X_{org}^{z_i} \qquad 1\text{-}10$$

At an electrified interface, the applied external potential is an additional parameter to control the formed equilibrium at the interface and adjust the position of the equilibrium.[90] In this case, ion transfer current can be written using Butler-Volmer formalism, eq. 1-11, as:[115]

$$i = zFAk_0[c_{aq} e^{\frac{\alpha zF}{RT}(\Delta_o^w\phi - \Delta_o^w\phi^\circ)} - c_{org} e^{\frac{-(1-\alpha)zF}{RT}(\Delta_o^w\phi - \Delta_o^w\phi^\circ)}] \qquad 1\text{-}11$$

where z, F, A, k_0, c_{aq}, c_{org}, R, and T are the transferring ion's charge, Faraday constant, area of the ITIES, transfer coefficient, the ideal gas constant, temperature and ion concentration in the aqueous (w) or organic (o) phase, respectively. $\Delta_o^w\phi$ and $\Delta_o^w\phi^\circ$ are the Galvani potential difference across the interface and standard ion transfer potential.

1.5.2. Heterogenous Electron Transfer (HET)

For a heterogeneous electron transfer between two redox couples, O_1/R_1 in aqueous and O_2/R_2 in organic phases, the reaction can be written as in eq. 1-12:

$$n_1O_{1,w}+n_2R_{2,org} \leftrightharpoons n_1R_{1,w}+n_2O_{2,org} \quad \textit{1-12}$$

where n_1 and n_2 are the stoichiometric coefficients for each redox couple; in this reaction, $O_{1,w}$ is an oxidizing agent in the aqueous phase, which reacts with $R_{2,org}$ in the organic phase. In a chemical equilibrium, the Fermi levels of the aqueous and organic phases must be equal.[47,90] As a result of the equilibrium, the Galvani potential difference for the electron transfer reaction ($\Delta_o^w\phi_{el}$) can be written as in eq. 1-13:[90]

$$\Delta_o^w\phi_{el}=E^o_{O_2/R_2,\,org}-E^o_{O_1/R_1,\,w}+\frac{RT}{n_1n_2F}\ln\frac{a^{n_1}_{R_{1,w}}a^{n_2}_{O_{2,org}}}{a^{n_1}_{O_{1,w}}a^{n_2}_{R_{2,org}}} \quad \textit{1-13}$$

where $E^o_{O_1/R_1,\,w}$ and $E^o_{O_2/R_2,\,org}$ are standard reduction potentials of O_1/R_1 and O_2/R_2 redox couples in the aqueous and organic phases, respectively, and *a* is the activity of the species in each corresponding phase. Both redox couples must be at a certain distance from the interface for a HET reaction to take place. Hence the reaction's rate depends on the frequency of such encounters.[90]

There is a sign convention for current and Galvani potential difference at an ITIES. For the Galvani potential difference, the sign convention is, eq. 1-14:[116]

$$\Delta_o^w\phi=\phi_w-\phi_o \quad \textit{1-14}$$

which means that by applying the external potential field, the potential of the aqueous phase is changed toward the organic phase. For measured current, according to the sign convention, when a positively charged species crosses the interface from the aqueous to the organic phase, the current signal will be positive, and for a negatively charged species, the current will be negative. However, if a positively charged species crosses the interface from the organic to the aqueous phase, the current will be negative, and for a negatively charged species, the current will be positive.[48,116]

This assumption is made to be able to compare the results with solid electrode/electrolyte interfaces.[116]

1.6. Scope of the Thesis

The primary aim of this study was to construct a pliable, free-standing conductive nanocomposite thin film with customizable properties and composition for various applications, including electrocatalysis, electrosynthesis, electroanalysis, bio-implantation, and personal electronics. However, to achieve this overarching goal, the focus of this research was on micro-scale electrogeneration of the thin film, allowing for the production of small, soft probes and sensors for point-of-care devices. Miniaturization of the interface between two immiscible electrolyte solutions (ITIES) enables more control of the electrosynthesis process, facilitating the development of a comprehensive understanding of interfacial charge transfer reactions, as well as the various chemical and physical processes involved in different stages of nanocomposite thin film formation.

Chapter 2 of this study employed voltammetric techniques to investigate a HET reaction between a reducing agent, Fc(org), and a metal salt, $KAuCl_4$(aq), at the micro-interface between water and 1,2-dichloroethane (w|DCE). The size and morphology of the Au NPs, ranging from 20-400 nm and spherical or cubic, respectively, were controlled by varying pH, Au salt:Fc concentration ratio, potential, and reaction time. The findings of this study have been published in *Electrochemistry Communications.*[100]

In Chapter 3, the electrogeneration of Au nanoparticles (NPs) at a water|ionic liquid (w|IL) immiscible micro-interface with a diameter of 25 μm was investigated and compared with the results obtained at a water|oil (w|o) interface. $KAuCl_4$ was dissolved in the aqueous phase and

reacted under external potential control at the water|$P_{8888}TB$ (tetraoctylphosphonium tetrakis(pentafluorophenyl)borate) with tri-octyl(ferrocenylhexanoyl)phosphonium tetrakis(pentafluorophenyl)borate (FcIL), an electron donor and redox-active IL. The voltammetric characterization of the simple ion transfer of $AuCl_4^-$ and $AuCl_{(4-\gamma)}(OH)_\gamma$ at the w|$P_{8888}TB$ micro-interface, as well as their heterogeneous electron transfer reaction with FcIL, were conducted. The interfacial reaction led to the generation of Au NPs, the size of which can be thermodynamically controlled by modifying the pH of the aqueous phase. The findings of this research have been published in *Nanomaterials.*[99]

Chapter 4 of this work focuses on the generation of a free-standing thin-film via the incorporation of Au NPs, which were electrogenerated in situ by the reduction of gold salt in the aqueous phase, and using 2,2′:5′,2″-terthiophene (TT) as the monomer/electron donor dissolved in the DCE phase, at a micro liquid-liquid interface. The influence of pH on the quality of the electrogenerated films at the ITIES was examined using TEM and AFM techniques, while impedance spectroscopy measurements were employed to investigate the electrochemical properties of the ITIES and provide insights into the reaction mechanism. This research has been published in *Electrochimica Acta.*[101]

The ITIES then was exploited for simultaneous electropolymerization of 2,2′:5′,2″-terthiophene (TT) and reduction of Cu^{2+} to Cu nanoparticles (NPs), resulting in a flexible electrocatalytic composite electrode material, as explained in Chapter 5. The process of nanocomposite formation was investigated using cyclic voltammetry and electrochemical impedance spectroscopy (EIS), while SEM and TEM were used to examine and analyze the resulting Cu NP/poly-TT composites. The preliminary results of electrocatalysis on a nanocomposite-modified large glassy carbon electrode indicated a more than twofold increase in

CO_2 reduction currents compared to an unmodified electrode. This research has been published in *Scientific Reports*.[59]

Chapter 6 presents a study on the reproducible electrogeneration of conductive polymer films containing low dispersity Au nanoclusters, with a thickness of approximately 2 nm, at a micro liquid-liquid interface. The study investigated the heterogeneous electron transfer process between $KAuCl_4$(aq) and a dithiafulvenyl-substituted pyrene monomer, 4,5-didecoxy-1,8-bis(dithiafulven-6-yl)pyrene (bis(DTF)pyrene), in oil. The conductivity of the films was measured, and the results indicate that the electrogenerated films exhibit high conductivity. This work has been published in *Nanoscale*.[60]

Finally, in Chapter 7, a summary of the results and a perspective of forming a nanocomposite thin film at a micro-interface and its potential applications in electrocatalysis will be presented, based on the findings from the previous chapters which demonstrate the successful electrogeneration of various nanocomposite materials using different monomers and metal salts at micro and macro liquid-liquid interfaces. The reproducible and tunable properties of these materials, as well as their promising electrochemical performance, suggest that they hold great potential for a wide range of practical applications in the field of nanotechnology.

1.7. References

(1) Espay, A. J.; Bonato, P.; Nahab, F. B.; Maetzler, W.; Dean, J. M.; Klucken, J.; Eskofier, B. M.; Merola, A.; Horak, F.; Lang, A. E.; Reilmann, R.; Giuffrida, J.; Nieuwboer, A.; Horne, M.; Little, M. A.; Litvan, I.; Simuni, T.; Dorsey, E. R.; Burack, M. A.; Kubota, K.; Kamondi, A.; Godinho, C.; Daneault, J. F.; Mitsi, G.; Krinke, L.; Hausdorff, J. M.; Bloem, B. R.; Papapetropoulos, S.

Technology in Parkinson's Disease: Challenges and Opportunities. *Mov. Disord.* **2016**, *31* (9), 1272–1282. https://doi.org/10.1002/mds.26642.

(2) Strakosas, X.; Biesmans, H.; Abrahamsson, T.; Hellman, K.; Silverå Ejneby, M.; Donahue, M. J.; Ekström, P.; Ek, F.; Savvakis, M.; Hjort, M.; Bliman, D.; Linares, M.; Lindholm, C.; Stavrinidou, E.; Gerasimov, J. Y.; Simon, D. T.; Olsson, R.; Berggren, M. Metabolite-Induced in Vivo Fabrication of Substrate-Free Organic Bioelectronics. *Science*, **2023** 379(6634), pp.795-802. https://www.science.org/doi/10.1126/science.adc9998.

(3) Wang, Yingli, Chen Zhao, Jingjing Wang, Xuan Luo, Lijuan Xie, Shijie Zhan, Jongmin Kim, Xiaozhi Wang, Xiangjiang Liu, and Yibin Ying. Wearable plasmonic-metasurface sensor for noninvasive and universal molecular fingerprint detection on biointerfaces. Sci. Adv. **2021** 7(4). https://doi.org/10.1002/eabe4553.

(4) Sun, C.; Wang, X.; Auwalu, M. A.; Cheng, S.; Hu, W. Organic Thin Film Transistors-based Biosensors. *EcoMat.* **2021**, *3* (2), e12094. https://doi.org/10.1002/eom2.12094.

(5) Zhang, F.; Fan, J.; Wang, S. Interfacial Polymerization: From Chemistry to Functional Materials. *Angew. Chem.* **2020**, *59*, 21840. https://doi.org/10.1002/ange.201916473.

(6) Liu, Y.; Qiu, X.; Soni, S.; Chiechi, R. C. Charge Transport through Molecular Ensembles: Recent Progress in Molecular Electronics. *Chem. Phys. Rev.* **2021**, *2* (2), 021303. https://doi.org/10.1063/5.0050667.

(7) Veith, C.; Diot-Néant, F.; Miller, S. A.; Allais, F. Synthesis and Polymerization of Bio-Based Acrylates: A Review. *Polym. Chem*. **2020**, 11(47), 7452–7470. https://doi.org/10.1039/d0py01222j.

(8) Staub, M. C.; Li, C. Y. Polymer Crystallization at Liquid-Liquid Interface. *Polym. Crys*. **2018**. 1(4), e10045. https://doi.org/10.1002/pcr2.10045.

(9) Zarbin, A. J. G. Liquid–Liquid Interfaces: A Unique and Advantageous Environment to Prepare and Process Thin Films of Complex Materials. *Mater. Horiz.* **2021**, *8* (5), 1409–1432. https://doi.org/10.1039/D0MH01676D.

(10) Lovell, P. A.; Schork, F. J. Fundamentals of Emulsion Polymerization. *Biomacromolecules*. **2020**, 21(11), 4396–4441. https://doi.org/10.1021/acs.biomac.0c00769.

(11) Zhou, Y. N.; Li, J. J.; Wu, Y. Y.; Luo, Z. H. Role of External Field in Polymerization: Mechanism and Kinetics. *Chem. Rev.* **2020**, 120(5), 2950–3048. https://doi.org/10.1021/acs.chemrev.9b00744.

(12) Grill, L.; Hecht, S. Covalent On-Surface Polymerization. *Nat. Chem.* **2020**, 12(2), 115–130. https://doi.org/10.1038/s41557-019-0392-9.

(13) Parkatzidis, K.; Wang, H. S.; Truong, N. P.; Anastasaki, A. Recent Developments and Future Challenges in Controlled Radical Polymerization: A 2020 Update. *Chem*. **2020**, 6(7), 1575–1588. https://doi.org/10.1016/j.chempr.2020.06.014.

(14) Uehara, A.; Hashimoto, T.; Dryfe, R. A. W. Au Electrodeposition at the Liquid-Liquid Interface: Mechanistic Aspects. *Electrochim. Acta.* **2014**, 118, 26–32. https://doi.org/10.1016/j.electacta.2013.11.162.

(15) Lehane, R. A.; Gamero-Quijano, A.; Malijauskaite, S.; Holzinger, A.; Conroy, M.; Laffir, F.; Kumar, A.; Bangert, U.; McGourty, K.; Scanlon, M. D. Electrosynthesis of Biocompatible Free-Standing PEDOT Thin Films at a Polarized Liquid|Liquid Interface. *J. Am. Chem. Soc.* **2022**, 144 (11), 4853–4862. https://doi.org/10.1021/jacs.1c12373.

(16) Dryfe, R. A. W.; Uehara, A.; Booth, S. G. Metal Deposition at the Liquid-Liquid Interface. *Chem. Rec.* **2014**, *14* (6), 1013–1023. https://doi.org/10.1002/tcr.201402027.

(17) Liu, C.; Yang, J.; Guo, B. B.; Agarwal, S.; Greiner, A.; Xu, Z. K. Interfacial Polymerization at the Alkane/Ionic Liquid Interface. *Angew. Chem.* **2021**, 133 (26), 14636–14643. https://doi.org/10.1002/anie.202103555.

(18) Pollok, D.; Waldvogel, S. R. Electro-Organic Synthesis-a 21st Century Technique. *Chem*. **2020**, 11(46), 12386–12400. https://doi.org/10.1039/d0sc01848a.

(19) Piradashvili, K.; Alexandrino, E. M.; Wurm, F. R.; Landfester, K. Reactions and Polymerizations at the Liquid-Liquid Interface. *Chem. Rev*. **2016**, 116, 2141–2169. https://doi.org/10.1021/acs.chemrev.5b00567.

(20) Chanda, A.; Fokin, V. V. Organic Synthesis "on Water." *Chem. Rev*. **2009**, 109(2), 725–748. https://doi.org/10.1021/cr800448q.

(21) Zhang, L.; Zhan, W.; Dong, Y.; Yang, T.; Zhang, C.; Ouyang, M.; Li, W. Liquid | Liquid Interfacial Suzuki Polymerization Prepared Novel Triphenylamine-Based Conjugated Polymer Films with Excellent Electrochromic Properties. *ACS. Appl. Mater. Interfaces.* **2021**, 13 (17), 20810–20820. https://doi.org/10.1021/acsami.1c02745.

(22) Miyazawa, K. Synthesis of Fullerene Nanowhiskers Using the Liquid-Liquid Interfacial Precipitation Method and Their Mechanical, Electrical and Superconducting Properties. *Sci. Technol. Adv. Mate*. **2015**, 23(1), 199-224. https://doi.org/10.1088/1468-6996/16/1/013502.

(23) Shrestha, L. K.; Yamauchi, Y.; Hill, J. P.; Miyazawa, K.; Ariga, K. Fullerene Crystals with Bimodal Pore Architectures Consisting of Macropores and Mesopores. *J. Am. Chem. Soc.* **2013**, *135* (2), 586–589. https://doi.org/10.1021/ja3108752.

(24) Issa, A. A.; Luyt, A. S. Kinetics of Alkoxysilanes and Organoalkoxysilanes Polymerization: A Review. *Polym*. **2019**, 11(3), 537. https://doi.org/10.3390/polym11030537.

(25) Biswas, S.; Drzal, L. T. A Novel Approach to Create a Highly Ordered Monolayer Film of Graphene Nanosheets at the Liquid-Liquid Interface. *Nano. Lett.* **2009**, *9* (1), 167–172. https://doi.org/10.1021/nl802724f.

(26) Wen, P.; Yang, F.; Ge, C.; Li, S.; Xu, Y.; Chen, L. Self-Assembled Nano-Ag/Au@Au Film Composite SERS Substrates Show High Uniformity and High Enhancement Factor for Creatinine Detection. *Nanotechnology.* **2021**, 32 (39), 395502. https://doi.org/10.1088/1361-6528/ac0ddd.

(27) Bai, X. J.; Chen, D.; Li, L. L.; Shao, L.; He, W. X.; Chen, H.; Li, Y. N.; Zhang, X. M.; Zhang, L. Y.; Wang, T. Q.; Fu, Y.; Qi, W. Fabrication of MOF Thin Films at Miscible Liquid-Liquid Interface by Spray Method. *ACS. Appl. Mater. Interfaces.* **2018**, 10 (31), 25960–25966. https://doi.org/10.1021/acsami.8b09812.

(28) Matsui, J.; Shibata, T.; Yamamoto, K.; Yokoyama, T.; Masuhara, A.; Kasai, H.; Oikawa, H.; Miyashita, T. Densely Packed Organic Nanocrystals Ultrathin Film Using a Liquid-Liquid Interface. *Synth. Met.* **2009**, 159 (9–10), 847–850. https://doi.org/10.1016/j.synthmet.2009.01.025.

(29) Scanlon, M. D.; Smirnov, E.; Stockmann, T. J.; Peljo, P. Gold Nanofilms at Liquid-Liquid Interfaces: An Emerging Platform for Redox Electrocatalysis, Nanoplasmonic Sensors, and Electrovariable Optics. *Chem. Rev.* **2018**, 118 (7), 3722–3751. https://doi.org/10.1021/acs.chemrev.7b00595.

(30) Hoseini, S. J.; Rashidi, M.; Bahrami, M. Platinum Nanostructures at the Liquid-Liquid Interface: Catalytic Reduction of *p*-Nitrophenol to *p-Aminophenol*. *J. Mater. Chem.* **2011**, 21 (40), 16170–16176. https://doi.org/10.1039/c1jm11814e.

(31) Yao, K. S.; Zhao, H. L.; Wang, N.; Li, T. J.; Zhao, S.; Lu, W. W. Facile Synthesis of Ultra-Large, Single-Crystal Ag Nanosheet-Assembled Films at Chloroform-Water Interface. *J. Solid. State. Chem.* **2019**, 278, 120912. https://doi.org/10.1016/j.jssc.2019.120912.

(32) Sathaye, S. D.; Patil, K. R.; Paranjape, D. v.; Mitra, A.; Awate, S. v.; Mandale, A. B. Preparation of Q-Cadmium Sulfide Ultrathin Films by a New Liquid-Liquid Interface Reaction Technique (LLIRT). *Langmuir.* **2000**, *16* (7), 3487–3490. https://doi.org/10.1021/la991276r.

(33) Wang, W.; Chen, H.; Yue, Y.; Zhang, R.; Liu, J. Electropolymerization of V-Shape D-A-D Type Monomers for Efficient and Tunable Electrochromics. *Dyes. Pigm.* **2021**, 194, 109615. https://doi.org/10.1016/j.dyepig.2021.109615.

(34) Palma-Cando, A.; Rendón-Enríquez, I.; Tausch, M.; Scherf, U. Thin Functional Polymer Films by Electropolymerization. *Nanomaterials.* **2019**, 9 (8), 1125. https://doi.org/10.3390/nano9081125.

(35) Corbin, N.; Junor, G. P.; Ton, T. N.; Baker, R. J.; Manthiram, K. Toward Improving the Selectivity of Organic Halide Electrocarboxylation with Mechanistically Informed Solvent Selection. *J. Am. Chem. Soc.* **2023**, 145(3), 1740-1748. https://doi.org/10.1021/jacs.2c10561.

(36) Okhay, O.; Tkach, A. Polyaniline—Graphene Electrodes Prepared by Electropolymerization for High-Performance Capacitive Electrodes: A Brief Review. *Batteries*. **2022**. 8 (10), 191. https://doi.org/10.3390/batteries8100191.

(37) Zhang, M.; Nautiyal, A.; Du, H.; Wei, Z.; Zhang, X.; Wang, R. Electropolymerization of Polyaniline as High-Performance Binder Free Electrodes for Flexible Supercapacitor. *Electrochim. Acta.* **2021**, 376, 138037. https://doi.org/10.1016/j.electacta.2021.138037.

(38) Shi, K.; Zou, H.; Sun, B.; Jiang, P.; He, J.; Huang, X. Dielectric Modulated Cellulose Paper/PDMS-Based Triboelectric Nanogenerators for Wireless Transmission and

Electropolymerization Applications. *Adv. Funct. Mater.* **2020**, 30 (4), 1904536. https://doi.org/10.1002/adfm.201904536.

(39) Rodgers, A. N. J.; Booth, S. G.; Dryfe, R. A. W. Particle Deposition and Catalysis at the Interface between Two Immiscible Electrolyte Solutions (ITIES): A Mini-Review. *Electrochem. Commun.* **2014**, 47, 17–20. https://doi.org/10.1016/j.elecom.2014.07.009.

(40) Gawron, E. L.; Mayall, R. M.; Kedzior, S. A.; Kinkead, B.; Wotton, R.; Kapadia, W.; Sebastian, H. B.; Bryant, S. L. Liquid–Liquid Interfacial Films: A Tunable One-Pot Nanocomposite Preparation Method and Platform Technology. *Mater.* **2019**, 8, 100468. https://doi.org/10.1016/j.mtla.2019.100468.

(41) Gniadek, M.; Malinowska, S.; Rapecki, T.; Stojek, Z.; Donten, M. Synthesis of Polymer-Metal Nanocomposites at Liquid-Liquid Interface Supported by Ultrasonic Irradiation. *Synth. Met.* **2014**, 187 (1), 193–200. https://doi.org/10.1016/j.synthmet.2013.10.031.

(42) Luo, G.; Malkova, S.; Yoon, J.; Schultz, D. G.; Lin, B.; Meron, M.; Benjamin, I.; Vanýsek, P.; Schlossman, M. L. Ion Distributions at the Nitrobenzene-Water Interface Electrified by a Common Ion. *J. Electroanal. Chem.* **2006**, 593 (1–2), 142–158. https://doi.org/10.1016/j.jelechem.2006.03.051.

(43) Knake, R.; Fahmi, A. W.; Tofail, S. A. M.; Clohessy, J.; Mihov, M.; Cunnane, V. J. Electrochemical Nucleation of Gold Nanoparticles in a Polymer Film at a Liquid−Liquid Interface. *Langmuir.* **2005**, 21 (3), 1001–1008. https://doi.org/10.1021/la048277q.

(44) Dryfe, R. A. W. Modifying the Liquid | Liquid Interface: Pores, Particles and Deposition. *Phys. Chem. Chem. Phys.* **2006**, 8 (16), 1869–1883. https://doi.org/10.1039/b518018j.

(45) Luo, K.; Dryfe, R. A. W. The Formation of Silver Nanofibres by Liquid | Liquid Interfacial Reactions: Mechanistic Aspects. *New. J. Chem.* **2009**, 33 (1), 157–163. https://doi.org/10.1039/b809654f.

(46) Wang, Y.; Li, M. Controlled Electropolymerization Based on Self-Dimerizations of Monomers. *Curr. Opin. Electrochem*. Elsevier B.V. **2022**, 33, 100952. https://doi.org/10.1016/j.coelec.2022.100952.

(47) Cunnane, V. J.; Evans, U. Formation of Oligomers of Methyl- and Phenyl-Pyrrole at an Electrified Liquid|Liquid Interface. *ChemComm.* **1998**, 19, 2163–2164. https://doi.org/10.1039/a806365f.

(48) Gorgy, K.; Fusalba, F.; Evans, U.; Kontturi, K.; Cunnane, V. J. Electropolymerization of 2,2′:5′,2″ Terthiophene at an Electrified Liquid-Liquid Interface. *Synth. Met.* **2001**, 125 (3), 365–373. https://doi.org/10.1016/S0379-6779(01)00474-X.

(49) Johans, C.; Clohessy, J.; Fantini, S.; Kontturi, K.; Cunnane, V. J. Electrosynthesis of Polyphenylpyrrole Coated Silver Particles at a Liquid-Liquid Interface. *Electrochem. Commun.* **2002**, 4 (3), 227–230. https://doi.org/10.1016/S1388-2481(02)00256-4.

(50) Evans-Kennedy, U.; Clohessy, J.; Cunnane, V. J. Spectroelectrochemical Study of 2,2′:5′,2″-Terthiophene Polymerization at a Liquid | Liquid Interface Controlled by Potential-Determining Ions. *Macromolecules.* **2004**, 37 (10), 3630–3634. https://doi.org/10.1021/ma0348223.

(51) Vignali, M.; Edwards, R.; Cunnane, V. J. Characterization of Doping and Electropolymerization of Free-Standing Films of Polyterthiophene. *J. Electroanal. Chem.* **2006**, 592 (1), 37–45. https://doi.org/10.1016/j.jelechem.2006.04.020.

(52) Lepková, K.; Clohessy, J.; Cunnane, V. J. The PH-Controlled Synthesis of a Gold Nanoparticle/Polymer Matrix via Electrodeposition at a Liquid-Liquid Interface. *J. Condens. Matter. Phys.* **2007**, 19 (37). https://doi.org/10.1088/0953-8984/19/37/375106.

(53) Nishi, N.; Yajima, I.; Amano, K.-I.; Sakka, T. Janus-Type Gold/Polythiophene Composites Formed via Redox Reaction at the Ionic Liquid|Water Interface. *Langmuir.* **2018**, 34 (7), 2441–2447. https://doi.org/10.1021/acs.langmuir.7b03792.

(54) Toth, P. S.; Rabiu, A. K.; Dryfe, R. A. W. Controlled Preparation of Carbon Nanotube-Conducting Polymer Composites at the Polarisable Organic/Water Interface. *Electrochem. Commun.* **2015**, 60, 153–157. https://doi.org/10.1016/j.elecom.2015.08.022.

(55) Mareček, V.; Jänchenová, H.; Stibor, I.; Budka, J. Compact Poly-Pyrrole Layers Formed at a Liquid|liquid Interface. *J. Electroanal. Chem.* **2005**, 575 (2), 293–299. https://doi.org/10.1016/j.jelechem.2004.09.021.

(56) Maeda, K.; Jänchenová, H.; Lhotský, A.; Stibor, I.; Budka, J.; Mareček, V. Formation of a Polymer Layer from Monomers Adsorbed at a Liquid | Liquid Interface. *J. Electroanal. Chem.* **2001**, 516 (1–2), 103–109. https://doi.org/10.1016/S0022-0728(01)00658-1.

(57) Moshrefi, R.; P. Connors, E.; Merschrod, E.; Stockmann, T. J. Simultaneous Electropolymerization/Au Nanoparticle Generation at an Electrified Liquid|Liquid Micro-Interface. *Electrochim. Acta.* **2022**, 426, 140749. https://doi.org/10.1016/j.electacta.2022.140749.

(58) Moshrefi, R.; Przybyła, H.; Stockmann, T. J. Simultaneous Electro-Generation/Polymerization of Cu Nanocluster Embedded Conductive Poly(2,2′:5′,2″-Terthiophene) Films at Micro and Macro Liquid|Liquid Interfaces. *Sci. Rep.* **2023**, 13 (1), 1201. https://doi.org/10.1038/s41598-023-28391-9.

(59) Moshrefi, R.; Ryan, K.; Connors, E. P.; Walsh, J. C.; Merschrod, E.; Bodwell, G. J.; Stockmann, T. J. Electrosynthesis of Au Nanocluster Embedded Conductive Polymer Films at Soft Interfaces Using Dithiafulvenyl-Functionalized Pyrene. *Nanoscale.* **2023**, 15 (12), 5834–5842. https://doi.org/10.1039/D2NR06519C.

(60) Lepková, K.; Clohessy, J.; Cunnane, V. J. Electrodeposition of Metal-Based Nanocomposites at a Liquid-Liquid Interface Controlled via the Interfacial Galvani Potential Difference. *Electrochim. Acta.* **2008**, 53 (21), 6273–6277. https://doi.org/10.1016/j.electacta.2008.04.025.

(61) Robayo-Molina, I.; Molina-Osorio, A. F.; Guinane, L.; Tofail, S. A. M.; Scanlon, M. D. Pathway Complexity in Supramolecular Porphyrin Self-Assembly at an Immiscible Liquid–Liquid Interface. *J. Am. Chem. Soc.* **2021**, 70(4), 1640-1644. https://doi.org/10.1021/jacs.1c02481.

(62) Raaijmakers, M. J. T.; Benes, N. E. Current Trends in Interfacial Polymerization Chemistry. *Prog. Polym. Sci.* **2016**, 63, 86–142. https://doi.org/10.1016/j.progpolymsci.2016.06.004.

(63) Lepková, K.; Clohessy, J.; Cunnane, V. J. Electrodeposition of Metal-Based Nanocomposites at a Liquid-Liquid Interface Controlled via the Interfacial Galvani Potential Difference. *Electrochim. Acta.* **2008**, 53 (21), 6273–6277. https://doi.org/10.1016/j.electacta.2008.04.025.

(64) Suárez-Herrera, M. F.; Gamero-Quijano, A.; Scanlon, M. D. Electrosynthesis of Poly(2,5-Dimercapto-1,3,4-Thiadiazole) Films and Their Composites with Gold Nanoparticles at a Polarised Liquid|liquid Interface. *Electrochim. Acta.* **2022**, 424*, 140677*. https://doi.org/10.1016/j.electacta.2022.140677.

(65) Nishi, N.; Yajima, I.; Amano, K. I.; Sakka, T. Janus-Type Gold/Polythiophene Composites Formed via Redox Reaction at the Ionic Liquid|Water Interface. *Langmuir.* **2018**, 34 (7), 2441–2447. https://doi.org/10.1021/acs.langmuir.7b03792.

(66) Booth, S. G.; Dryfe, R. A. W. Assembly of Nanoscale Objects at the Liquid|Liquid Interface. *J. Phys. Chem C.* **2015**, 119 (41), 23295–23309. https://doi.org/10.1021/acs.jpcc.5b07733.

(67) Cheng, Y.; Schiffrin, D. J. Electrodeposition of Metallic Gold Clusters at the Water|1,2-Dichloroethane Interface. *J. Chem. Soc., Faraday Trans.* **1996**, 92 (20), 3865–3871. https://doi.org/10.1039/ft9969203865.

(68) Bresme, F.; Oettel, M. Nanoparticles at Fluid Interfaces. *J. Condens. Matter. Phys.* **2007**, 19 (41), 413101. https://doi.org/10.1088/0953-8984/19/41/413101.

(69) Dryfe, R. A. W.; Uehara, A.; Booth, S. G. Metal Deposition at the Liquid-Liquid Interface. *Chem. Rec.* **2014**, 14 (6), 1013–1023. https://doi.org/10.1002/tcr.201402027.

(70) Xu, S.; Cao, D.; Liu, Y.; Wang, Y. Role of Additives in Crystal Nucleation from Solutions: A Review. *Cryst. Growth. Des*. **2021**, 22 (3), 2001–2022. https://doi.org/10.1021/acs.cgd.1c00776.

(71) Gründer, Y.; Ho, H. L. T.; Mosselmans, J. F. W.; Schroeder, S. L. M.; Dryfe, R. A. W. Inhibited and Enhanced Nucleation of Gold Nanoparticles at the Water1,2-Dichloroethane Interface. *Phys. Chem. Chem. Phys.* **2011**, 13 (34), 15681–15689. https://doi.org/10.1039/c1cp21536a.

(72) Wei, Y.; Chan, C. C.; Tian, J.; Jang, G. W.; Hsueh, K. F. Electrochemical Polymerization of Thiophenes in the Presence of Bithiophene or Terthiophene: Kinetics and Mechanism of the Polymerization. *Chem. Mater.* **1991**, 3 (5), 888–897. https://doi.org/10.1021/cm00017a026.

(73) Sarac, S. S.; Evans, U.; Serantoni, M.; Clohessy, J.; Cunnane, V. J. Electrochemical and Morphological Study of the Effect of Polymerization Conditions on Poly(Terthiophene). *Surf Coat. Technol.* **2004**, 182 (1), 7–13. https://doi.org/10.1016/j.surfcoat.2003.08.002.

(74) Deng, H.; Peljo, P.; Momotenko, D.; Cortés-Salazar, F.; Jane Stockmann, T.; Kontturi, K.; Opallo, M.; Girault, H. H. Kinetic Differentiation of Bulk/Interfacial Oxygen Reduction Mechanisms at/near Liquid | Liquid Interfaces Using Scanning Electrochemical Microscopy. *J. Electroanal. Chem.* **2014**, 732, 101–109. https://doi.org/10.1016/j.jelechem.2014.08.031.

(75) Stockmann, T. J.; Montgomery, A. M.; Ding, Z. Determination of Alkali Metal Ion Transfers at Liquid|liquid Interfaces Stabilized by a Micropipette. *J. Electroanal. Chem.* **2012**, 684, 6–12. https://doi.org/10.1016/j.jelechem.2012.08.013.

(76) Stockmann, T. J.; Noël, J.-M.; Abou-Hassan, A.; Combellas, C.; Kanoufi, F. Facilitated Lewis Acid Transfer by Phospholipids at a (Water|$CHCl_3$) Liquid|Liquid Interface toward Biomimetic and Energy Applications. *J. Phys. Chem. C.* **2016**, 120 (22), 11977–11983. https://doi.org/10.1021/acs.jpcc.6b02354.

(77) Burgoyne, E. D.; Stockmann, T. J.; Molina-Osorio, A. F.; Shanahan, R.; McGlacken, G. P.; Scanlon, M. D. Electrochemical Detection of Pseudomonas Aeruginosa Quorum Sensing Molecules at a Liquid|Liquid Interface. *J. Phys. Chem. C.* **2019**, 123 (40), 24643–24650. https://doi.org/10.1021/acs.jpcc.9b08350.

(78) Stockmann, T. J.; Ding, Z. Electrochemical Behaviour of Ferrocenes in Tributylmethylphosphonium Methyl Sulfate Mixtures with Water and 1,2-Dichloroethane. *Can J Chem.* **2015**, 93 (1), 13–21. https://doi.org/10.1139/cjc-2014-0006.

(79) Stockmann, T. J.; Ding, Z. Hydrophobicity of Room Temperature Ionic Liquids Assessed by the Galvani Potential Difference Established at Micro Liquid|Liquid Interfaces. *J. Electroanal. Chem.* **2010**, 649 (1–2), 23–31. https://doi.org/10.1016/j.jelechem.2009.12.024.

(80) Stockmann, T. J.; Ding, Z. Facile Determination of Formal Transfer Potentials for Hydrophilic Alkali Metal Ions at Water Ionic Liquid Microinterfaces. *Phys. Chem. Chem. Phys.* **2012**, 14 (40), 13949–13954. https://doi.org/10.1039/c2cp42107k.

(81) Stockmann, T. J.; Zhang, J.; Montgomery, A. M.; Ding, Z. Electrochemical Assessment of Water|ionic Liquid Biphasic Systems towards Cesium Extraction from Nuclear Waste. *Anal. Chim. Acta.* **2014**, 821, 41–47. https://doi.org/10.1016/j.aca.2014.03.012.

(82) Stockmann, T. J.; Ding, Z. Electrochemical Evaluation of Ionic Liquids for Biphasic Electrochemical Evaluation of Ionic Liquids for Biphasic Extraction of Metal Ions Common to Spent Nuclear Fuel Extraction of Metal Ions Common to Spent Nuclear Fuel, **2013**, Ph.D. Thesis, The University of Western Ontario.

(83) Stockmann, T. J.; Guterman, R.; Ragogna, P. J.; Ding, Z. Trends in Hydrophilicity/Lipophilicity of Phosphonium Ionic Liquids As Determined by Ion-Transfer Electrochemistry. *Langmuir.* **2016**, 32 (49), 12966–12974. https://doi.org/10.1021/acs.langmuir.6b03031.

(84) Kuroyama, Y.; Nishi, N.; Sakka, T. Electrochemical Liquid-Liquid Interface between Oil and Ionic Liquid for Reductive Deposition of Metal Nanostructures. *J. Electroanal. Chem.* **2021**, 881, 114959. https://doi.org/10.1016/j.jelechem.2020.114959.

(85) Gschwend, G. C.; Girault, H. H. Discrete Helmholtz Charge Distribution at Liquid-Liquid Interfaces: Electrocapillarity, Capacitance and Non-Linear Spectroscopy Studies. *J. Electroanal. Chem.* **2020**, 872, 114240. https://doi.org/10.1016/j.jelechem.2020.114240.

(86) Gschwend, G.; Olaya, A.; Reynard, D.; Girault, H. Development and Applications of Electrochemistry at Soft Interfaces and Nanoparticles. *Rev. Polarogr.* **2021**, 67 (1), 3–10. https://doi.org/10.5189/revpolarography.67.3.

(87) Gschwend, G. C.; Olaya, A.; Peljo, P.; Girault, H. H. Structure and Reactivity of the Polarised Liquid–Liquid Interface: What We Know and What We Do Not. *Curr. Opin. Electrochem.* **2020**, 19, 137–143. https://doi.org/10.1016/J.COELEC.2019.12.002.

(88) Smirnov, E.; Peljo, P.; Scanlon, M. D.; Girault, H. H. Gold Nanofilm Redox Catalysis for Oxygen Reduction at Soft Interfaces. *Electrochim. Acta.* **2016**, 197, 362–373. https://doi.org/10.1016/j.electacta.2015.10.104.

(89) Deng, H.; Stockmann, T. J.; Peljo, P.; Opallo, M.; Girault, H. H. Electrochemical Oxygen Reduction at Soft Interfaces Catalyzed by the Transfer of Hydrated Lithium Cations. *J. Electroanal. Chem.* **2014**, 731, 28–35. https://doi.org/10.1016/j.jelechem.2014.07.040.

(90) Smirnov, E.; Peljo, P.; Scanlon, M. D.; Girault, H. H. Interfacial Redox Catalysis on Gold Nanofilms at Soft Interfaces. *ACS. Nano.* **2015**, 9 (6), 6565–6575. https://doi.org/10.1021/acsnano.5b02547.

(91) Peljo, P.; Smirnov, E.; Girault, H. H. Heterogeneous versus Homogeneous Electron Transfer Reactions at Liquid–Liquid Interfaces: The Wrong Question? *J. Electroanal. Chem.* **2016**, 779, 187–198. https://doi.org/10.1016/j.jelechem.2016.02.023.

(92) Rivier, L.; Stockmann, T. J.; Méndez, M. A.; Scanlon, M. D.; Peljo, P.; Opallo, M.; Girault, H. H. Decamethylruthenocene Hydride and Hydrogen Formation at Liquid|Liquid Interfaces. *J. Phys. Chem. C.* **2015**, 119 (46), 25761–25769. https://doi.org/10.1021/acs.jpcc.5b08148.

(93) Stockmann, T. J.; Lu, Y.; Zhang, J.; Girault, H. H.; Ding, Z. Interfacial Complexation Reactions of Sr^{2+} with Octyl(Phenyl)-n,n-Diisobutylcarbamoylmethylphosphine Oxide for Understanding Its Extraction in Reprocessing Spent Nuclear Fuels. *Eur. J. Chem.* **2011**, 17 (47), 13206–13216. https://doi.org/10.1002/chem.201102491.

(94) Burgoyne, E. D.; Molina-Osorio, A. F.; Moshrefi, R.; Shanahan, R.; McGlacken, G. P.; Stockmann, T. J.; Scanlon, M. D. Detection of: Pseudomonas Aeruginosa Quorum Sensing Molecules at an Electrified Liquid|liquid Micro-Interface through Facilitated Proton Transfer. *Anlst.* **2020**, 145 (21), 7000–7008. https://doi.org/10.1039/d0an01245a.

(95) Jiang, Q.; Reader, H. E.; Stockmann, T. J. Electrochemical Characterization of Fe(II) Complexation Reactions at an Electrified Micro Liquid-Liquid Interface. *ChemElectroChem.* **2021**, 8(9), 1–9. https://doi.org/10.1002/celc.202100127.

(96) Stockmann, T. J.; Deng, H.; Peljo, P.; Kontturi, K.; Opallo, M.; Girault, H. H. Mechanism of Oxygen Reduction by Metallocenes near Liquid|liquid Interfaces. *J. Electroanal. Chem.* **2014**, 729, 43–52. https://doi.org/10.1016/j.jelechem.2014.07.001.

(97) Su, B.; Abid, J. P.; Fermín, D. J.; Girault, H. H.; Hoffmannová, H.; Krtil, P.; Samec, Z. Reversible Voltage-Induced Assembly of Au Nanoparticles at Liquid|Liquid Interfaces. *J. Am. Chem. Soc.* **2004**, 126 (3), 915–919. https://doi.org/10.1021/ja0386187.

(98) Smirnov, E.; Scanlon, M. D.; Momotenko, D.; Vrubel, H.; Méndez, M. A.; Brevet, P. F.; Girault, H. H. Gold Metal Liquid-like Droplets. *ACS. Nano.* **2014**, 8 (9), 9471–9481. https://doi.org/10.1021/nn503644v.

(99) Moshrefi, R.; Stockmann, T. J. Electrodeless Synthesis of Low Dispersity Au Nanoparticles and Nanoclusters at an Immiscible Micro Water|Ionic Liquid Interface. *Nanomaterials.* **2022**, 12 (16). https://doi.org/10.3390/nano12162748.

(100) Moshrefi, R.; Suryawanshi, A.; Stockmann, T. J. Electrochemically Controlled Au Nanoparticle Nucleation at a Micro Liquid | Liquid Interface Using Ferrocene as Reducing Agent. *Electrochem. Commun.* **2021**, 122, 106894. https://doi.org/10.1016/j.elecom.2020.106894.

(101) Moshrefi, R.; P. Connors, E.; Merschrod, E.; Stockmann, T. J. Simultaneous Electropolymerization/Au Nanoparticle Generation at an Electrified Liquid | Liquid Micro-Interface. *Electrochim. Acta.* **2022**, 426, 140749. https://doi.org/10.1016/j.electacta.2022.140749.

(102) Stockmann, T. J.; Ding, Z. Uranyl Ion Extraction with Conventional PUREX/TRUEX Ligands Assessed by Electroanalytical Chemistry at Micro Liquid | Liquid Interfaces. *Anal. Chem.* **2011**, 83 (19), 7542–7549. https://doi.org/10.1021/ac2018684.

(103) Stockmann, T. J.; Montgomery, A. M.; Ding, Z. Correlation of Stoichiometries for Rb + Extraction Determined by Mass Spectrometry and Electrochemistry at Liquid|liquid Interfaces. *Anal. Chem.* **2012**, 84 (14), 6143–6149. https://doi.org/10.1021/ac301051e.

(104) Stockmann, T. J.; Lu, Y.; Zhang, J.; Girault, H. H.; Ding, Z. Interfacial Complexation Reactions of Sr 2+ with Octyl(Phenyl)-n,n-Diisobutylcarbamoylmethylphosphine Oxide for Understanding Its Extraction in Reprocessing Spent Nuclear Fuels. *Eur. J. Chem.* **2011**, 17 (47), 13206–13216. https://doi.org/10.1002/chem.201102491.

(105) Stockmann, T. J.; Angelé, L.; Brasiliense, V.; Combellas, C.; Kanoufi, F. Platinum Nanoparticle Impacts at a Liquid|Liquid Interface. *Angew. Chem.* **2017**, 56 (43), 13493–13497. https://doi.org/10.1002/anie.201707589.

(106) Tang, X.; Raskin, J. P.; Kryvutsa, N.; Hermans, S.; Slobodian, O.; Nazarov, A. N.; Debliquy, M. An Ammonia Sensor Composed of Polypyrrole Synthesized on Reduced Graphene Oxide by Electropolymerization. *Sens. Actuators. B. Chem.* **2020**, 305, 127423. https://doi.org/10.1016/j.snb.2019.127423.

(107) Gschwend, G. C.; Olaya, A.; Girault, H. H. How to Polarise an Interface with Ions: The Discrete Helmholtz Model. *Chem. Sci.* **2020**, 11 (39), 10807–10813. https://doi.org/10.1039/d0sc00685h.

(108) Girault, H. H. Analytical and Physical Electrochemistry; EPFL press, 2004.

(109) Peljo, P.; Girault, H. H. Liquid|Liquid Interfaces, Electrochemistry At

- Update Based on the Original Article by Frédéric Reymond, Hubert H. Girault, *Encyclopedia of Analytical Chemistry* , 2000, John Wiley & Sons, Ltd .
  In *Encyclopedia of Analytical Chemistry* (eds R.A. Meyers and R.A. Meyers). **2012**. https://doi.org/10.1002/9780470027318.a5306.pub2.

(110) Levine, I. N. Physical Chemistry, ; Hodge, TL, Oberbroeckling, SR, Eds. McGraw-Hill Education: New York, NY 2008.

(111) Riva, J. S.; Bassetto, V. C.; Girault, H. H.; Olaya, A. J. Standard Ion Transfer Potential at the Water|butyronitrile Interface. *J. Electroanal. Chem.* **2019**, 835, 192–196. https://doi.org/10.1016/j.jelechem.2019.01.041.

(112) Samec, Z.; Mareček, V.; Weber, J. Detection of an Electron Transfer across the Interface between Two Immiscible Electrolyte Solutions by Cyclic Voltammetry with Four-Electrode System. *J. Electroanal. Chem. Interfacial. Electrochem.* **1979**, 96 (2), 245–247. https://doi.org/10.1016/S0022-0728(79)80382-4.

(113) Deng, H.; Peljo, P.; Huang, X.; Smirnov, E.; Sarkar, S.; Maye, S.; Girault, H. H.; Mandler, D. Ionosomes: Observation of Ionic Bilayer Water Clusters. *J. Am. Chem. Soc.* **2021**, 143 (20), 7671–7680. https://doi.org/10.1021/jacs.0c12250.

(114) Mareček, V. Electrochemical Monitoring of the Co-Extraction of Water with Hydrated Ions into an Organic Solvent. *Electrochem. Commun.* **2018**, 88 (December 2017), 57–60. https://doi.org/10.1016/j.elecom.2018.01.017.

(115) Mareček, V.; Samec, Z. Ion Transfer Kinetics at the Interface between Two Immiscible Electrolyte Solutions Supported on a Thick-Wall Micro-Capillary. A Mini Review. *Curr. Opin. Electrochem.* **2017**, 1 (1), 133–139. https://doi.org/10.1016/j.coelec.2016.11.004.

(116) Cheng, Y.; Schiffrin, D. J. A.C. Impedance Study of Rate Constants for Two-Phase Electron-Transfer Reactions. *J. Chem. Soc., Faraday Trans.* **1993**, 89 (2), 199. https://doi.org/10.1039/ft9938900199.

Chapter 2

2. Electrochemically controlled Au nanoparticle nucleation at a micro liquid|liquid interface using ferrocene as reducing agent

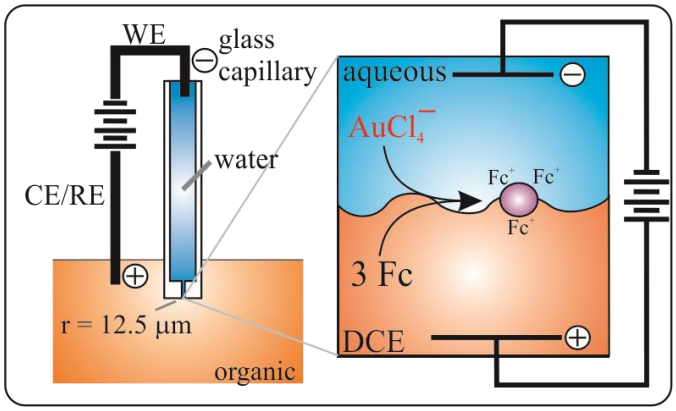

2.1. Statement of Co-Authorship

This chapter has been published under the above title in *Electrochemistry Communications* **2021**, 122, 106894. It is presented here in a modified format that includes all contributions for completeness and context.

Authors: Reza Moshrefi, Abhishek Suryawanshi, and Dr. T. Jane Stockmann

This article was a group effort combining the work of co-authors from the research groups of T. Jane Stockmann

Reza Moshrefi (listed in the paper as 1st author): Performed electrochemical experiments, material characterization, contributed to formal analysis, investigation, writing - review & editing, and validation.

Abhishek Suryawanshi: Contributed to material characterization.

Dr. T. Jane Stockmann: Is the principal investigator of this work, who led the project and contributed to conceptualization, methodology, writing – original draft, validation, supervision, project administration, funding acquisition.

2.2. Introduction

Owing to their catalytic[1–6] and physicochemical[7–10] properties, metal nanoparticles (NPs) have been exploited for numerous analytical[11–15], energy[6,16–18] and biological[19–21] applications. For example, Ma *et al.*[15] constructed a tunable nanoplasmonic mirror using Au NPs that can be reversibly and controllably deposited on the TiN coated Ag substrate through the application of a potential. Through this system, the authors were able to reproducibly tune the reflectance properties of the material surface and garner valuable kinetic information concerning NP assembly/disassembly. Pt NPs have been used effectively as catalysts for hydrogen and ethanol/methanol fuel cell oxidation[17,18] as well as to catalyze the oxygen reduction reaction at liquid|liquid interfaces.[16,22,23]

Applications such as these have spurred research towards enhanced preparation methods to control NP size and morphology. In 1994, Brust *et al.*[24] published their seminal work of Au NP preparation at an immiscible liquid|liquid, water|toluene, interface using $LiBH_4$ in the presence of an alkanethiol. Alkanethiol (SR) is first introduced to the system and has a complex chemical interplay with the dissolved Au(III) acting as both reductants, forming Au(I), and finally capping agent after $LiBH_4$ further reduces Au(I) to Au(0).[25] Indeed, at low Au(III):SR ratios, SR acts solely as a reducing agent; however, at higher ratios, $[Au(I)SR]_n$ polymeric species may form which is highly dependent on reaction conditions.[26,27] Multiple groups have since studied NP nucleation at

liquid|liquid interfaces generating Au[27–38], Pt[23,39,40], and other precious metal NPs.[41,42] However, Au NPs are of particular interest due to their biocompatibility[19] and long-term stability.[6,24] Au salts readily dissolve in aqueous solutions; however, they can undergo ligand substitution which complicates their redox chemistry.[30]

The liquid|liquid interface, or interface between two electrolytic solutions (ITIES), exploited by Brust *et al.*[24] is advantageous since it is highly reproducible and can be easily polarized by electrodes positioned in either phase creating a Galvani potential difference localized across the water|oil (w|o) interface; ($\phi_w - \phi_o = \Delta_o^w\phi$).[6,43,44] The ITIES is also molecularly smooth which can inhibit particle growth through an absence of nucleation sites.[33] Uehara and Dryfe's groups have been extensively investigating Au NP formation at the w|o interface for more than a decade.[27,29–31] They characterized the so-called Brust-Schiffrin Au NP mechanism of formation at the water|1,2-dichloroethane (w|DCE) interface using ion transfer voltammetry coupled with X-ray absorption fine structure (XAF) and transmission electron microscopy (TEM). They discovered that if the alkanethiol concentration exceeded the stoichiometric requirement an insoluble form of $[Au(I)(SR)]_n$ precipitate formed that could not be further reduced; furthermore, they noted that the Au NP size was linked to the alkanethiol:gold salt ratio.[27] They also investigated Au ligand exchange using $Fe(II)(CN)_6^{4-}$ as reducing agent in the aqueous phase and $AuCl_4^-$ installed in the organic phase; however, Au NP formation was found to be hindered without the presence of artificial nucleation sites such as Pd NPs, which the group prepared ex situ and adsorbed at the ITIES.[30,33] Recently, Nishi and co-workers were able to generate Janus-type Au/polythiophene NPs at a water|ionic liquid interface using terthiophene as the electron donor which also polymerizes, coating one-half of the NP, while the ionic liquid phase influenced particle growth towards its side of the ITIES.[28] These works focused on the large-ITIES (mm scale) and only used

the micro-ITIES, often positioned at a microhole, for diagnostic interrogation to identify the ion species transferring at a given applied potential.

Herein, Au NP nucleation at a micro-ITIES between w|DCE has been investigated with ferrocene (Fc) employed as electron donor over three pH regimes and multiple [Au salt]:[Fc] ratios. Fc and its derivatives are ubiquitous in electrochemical investigations owing to their reversible redox behavior and chemical stability.[45,46] By employing a micro-ITIES combined with potential, aqueous phase pH, and Au salt:Fc concentration ratio control, the driving force of $AuCl_4^-$ reduction can be finetuned to control Au NP size and morphology. The electrolytic cell employed is amendable to parallelization/scale up and could be a platform for industrialization/manufacturing of NP modified substrate surfaces.

2.3. Material and methods

All reagents were used as received without additional purification unless otherwise indicated. All aqueous solutions were made using ultrapure water from a MilliQ filtration system (>18.2 MΩ cm). Potassium tetrachloroaurate ($KAuCl_4$, >98%), hydrochloric acid (HCl, >37%), sodium hydroxide (NaOH, ≥98%), trioctylphosphine (97%), bromooctane (99%), and 1,2-dichloroethane (DCE, ≥99.0%) were obtained from Sigma-Aldrich. Tetrakis(pentaflorophenyl)borate lithium etherate (LiTB, >99%) was bought from Boulder Scientific. The ionic liquid tetraoctylphosphonium tetrakis(pentafluorophenyl)borate ($P_{8888}TB$) was prepared as reported elsewhere[47] and used as a supporting electrolyte in the organic phase.

Transmission electron microscopy (TEM) images were acquired using a Tecnai Spirit Transmission Electron Microscope with samples prepared on 200 Mesh Cu ultrathin/lacey carbon grids (Electron Microscopy Sciences).

All electrochemical measurements were recorded using the PG-618-USB potentiostat (HEKA Electroniks) along with a modified pipette holder with integrated working electrode (WE) connected to an integrated Au wire (0.2 mm diameter, Fisher Scientific). The Au wire was soldered into place and a liberal coating of 'Liquid electrical tape' (Canadian Tire) was applied to inhibit $AuCl_4^-(aq)$ reaction with the solder (96.5% Sn, 3.0% Ag, 0.5% Cu). A Pt wire served as the counter/reference electrode (CE/RE) and was immersed in the organic solvent phase. The modified holder was used to support the aqueous phase held in a pulled borosilicate glass capillary (Goodfellow) with a 25 μm diameter orifice at the tip; detailed micropipette fabrication is provided elsewhere.[48,49] The liquid|liquid interface was maintained at the tip and monitored using a 12 × zoom lens assembly (Navitar) and 18 megapixel CCD camera (AmScope). The electrolytic cells employed have been summarized in Scheme 2-1.

$$\mathrm{Au}\left|\mathrm{AuCl_3}\right|\begin{matrix}x\ \mathrm{mM\ KAuCl_4}\\(aq)\end{matrix}\Big\|\begin{matrix}y\ \mathrm{mM\ Fc}\\5\ \mathrm{mM\ P_{8888}TB}\\(DCE)\end{matrix}\Big|\mathrm{PtTB}\left|\mathrm{Pt}\right. \qquad \text{[Cell 2-1]}$$

$$\mathrm{Au}\left|\mathrm{AuCl_3}\right|\begin{matrix}z\ \mathrm{mM\ HCl}\\x\ \mathrm{mM\ KAuCl_4}\\(aq)\end{matrix}\Big\|\begin{matrix}y\ \mathrm{mM\ Fc}\\5\ \mathrm{mM\ P_{8888}TB}\\(DCE)\end{matrix}\Big|\mathrm{PtTB}\left|\mathrm{Pt}\right. \qquad \text{[Cell 2-2]}$$

$$\mathrm{Au}\left|\mathrm{AuCl_3}\right|\begin{matrix}w\ \mathrm{mM\ NaOH}\\x\ \mathrm{mM\ KAuCl_4}\\(aq)\end{matrix}\Big\|\begin{matrix}y\ \mathrm{mM\ Fc}\\5\ \mathrm{mM\ P_{8888}TB}\\(DCE)\end{matrix}\Big|\mathrm{PtTB}\left|\mathrm{Pt}\right. \qquad \text{[Cell 2-3]}$$

Scheme 2-1 electrolytic cells employed, where w, x, y, and z indicate the concentrations of NaOH, $KAuCl_4$, Fc (ferrocene), and HCl used, respectively. In each case, 5 mM of $P_{8888}TB$ (tetraoctylphosphonium tetrakis(pentafluorophenyl)borate) was added to the DCE phase as supporting electrolyte. The double line indicates the immiscible, polarizable liquid/liquid interface.

2.4. Results and discussion

Cyclic voltammograms (CVs) recorded using Cell 2-1 and 2-2 (see Scheme 2-1) without ferrocene (Fc) added to the DCE phase ($y = 0$) have been plotted in Figure 2-1. The black, solid trace (Cell 2-1) is the *i*-V response with only 0.5 mM $KAuCl_4$ in the aqueous phase as analyte and

supporting electrolyte. At positive potentials, the polarizable potential window (PPW) was limited by K^+ transfer from w → o seen as a sharp increase in current at ~0.5 V. The negative potential limit was not reached; instead, as the potential was scanned from positive to negative three peak-shaped waves were observed at 0.126, –0.068, and –0.507 V corresponding to $AuCl_4^-$, $AuCl_3(OH)^-$, and Cl^- transfer, respectively, from w → o.[30] The potential was referenced to formal Cl^- transfer taken to be $\Delta_o^w\phi_{Cl^-}^{o'} = -0.479$ V.[31,50] Thus, the respective simple ion transfer potentials of $AuCl_3(OH)^-$and $AuCl_4^-$ were observed to be –0.040 and 0.154 V, which are close to reported values.[27,30] Scanning the potential back from negative to positive, three steady state waves were observed at –0.479, –0.040, and 0.154 V, and are indicative of the respective reversible Cl^-, $AuCl_3(OH)^-$and $AuCl_4^-$ transfer back from o → w. The asymmetric *i*-V signal is owing to the pipette geometry which gives rise to an asymmetry in the diffusion regimes inside (linear diffusion) and outside (hemispherical diffusion) the pipette; these results are in good agreement with those described previously for ion transfer at a micropipette.[48,51–54] The addition of 10 mM of HCl(aq) (Cell 2-2 in Scheme 2-1), red, dashed curve in Figure 2-1, results in the disappearance of the proposed $AuCl_3(OH)^-$ transfer wave owing to the acid stabilization of $AuCl_4^-$.[30,35] Speciation of $AuCl_{(4-\gamma)}(OH)_\gamma^-$ has been characterized extensively both photometrically[35] as well as electrochemically [30] and it is possible that $AuCl_2(OH)_2$ species also contribute to the central peak in the black[30] trace in Figure 2-1. Therefore, the Au salt concentrations indicated in Scheme 2-1 for Cell 2-1 (*x*) describe the total Au salt concentration.

Next, the electrochemical response of Cells 2-1 and 2-2 were investigated towards changing [Fc] in the organic phase. With increasing [Fc] in Cell 2-1 (Figure 2-2D-F) the $AuCl_4/AuCl_3(OH)$ transfer waves steadily decrease in current intensity and are replaced by a positive peak-shaped curve at ~0.330 V. This is exemplified in Figure 2-2B where [$KAuCl_4$] = 5 mM and [Fc] was

increased incrementally in DCE from 0.05 to 15 mM; for Figure 2-2B–F, the final Fc concentration was chosen to be in a 1:3 concentration ratio of $KAuCl_4$:Fc in order to satisfy the stoichiometric $3e^-$ requirement for reduction of $AuCl_4^-$ to Au^0 if Fc behaves as a 1*e* donor. At [Fc] = 1 mM in Figure 2-2B the negative $AuCl_4^-$ transfer wave is diminished in intensity and a positive sigmoidal wave begins to emerge; while at [Fc] = 5 mM, the $AuCl_4^-$ wave has been completely replaced by a positive peak-shaped wave with a peak potential at ~0.340 V. Similar experiments were also performed at pH = 8.5 (Cell 2-3) and elicited a similar trend with changing [Fc] (see Figure A1 of Appendix A). Optical images were taken before and after each CV (Figure 2-3A and B, respectively) and show a purple precipitate has formed near and above the microchannel after a single CV cycle was performed.

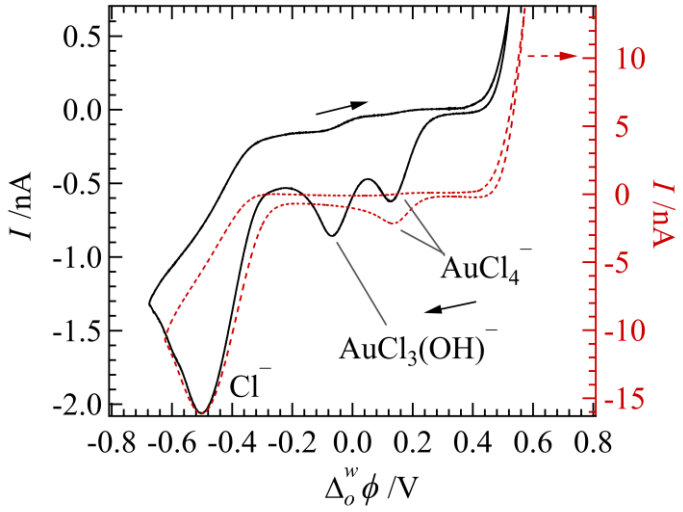

Figure 2-1 Cyclic voltammograms recorded using Cells 2-2 (red, dashed curve) with and 2-1 without (black, solid curve) 10 mM HCl (aq) at 20 mV s^{-1} without ferrocene (Fc) in DCE (y =0) and with 0.5 mM $KAuCl_4$ (aq). Black, solid arrows indicate scan direction while the red, dashed arrow indicates the associated axis. Peaks have been labelled with the ion undergoing simple ion transfer.

Based on these results, it was hypothesized that Fc, operating as an electron donor, reduces $AuCl_4^-$ to Au nanoparticles (NPs) at the liquid|liquid interface through the following two possible interfacial mechanisms,

$$AuCl_4^-(aq) + 3Fc(org) \rightarrow Au(s) + 3Fc^+(org) + 4Cl^-(aq) \qquad 2\text{-}1$$

$$AuCl_{(4-\gamma)}(OH)_\gamma^-(aq) + \gamma H^+(aq) + 3Fc(org) \rightarrow Au(s) + 3Fc^+(org) + (4-\gamma)Cl^-(aq) + \gamma H_2O \qquad 2\text{-}2$$

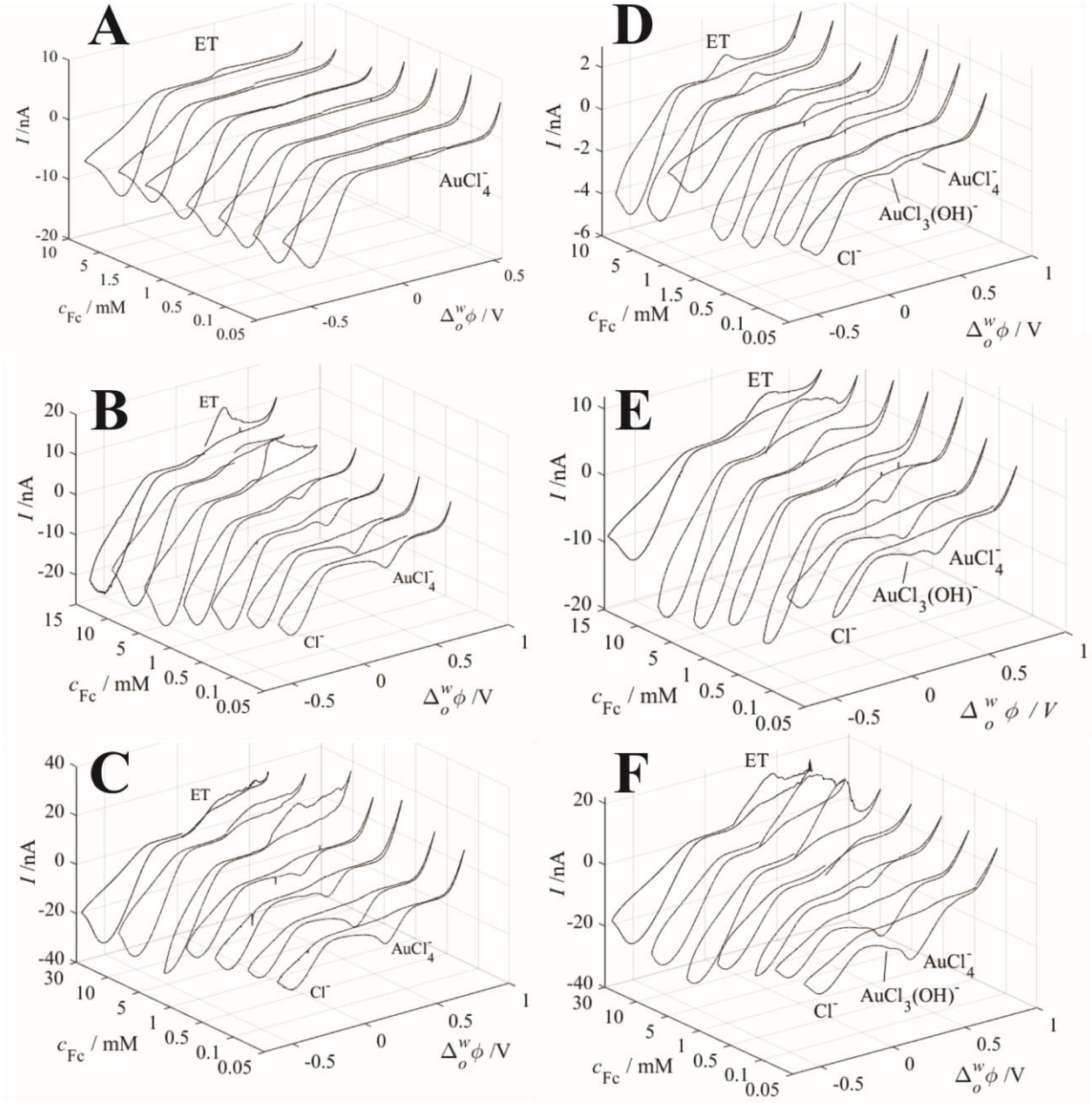

Figure 2-2 Overlay of CVs recorded using Cell 2-1 (D-F) and 2-2 (A-C, [HCl] =10 mM) while changing [Fc] (c_{Fc}). Initial gold salt concentrations where 0.5 (A, D), 5 (B, E), and 10 mM (C, F). All instrumental parameters were the same as those employed in Figure 2-1. Ions associated with various transfer peaks have been labelled; ET = electron transfer peak.

Thus, the positive peak current observed at high [Fc] in Figure 2-2 is the result of electron transfer from o → w in which the process is diffusion limited by $AuCl_4^-$ in the aqueous phase. This agrees with a recent study utilizing the water|diethyl ether interface.[55] At high [Fc] and [$KAuCl_4$] large disruptions in the *i*-V signal were recorded (*e.g.*, see Figure 2-2C, c_{Fc} = 30 mM). It is hypothesized that these large fluctuations in current are owing to the disruption of the interface through Au NP formation which generates Marangoni type changes in surface tension. Additionally, the simple ion transfer of Fc^+ is well characterized[56] with $\Delta_o^w\phi'^o_{Fc^+}$= –0.016 V[57]; however, no simple Fc^+ transfer was recorded. Therefore, it is likely that Fc^+ acts as a capping agent and is adsorbed onto the Au NPs at the ITIES surface. Thus, Fc^+ is not available to undergo simple ion transfer. Fc behaving as a capping agent further agrees with the results of Ciganda *et al.*[55]

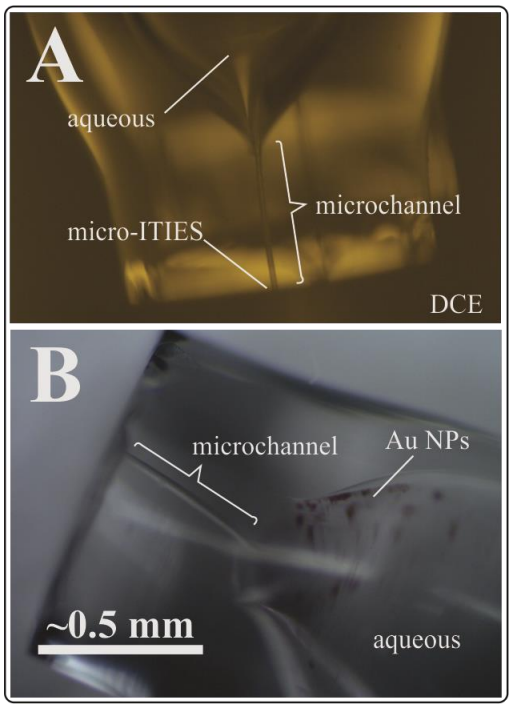

Figure 2-3 Optical micrographs of the pipette tip before (A) and after (B) electrolytically induced interfacial reaction of $AuCl_4$(aq) with Fc(org) via one CV cycle at 0.020 V s^{-1} as shown in Figure 2-2.

The mechanism of how Au NPs arrived at the top of the microchannel (see Figure 2-3B) is unclear. However, Ciganda *et al.* previously measured the ζ-potential for similar Fc-capped NPs to be – 0.015 V[55]; therefore, it is hypothesized that the NPs are attracted up the microchannel under an extreme positive electric field gradient in the direction of the aqueous electrode. Admittedly, this is still an open question that will be addressed in future work.

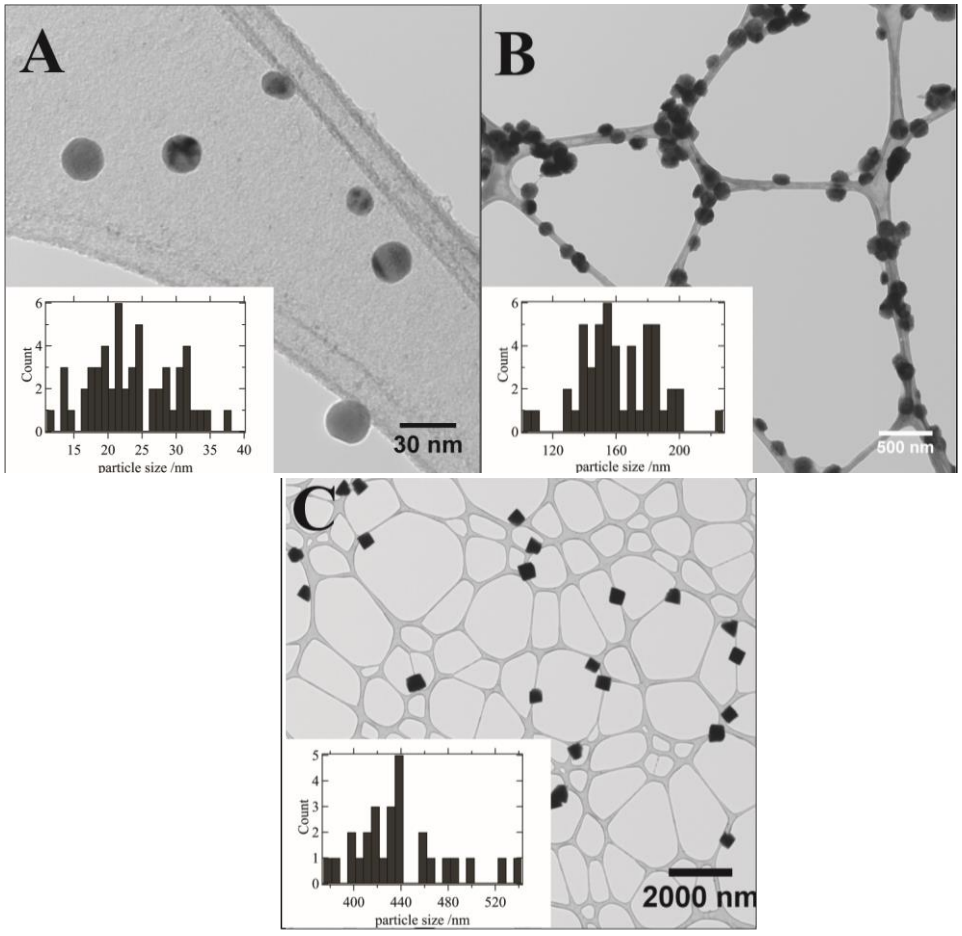

Figure 2-4 TEM micrographs of Au NPs acquired using [Fc] =3 mM and [$KAuCl_4$] =1 mM at pH 2 (A), ~5.5 (B), and 8.5 (C) in the aqueous phase for Cells 2-2, 2-1, and 2-3, respectively. Histograms of particle sizes are inset.

TEM samples of the NPs were acquired by removing the pipette from the organic phase after a particular potential program/waveform was applied and ejecting a droplet onto a TEM grid; the grid was then dried under N_2. TEM micrographs are illustrated in Figure 2-4 using Cells 2-1 – 2-

3 while varying the pH and maintaining the [Fc] and [$KAuCl_4$] at 3 and 1 mM, respectively, and after a single CV was performed as depicted in Figure 2-2. At pH 2 and ~5.5 spherical Au NPs were observed with average sizes of 24 and 228 nm, respectively; at pH 8.5 the average size further increased to 439 nm and the NP shape changed from spherical to cubic indicating a transition to bulk Au metal-like formation. Integration of the ET peak-current signal for the 3–1 mM, Fc to $KAuCl_4$ case at pH 2, 5.5, and 8.5 resulted in an average charge transfer of ~3 μC for each pH region. This suggests that roughly the same amount of Au salt is reduced at each pH; therefore, it is likely that a greater number of smaller Au NPs are formed a low pH, while fewer, larger NPs are generated towards high pH. These calculations agree with particle counts roughly determined through TEM optical images.

The formal reduction potential of $AuCl_4^-/Au$ $\left(E^{o',H_2O}_{Au(III)/Au}\right)$ in aqueous is 1.002 V, while the Fc^+/Fc $\left(E^{o',DCE}_{Fc^+/Fc}\right)$ couple in DCE is 0.640 V.[56,58] Using Eq. (2-2), a general formulation for electron transfer across the liquid|liquid interface ($\Delta^w_o\phi_{ET}$) can be derived from the Nernst equation[22,58], such that,

$$\Delta^w_o\phi_{ET} \approx E^{o',DCE}_{Fc^+/Fc} - E^{o',H_2O}_{Au(III)/Au} - \frac{(0.059\ V)}{3}\log\left(\left[H^+\right]^\gamma\right) \qquad 2\text{-}3$$

Since Fc can partition into the aqueous phase[59] (see Figure A3 of Appendix A), it is of interest to determine the homogeneous, aqueous thermodynamic case as well for electron transfer (E_{cell}), which is calculated somewhat differently,

$$E_{cell} \approx E^{o',H_2O}_{Fc^+/Fc} - E^{o',H_2O}_{Au(III)/Au} - \frac{(0.059\ V)}{3}\log\left(\left[H^+\right]^\gamma\right) \qquad 2\text{-}4$$

For the complete algebraic formulation of Eqs. (2-3) and (4) see Appendix A. In Eq. (2-4) $E^{o',DCE}_{Fc^+/Fc}$ was assumed to be 0.310 V.[60] At low pH, the final term in Eqs. (2-3) and (2-4) can be

neglected since the $AuCl_4^-$ species dominates (γ =0), while at higher pH it becomes a factor with $AuCl_{(4-\gamma)}^-(OH)_\gamma^-$ speciation. In this way, $\Delta_o^w\phi_{ET}$ was calculated to be –0.362, –0.254, and –0.194 V, while E_{cell} was determined to be 0.692, 0.584, and 0.524 V for pH 2, 5.5, and 8.5, respectively. Thus, for interfacial electron transfer the electromotive force (emf) is greatly reduced at low pH and an applied potential is required to induce electron transfer. This is reflective of the lack of nucleation sites at the liquid|liquid interface for nascent NPs to grow, which is much easier on a metal/solid surface.[31,61,62] These *back-of-the-envelope* calculations agree with the voltametric responses at each pH tested in which an applied potential was necessary to induce heterogeneous electron transfer. For the homogeneous electron transfer case where Fc partitions to the aqueous phase, the reaction should be spontaneous regardless of pH. However, Fc partitioning is limited[16,59] so if the potential pulse/program is started quickly enough, then the interfacial electron transfer mechanism should be thermodynamically favoured[63] and hence this is likely why all the NPs observed after CV deposition are uniform in size and morphology.

To test this the pipette tip was submerged in the organic phase for 10–30 s, removed, and then sampled; whereby, the potential was not controlled, i.e., left at open circuit potential (OCP), and where an applied amperometric pulse at 500 mV (high overpotential) was maintained. In each instance Cell 2-2 was used containing 3 mM Fc (org) as well as 1 mM $KAuCl_4$ and 10 mM HCl (aq). After each run, a TEM sample was obtained and rinsed with MilliQ water; Figure A2 (see Appendix A) shows 3 examples of TEM micrographs generated from these experiments. At OCP a mixture of Au nano-sheets, spheres, rods, and cubes at a broad range of sizes were imaged (Figure A2A of the Appendix A). For the 10 and 20 s applied potential (Figure A2B of the Appendix A) only nano-sheets and spheres were recorded; however, for the 30 s applied potential case only highly disperse cubes were observed (see Figure A2C in the Appendix A). The formation

of nano-sheets agrees with a recent study by Sachdev *et al.*[45] in which they used a micro-emulsion (water|hexane) in a flow reactor and decamethylferrocene $\left(FeCp_2^*\right)$ as the reducing agent to generate Au NPs and nano-sheets. In that work,[45] the ITIES was essentially at OCP since no common ion or phase transfer catalyst was employed; however, the authors were able control the Au NP size by controlling the size of the emulsion droplet and $\left[FeCp_2^*\right]$. Moreover, it is likely that at a large-ITIES the turbulent, convective mixing generated as a result of constructing the cell just to perform the experiment, as well as that generated in a flow reactor, would likely enhance partitioning of Fc. In other words, the Fc partitioning route starts far from equilibrium; however, with mixing, this pathways position towards equilibrium is advanced and the homogeneous electron transfer route is favoured. Hence, interfacial size and convection play an important role.

It is hypothesized that at OCP Fc can partition more freely and the aqueous, homogeneous electron transfer route from Fc to Au(III) is enhanced. However, while under cyclic voltammetric polarization the interfacial route is preferred. The latter agrees with a computational study by Hirano *et al.*[63] at the water|CH_2Cl_2 interface for electron transfer between Fc and $Fe(CN)_6^{3-}$. The mechanistic difference between CV and amperometrically deposited Au NPs is unclear but will be the focus of future optical studies beyond the scope of the present work.

As noted by Brust *et al.*[24], $AuCl_4^-/AuCl_{(4-\gamma)}^-(OH)_\gamma^-$ species can partition into low polarity organic solvents; however, due to the orientation of the pipette, it was not possible to successfully sample the organic phase for TEM analysis.

2.5. Conclusion

Herein, we have demonstrated the reproducible generation of Au NPs at a micro-ITIES with size control exhibited through pH and over-potential application. By varying the concentration of

Fc in the DCE phase, the transition from simple $AuCl_4^-/AuCl_{(4-\gamma)}(OH)_\gamma^-$ transfer to interfacial electron transfer between Fc and the Au salt was observed. Owing to the slightly high overpotentials combined with the small interfacial size (25 μm in diameter) Fc partitioning to the aqueous phase can be limited and an interfacial electron transfer mechanism can become preferred. This results in Au NP size control from between 20 and 400 nm. We are currently exploring the effect of pipette geometry and different pulse/waveform programs on NP size as well as the mechanistic routes to nano-sheet, rod, and cube formation.

Finally, one can imagine that the micropipette method would be highly amenable to industrialization through parallelization; whereby, the micropipette is first immersed in an organic solution containing the electron donor (e.g., Fc), the NPs are electrochemically generated, the pipette is removed from the solution, and then the aqueous NP solution is dispensed onto a substrate of interest such as a solid electrode material.

2.6. References

(1) Xu, Z.; Xiao, F.-S.; Purnell, S. K.; Alexeev, O.; Kawi, S.; Deutsch, S. E.; Gates, B. C. Size-Dependent Catalytic Activity of Supported Metal Clusters. *Nature.* **1994**, *372* (6504), 346–348. https://doi.org/10.1038/372346a0.

(2) J. Albero, H. Garcia. Catalysis by supported gold nanoparticles. *Nanosci. Nanotechnol*. **2019**, 91-108. https://doi.org/10.1016/B978-0-12-803581-8.11279-2

(3) Xie, C.; Niu, Z.; Kim, D.; Li, M.; Yang, P. Surface and Interface Control in Nanoparticle Catalysis. *Chem. Rev.* **2020**, *120* (2), 1184–1249. https://doi.org/10.1021/acs.chemrev.9b00220.

(4) Wang, Q.; Astruc, D. State of the Art and Prospects in Metal-Organic Framework (MOF)-Based and MOF-Derived Nanocatalysis. *Chem. Rev.* **2020**, *120* (2), 1438–1511. https://doi.org/10.1021/acs.chemrev.9b00223.

(5) Wang, F.; Wong, R. J.; Ho, J. H.; Jiang, Y.; Amal, R. Sensitization of Pt/TiO_2 Using Plasmonic Au Nanoparticles for Hydrogen Evolution under Visible-Light Irradiation. *ACS. Appl. Mater. Int.* **2017**, *9* (36), 30575–30582. https://doi.org/10.1021/acsami.7b06265.

(6) Scanlon, M. D.; Smirnov, E.; Stockmann, T. J.; Peljo, P. Gold Nanofilms at Liquid-Liquid Interfaces: An Emerging Platform for Redox Electrocatalysis, Nanoplasmonic Sensors, and Electrovariable Optics. *Chem. Rev.* **2018**, *118* (7), 3722–3751. https://doi.org/10.1021/acs.chemrev.7b00595.

(7) Roduner, E. Size Matters: Why Nanomaterials Are Different. *Chem. Soc. Rev.* **2006**, *35* (7), 583–592. https://doi.org/10.1039/b502142c.

(8) Sokolov, S. v.; Eloul, S.; Kätelhön, E.; Batchelor-McAuley, C.; Compton, R. G. Electrode–Particle Impacts: A Users Guide. *Phys. Chem. Chem. Phys.* **2017**, *19* (1), 28–43. https://doi.org/10.1039/c6cp07788a.

(9) Robbs, P. H.; Rees, N. V. Nanoparticle Electrochemistry. *Phys. Chem. Chem. Phys.* **2016**, *18* (36), 24812–24819. https://doi.org/10.1039/c6cp05101d.

(10) Rees, N. V. Electrochemical Insight from Nanoparticle Collisions with Electrodes: A Mini-Review. *Electrochem. Commun.* **2014**, *43*, 83–86. https://doi.org/10.1016/j.elecom.2014.03.018.

(11) Wang, H.; Zhang, T.; Zhou, X. Dark-Field Spectroscopy: Development, Applications and Perspectives in Single Nanoparticle Catalysis. *J. Phys. Condens. Matter.* **2019**, *31* (47), 473001. https://doi.org/10.1088/1361-648X/ab330a.

(12) Nadappuram, B. P.; Cadinu, P.; Barik, A.; Ainscough, A. J.; Devine, M. J.; Kang, M.; Gonzalez-Garcia, J.; Kittler, J. T.; Willison, K. R.; Vilar, R.; Ivanov, A. P.; Edel, J. B. Nanoscale Tweezers for Single-Cell Biopsies. *Nat. Nanotechnol.* **2019**, *14* (1), 80–88. https://doi.org/10.1038/s41565-018-0315-8.

(13) Montelongo, Y.; Sikdar, D.; Ma, Y.; McIntosh, A. J. S.; Velleman, L.; Kucernak, A. R.; Edel, J. B.; Kornyshev, A. A. Electrotunable Nanoplasmonic Liquid Mirror. *Nat. Mater.* **2017**, *16* (11), 1127–1135. https://doi.org/10.1038/NMAT4969.

(14) Lemineur, J.-F.; Stockmann, T. J.; Médard, J.; Smadja, C.; Combellas, C.; Kanoufi, F. Optical Nanoimpacts of Dielectric and Metallic Nanoparticles on Gold Surface by Reflectance Microscopy: Adsorption or Bouncing? *J. Anal. Test.* **2019**, *3* (2), 175–188. https://doi.org/10.1007/s41664-019-00099-8

(15) Ma, Y.; Zagar, C.; Klemme, D. J.; Sikdar, D.; Velleman, L.; Montelongo, Y.; Oh, S.-H.; Kucernak, A. R.; Edel, J. B.; Kornyshev, A. A. A Tunable Nanoplasmonic Mirror at an Electrochemical Interface. *ACS. Photon.* **2018**, *5* (11), 4604–4616. https://doi.org/10.1021/acsphotonics.8b01105.

(16) Stockmann, T. J.; Angelé, L.; Brasiliense, V.; Combellas, C.; Kanoufi, F. Platinum Nanoparticle Impacts at a Liquid|Liquid Interface. *Angew. Chem. Int. Ed.* **2017**, *56* (43), 13493–13497. https://doi.org/10.1002/anie.201707589.

(17) Zhang, Q.; Sayadi, A.; Pickup, P. G. Separation of Kinetic and Mass Transport Effects in the Electrolysis of Formic Acid in a Flow-through Cell. *Electrochim. Acta.* **2019**, *294*, 110–116. https://doi.org/10.1016/j.electacta.2018.10.088.

(18) Brueckner, T. M.; Hawboldt, K. A.; Pickup, P. G. Electrolysis of Pyrolysis Oil Distillates and Permeates in a Multi-Anode Proton Exchange Membrane Cell. *Appl. Catal. B.* **2019**, *256*, 117892. https://doi.org/10.1016/j.apcatb.2019.117892.

(19) Elahi, N.; Kamali, M.; Baghersad, M. H. Recent Biomedical Applications of Gold Nanoparticles: A Review. *Talanta.* **2018**, *184*, 537–556. https://doi.org/10.1016/j.talanta.2018.02.088.

(20) Aurand, E. R.; Usmani, S.; Medelin, M.; Scaini, D.; Bosi, S.; Rosselli, F. B.; Donato, S.; Tromba, G.; Prato, M.; Ballerini, L. Nanostructures to Engineer 3D Neural-Interfaces: Directing Axonal Navigation toward Successful Bridging of Spinal Segments. *Adv. Funct. Mater.* **2018**, *28* (12), 1700550. https://doi.org/10.1002/ADFM.201700550.

(21) Nemati, Z.; Um, J.; Zamani Kouhpanji, M. R.; Zhou, F.; Gage, T.; Shore, D.; Makielski, K.; Donnelly, A.; Alonso, J. Magnetic Isolation of Cancer-Derived Exosomes Using Fe/Au Magnetic Nanowires. *ACS. Appl. Nano. Mater.* **2020**, *3* (2), 2058–2069. https://doi.org/10.1021/acsanm.0c00263.

(22) Trojánek, A.; Langmaier, J.; Samec, Z. Electrocatalysis of the Oxygen Reduction at a Polarised Interface between Two Immiscible Electrolyte Solutions by Electrochemically Generated Pt Particles. *Electrochem. Commun.* **2006**, *8* (3), 475–481. https://doi.org/10.1016/J.ELECOM.2006.01.004.

(23) Nieminen, J. J.; Hatay, I.; Ge, P.; Méndez, M. A.; Murtomäki, L.; Girault, H. H. Hydrogen Evolution Catalyzed by Electrodeposited Nanoparticles at the Liquid|Liquid Interface. *Chem. Commun.* **2011**, *47* (19), 5548–5550. https://doi.org/10.1039/c1cc10637f.

(24) Brust, M.; Walker, M.; Bethell, D.; Schiffrin, D. J.; Whyman, R. Synthesis of Thiol-Derivatised Gold Nanoparticles in a Two-Phase Liquid–Liquid System. *J. Chem. Soc., Chem. Commun.* **1994**, 7, 801–802. https://doi.org/10.1039/C39940000801.

(25) Goulet, P. J. G.; Lennox, R. B. New Insights into Brust-Schiffrin Metal Nanoparticle Synthesis. *J. Am. Chem. Soc.* **2010**, *132* (28), 9582–9584. https://doi.org/10.1021/ja104011b.

(26) Zhu, L.; Zhang, C.; Guo, C.; Wang, X.; Sun, P.; Zhou, D.; Chen, W.; Xue, G. New Insight into Intermediate Precursors of Brust-Schiffrin Gold Nanoparticles Synthesis. *J. Phys. Chem. C.* **2013**, *117* (21), 11399–11404. https://doi.org/ 10.1021/jp402116x.

(27) Uehara, A.; Booth, S. G.; Chang, S. Y.; Schroeder, S. L. M.; Imai, T.; Hashimoto, T.; Mosselmans, J. F. W.; Dryfe, R. A. W. Electrochemical Insight into the Brust–Schiffrin Synthesis of Au Nanoparticles. *J. Am. Chem. Soc.* **2015**, *137* (48), 15135–15144. https://doi.org/10.1021/jacs.5b07825.

(28) Nishi, N.; Yajima, I.; Amano, K.-I.; Sakka, T. Janus-Type Gold/Polythiophene Composites Formed via Redox Reaction at the Ionic Liquid|Water Interface. *Langmuir.* **2018**, *34* (7), 2441–2447. https://doi.org/10.1021/acs.langmuir.7b03792.

(29) Booth, S. G.; Uehara, A.; Chang, S.-Y.; la Fontaine, C.; Fujii, T.; Okamoto, Y.; Imai, T.; Schroeder, S. L. M.; Dryfe, R. A. W. The Significance of Bromide in the Brust-Schiffrin Synthesis of Thiol Protected Gold Nanoparticles. *Chem. Sci.* **2017**, *8* (12), 7954–7962. https://doi.org/10.1039/c7sc03266h.

(30) Uehara, A.; Chang, S.-Y.; Booth, S. G.; Schroeder, S. L. M.; Mosselmans, J. F. W.; Dryfe, R. A. W. Redox and Ligand Exchange during the Reaction of Tetrachloroaurate with Hexacyanoferrate(II) at a Liquid-Liquid Interface: Voltammetry and X-Ray Absorption Fine-

Structure Studies. *Electrochim. Acta.* **2016**, *190*, 997–1006. https://doi.org/10.1016/j.electacta.2015.12.108.

(31) Uehara, A.; Hashimoto, T.; Dryfe, R. A. W. Au Electrodeposition at the Liquid-Liquid Interface: Mechanistic Aspects. *Electrochim. Acta.* **2014**, *118*, 26–32. https://doi.org/10.1016/j.electacta.2013.11.162.

(32) Kaminska, I.; Jonsson-Niedziolka, M.; Kaminska, A.; Pisarek, M.; Hołyst, R.; Opallo, M.; Niedziolka-Jonsson, J. Electrodeposition of Well-Adhered Multifarious Au Particles at a Solid|Toluene|Aqueous Electrolyte Three-Phase Junction. *J. Phys. Chem. C.* **2012**, *116* (42), 22476–22485. https://doi.org/10.1021/jp307674k.

(33) Gründer, Y.; Ho, H. L. T.; Mosselmans, J. F. W.; Schroeder, S. L. M.; Dryfe, R. A. W. Inhibited and Enhanced Nucleation of Gold Nanoparticles at the Water1,2-Dichloroethane Interface. *Phys. Chem. Chem. Phys.* **2011**, *13* (34), 15681–15689. https://doi.org/10.1039/c1cp21536a.

(34) Kaminska, I.; Niedziolka-Jonsson, J.; Roguska, A.; Opallo, M. Electrodeposition of Gold Nanoparticles at a Solid|ionic Liquid|aqueous Electrolyte Three-Phase Junction. *Electrochem. Commun.* **2010**, *12* (12), 1742–1745. https://doi.org/10.1016/j.elecom.2010.10.011.

(35) Usher, A.; McPhail, D. C.; Brugger, J. A Spectrophotometric Study of Aqueous Au(III) Halide-Hydroxide Complexes at 25-80 °C. *Geochim. Cosmochim. Acta.* **2009**, *73* (11), 3359–3380. https://doi.org/10.1016/j.gca.2009.01.036.

(36) Campbell, A. I.; Dryfe, R. A. W.; Haw, M. D. Deposition and Aggregation of Au at the Liquid | Liquid Interface. *Anal. Sci.* **2009**, *25* (2), 307–310. https://doi.org/10.2116/analsci.25.307.

(37) Lepková, K.; Clohessy, J.; Cunnane, V. J. Electrodeposition of Metal-Based Nanocomposites at a Liquid-Liquid Interface Controlled via the Interfacial Galvani Potential Difference. *Electrochim. Acta.* **2008**, *53* (21), 6273–6277. https://doi.org/10.1016/j.electacta.2008.04.025.

(38) Cheng, Y.; Schiffrin, D. J. Electrodeposition of Metallic Gold Clusters at the Water | 1,2-Dichloroethane Interface. *J. Chem. Soc. - Faraday Trans.* **1996**, *92* (20), 3865–3871. https://doi.org/10.1039/ft9969203865.

(39) Platt, M.; Dryfe, R. A. W.; Roberts, E. P. L. Structural and Electrochemical Characterisation of Pt and Pd Nanoparticles Electrodeposited at the Liquid|Liquid Interface. *Electrochim. Acta.* **2004**, *49*, 3937–3945. https://doi.org/10.1016/j.electacta.2004.02.050.

(40) Trojánek, A.; Langmaier, J.; Samec, Z. Random Nucleation and Growth of Pt Nanoparticles at the Polarised Interface between Two Immiscible Electrolyte Solutions. *J. Electroanal. Chem.* **2007**, *599* (2), 160–166. https://doi.org/10.1016/j.jelechem.2005.12.004.

(41) Guainazzi, M.; Silvestri, G.; Serravalle, G. Electrochemical Metallization at the Liquid-Liquid Interfaces of Non-Miscible Electrolytic Solutions. *J. Chem. Soc. Chem. Commun.* **1975**, No. 6, 200–201. https://doi.org/10.1039/C39750000200.

(42) Luo, K.; Dryfe, R. A. W. The Formation of Silver Nanofibres by Liquid | Liquid Interfacial Reactions: Mechanistic Aspects. *New. J. Chem.* **2009**, *33* (1), 157–163. https://doi.org/10.1039/b809654f.

(43) Peljo, P.; Girault, H. H. Liquid | Liquid Interfaces, Electrochemistry AtUpdate Based on the Original Article by Frédéric Reymond, Hubert H. Girault, Encyclopedia of Analytical Chemistry , © 2000, John Wiley & Sons, Ltd . *Encyclopedia of Analytical Chemistry* **2012**. https://doi.org/10.1002/9780470027318.a5306.pub2.

(44) Samec, Z.; Langmaier, J.; Kakiuchi, T. Charge-Transfer Processes at the Interface between Hydrophobic Ionic Liquid and Water. *Pure. Appl. Chem.* **2009**, *81* (8), 1473–1488. https://doi.org/10.1351/PAC-CON-08-08-36.

(45) Sachdev, S.; Maugi, R.; Woolley, J.; Kirk, C.; Zhou, Z.; Christie, S. D. R.; Platt, M. Synthesis of Gold Nanoparticles Using the Interface of an Emulsion Droplet. *Langmuir.* **2017**, *33* (22), 5464–5472. https://doi.org/10.1021/acs.langmuir.7b00564.

(46) Polcari, D.; Dauphin-Ducharme, P.; Mauzeroll, J. Scanning Electrochemical Microscopy: A Comprehensive Review of Experimental Parameters from 1989 to 2015. *Chem. Rev.* **2016**, *116* (22), 13234–13278. https://doi.org/10.1021/acs.chemrev.6b00067.

(47) Stockmann, T. J.; Boyle, P. D.; Ding, Z. Preparation and Crystal Structure of Tetraoctylphosphonium Tetrakis(Pentafluorophenyl)Borate Ionic Liquid for Electrochemistry at Its Interface with Water. *Catal. Today.* **2017**, *295*, 89–94. https://doi.org/10.1016/j.cattod.2017.05.030.

(48) Stockmann, T. J.; Lu, Y.; Zhang, J.; Girault, H. H.; Ding, Z. Interfacial Complexation Reactions of Sr^{2+} with Octyl(Phenyl)-*N,N*-Diisobutylcarbamoylmethylphosphine Oxide for Understanding Its Extraction in Reprocessing Spent Nuclear Fuels. *Chem. Eur. J.* **2011**, *17* (47), 13206–13216. https://doi.org/10.1002/chem.201102491.

(49) Stockmann, T. J.; Montgomery, A.-M.; Ding, Z. Formal Transfer Potentials of Strontium and Uranyl Ions at Water|1,2-Dichloroethane Interfaces. *Can. J. Chem.* **2012**, *90* (10), 836–842. https://doi.org/10.1139/v2012-068.

(50) Zhou, M.; Gan, S.; Zhong, L.; Dong, X.; Ulstrup, J.; Han, D.; Niu, L. Improvement in the Assessment of Direct and Facilitated Ion Transfers by Electrochemically Induced Redox

Transformations of Common Molecular Probes. *Phys. Chem. Chem. Phys.* **2012**, *14* (10), 3659–3668. https://doi.org/10.1039/c2cp23184k.

(51) Liu, S.; Li, Q.; Shao, Y. Electrochemistry at Micro- and Nanoscopic Liquid | Liquid Interfaces. *Chem. Soc. Rev.* **2011**, *40* (5), 2236–2253. https://doi.org/10.1039/c0cs00168f.

(52) Rodgers, P. J.; Amemiya, S.; Wang, Y.; Mirkin, M. V. Nanopipet Voltammetry of Common Ions across the Liquid-Liquid Interface. Theory and Limitations in Kinetic Analysis of Nanoelectrode Voltammograms. *Anal. Chem.* **2010**, *82* (1), 84–90. https://doi.org/10.1021/ac9022428.

(53) Campbell, J. A.; Girault, H. H. Steady State Current for Ion Transfer Reactions at a Micro Liquid | Liquid Interface. *J. Electroanal. Chem.* **1989**, *266* (2), 465–469. https://doi.org/10.1016/0022-0728(89)85091-0.

(54) Burgoyne, E. D.; Molina-Osorio, A. F.; Moshrefi, R.; Shanahan, R.; McGlacken, G. P.; Stockmann, T. J.; Scanlon, M. D. Detection of: Pseudomonas Aeruginosa Quorum Sensing Molecules at an Electrified Liquid|liquid Micro-Interface through Facilitated Proton Transfer. *Analyst.* **2020**, *145* (21), 7000–7008. https://doi.org/10.1039/d0an01245a.

(55) Ciganda, R.; Irigoyen, J.; Gregurec, D.; Hernández, R.; Moya, S.; Wang, C.; Ruiz, J.; Astruc, D. Liquid-Liquid Interfacial Electron Transfer from Ferrocene to Gold(III): An Ultrasimple and Ultrafast Gold Nanoparticle Synthesis in Water under Ambient Conditions. *Inorg. Chem.* **2016**, *55* (13), 6361–6363. https://doi.org/10.1021/acs.inorgchem.6b01183.

(56) Fermin, D. J.; Lahtinen, R. Dynamic Aspects of Heterogeneous Electron-Transfer Reactions at Liquid-Liquid Interfaces. *Surfactant. Sci. Ser.* **2001**, 179–228.

(57) Jane Stockmann, T.; Deng, H.; Peljo, P.; Kontturi, K.; Opallo, M.; Girault, H. H. Mechanism of Oxygen Reduction by Metallocenes near Liquid|liquid Interfaces. *J. Electroanal. Chem.* **2014**, *729*, 43–52. https://doi.org/10.1016/j.jelechem.2014.07.001.

(58) Méndez, M. A.; Partovi-Nia, R.; Hatay, I.; Su, B.; Ge, P.; Olaya, A.; Younan, N.; Hojeij, M.; Girault, H. H. Molecular Electrocatalysis at Soft Interfaces. *Phys. Chem. Chem. Phys.* **2010**, *12* (46), 15163–15171. https://doi.org/10.1039/c0cp00590h.

(59) Hotta, H.; Ichikawa, S.; Sugihara, T.; Osakai, T. Clarification of the Mechanism of Interfacial Electron-Transfer Reaction between Ferrocene and Hexacyanoferrate(III) by Digital Simulation of Cyclic Voltammograms. *J. Phys. Chem. B.* **2003**, *107* (36), 9717–9725. https://doi.org/10.1021/jp035058p.

(60) Bard, A. J.; Faulkner, L. R. Electrochemical Methods: Fundamentals and Applications (2nd ed.), *John Wiley*, New York **2001**

(61) Dryfe, R. A. W.; Uehara, A.; Booth, S. G. Metal Deposition at the Liquid-Liquid Interface. *Chem. Rec.* **2014**, *14* (6), 1013–1023. https://doi.org/10.1002/tcr.201402027.

(62) Johans, C.; Lahtinen, R.; Kontturi, K.; Schiffrin, D. J. Nucleation at Liquid|liquid Interfaces: Electrodeposition without Electrodes. *J. Electroanal. Chem.* **2000**, *488* (2), 99–109. https://doi.org/10.1016/S0022-0728(00)00185-6.

(63) Hirano, T.; Morita, A. Electron Transfer Mechanism at the Oil | Water Interface Revealed by Multidimensional Free Energy Calculations. *J. Phys. Chem. B.* **2020**, *124* (18), 3811–3827. https://doi.org/10.1021/acs.jpcb.0c01467.

Chapter 3

3. Electrodeless synthesis of low dispersity Au nanoparticles and nanoclusters at an immiscible micro water|ionic liquid interface

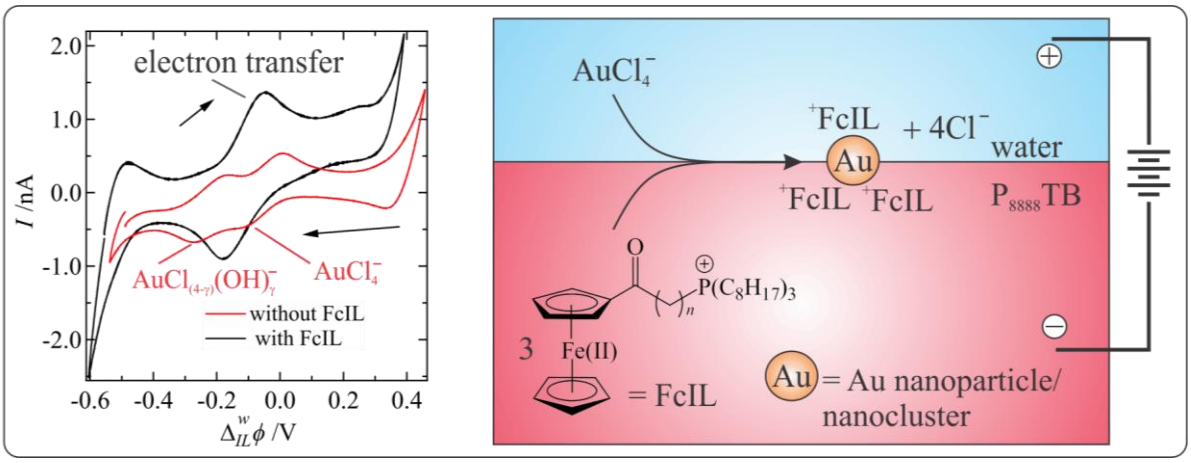

3.1. Statement of Co-Authorship

This chapter has been published under the above title in *Nanomaterials* **2022**, 12(16), p.2748. It is presented here in a modified format that includes all contributions for completeness and context.

Authors: Reza Moshrefi, and Dr. T. Jane Stockmann

Reza Moshrefi (listed in the paper as 1st author): Performed electrochemical data, material characterization and contributed to formal analysis, investigation, writing - review & editing, validation.

Dr. T. Jane Stockmann: Is the principal investigator of this work, who led the project and contributed to conceptualization, methodology, writing - original draft, validation, supervision, project administration, funding acquisition.

3.1. Introduction

Au nanoparticles (NPs) have been of continued interest owing to their unique optical and (electro)catalytic properties[1,2], as well as for biomedical applications.[2] Over the passed three decades multiple, relatively straightforward chemical means of generating low dispersity, small (<20 nm) Au NPs have been developed. Many of these have exploited an immiscible liquid|liquid interface as a means of species and charge separation. For example, the Brust-Schiffrin method[3] originally employed the water|toluene interface, in conjunction with BH_4^- as a reducing agent and an alkanethiol (RSH) as a capping agent; however, it was later revealed by Uehara *et al.* that alkanethiols role was far more complicated, such as the formation of $[Au(I)SR]_n$ species.[4]

Moreover, the liquid|liquid interface, or immiscible interface between two electrolyte solutions (ITIES), has become of increasing interest as a platform for electrodeless synthesis of a variety of materials.[5–18] While at first this relied on spontaneous chemical reactions, increasingly electrochemical control via an applied external potential is being turned to. This is achieved through immersion of two electrodes, one in either electrolyte phase, so that the Galvani potential difference is localized across the liquid|liquid interface, i.e., $\phi_w - \phi_o = \Delta_o^w\phi$.[2] Cheng and Schiffrin[19] demonstrated the first electrochemically controlled Au NP generation at an ITIES; whereby, tetraoctylammonium tetrachloroaurate ($TOAAuCl_4$) was dissolved in 1,2-dichloroethane (DCE) and was used as both the source of Au as well as an electron acceptor, while potassium hexacyanoferrate(II) ($K_4Fe(CN)_6$) in the aqueous phase served as the electron donor. Thus, the authors were able to exploit the hydrophobicity and hydrophilicity of the electron acceptor and donor, respectively, and limit electron transfer to a heterogeneous process localized across the ITIES. Soon after Johans *et al.*[20–23] began investigating the thermodynamics of nanoparticle generation at an interface with seemingly few nucleation sites. $TOAAuCl_4$ is a special case and

most contemporary studies have employed a hydrophilic metal salt, (e.g., $KAuCl_4$ or Cu_2SO_4), paired with a hydrophobic electron donor, *e.g.*, ferrocene (Fc)[14,15] or decamethylferrocene[16]. In this way, the interfacial or heterogeneous electron transfer pathway can be described as shown in Scheme 3-1 (mechanism 2). Partitioning of Fc into water (mechanism 1) or $AuCl_4^-$ into oil (mechanism 3) with subsequent homogeneous electron transfer is also depicted.

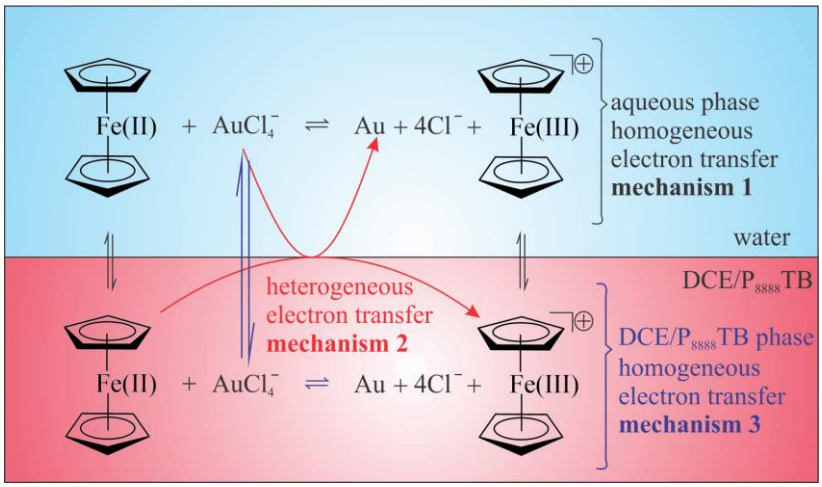

Scheme 3-1 The three electron transfer mechanisms considered between ferrocene (Fc) (or other metallocene derivatives) and $AuCl_4^-$ at a water|1,2-dichloroethane (w|DCE) or w|P_{8888}TB (tetraoctylphosphonium tetrakis(pentafluorophenyl)borate) interface.

These previous reports have focused on the water|oil (w|o) interface; however, recently the water|ionic liquid (w|IL) one has emerged.[7–10,24,25] Ionic liquids (ILs) are large – on a molecular scale – organic salts with melting points typically below ambient temperature whose molecular architecture can be tuned to obtain a wide variety of physicochemical properties. They are desirable for several reasons, including excellent thermal and electronic stability, as well as enhanced catalytic properties and as a medium for NP preparation.[26] Indeed, NPs prepared in an IL phase are typically small (<10-20 nm) and have low dispersity; this is hypothesized to be owing to the supramolecular fluidic nature of ILs which contains nanoscale pockets sandwiched between ion aggregates/contact ion pairs within which NPs can grow.[26–30] Nishi *et al.*[31] first investigated

electrochemically controlled Au NP synthesis at a micro w|IL interface using tri-p-tolylamine as the reducing agent dissolved in the IL, trioctylmethylammonium bis(nonafluorobutanesulfonyl)amide ($[TOMA^+][C_4C_4N^-]$), and were able to generate nanodendrites. However, in order to elucidate electron transfer between the w and IL phase, Nishi *et al.*[31] employed an ECSOW (electron conductor separating an oil|water phase) system. In ECSOW the IL and w phases are not directly in contact; however, a metal wire bridged between the two solutions acts as an electrical connection. Next, they employed a redox active IL (RAIL), (ferrocenylmethyl)dodecyldimethylammonium bis(nonafluorobutanesulfonyl)amide ($[FcMDDA]^+[C_4C_4N]^-$), to generate Pd nanofiber arrays at the w|RAIL interface through a spontaneous process, i.e., without external electronic control.[9] In their proposed mechanism the RAIL partitions into the water phase and undergoes homogeneous electron transfer with H_2PdCl_4(aq).

Herein, we have investigated electron transfer at a w|IL micro-interface using either of two electron donors, Fc or trioctyl(ferrocenylheptanoyl)phosphonium tetrakis(pentafluorophenyl)-borate, FcIL (see Figure 3-1), in which a Fc moiety is tethered to the phosphonium core by way of an acyl chain. Using either Fc or FcIL dissolved in P_{8888}TB (tetraoctylphosphonium tetrakispentafluorophenyl)borate) heterogeneous electron transfer was recorded and resolved at a micro-ITIES for the first time without the need to resort to an ECSOW system. Additionally, the influence of aqueous phase pH was interrogated, and low pH elicited thermodynamically inhibited Au NP generation that favoured nanocluster formation, i.e., diameters ~1.7 nm. Additionally, owing to the intermediate hydrophobicity of $AuCl_4^-$ and Fc, by employing the highly hydrophobic electron donor, FcIL, in combination with the P_{8888}TB phase, partitioning of either $AuCl_4^-$ or the electron donor was hindered such that mechanisms 1 and 3 in Scheme 3-1 were not favoured.

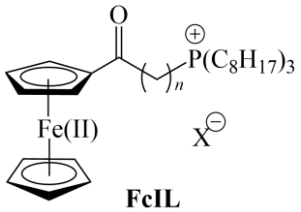

Figure 3-1 Structure of trioctyl(ferrocenylhexanoyl)phosphonium ionic liquid (FcIL) in which n = 5 and $X^- = B(C6F5)_4^-$ (i.e., TB).

3.2. Materials and Methods

All chemicals were used as received without purification, while all aqueous solutions were prepared using MilliQ ultrapure water (≥18.2 MΩ cm). Potassium chloride (KCl, >99%), 1-bromooctane (98%), 6-bromohexanoic acid (97%), trioctylphosphine (>97%), tetramethylammonium chloride (TMACl, ≥98%), ferrocene (Fc, >98%), and 1,2-dichloroethane (DCE, ≥99.0%) were sourced from Sigma-Aldrich. Lithium tetrakis(pentafluorophenyl)borate etherate (LiTB, >99%) was purchased from Boulder Scientific. The Fc modified ionic liquid FcIL (see Figure 3-1) and $P_{8888}TB$ (tetraoctylphosphonium tetrakis(pentafluorophenyl)borate) were prepared as described previously by Weaver *et al.*[32] and Stockmann *et al.*[33], respectively.

A Heka Electroniks PG-618-USB potentiostat equipped with a head-stage was employed for all electrochemical measurements. All measurements were conducted at a 25 µm diameter micro-ITIES held at the tip of a micropipette and with a scan rate of 0.020 V s^{-1} in a two-electrode mode unless otherwise indicated. The electrolytic cells employed have been drawn in Scheme 3-2. A specialized micropipette holder was employed with an integrated Au wire, used as the working electrode (WE), and a syringe to back-fill the pipette and maintain the ITIES at the tip. $KAuCl_4$ is a powerful oxidant; thus, Ag, or even Pt electrodes were found to be unsuitable as WEs. A CCD

camera (AmScope) equipped with a magnifying lens assembly (Navitar) was used to monitor the ITIES position in situ. A second Ag wire (Goodfellow, Inc., Delson, QC, Canada) was immersed in the DCE or $P_{8888}TB$ phase and connected to the counter/quasi-reference electrode port of the head-stage.

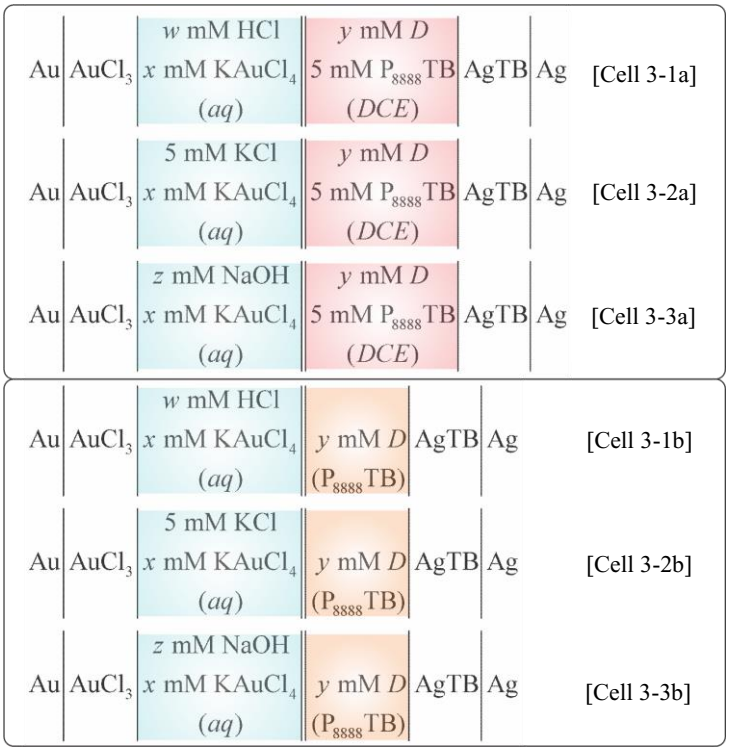

Scheme 3-2 The electrolytic cells employed in which the pH of Cells 3-1a/b and 3-3a/b were adjusted using w and z mM of HCl and NaOH to be pH 2 and 8.5, respectively as confirmed using a pH meter (sympHony, model#B10P), while x and y mM of $KAuCl_4$ and an electron donor, D, were added to the aqueous and DCE or $P_{8888}TB$ (tetraoctylphosphonium tetrakis(pentafluorophenyl)borate), ionic liquid phases, respectively. D was either Fc or FcIL. The double bar indicates the polarizable potential interface maintained at the pipette tip which, unless otherwise specified, had a diameter of 25 µm. Cells 3-(1b-3b) were measured at ~60°C using a water circulator (Polystat, Cole-Parmer).

Micropipettes (25 µm diameter) as well as inlaid disc Pt and carbon fiber ultramicroelectrodes (UME), 25 and 7 µm in diameter, respectively, were prepared as has been described elsewhere.[14,27] UMEs were employed in a two-electrode mode in conjunction with an Ag wire which served as the counter/quasi-reference electrode.

Transmission electron microscopy (TEM) imaging was performed using a Tecnai Spirit TEM with samples deposited on 200 mesh Au ultrathin/lacey carbon grids.

3.3. Results and Discussion

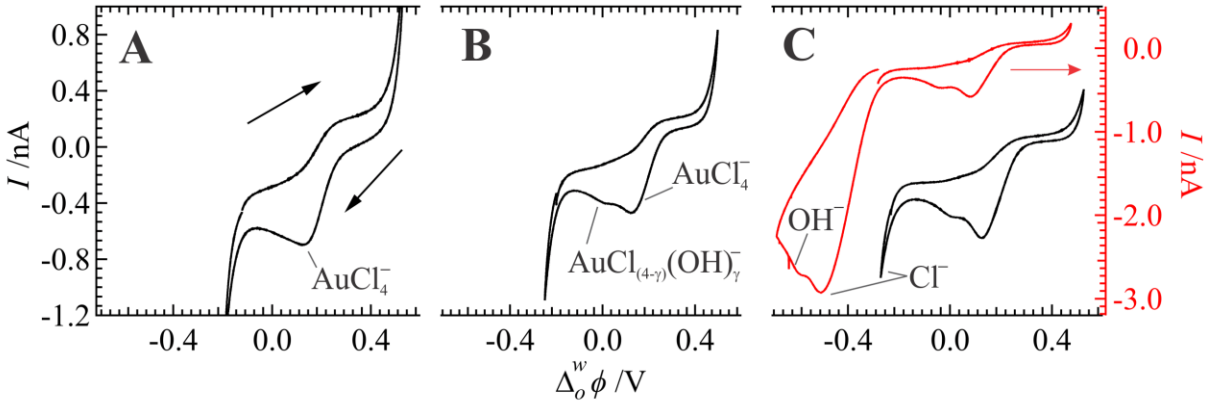

Figure 3-2 Cyclic voltammograms (CVs) measured using Cells 3-1a - 3-3a (A-C) with no electron donor added to the DCE phase. 1 mM of $KAuCl_4$ was dissolved in the aqueous phase with the pH = 2, 5.5-6, and 8.5 for the top, middle, and bottom panels, respectively. A 25 µm diameter ITIES was used with a scan rate of 0.020 V s^{-1}. The red arrow indicates the axes plotted against, black arrows indicate scan direction, and the peak currents have been labelled with the associated simple ion transfer process taking place.

Figure 3-2 depicts the cyclic voltammograms (CVs) obtained at a 25 µm diameter interface using 1 mM of $KAuCl_4$(aq) in Cells 3-1a - 3-3a (A-C), or pH 2, 5.5-6, and 8.5, respectively, at the w|DCE interface with no electron donor (*D*) added to the DCE phase, (i.e., $y = 0$), with at scan rate of 0.020 V s^{-1}. The polarizable potential window (PPW) was limited at positive and negative potentials by the transfer of the supporting electrolyte ions, (i.e., K^+/Na^+ and Cl^-/OH^-), which is seen by the exponential increase or decrease in the current at approximately +0.5 and –0.5 V, respectively.[34–36] The use of the micropipette holder makes the system resistant to electrophoretic movement of the micro-ITIES and allows one to scan beyond the usual PPW.[2,15,34,36] In this case, it allows for the observation of Cl^- and OH^- simple ion transfer processes (see Figure 3-2C). Simple Cl^- transfer was used to reference the potential to the Galvani scale.[37]

The *i*-V response at the w|DCE micro-interface is asymmetric; for example, in Figure 3-2A, during the scan from roughly 0.4 to –0.3 V, a negative peak-shaped wave can be observed with a peak potential at 0.126 V; while during the reverse scan, back towards positive potentials, a sigmoidal wave was recorded with a half-wave potential at 0.172 V. This signal is owing to simple $AuCl_4^-$ transfer from water to oil (w→o) and back from o→w, respectively. The signal asymmetry is owing the pipette geometry which elicits hemispherical diffusion outside the pipette and when undergoing charge transfer from o→w and linear diffusion during ion transfer from w→o inside; these curves agree well with previous reports.[38,39]

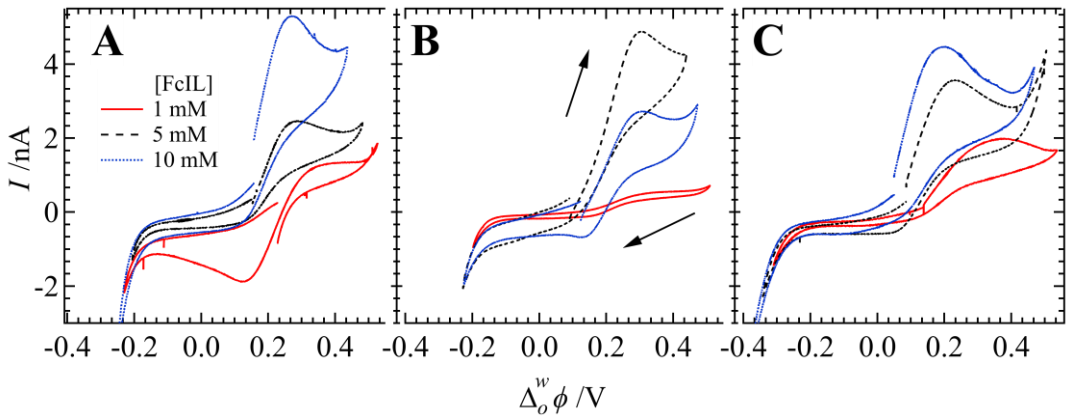

Figure 3-3 Voltammetric responses for increasing additions of FcIL of y as indicated in set to the DCE phase, respectively, with [KAuCl4] = 1 mM in Cells 3-1a - 3-3a or pH's 2 (A), 5.5-6 (B), and 8 (C). A 0.020 V s^{-1} scan rate was employed with a 25 µm diameter ITIES, while the scan direction is indicated by black arrows.

As the pH increases a second ion transfer wave appears with a peak potential at ~0.017 V during the negative scan and a sigmoidal wave at ~0.020 V during the scan towards positive potentials. $AuCl_4^-$ ligand speciation to $AuCl_{(4-\gamma)}(OH)_\gamma^-$ with hydroxide replacing chloride on the Au core has been well characterized electrochemically[40] and spectrophotometrically[41]; therefore, the second wave is likely owing to a combination of simple $AuCl_{(4-\gamma)}(OH)_\gamma^-$ transfer consisting of different values of γ. These results are in good agreement with other articles.[4,15]

After addition of 1, 5, and 10 mM of FcIL to the DCE phase in Cells 3-1a - 3-3a, the negative peak-shaped wave associated with $AuCl_4^-/AuCl_{(4-\gamma)}(OH)_\gamma^-$ disappeared and was replaced by a positive peak signal at ~0.3 V (Figure 3-3). At [FcIL] = 1 mM and at low pH (red trace in Figure 3-3A), the $AuCl_4^-$ wave was still present; however, at pH 5.5, a sigmoidal wave was observed in both forward and reverse scans with a $\Delta_o^w\phi_{1/2}$ of 0.222 V, while at pH 8.5, a positive peak-shaped wave, with an onset potential of ~0.15 V, has completely replaced the $AuCl_4^-$ transfer signal. At [FcIL] = 5 mM, the onset potential shifted to more negative values by increasing the pH from 2 to 8.5; however, at [FcIL] = 10 mM the onset potentials were difficult to decern, and this may be owing to a competing homogeneous electron transfer reaction taking place in the DCE phase (see mechanism 3 in Scheme 3-1).

Figure 3-4A depicts the CVs recorded using Cell 3-2a with 0, 1, and 5 mM of FcIL in DCE and selecting an initial potential near the negative limit of the PPW. With no electron donor added to the DCE phase the initial current is roughly –0.2 nA; however, with even a modest amount of FcIL added to DCE a relatively large negative current offset of –3-4 nA was observed. The current offset was still present even when a 2-5 s potentiostatic pulse was applied just prior to initiating the *i*-V scan. This is likely owing to the spontaneous transfer of $AuCl_4^-/AuCl_{(4-\gamma)}(OH)_\gamma^-$ from w→o which is caused by the Au salts consumption in a homogeneous, organic phase electron transfer reaction with FcIL (Scheme 3-1, mechanism 3). This current offset was only observed in the presence of an electron donor in the organic phase. Thus, at high [FcIL], the peak currents and onset potentials in Figure 3-3 were not reproducible; however, the latter demonstrated a general trend of decreasing toward negative potentials with a concomitant increase in pH.

During the second scan at the w|DCE interface, the positive peak current disappeared (Figure 3-4B). It is unclear if this is owing to the depletion of the local concentration of FcIL, since the negative peak-shaped wave associated with $AuCl_4^-$ ion transfer seemed to still be present; however, it may be that the intensity of the electron transfer wave only decreased and had taken on a sigmoidal shape.

Owing to the high hydrophobicity of FcIL, it is unlikely that it partitions to the aqueous phase; thus, the positive signal observed in Figure 3-3 is wholly heterogeneous electron transfer from FcIL in DCE to the $AuCl_4^-/AuCl_{(4-\gamma)}(OH)_\gamma^-$ in the aqueous phase (Scheme 3-1, mechanism 2). These data agree with our previous results using unmodified Fc at the w|DCE micro-interface.[15] Even as the concentration of the electron donor increases, the electron transfer signal is stable, and large current oscillations were not observed while using FcIL, unlike during our previous work using Fc where large current fluctuations were common.[15] This may indicate that Fc partitioning to the aqueous phase with subsequent homogeneous electron transfer from Fc to $AuCl_4^-$ destabilizes the ITIES. Thus, using a more hydrophobic electron donor decreases the strain on the liquid|liquid interface. Regardless, the Au salt is likely reduced to Au nanoparticles and the oxidized form of FcIL subsequently behaves as a nanoparticle capping agent.

In this way, the following chemical reactions can be written for the heterogeneous electron transfer process,

$$AuCl_4^-(aq) + 3FcIL(org) \rightarrow Au(s) + 3FcIL^+(org) + 4Cl^-(aq) \quad 3\text{-}1$$

$$AuCl_{(4-\gamma)}(OH)_\gamma^-(aq) + \gamma H^+(aq) + 3FcIL(org) \rightarrow Au(s) + 3FcIL^+(org) + (4-\gamma)Cl^-(aq) + \gamma H_2O \quad 3\text{-}2$$

Where a generalized electron transfer potential at moderate to high pH for the process can be written as,[15,42]

$$\Delta_o^w\phi_{ET} \approx E^{o',DCE}_{FcIL^+/FcIL} - E^{o',H_2O}_{Au(III)/Au} - \frac{(0.059)}{3}\log([H^+]^\gamma) \qquad 3\text{-}3$$

Where $E^{o',H_2O}_{Au(III)/Au}$ and $E^{o',DCE}_{FcIL^+/FcIL}$ are the standard redox potentials for $AuCl_4^-$/Au (1.002 V)[43] and $FcIL^+$/FcIL in the aqueous and DCE phases, respectively. $E^{o',DCE}_{FcIL^+/FcIL}$ was determined to be 0.91 V using cyclic voltammetry at an inlaid Pt disc UME through a comparison to Fc^+/Fc (see Figure B1 of Appendix B).

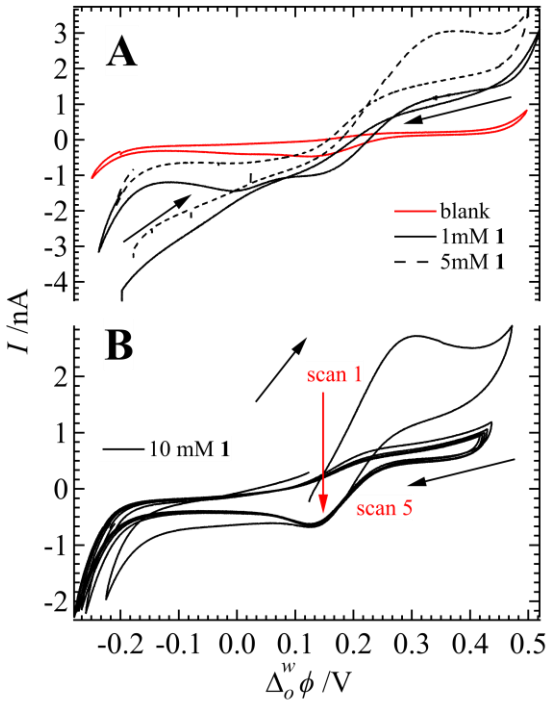

Figure 3-4 i-V measurements using Cell 3-2a at a 25 µm diameter interface with [FcIL], or y, equal to 0, 1, and 5 mM (A) as well as [FcIL] = 10 mM (B) with multiple scans as indicated inset, performed with a scan rate of 0.020 V s^{-1}. Black arrows show scan direction.

Thus, $\Delta_o^w\phi_{ET}$ was calculated to be –0.089, 0.019, and 0.078 V for pH 2, 5.5-6, and 8.5, respectively, assuming $\gamma \approx 1$ for pH >5 and $n = 3$ for the number of e^- transferred. Thus, as the pH increases

heterogeneous electron transfer becomes more favourable. This agrees well with the general trend of decreasing onset potentials of $\Delta_o^w\phi_{ET}$ observed in Figure 3-3 and with our previous work using Fc.[15]

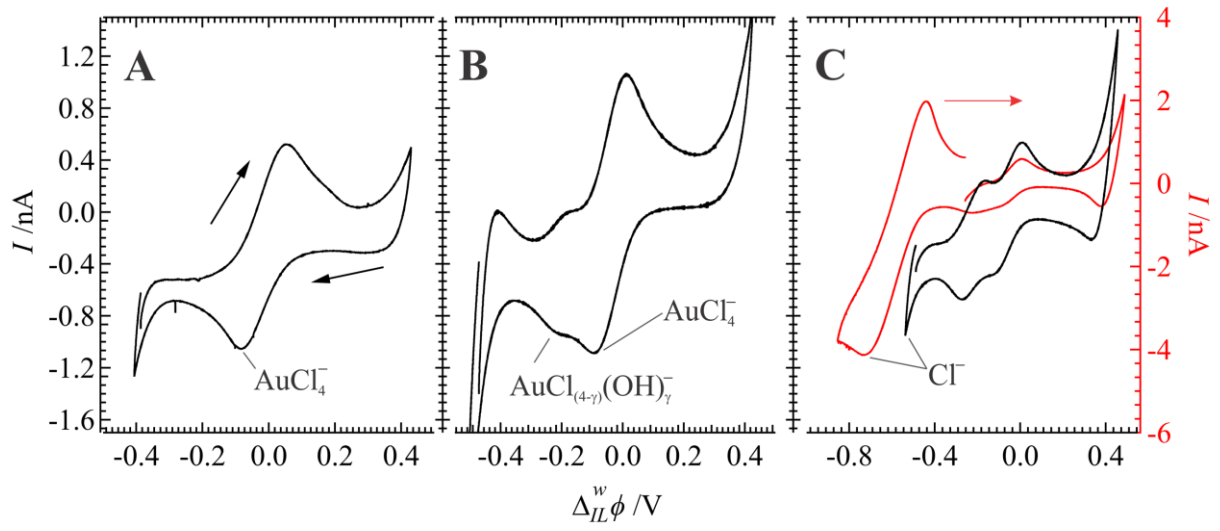

Figure 3-5 CV responses at a w|P_{8888}TB 25 µm diameter interface described by Cells 3-1b - 3-3b in which the aqueous pH increases from 2 to 5.5-6 and 8.5 (A-C). Black and red arrows indicate scan direction and the axes the CV is plotted against, respectively. The cell was maintained at 60°C using a water circulator (Polystat, Cole-Parmer).

Figures 3-5, A-C show the *i*-V curves obtained if the DCE phase is replaced with P_{8888}TB, with no electron donor added, *i.e.*, y = 0 mM, and performed at 60 °C using a water heater/circulator. The heater/circulator was connected to a mantle built into the stage and surrounding the vial containing the IL phase. Owing to the high viscosity/low diffusion coefficient in the ionic liquid phase, ion transfer from IL→w elicits a peak-shaped wave rather than a sigmoidal one, *i.e.*, the diffusion regime in the IL phase is linear. These results agree well with previous reports of ion transfer at a w|IL micro-interface[10,33]. The red trace in Figure 3-5C shows the *i*-V results if the potential is scanned beyond the conventional PPW to reveal simple Cl^- transfer with a peak-to-peak (ΔE) separation between the forward and reverse scans of ~0.290 V and a half-wave potential, $\Delta_o^w\phi_{1/2,\,Cl^-} \approx$ –0.58 V. The latter was calculated as the mid-point between the forward ($E_{p,fwd}$) and reverse ($E_{p,rev}$) peak potentials for ion transfer, (*i.e.*, ($E_{p,fwd}$ + $E_{p,rev}$)/2) while

ΔE suggests that Cl^- is quasi-reversible. Large peak-to-peak separations for redox processes in ILs in the range of 0.1-0.15 V are common[33,44,45] and may be related to the reorganization of the interface on the IL side. It has been shown that the electric double layer (EDL) at the solid|IL[46] and w|IL[47] interfaces is highly organized with alternating anion/cation layers that can extend several times into the IL phase and that have ultraslow relaxation energies. Pushing the PPW far beyond its typical limit likely has a commensurate impact on the EDL relaxation energies exacerbating ΔE. As a first approximation, $\Delta_o^w\phi_{1/2,\,Cl^-}$ was employed to reference the potential to the Galvani scale. Thus, a ΔE for $AuCl_4^-$ and $AuCl_{(4-\gamma)}(OH)_\gamma^-$ were measured to be 0.138 and 0.108 V, with $\Delta_o^w\phi_{1/2,\,AuCl^-}$ and $\Delta_o^w\phi_{1/2,\,AuCl_{(4-\gamma)}(OH)_\gamma^-}$ equal to roughly –0.015 and –0.220 V obtained from the black traces in Figures 3-5A and 3-5C at pH 2 and 8.5, respectively.

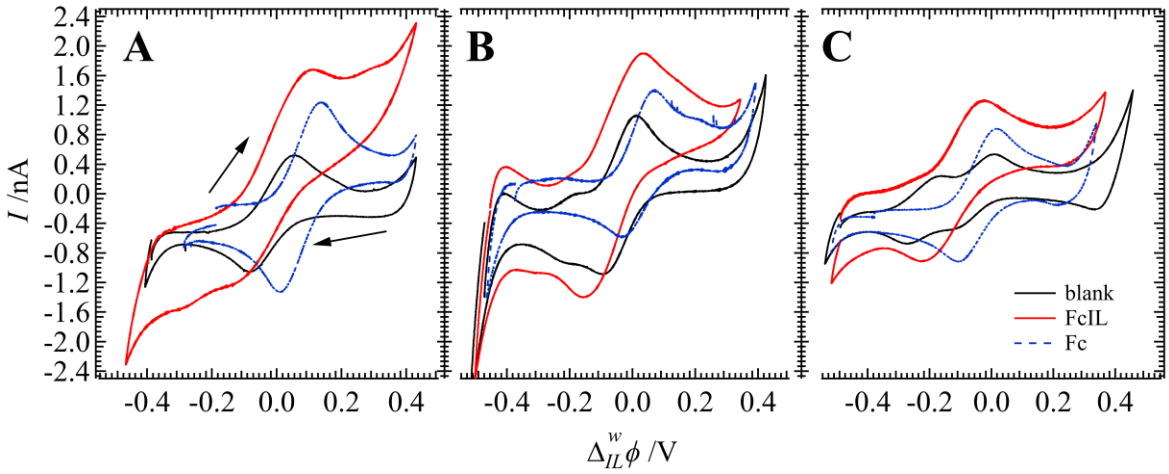

Figure 3-6 CVs acquired at a 25 µm diameter ITIES between w|$P_{8888}TB$ at ~60°C and 0.020 V s^{-1} using Cells 3-1b - 3-3b (A-C) with 1 mM $KAuCl_4$(aq) and 100 mM of Fc (blue, dashed trace) or FcIL (red, solid curve) added to the $P_{8888}TB$ phase, as shown inset. Black traces depict CVs obtained without an electron donor added to $P_{8888}TB$.

Figure 3-6 shows the *i*-V curves recorded at the w|$P_{8888}TB$ micro-interface (Cells 3-1b - 3-3b, see Scheme 3-2) at 60 °C with 100 mM of either Fc or FcIL added to the $P_{8888}TB$ phase, as indicated inset, while increasing the pH from 2 to 5.5-6 and 8.5 for panels A-C, respectively. The black traces in Figure 3-6 are for the system without an electron donor added. At pH 2 (Figure 3-

6A), the peak intensity increased from 1.0 to 1.6 or 2.0 nA with the addition of 100 mM of Fc or FcIL, respectively.

Table 3-1 Data obtained from electron transfer waves depicted in Figure 3-6 and Figure 3-7, including the forward ($E_{p,fwd}$) and reverse ($E_{p,rev}$) peak potentials, the peak-to-peak separation (ΔE), and the electron transfer half-wave potential $\Delta_o^w\phi_{1/2,ET}$, as well as the peak current (i_p) and total charge transferred (Q) as obtained for the forward wave.

[FcIL] /mM	pH	$E_{p,fwd}$ /V	$E_{p,rev}$ /V	ΔE /V	$\Delta_o^w\phi_{1/2,ET}$ /V	i_p /nA	Q /µC
20	2	0.069	–0.051	0.120	0.0086	1.38	38.7
100	2	0.108	–0.147	0.255	–0.0194	2.03	160.2
500	2	0.124	–0.122	0.245	0.00124	2.21	282.2
20	5.5-6	–0.092	–0.125	0.034	–0.109	1.23	123.2
100	5.5-6	0.031	–0.157	0.188	–0.063	1.52	96.0
500	5.5-6	–0.001	–0.243	0.242	–0.122	2.81	265.2
20	8.5	–0.038	–0.160	0.122	–0.099	0.45	41.8
100	8.5	–0.066	–0.266	0.200	–0.127	0.95	160.3
500	8.5	–0.048	–0.182	0.134	–0.115	1.18	166.4
[Fc] /mM							
100	2	0.136	0.008	0.128	0.072	1.58	28.3
100	5.5-6	0.068	–0.032	0.101	0.018	1.23	82.4
100	8.5	0.017	–0.107	0.124	–0.045	1.08	21.0

At neutral to high pH (Figures 3-6B and 3-6C), the two signals for $AuCl_4^-$ and $AuCl_{(4-\gamma)}(OH)_\gamma^-$ transfer have been replaced by a single one with peak-shaped waves during the forward and reverse scans with similar increased peak current intensities. Therefore, a similar heterogeneous electron transfer process occurs at the w|P_{8888}TB micro-interface and analogous equations 3-1 and 3-2 can similarly be written. No current offset was observed at the w|P_{8888}TB interface with the addition of an electron donor, unlike at the w|DCE one (see Figure 3-4A). The

$AuCl_4^-/AuCl_{(4-\gamma)}(OH)_\gamma^-$ transfer potentials at the w|P_{8888}TB interface are similar to the those observed at the w|DCE one; therefore, these ions have similar affinities towards the P_{8888}TB phase as they do towards the DCE one. It is likely that the w|IL EDL organization and high IL viscosity limit the degree of penetration of these ions into the IL phase.

Thus, mechanism 3 (see Scheme 3-1), whereby $AuCl_4^-/AuCl_{(4-\gamma)}(OH)_\gamma^-$ partitions into the P_{8888}TB phase and then is consumed by a homogeneous electron transfer with the electron donor, is inhibited. In this way, the w|IL interface can be exploited as a means to restrict electrodeless, electrosynthetic methods to prefer interfacial electron transfer pathways. The half-wave potential for the electron transfer wave, with [Fc] = 100 mM shifted toward more negative potentials of 0.072 V to –0.045 V, with an increase in pH from 2-8.5, while [FcIL] = 100 mM, was also found to shift from –0.019 to –0.127 V, with an increase in pH (see Table 3-1). ΔE's for Fc were between 0.101 and 0.128 V, while for FcIL, the ΔE was twice as high, between 0.188 and 0.255 V. These data suggest that electron transfer between the Au salt and FcIL is more thermodynamically favoured versus Fc; however, since FcIL is an IL itself, it likely interacts much more with the IL's highly organized EDL, which either influences the electron transfer kinetics or disrupts the EDL on the IL side, increasing its relaxation energy. Both possibilities likely contribute to the large observed ΔE for electron transfer with FcIL.

Figure 3-7 shows comparison CVs with changing [FcIL] to 20 or 500 mM while altering the aqueous phase pH. At [FcIL] = 20 mM, simple $AuCl_4^-/AuCl_{(4-\gamma)}(OH)_\gamma^-$ is not yet suppressed and likely occurs simultaneously, along with heterogeneous electron transfer. When [FcIL] is increased to 500 mM, two peak shaped waves can be observed on the forward scan towards positive potentials. The second peak at ~0.2-0.3 V may be owing to interfacial coordination of the

Fc moiety on FcIL with either H^+ or K^+ in the aqueous phase (i.e., a facilitated ion transfer mechanism). Metallocenes have been shown to undergo protonation or lithiation to the cyclopentadienyl ring and likely interact with the water molecules within the hydration shell of K^+ or other metal cations used as supporting electrolytes.[48–50] Generally, as [FcIL] increases the peak current (i_p) and the total charge transferred (Q) increase, while $\Delta_o^w\phi_{1/2,ET}$ shifts to more negative potentials; the latter is indicative of a more thermodynamically favourable reaction. While the standard redox potentials of FcIL $\left(E^{o',P_{8888}TB}_{FcIL^+/FcIL}\right)$ and Fc $\left(E^{o',P_{8888}TB}_{Fc^+/Fc}\right)$ in the $P_{8888}TB$ phase are unknown, at low pH the third term in Equation 3-3 can be ignored and this can be used as an indirect means for determining $E^{o',P_{8888}TB}_{Fc^+/Fc}$. Thus, $E^{o',P_{8888}TB}_{Fc^+/Fc}$ was calculated to be 0.99 V vs SHE. Figure B2 (see Appendix B) depicts the CV obtained at a 7 µm diameter carbon fiber UME immersed in a $P_{8888}TB$ solution containing 100 mM of Fc and FcIL; in this way, $E^{o',P_{8888}TB}_{FcIL^+/FcIL}$ was determined to be ~1.3 V.

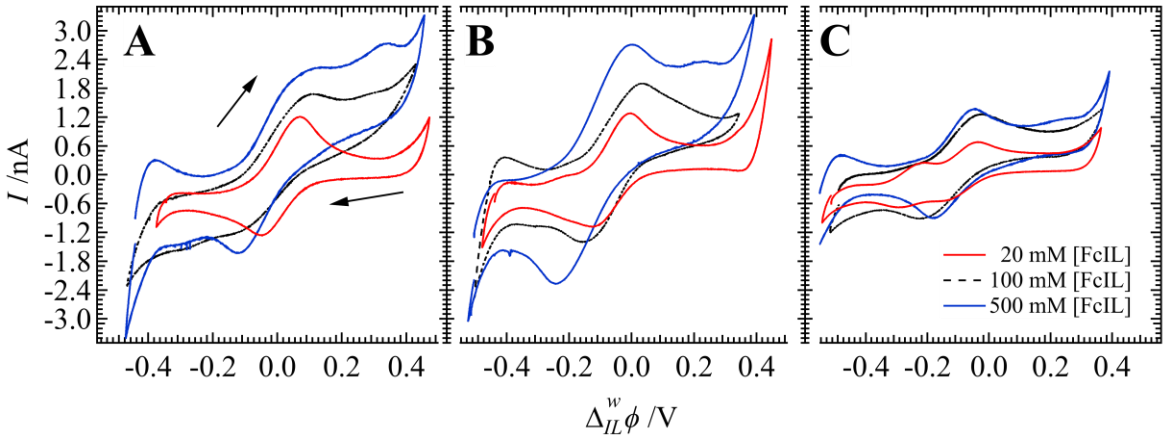

Figure 3-7 CVs measured using Cells 3-1b - 3-3b (A-C) with 1 mM of $KAuCl_4$(aq) at a 25 µm diameter interface, 0.020 V s^{-1}, and 60 °C, with increasing concentrations of FcIL added to the $P_{8888}TB$ phase, as indicated inset.

At both the w|DCE and w|P_{8888}TB micro-interfaces, the aqueous phase was sampled after one *i*-V cycle and a single drop was deposited on a lacey carbon Au TEM grid and imaged. Selected TEM micrographs obtained at the w|DCE and w|P_{8888}TB interfaces are shown in Figures 3-8(A-C) and 3-8(D-F), respectively. Figure 3-9 shows the nanoparticle size analysis performed for select TEM micrographs using ImageJ software and curve fitting the histograms with a Gaussian function (red traces). The peaks from the Gaussian fittings were taken as the average particle size. At low pH, particles were consistently found with a microenvironment of IL surrounding them (see Figure 3-8A and 3-8D); however, this was also observed occasionally at higher pH's (Figure 3-8F). At the w|DCE interface, at neutral to high pH, nanoparticle sizes were consistent, averaging 27.6 and 30.1 nm in diameter at pH 5.5-6 and 8.5, with [FcIL] = 5 and 500 mM respectively. With [FcIL] = 100 mM in P_{8888}TB at the w|IL interface, average Au nanoparticle sizes were 1.4, 31.1, and 14.0 nm in diameter for pH's 2, 5.5-6, and 8.5 as shown in Figures 3-8(D-F), respectively. The concentration of FcIL did not have a large influence on nanoparticle size at either the w|DCE or w|P_{8888}TB micro-interface. For example, increasing [FcIL] to 500 mM in the P_{8888}TB elicited Au nanoparticles that averaged 20.94 nm in diameter, see Figure B3 in Appendix B. However, the increase in total charge transferred (Q), as shown in Table 3-1, indicates that likely more NPs are formed. Our recent results[15] obtained using unmodified Fc at a w|DCE micro-ITIES showed a large dependence on aqueous phase pH with sub-micron particles, 400-600 nm in diameter, being generated at high pH, while 20 nm diameter particles were obtained at low pH. This may indicate that mechanism 1 (Scheme 3-1) is a major component to enhanced NP formation. Thus, the combination of a hydrophobic electron donor and a w|IL micro-ITIES provides control over NP formation and dispersity. Interestingly, when combining a low pH aqueous phase with a w|P_{8888}TB micro interface and highly hydrophobic electron donor, one can generate small, low dispersity Au nanoclusters.[51] However, the IL microenvironment seems

necessary for the formation of smaller NPs/nanoclusters, which this may be owing to its supramolecular fluidic nature.[27,30,52]

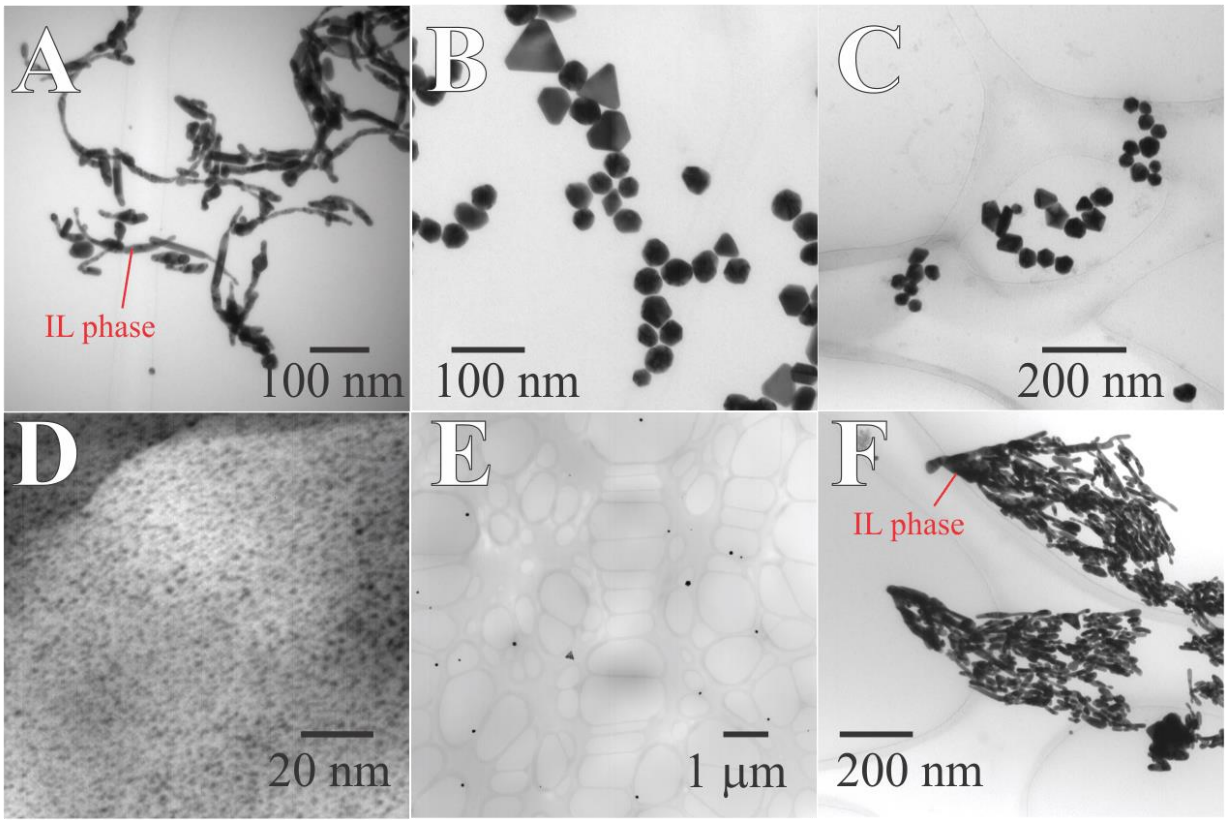

Figure 3-8 TEM micrographs of samples taken from the aqueous phase after one cyclic voltammetric scan performed at a 25 µm diameter w|DCE (A-C) or w|IL (D-F) interface at pH 2, 5.5-6, and 8.5 for the left-hand, center, and right-hand panels, respectively. [$KAuCl_4$] = 1 mM throughout; however, [FcIL] = 10 (A), 5 (B), 20 (D and E), and 500 mM (C, F), 'IL phase indicated residual ionic liquid surrounding the NPs.

At low pH only spherical nanoparticles were seen; however, with increasing pH lower symmetry nanoparticles were observed with various polyhedrons represented as can be seen in Figure 3-8B, including octahedral, tetrahedron, and triangular/pentagonal/hexagonal prism.

These shapes agree well with the typical growth pattern of Au nanoparticles.[29] Surfactants have been known to influence the shape of nanoparticle growth,[53] and recently computational studies have emerged elucidating the impact of their presence on nanoparticle/nanocluster-IL interactions.[54] Simultaneously, high-resolution TEM has been used to image nanoparticle growth

in situ within an IL environment.[29] Based on these images in which an IL microenvironment was associated with smaller nanoparticles/clusters and the fact that the water phase was sampled, it may be concluded that as the particles move into the aqueous phase, they undergo continued growth or Ostwald ripening. Presently, successfully sampling the IL phase for TEM imaging is technically challenging; however, future work will shift to include optical monitoring of NP electrodeless synthesis in situ with an aim to better understand the interfacial dynamics of this process. Nevertheless, these results agree with previous works that indicate that the IL supramolecular fluid plays a critical role in nanoparticle growth.[30]

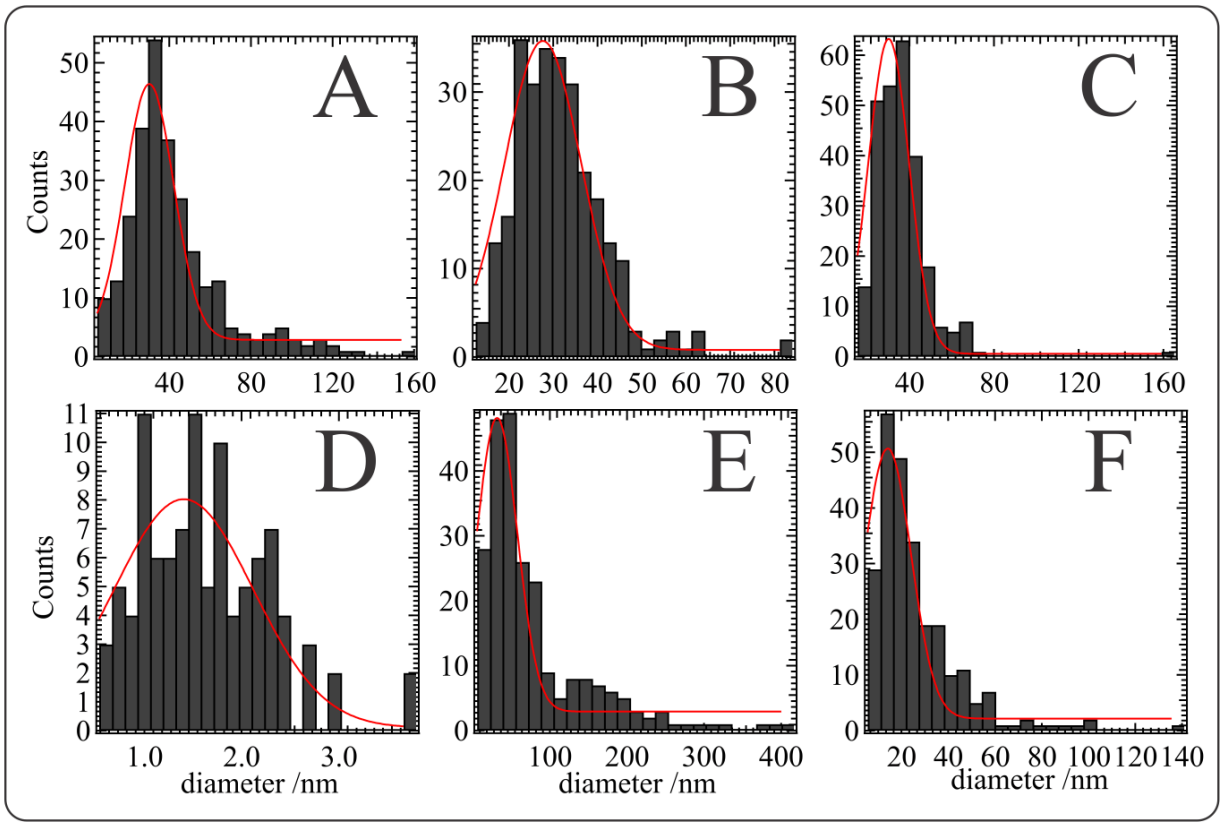

Figure 3-9 Histograms of nanoparticle diameters measured from TEM micrographs taken after one i-V cycle of electrochemical Au NP generation at a w|DCE (A-C) or w|P_{8888}TB (D-F) at aqueous phase pH of 2, 5.5-6, and 8.5 for the left-hand, middle, and right-hand panels, respectively, with 10 (A), 5 (B), or 500 mM (C) of FcIL in DCE, while 100 mM of FcIL was used in P_{8888}TB (D-F). Red traces are products of Gaussian curve fitting.

3.4. Conclusions

Herein, an electrodeless synthetic method for generating Au NPs and nanoclusters has been demonstrated exploiting the w|IL micro-interface paired with a second IL with a Fc moiety tethered to the phosphonium core by an acyl chain. The effect of altering the aqueous pH on Au NP growth was investigated by TEM images of droplets extracted from the aqueous phase after a single cyclic voltammetric scan. Importantly, by lowering the pH of the aqueous phase, the thermodynamics of the reaction can be inhibited, favouring Au nanocluster formation, (i.e., <1.7 nm in diameter particles). Moreover, the IL supramolecular fluidic microenvironment plays an important role in the size and shape of the particles formed, in agreement with previous works.[7,9,29] Unlike at the w|DCE micro-interface,[15] large sub-micron (~500 nm diameter) particles were avoided at high pH. This is likely owing to the inhibition of homogeneous electron transfer, either from the electron donor partitioning into the aqueous phase or by $AuCl_4^-/AuCl_{(4-\gamma)}(OH)_\gamma^-$ transferring to the oil|IL phase (see Scheme 3-1, mechanisms 1 and 3). Thus, only mechanism 2 (Scheme 3-1) prevailed.

Increasingly, electrochemical control of the liquid|liquid interface is becoming a favoured method for electrodeless synthesis of novel materials. While this work builds on those fundamental concepts and provides thermodynamic physical insights into NP growth, more importantly, this method affords a novel platform for controlling NP/nanocluster formation and morphology. The latter will be important for widespread manufacture of these materials for catalytic and biomedical applications.

3.5. References

(1) Roy, D.; Pal, A.; Pal, T. Electrochemical Aspects of Coinage Metal Nanoparticles for Catalysis and Spectroscopy. *RSC. Advances*. **2022**, 12, 12116–12135. https://doi.org/10.1039/d2ra00403h.

(2) Scanlon, M. D.; Smirnov, E.; Stockmann, T. J.; Peljo, P. Gold Nanofilms at Liquid-Liquid Interfaces: An Emerging Platform for Redox Electrocatalysis, Nanoplasmonic Sensors, and Electrovariable Optics. *Chem. Rev.* **2018**, *118* (7), 3722–3751. https://doi.org/10.1021/acs.chemrev.7b00595.

(3) Brust, M.; Walker, M.; Bethell, D.; Schiffrin, D. J.; Whyman, R. Synthesis of Thiol-Derivatised Gold Nanoparticles in a Two-Phase Liquid–Liquid System. *J Chem Soc., Chem. Commun.* **1994**, 7, 801–802. https://doi.org/10.1039/C39940000801.

(4) Uehara, A.; Booth, S. G.; Chang, S. Y.; Schroeder, S. L. M.; Imai, T.; Hashimoto, T.; Mosselmans, J. F. W.; Dryfe, R. A. W. Electrochemical Insight into the Brust–Schiffrin Synthesis of Au Nanoparticles. *J. Am. Chem. Soc.* **2015**, *137* (48), 15135–15144. https://doi.org/10.1021/jacs.5b07825.

(5) Al Nasser, H. A.; Kim, C.; Li, Q.; Bissett, M. A.; Haigh, S. J.; Dryfe, R. A. W. The Modified Liquid | Liquid Interface: An Electrochemical Route for the Electrode-Less Synthesis of MoS2 Metal Composite Thin Films. *Electrochim. Acta.* **2022**, *424*, 140609. https://doi.org/10.1016/j.electacta.2022.140609.

(6) al Nasser, H. A.; Bissett, M. A.; Dryfe, R. A. W. The Modified Liquid-Liquid Interface: The Effect of an Interfacial Layer of MoS2 on Ion Transfer. *Chem. Electro. Chem.* **2021**, *8* (23), 4445–4455. https://doi.org/10.1002/celc.202100820.

(7) Koya, I.; Yokoyama, Y.; Sakka, T.; Nishi, N. Formation of Au Nanofiber/Fullerene Nanowhisker 1D/1D Composites via Reductive Deposition at the Interface between an Ionic Liquid and Water. *Chem. Lett.* **2022**, *51(6)*, 643–645. https://doi.org/10.1246/cl.220134.

(8) Kuroyama, Y.; Nishi, N.; Sakka, T. Electrochemical Liquid-Liquid Interface between Oil and Ionic Liquid for Reductive Deposition of Metal Nanostructures. *J. Electroanal. Chem.* **2021**, *881*, 114959. https://doi.org/10.1016/j.jelechem.2020.114959.

(9) Zhang, Y.; Nishi, N.; Sakka, T. Template-Free and Spontaneous Formation of Vertically Aligned Pd Nanofiber Arrays at the Liquid-Liquid Interface between Redox-Active Ionic Liquid and Water. *ACS. Appl. Mater. Interfaces.* **2019**, *11* (26), 23731–23740. https://doi.org/10.1021/acsami.9b05255.

(10) Nishi, N.; Yajima, I.; Amano, K.-I.; Sakka, T. Janus-Type Gold/Polythiophene Composites Formed via Redox Reaction at the Ionic Liquid|Water Interface. *Langmuir.* **2018**, *34* (7), 2441–2447. https://doi.org/10.1021/acs.langmuir.7b03792.

(11) Lehane, R. A.; Gamero-Quijano, A.; Malijauskaite, S.; Holzinger, A.; Conroy, M.; Laffir, F.; Kumar, A.; Bangert, U.; McGourty, K.; Scanlon, M. D. Electrosynthesis of Biocompatible Free-Standing PEDOT Thin Films at a Polarized Liquid|Liquid Interface. *J. Am. Chem. Soc.* **2022**, *144* (11), 4853–4862. https://doi.org/10.1021/jacs.1c12373.

(12) Robayo-Molina, I.; Molina-Osorio, A. F.; Guinane, L.; Tofail, S. A. M.; Scanlon, M. D. Pathway Complexity in Supramolecular Porphyrin Self-Assembly at an Immiscible Liquid–Liquid Interface. *J. Am. Chem. Soc.* **2021**, *143*, 9060-9069. https://doi.org/10.1021/jacs.1c02481.

(13) Molina-Osorio, A. F.; Yamamoto, S.; Robayo-Molina, I.; Gamero-Quijano, A.; Nagatani, H.; Scanlon, M. D. A Soft on/off Switch Based on the Electrochemically Reversible H-J Interconversion of a Floating Porphyrin Membrane. *Chem. Sci.* **2021**, *12* (30), 10227–10232. https://doi.org/10.1039/d0sc05786j.

(14) Moshrefi, R.; P. Connors, E.; Merschrod, E.; Stockmann, T. J. Simultaneous Electropolymerization/Au Nanoparticle Generation at an Electrified Liquid | Liquid Micro-Interface. *Electrochim. Acta.* **2022**, *426*, 140749. https://doi.org/10.1016/j.electacta.2022.140749.

(15) Moshrefi, R.; Suryawanshi, A.; Stockmann, T. J. Electrochemically Controlled Au Nanoparticle Nucleation at a Micro Liquid | Liquid Interface Using Ferrocene as Reducing Agent. *Electrochem. Commun.* **2021**, *122*, 106894. https://doi.org/10.1016/j.elecom.2020.106894.

(16) Nieminen, E.; Murtomäki, L. Kinetics of Cu2+ Reduction and Nanoparticle Nucleation at Micro-Scale 1,2-Dichlorobenzene-Water Interface Studied by Cyclic Voltammetry and Square-Wave Voltammetry. *Electroanalysis.* **2021**, *33* (9), 2087–2095. https://doi.org/10.1002/elan.202100172.

(17) Sipa, K.; Kowalewska, K.; Leniart, A.; Walcarius, A.; Herzog, G.; Skrzypek, S.; Poltorak, L. Electrochemically Assisted Polyamide Deposition at Three-Phase Junction. *Electrochem. Commun.* **2021**, *123*, 106910. https://doi.org/10.1016/j.elecom.2020.106910.

(18) Gamero-Quijano, A.; Dossot, M.; Walcarius, A.; Scanlon, M. D.; Herzog, G. Electrogeneration of a Free-Standing Cytochrome c - Silica Matrix at a Soft Electrified Interface. *Langmuir.* **2021**, *37* (13), 4033–4041. https://doi.org/10.1021/acs.langmuir.1c00409.

(19) Cheng, Y.; Schiffrin, D. J. Electrodeposition of Metallic Gold Clusters at the Water | 1,2-Dichloroethane Interface. *J. Chem. Soc. - Faraday Trans.* **1996**, *92* (20), 3865–3871. https://doi.org/10.1039/ft9969203865.

(20) Johans, C.; Liljeroth, P.; Kontturi, K. Electrodeposition at Polarisable Liquid|liquid Interfaces: The Role of Interfacial Tension on Nucleation Kinetics. In *Phys. Chem. Chem. Phys.* **2002,** 4, 1067–1071. https://doi.org/10.1039/b110182j.

(21) Johans, C.; Kontturi, K.; Schiffrin, D. J. Nucleation at Liquid \ Liquid Interfaces: Galvanostatic Study. *J. Electroanal. Chem.* **2002**, *526* (1–2), 29–35. https://doi.org/10.1016/S0022-0728(02)00763-5.

(22) Johans, C.; Clohessy, J.; Fantini, S.; Kontturi, K.; Cunnane, V. J. Electrosynthesis of Polyphenylpyrrole Coated Silver Particles at a Liquid-Liquid Interface. *Electrochem. Commun.* **2002**, *4* (3), 227–230. https://doi.org/10.1016/S1388-2481(02)00256-4.

(23) Johans, C.; Lahtinen, R.; Kontturi, K.; Schiffrin, D. J. Nucleation at Liquid|liquid Interfaces: Electrodeposition without Electrodes. *J. Electroanal. Chem.* **2000**, *488* (2), 99–109. https://doi.org/10.1016/S0022-0728(00)00185-6.

(24) Chen, Y.; Chen, M.; Shi, J.; Yang, J.; Zhang, D. Fabrication of "Clean" Nano-Structured Metal Materials on Ionic Liquid|Water Interface. *Mater. Lett.* **2014**, *132*, 153–156. https://doi.org/10.1016/j.matlet.2014.06.052.

(25) Takagi, S.; Nishi, N.; Sakka, T. Ionic Liquid-in-Water Emulsion-Templated Synthesis of Gold Nanoshells at the Liquid-Liquid Interface between Water and Primary Ammonium-Based Ionic Liquids. *Chem. Lett.* **2019**, *48* (6), 589–592. https://doi.org/10.1246/cl.190146

(26) Seitkalieva, M. M.; Samoylenko, D. E.; Lotsman, K. A.; Rodygin, K. S.; Ananikov, V. P. Metal Nanoparticles in Ionic Liquids: Synthesis and Catalytic Applications. *Coord. Chem. Rev*. **2021**, *445*, 213982. https://doi.org/10.1016/j.ccr.2021.213982.

(27) Ahmadinasab, N.; Stockmann, T. J. Single-Entity Electrochemical Detection of As-Prepared Metallic and Dielectric Nanoparticle Stochastic Impacts in a Phosphonium Ionic Liquid. *Chem Electro. Chem.* **2022**, *9* (13), e202200162. https://doi.org/10.1002/CELC.202200162.

(28) Stockmann, T. J.; Lemineur, J. F.; Liu, H.; Cometto, C.; Robert, M.; Combellas, C.; Kanoufi, F. Single LiBH 4 Nanocrystal Stochastic Impacts at a Micro Water|ionic Liquid Interface. *Electrochim. Acta.* **2019**, *299*, 222–230. https://doi.org/10.1016/j.electacta.2018.12.105.

(29) Uematsu, T.; Baba, M.; Oshima, Y.; Tsuda, T.; Torimoto, T.; Kuwabata, S. Atomic Resolution Imaging of Gold Nanoparticle Generation and Growth in Ionic Liquids. *J. Am. Chem. Soc.* **2014**, *136* (39), 13789–13797. https://doi.org/10.1021/ja506724w.

(30) Bryant, K.; Hammond-Pereira, E.; Saunders, S. R. Ionic Liquid Aggregation Mechanism for Nanoparticle Synthesis. *J. Phys. Chem B.* **2021**, *125* (1), 253–263. https://doi.org/10.1021/acs.jpcb.0c08908.

(31) Nishi, N.; Kakinami, T.; Sakka, T. Dendritic Nanofibers of Gold Formed by the Electron Transfer at the Interface between Water and a Highly Hydrophobic Ionic Liquid. *Chem. Commun.* **2015**, *51* (71), 13638–13641. https://doi.org/10.1039/c5cc05476a.

(32) Weaver, J. E. F.; Breadner, D.; Deng, F.; Ramjee, B.; Ragogna, P. J.; Murray, R. W. Electrochemistry of Ferrocene-Functionalized Phosphonium Ionic Liquids. *J. Phys. Chem. C.* **2011**, *115* (39), 19379–19385. https://doi.org/10.1021/jp206927w.

(33) Stockmann, T. J.; Ding, Z. Tetraoctylphosphonium Tetrakis(Pentafluorophenyl)Borate Room Temperature Ionic Liquid toward Enhanced Physicochemical Properties for Electrochemistry. *J. Phys. Chem. B.* **2012**, *116* (42), 12826–12834. https://doi.org/10.1021/jp3081832.

(34) Stockmann, T. J.; Guterman, R.; Ragogna, P. J.; Ding, Z. Trends in Hydrophilicity/Lipophilicity of Phosphonium Ionic Liquids As Determined by Ion-Transfer Electrochemistry. *Langmuir.* **2016**, *32* (49), 12966–12974. https://doi.org/10.1021/acs.langmuir.6b03031.

(35) Olaya, A. J.; Méndez, M. A.; Cortes-Salazar, F.; Girault, H. H. Voltammetric Determination of Extreme Standard Gibbs Ion Transfer Energy. *J. Electroanal. Chem.* **2010**, *644* (1), 60–66. https://doi.org/10.1016/j.jelechem.2010.03.030.

(36) Stockmann, T. J.; Montgomery, A. M.; Ding, Z. Determination of Alkali Metal Ion Transfers at Liquid|liquid Interfaces Stabilized by a Micropipette. *J. Electroanal. Chem.* **2012**, *684*, 6–12. https://doi.org/10.1016/j.jelechem.2012.08.013.

(37) Zhou, M.; Gan, S.; Zhong, L.; Dong, X.; Ulstrup, J.; Han, D.; Niu, L. Improvement in the Assessment of Direct and Facilitated Ion Transfers by Electrochemically Induced Redox Transformations of Common Molecular Probes. *Phys. Chem. Chem. Phys.* **2012**, *14* (10), 3659–3668. https://doi.org/10.1039/c2cp23184k.

(38) Liu, S.; Li, Q.; Shao, Y. Electrochemistry at Micro- and Nanoscopic Liquid | Liquid Interfaces. *Chem. Soc. Rev.* **2011**, *40* (5), 2236–2253. https://doi.org/10.1039/c0cs00168f.

(39) Ying, Y. L.; Ding, Z.; Zhan, D.; Long, Y. T. Advanced Electroanalytical Chemistry at Nanoelectrodes. *Chem. Sci*. Royal Society of Chemistry **2017**, *8*, 3338–3348. https://doi.org/10.1039/c7sc00433h.

(40) Uehara, A.; Chang, S.-Y.; Booth, S. G.; Schroeder, S. L. M.; Mosselmans, J. F. W.; Dryfe, R. A. W. Redox and Ligand Exchange during the Reaction of Tetrachloroaurate with Hexacyanoferrate(II) at a Liquid-Liquid Interface: Voltammetry and X-Ray Absorption Fine-

Structure Studies. *Electrochim. Acta.* **2016**, *190*, 997–1006. https://doi.org/10.1016/j.electacta.2015.12.108.

(41) Usher, A.; McPhail, D. C.; Brugger, J. A Spectrophotometric Study of Aqueous Au(III) Halide-Hydroxide Complexes at 25-80 °C. *Geochim. Cosmochim. Acta.* **2009**, *73* (11), 3359–3380. https://doi.org/10.1016/j.gca.2009.01.036.

(42) Méndez, M. A.; Partovi-Nia, R.; Hatay, I.; Su, B.; Ge, P.; Olaya, A.; Younan, N.; Hojeij, M.; Girault, H. H. Molecular Electrocatalysis at Soft Interfaces. *Phys. Chem. Chem. Phys.* **2010**, *12* (46), 15163–15171. https://doi.org/10.1039/c0cp00590h.

(43) Vanýsek, P.; Haynes, W. M. Electrochemical Series, Ed. CRC Handbook of Chemistry and Physics*, CRC Press/Taylor,* Boca Raton, FL **2021**, 8.20-25.29.

(44) Stockmann, T. J.; Boyle, P. D.; Ding, Z. Preparation and Crystal Structure of Tetraoctylphosphonium Tetrakis(Pentafluorophenyl)Borate Ionic Liquid for Electrochemistry at Its Interface with Water. *Catal. Today.* **2017**, *295*, 89–94. https://doi.org/10.1016/j.cattod.2017.05.030.

(45) Batchelor-Mcauley, C.; Kätelhön, E.; Barnes, E. O.; Compton, R. G.; Laborda, E.; Molina, A. Recent Advances in Voltammetry. *Chem. Open.* **2015**, *4* (3), 224–260. https://doi.org/10.1002/open.201500042.

(46) Silvester, D. S.; Jamil, R.; Doblinger, S.; Zhang, Y.; Atkin, R.; Li, H. Electrical Double Layer Structure in Ionic Liquids and Its Importance for Supercapacitor, Battery, Sensing, and Lubrication Applications. *J. Phys. Chem C.* **2021**, *125* (25), 13707–13720. https://doi.org/10.1021/acs.jpcc.1c03253.

(47) Yasui, Y.; Kitazumi, Y.; Mizunuma, H.; Nishi, N.; Kakiuchi, T. A Comparison of the Ultraslow Relaxation Processes at the Ionic Liquid|water Interface for Three Hydrophobic Ionic Liquids. *Electrochem. Commun.* **2010**, *12* (11), 1479–1482. https://doi.org/10.1016/j.elecom.2010.08.011.

(48) Rastgar, S.; Teixeira Santos, K.; Angelucci, C. A.; Wittstock, G. Catalytic Activity of Alkali Metal Cations for the Chemical Oxygen Reduction Reaction in a Biphasic Liquid System Probed by Scanning Electrochemical Microscopy. *Chem. Eur. J.* **2020**, *26* (47), 10882–10890. https://doi.org/10.1002/chem.202001967.

(49) Jane Stockmann, T.; Deng, H.; Peljo, P.; Kontturi, K.; Opallo, M.; Girault, H. H. Mechanism of Oxygen Reduction by Metallocenes near Liquid|liquid Interfaces. *J. Electroanal. Chem.* **2014**, *729*, 43–52. https://doi.org/10.1016/j.jelechem.2014.07.001.

(50) Sharma, N.; Ajay, J. K.; Venkatasubbaiah, K.; Lourderaj, U. Mechanisms and Dynamics of Protonation and Lithiation of Ferrocene. *Phys. Chem. Chem. Phys.* **2015**, *17* (34), 22204–22209. https://doi.org/10.1039/c5cp03735b.

(51) Alvarez, M. M.; Khoury, J. T.; Schaaff, T. G.; Shafigullin, M.; Vezmar, I.; Whetten, R. L. Critical Sizes in the Growth of Au Clusters. *Chem. Phys. Lett.* **1997**, *266*, 91–98. https://doi.org/10.1016/S0009-2614(96)01535-7

(52) Zanatta, M.; Antunes, V. U.; Tormena, C. F.; Dupont, J.; dos Santos, F. P. Dealing with Supramolecular Structure for Ionic Liquids: A DOSY NMR Approach. *Phys. Chem. Chem. Phys.* **2019**, *21* (5), 2567–2571. https://doi.org/10.1039/c8cp07071g.

(53) Barmparis, G. D.; Lodziana, Z.; Lopez, N.; Remediakis, I. N. Nanoparticle Shapes by Using Wulff Constructions and First-Principles Calculations. *Beilstein. J. Nanotechnol*. **2015**, *6*, 361–368. https://doi.org/10.3762/bjnano.6.35.

(54) Jorabchi, M. N.; Abbaspour, M.; Goharshadi, E. K.; Wohlrab, S. Ag, Au, Pt, and Au-Pt Nanoclusters in [N1114][C1SO3] Ionic Liquid: A Molecular Dynamics Study. *J. Mol. Liq.* **2022**, *360*, 119447. https://doi.org/10.1016/j.molliq.2022.119447.

Chapter 4

4. Simultaneous electropolymerization/Au nanoparticle generation at an electrified liquid|liquid micro-interface

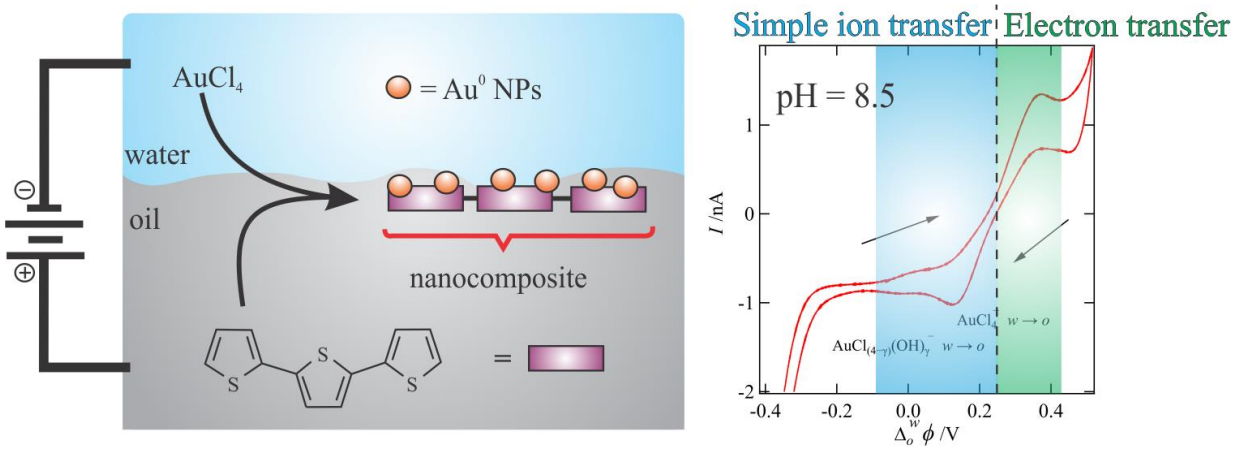

4.1. Statement of Co-Authorship

This chapter has been published under the above title in *Electrochimica Acta* **2022**, 426, 140749. It is presented here in a modified format that includes all contributions for completeness and context.

Authors: Reza Moshrefi, Evan P. Connors, Erika Merschrod, and T. Jane Stockmann

This article was a group effort combining the work of graduate student co-authors from the research groups of Erika Merschrod and T. Jane Stockmann

Reza Moshrefi (listed in the paper as 1st author): Performed electrochemical experiments, material characterization and contributed to formal analysis, investigation, writing - review & editing, validation.

Evan P. Connors and Erika Merschrod: Contributed to the collection and interpretation of AFM data

Dr. T. Jane Stockmann: Is the principal investigator of this work, who led the project and contributed to conceptualization, methodology, writing - original draft, validation, supervision, project administration, funding acquisition.

4.2. Introduction

Electrosynthesis of conductive polymer films has been of considerable interest for decades for a host of catalytic, senor, and biomedical applications.[1,2] Electropolymerization of conductive polymer films has been studied extensively at solid electrode/electrolyte interfaces using aniline[3,4], pyrrole[5,6], or thiophenes[7–9] as electroactive monomers. Recently, growth of 2D and 3D structures at the interface between two immiscible electrolyte solutions (ITIES) has gained attention, *e.g.*, between water|oil (w|o).[10–21] The liquid|liquid interface is advantageous as it is molecularly sharp/defect free;[22] moreover, the generated film is not covalently bonded to a solid electrode substrate making its removal much less complicated to create a free-standing film.[10,11] Additionally, surface defects in the solid electrode surface can be transcribed on to the polymer film and play a role in the final morphology, which can be avoided via polymerization at an ITIES.

In the 2000′s, Cunnane's group transposed electropolymerization to the macro-ITIES (mm scale), by dissolving the monomer species in 1,2-dichloroethane (DCE) and an oxidizing agent in the aqueous phase.[12–21] For example, they showed that $Fe_2(SO_4)_3/FeSO_4$(aq) could be employed as electron acceptors for the electrogeneration of 1-methyl- and 1-phenyl-pyrrole oligomers.[21] The interfacial electron transfer reaction can be summarized as follows,

$$Ox(aq)+D(org)\rightarrow Red(aq)+ D^{+}(org) \quad 4\text{-}1$$

Where D is the monomer/electron donor. Cunnane and Konturri's groups[20] also investigated 2,2′:5′,2″-terthiophene (TT) electro-polymerization at a large aqueous|1,2-dichloroethane (w|DCE) interface using the Ce(IV)/Ce(III) redox couple in the aqueous phase; however, Vignali *et al.*[14,15] reported the first free-standing film that could be extracted from the ITIES. Simultaneously, Johans *et al.*[23], Trojánek's group,[24] and Su *et al.*[25] were investigating metal nanoparticle (NP) nucleation and assembly/electrocatalysis at the ITIES as well as developing analytical solutions to the complex dynamic problem of NP nucleation at an interface which has no surface defects to act as nucleation sites. At solid surfaces, defect sites lower the overall thermodynamic driving force for NP formation/initiation. In the following decade, Uehara and Dryfe's groups would extensively investigate Au NP nucleation at the liquid|liquid interface[26–30] using different reducing agents and go on to characterize the Brust-Schiffrin mechanism for Au NP preparation,[28] first demonstrated by Brust *et al.*[31] in the mid 1990s. While recently our group[32] and others[33] have shown electrogeneration of metal NPs at a micro-ITIES using metallocenes as electron donors.

Combining these two efforts Johans *et al.*[19] and Lepková *et al.*[12,13] evidenced simultaneous electropolymerization and NP nucleation at a macro-ITIES, which in the latter reports resulted in polymer coated NPs whose size could be controlled by the applied Galvani potential difference across the ITIES $\left(\phi_{w} - \phi_{o} = \Delta_{o}^{w}\phi\right)$; however, no free-standing, nanocomposite thin-films where evidenced, only polymer coated NPs. Although, by employing tetraoctylammonium tetra-chloroaurate ($TOAAuCl_4$), this time dissolved in DCE and acting as the oxidizing agent, coupled with tyramine as the monomer dissolved in the aqueous phase, Cunnane's group were able to electrogenerate a Au nanoparticle (NP) incorporated conductive polymer film at the macro-ITIES.[16] They analyzed their nanocomposite material with X-ray photoelectron spectroscopy

(XPS), atomic force microscopy (AFM), and transmission electron microscopy (TEM). Investigation of electropolymerization at the ITIES has remained relatively dormant since the work of Cunnane's group in the mid-2000′s.

Herein, we demonstrate the affect of pH on the simultaneous electrogeneration of Au NPs and electropolymerization of TT or 2,2′-bithiophene (BT, see Figure 4-1). Our approach employs $KAuCl_4$ dissolved in the aqueous phase as an electron acceptor and TT dissolved in the organic phase as electron donor and monomer. In this way, small, <2 nm in diameter, Au NPs are generated in situ and incorporated into the growing TT thin film. By performing these experiments at a micro-ITIES (25 μm in diameter) positioned at the tip of a pulled borosilicate glass capillary, sensitive cyclic voltametric curves were able to record the interfacial electron transfer wave at relatively low overpotentials. This is critical to avoid overoxidation of the monomer and growing polymer film.[15,34] Our micro-ITIES platform can also be exploited as a mechanical delivery system for the free-standing film that, after formation, was deposited on a solid substrate for AFM imaging. AFM and SEM images indicate that the polymer/NP growth phase likely proceeds through several stages. Initially, when the interface is pristine, Au NPs are small; however, as the ITIES becomes occluded by the film, TT can no longer access the aqueous side and act as a capping agent but since the film is conductive, it can still mediate electron transfer. Therefore, later in the growth cycle Au NPs likely become large, >10 nm in diameter.

Electrochemical impedance spectroscopy (EIS) combined with TEM images provide semi-quantitative evidence that a Brønsted base is necessary to capture the protons from the intermediate TT radical cation ($TT^{+\bullet}$) and facilitate electropolymerization. Thus, electropolymerization is enhanced at high pH (~8.5) and inhibited at low pH. While TT electropolymerization mechanisms

have been investigated extensively,[7] the influence of biphasic w|o systems on the reaction pathway is shown herein for the first time.

4.3. Experimental methods

4.3.1. Chemicals and materials

Potassium tetrachloroaurate ($KAuCl_4$ >98%), hydrochloric acid (HCl >37%), sodium hydroxide (NaOH, ≥98%), trioctylphosphine (97%), bromooctane (99%), ferrocene (Fc, >99%), dichloromethane (CH_2Cl_2, >99%), terthiophene (TT, 99%), bithiophene (BT, 99%), and 1,2-dichloroethane (DCE, ≥99.0%) were acquired from Sigma-Aldrich and used without additional purification. Tetrakis(pentafluorophenyl)borate lithium etherate ($Li(Et_2O)_nB(C_6F_5)_4$) (>99%) was sourced from Boulder Scientific Inc. Ultrapure water from a MilliQ filtration system (>18.2 MΩ cm) was used throughout to generate aqueous solutions. The tetraoctylphosphonium tetrakis(pentafluorophenyl)borate ($P_{8888}TB$) IL was prepared as detailed elsewhere[35]; however, a brief description is included below.

First, tetraoctylphosphonium bromide ($P_{8888}Br$) was prepared by adding trioctylphosphine to a stoichiometric excess of 1-bromooctane under N_2 to a pressure tube (ACE glass). A stir bar was added, the vessel was sealed, and the reaction mixture stirred for ~48 h. After excess 1-bromooctane was removed under vacuum, a clear viscous liquid was obtained. This was confirmed to be $P_{8888}Br$ by ^1H- and ^{31}P- NMR[35]. Next, $P_{8888}Br$ and was combined with $Li(Et_2O)_nB(C_6F_5)_4$ in 1:1 stoichiometric equivalent in a 50%/50% (v/v) H_2O/CH_2Cl_2 solution and stirred for ~24 h. The CH_2Cl_2 phase was collected and washed 5 × with 100 mL of MilliQ water. Next, the solvent phase was removed under reduced vacuum to obtain a solid white crystal which was structurally confirmed through ^1H- and ^{31}P-NMR to be $P_{8888}TB$.[35]

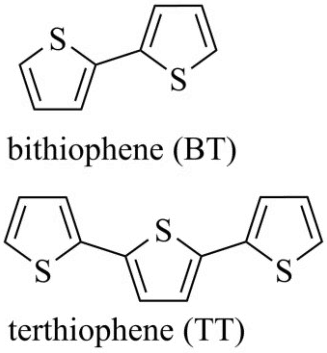

Figure 4-1 Chemical structures of 2,2′-bithiophene (BT) and 2,2′:5′,2″-terthiophene (TT).

4.3.2. Transmission and microscopy

All transmission electron microscopy (TEM) images were taken using the Tecnai Spirit Transmission Electron Microscope with samples pre-pared on 200 Mesh Cu ultrathin/lacey carbon grids. (Electron Microscopy Sciences).

4.3.3. Scanning electron microscopy (SEM)

SEM imaging was performed using a JEOL JSM 7100 F equipped with all energy dispersive X-ray (EDX) spectra were analyzed using DTSA II software from the National Institute of Standards and Technology (NIST) in the US; please see https://www.nist.gov/services-resources/software/nist-dtsa-ii.

4.3.4. Atomic force microscopy

The AFM employed was a MFP-3D from Asylum research equipped with NSC35/Al BS tips (MikroMasch) operating at a scan rate of 0.25 Hz

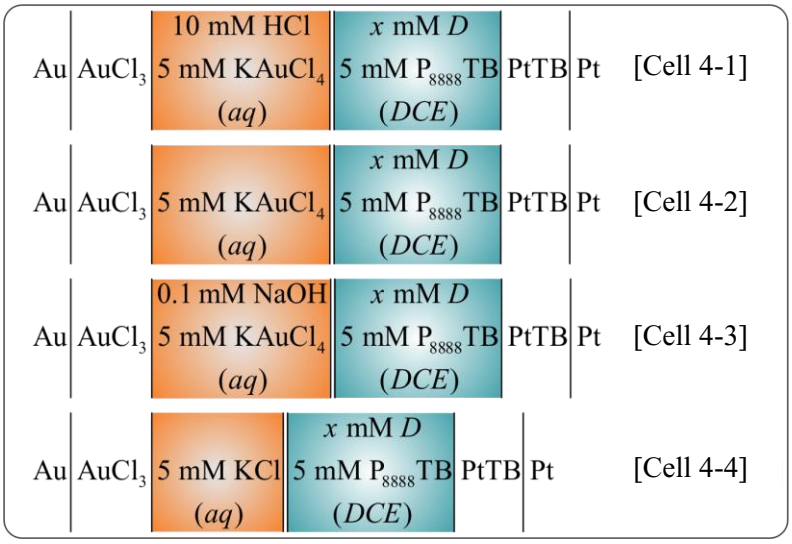

Scheme 4-1 Electrolytic cells employed, where x corresponds to the concentration D, the electron donor (i.e., 2,2':5',2''-terthiophene, TT, or 2,2'-biothiophene, BT). The pH of Cells 4-2 and 4 were roughly 5.5 (MilliQ ultrapure water), while Cells 4-1 and 4-3 were confirmed to be 2 and 8.5, respectively, using a pH meter (sympHony model# B10P, VWR). In each case, 5 mM of $P_{8888}TB$ (tetraoctylphosphonium tetrakis(pentafluorophenyl)borate) was added to the organic phase as a supporting electrolyte. The double line indicates the ITIES or polarizable liquid junction.

4.3.5. Electrochemistry

A HEKA Electroniks potentiostat (model# PG-618-USB) was used to record electrochemical measurements. A modified pipette holder with integrated connection to a gold (Au) wire (Goodfellows Inc.) served as the working electrode. The pipette (2.00 mm:1.16 mm, outer: inner diameter) was installed into a holder which was equipped with a syringe used to back-fill the pipette with the aqueous solution and maintain the micro-ITIES (25 µm in diameter) at the tip of the pipette. The pipette tip was then submerged into an organic phase. Micropipette fabrication has been described in Section 1 of Appendix C and elsewhere.[32,36–38] A Pt wire served as the counter/reference electrode (CE/RE) and was placed in the organic phase. Scheme 4-1 details the electrolytic cells employed in this study.

Electrochemical impedance spectroscopy (EIS) was performed with a frequency range between 10 and 20 kHz and by applying a 20 mV peak-to-peak perturbation.

4.4. Results and discussion

Figure 4-2 shows cyclic voltammograms (CVs) obtained at a w|DCE micro-ITIES at 0.020 V s^{-1} using Cells 4-1, 2, 3, and 4 (Scheme 4-1) at pH 2, ~5.5, 8.5, and ~5.5, respectively, with no electron donor added to the DCE phase (i.e., x =0). At pH 2 and ~5.5, the polarizable potential window (PPW) is limited at positive and negative ends by the respective transfer of K^+/H^+ and Cl^-.[39–43] At pH 2 (red curve in Figure 4-2) and when scanning from positive to negative potentials, the lone negative peak-shaped wave encountered at 0.126 V is associated with the free ion transfer of $AuCl_4^-$ from w to o; however, when moving from negative to positive potentials, a sigmoidal-shaped wave with a half-wave potential $\left(\Delta_o^w\phi_{1/2}\right)$ of 0.154 V was observed, which is the transfer of $AuCl_4^-$ back from o to w. The asymmetric *i*-V response is owing to geometric confinement inside the micropipette such that egress from the tip (from w→o) follows a linear diffusion behavior resulting in a peak-shaped response, while ingress of ions (from o→w) follows a hemispherical diffusion regime, generating a steady state current profile similar to an inlaid disk ultramicroelectrode.[44–46] $\Delta_o^w\phi_{1/2}$ for $AuCl_4^-$ agrees well with previous reports.[27,28,32] If the pH in the aqueous phase is increased, then a second negative peak appears (see Figure 4-2, black and green traces) at –0.015 V. This signal is the simple ion transfer of $AuCl_{(4-\gamma)}(OH)_\gamma^-$ from w→o since, at pH >2.5, tetrachloroaurate can undergo ligand speciation[47,48] with OH^-, i.e., γ =1–3.[27,49]

Figure 4-3 depicts the voltametric response once 30 mM of TT was added as electron donor to the DCE phase. Figure 4-3(A–C) show the initial CV scan, while Figure 4-3(D–F) contain plots for the *i*-V responses of scans 5–25 showing every 5th scan. The left, middle, and right-hand panels correspond to Cells 4-1, 2, and 3 or aqueous phase pH's of 2, 5.5–6, and 8.5, respectively. Before each CV a potentiostatic pulse was applied at the initial potential (~0.0 V) for ~1 s; however, a negative current offset was observed in all cases after addition of TT.

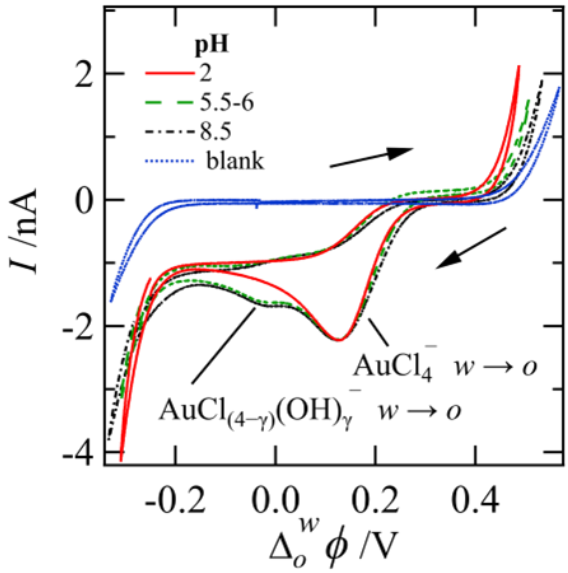

Figure 4-2 Cyclic voltammograms (CVs) obtained using Cells 4-1, 2, 3, and 4 at pH 2, ~5.5, and 8.5, respectively, in the aqueous phase as indicated inset. The blue, dotted CV was recorded using Cell 4-4 without $KAuCl_4$ or D added – a blank curve. A 0.020 V s^{-1} scan rate was employed throughout.

While TT is hydrophobic and likely does not partition into the aqueous phase, the intermediate hydrophilicity of $AuCl_4^-/AuCl_{(4-\gamma)}(OH)_\gamma^-$ means that it likely does partition. Furthermore, a homogeneous electron transfer mechanism between TT and $AuCl_4^-/AuCl_{(4-\gamma)}(OH)_\gamma^-$, taking place in the DCE phase, may act as an electrochemical gradient/driving force generating a flux of $AuCl_4^-/AuCl_{(4-\gamma)}(OH)_\gamma^-$ from w→o. This hypothesis would explain the initial negative current offset experienced during the initial scan in each case. However, during the first scan, the *i*-V response was observed to crossover at ~0.4 V in most cases (see Figs. 4-3E, F and C2 in Appendix C). This is a common feature of CVs when the interface is modified. For example, Kanoufi's group[50] observed a similar event during electrodeposition of a $Co/Co(OH)_2$ nanoparticle (NP) at the tip of a nanoelectrode followed by the particles subsequent re-oxidation (i.e., $Co^{2+} + 2e^- \rightarrow Co^0 + 2OH^- \rightarrow Co(OH)_2 + 2e^-$). Indeed, CV crossover events are common during electropolymerization of thiophenes and pyrroles at solid/electrolyte interfaces[1,2] and were

observed by Vignali *et al.*[14] during electropolymerization of TT using Ce(IV)/Ce(III) redox couple at a macro-ITIES, however, only at extremely high overpotentials. In the latter,[34] specialized 3- and 4-electrode liquid|liquid electrolytic cells were fabricated in order to mitigate capacitive currents and to achieve the high overpotentials the authors thought necessary for film formation, as well as eliminate the need for Luggin capillaries, which facilitated removal of the free-standing film afterwards. As Vignali *et al.* note, the use of high overpotentials runs the risk of over-oxidizing the monomer/polymer and, in the case of thiophenes, generating SO_2.[14,34]

Replacement of TT by BT resulted in no film formation and no electron transfer wave was observed (data not shown).

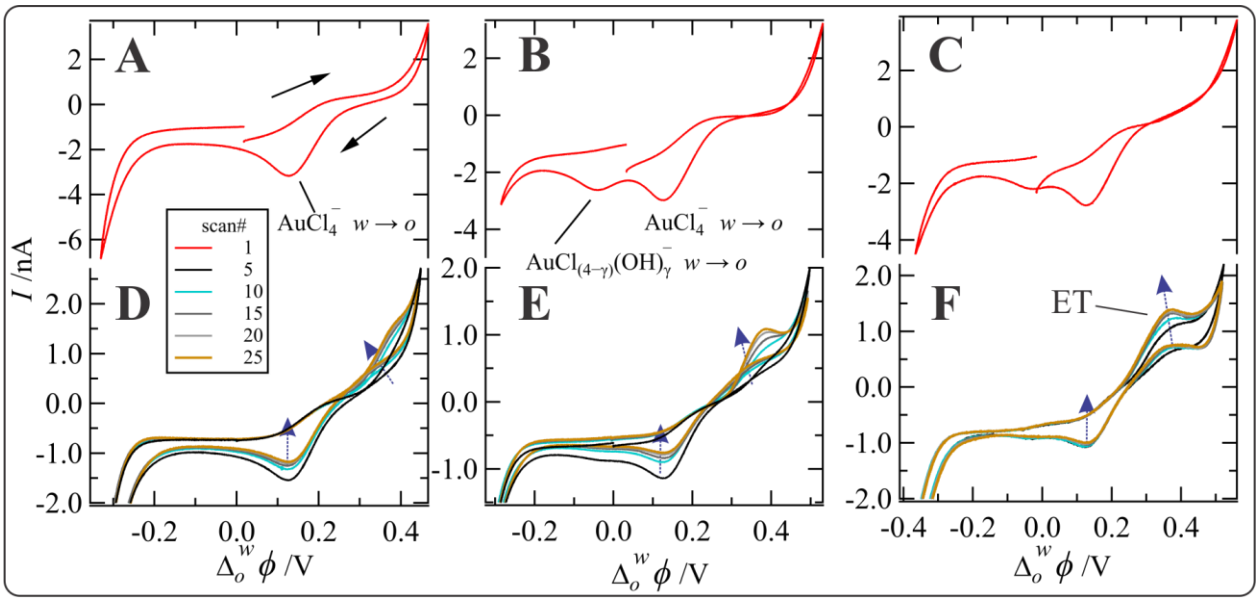

Figure 4-3 CVs recorded using Cells 4-1, 2, and 3 at aqueous pH of 2, 5.5-6, and 8, for the left-hand, middle, right-hand panels, respectively, with D = TT at a concentration x = 30 mM in DCE. Top panels show the first scan, while the bottom panels are overlays of the 5-25 scan showing every 5th trace. A scan rate of 0.020 V s^{-1} was used. Solid arrows indicate scan direction, while blue, dashed arrows indicate the direction of evolving/diminishing current signals. ET = electron transfer.

Upon application of repeated scans (Figure 4-3(D–F)) a positive steady state, and subsequently peak-shaped wave evolves with $\Delta_o^w\phi_{1/2} \approx 0.3$–$0.4$ V; the peak-shaped wave is more pronounced at higher pH (see Figure 4-3F). Simultaneously, the magnitude of the

$AuCl_4^-/AuCl_{(4-\gamma)}(OH)_\gamma^-$ transfer current diminishes on average from –2.8 to –1.0 nA. Based on these results, it was hypothesized that an irreversible, heterogeneous electron transfer process develops at positive potentials greater than $\Delta_o^w\phi_{\frac{1}{2},AuCl_4^-}$ which can be described very loosely by,

$$2AuCl_{(4-\gamma)}(OH)_\gamma^-(aq) + 3H_2\text{-}TT + (6-\gamma)H^-(aq) \rightarrow 2Au(s) + TT_3(s) + 8Cl^-(aq) + 6H_2O(l) \quad 4\text{-}2$$

H_2-TT represents the initial terthiophene molecule (see Figure C1 of the Appendix C), while TT_3 represents a terthiophene oligomer three units long. Eq. (4-2) is not intended to be a rigorous treatment of the polymerization reaction but allows one to arrive at a simple, *back-of-the-envelope* thermodynamic approximation for the initial steps of the reaction. A dynamic geometric simulation employing finite element analysis is in-preparation; however, is beyond the scope of this work. In Eq. (4-2), TT acts as a 2-e^- donor; furthermore, it is assumed that poly-TT precipitates at the interface favouring linear polymerization with addition at the α- or β-carbon at either end of the TT molecule. This is associated with the simultaneous reduction of the $AuCl_4^-/AuCl_{(4-\gamma)}(OH)_\gamma^-$ to Au^0, as NPs. The concerted reaction shown in Eq. (4-2) is unlikely and electro-polymerization/nucleation is probably a stepwise reaction mechanism as described by Vignali *et al.*[14] While Eq. (4-2) and its assumptions are a gross approximation, they facilitate a simplified thermodynamic calculation (see below). Repeated cycling of the potential is necessary to induce Au NP/polymer nucleation. Owing to the possible pH and [TT] dependence of Eq. (4-2), three pH regimes and [$KAuCl_4$]:[TT] concentration ratios (1:1, 1:2, and 1:3) were investigated (see also Figure C2 of Appendix C).

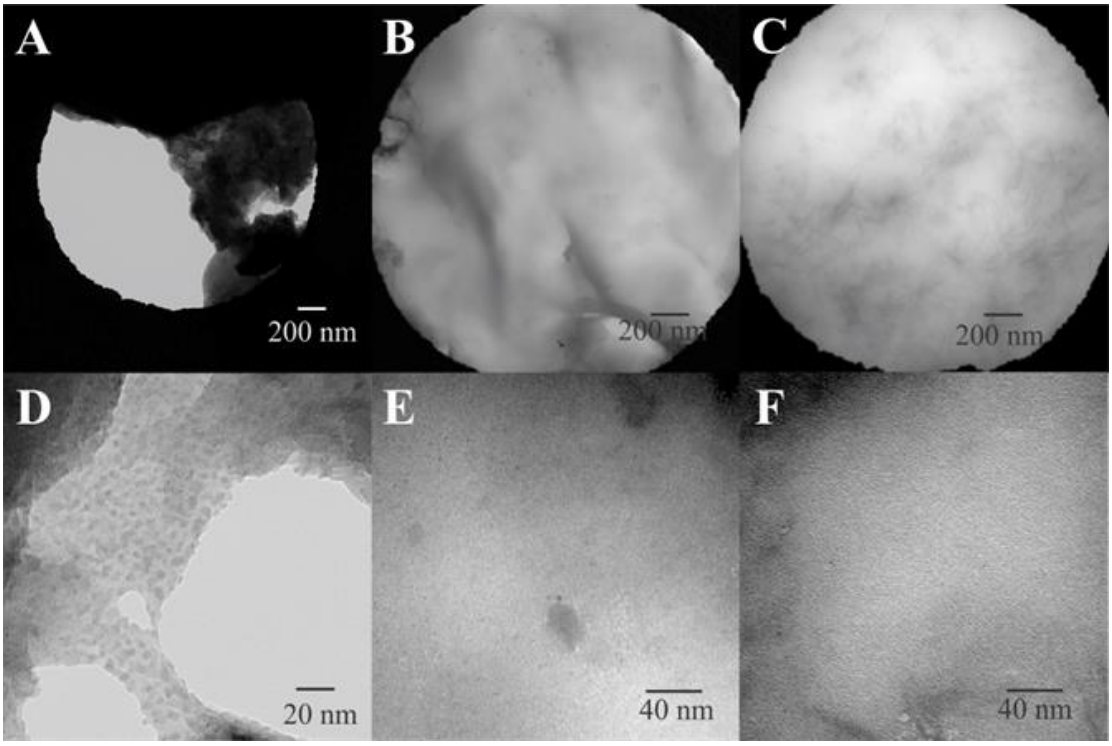

Figure 4-4 TEM micrographs of NP/polymer composite film deposited on 2 μm diameter porous Au TEM grids using Cells 4-1, 2, and 3 for the left-, center, and right-hand panels, respectively with [TT] = 30 mM. Top images show polymer film coverage of the 2 μm pore, while the bottom row is magnified to show NP inclusion.

To best describe the thermodynamics of TT oxidation in DCE, the redox potential of TT was measured in DCE using a 7 μm diameter carbon fiber ultramicroelectrode (UME) and using $P_{8888}TB$ as supporting electrolyte versus ferrocene (Fc^+/Fc, see Figure C3 of Appendix C). $E^{o',DCE}_{Fc^+/Fc}$ (vs. SHE) in DCE was assumed to be 0.64 V[51]; in this way, $E^{o',DCE}_{TT^+/TT}$ (vs. SHE) was calculated to be 1.20 V. Next, using the standard reduction potential of $AuCl_4^-$ in water ($E^{o,H_2O}_{AuCl_4^-/Au}$=1.002 V, vs. SHE)[52] and the above assumptions, one can calculate the approximate liquid|liquid, interfacial electron transfer potential ($\Delta^w_o\phi_{ET}$) by,[23,24,32,51]

$$\Delta^w_o\phi_{ET} \approx E^{o',DCE}_{Fc^+/Fc} - E^{o,H_2O}_{AuCl_4^-/Au} - \frac{(0.059)(6-\gamma)}{6}\log[OH^-] \qquad 4\text{-}3$$

For the algebraic derivation of Eq. (4-3), see Section 4 of the Appendix B. In this way, $\Delta^w_o\phi_{ET}$ was calculated to be 0.90, 0.62, and 0.41 V for aqueous pH = 2, 5.5, and 8.5, respectively. These

values indicate that ΔG of the reaction is >0 and decreases with increasing pH; these values agree semi-quantitatively with the observed position of electron transfer wave, e.g., the peak potential for scan 25 at pH 8.5 with [TT] = 30 mM was ~ 0.36 V. These values also indicate that a Brønsted base is needed to facilitate loss of two protons from each TT unit (see Figure C1 of Appendix C). It is likely that once nucleation sites are present at the ITIES, the necessary applied potential required to induce electropolymerization/NP formation is decreased and $\Delta_o^w\phi_{1/2,ET}$ shifts to more negative potentials as observed experimentally.

To investigate the possible formation of Au NPs and the polymer film, an aqueous droplet was ejected from the end of the micropipette onto a Au TEM sampling grid with 2 μm diameter holes and rinsed with MilliQ water. Figure 4-4 shows the TEM images obtained after 25 cycles, such that the left, center, and right-hand panels are for Cells 4-1, 2, and 3 (pH 2, 5.5–6, and 8.5), respectively, with [TT] =30 mM. At pH 2 (left-hand panel in Figure 4-4), the thin film does not cover the entire pore and the majority of pores on the grid were empty of film; however, at pH >5.5, the TEM grid was occluded by a thin NP/polymer film. NPs sizes were estimated by processing the TEM images using ImageJ software; Figure C-4 of Appendix C shows the histograms constructed and fit using a Gaussian equation. The peak from the Gaussian distribution was assumed to be the average NP size and was shown to be 0.7, 1.1, and 0.7 nm in diameter for pH's 2, 5.5–6, and 8.5, respectively.

These data indicate that at low pH the film is poorly/incompletely formed, while at high pH complete film formation is more facile. These results agree qualitatively with the thermodynamic and mechanistic hypotheses above that highlight the need for a proton acceptor to drive radical-cation coupling.

Similarly, NP/polymer films were mechanically deposited on Si wafers and imaged using atomic force microscopy (AFM) and scanning electron microscopy (SEM). Figure 4-5(A–C) show the AFM images obtained for pH's 2–8.5, respectively, while inset (right-hand side) are histograms of the NP radii which were determined from the measured peak heights and (left-hand side) SEM images. For simplicity, it was assumed that peaks >5 nm in height were NPs. Using the peak from a Gaussian curve fitting of the histogram, the average NP radius, r_{NP}, was determined to be 20, 40, and 14 nm for pH's 2, ~5.5, and 8.5, respectively. At low pH the film was incomplete and difficult to observe on the Si wafer, while this was the opposite at higher pH. Examining Figure 4-5, one can observe that the surface roughness increases with increasing pH, which is roughly equivalent to the observed NP density on the surface of the film. The average thickness of the composite film was determined to be ~0.4 μm for pH >5.5. SEM images (Figure 4-5, left-hand inset) show the distribution of Au NPs on the surface of the film confirmed by energy dispersive X-ray (EDX) spectroscopy (data not shown). Comparison of the AFM, SEM, and TEM results suggests that the Au NPs formed early in the electropolymerization process are small, <2 nm in diameter, and this size increases with distance from the w|DCE interface. Since TT is acting as a capping agent, as the polymer film blocks the ITIES TT can no longer access the aqueous side of the interface; however, because the film is still conductive it can mediate electron transfer between $AuCl_4^-$(aq) and TT(org). Thus, new Au NPs nucleate on the aqueous side of the film and their size is likely larger than those entirely enclosed in polymeric material. Similarly, on the DCE side, the film likely continues to grow, however, with no Au NPs incorporated. Therefore, the film is likely asymmetric; however, due to its small size, the formed films were difficult to image, and this will be a source of future research. Initial films composed of TT were roughly 2 mm in diameter when deposited onto the film after 25 scans; however, they were very fragile, brittle, and hard to manipulate. More work needs to be done to enhance the robustness of the film before it can be

used as a free-standing electrode. Moreover, the thickness and diameter of the film can likely be adjusted by the number of scans and the size of the interface; however, an indepth study is on-going and will be the focus of a future publication.

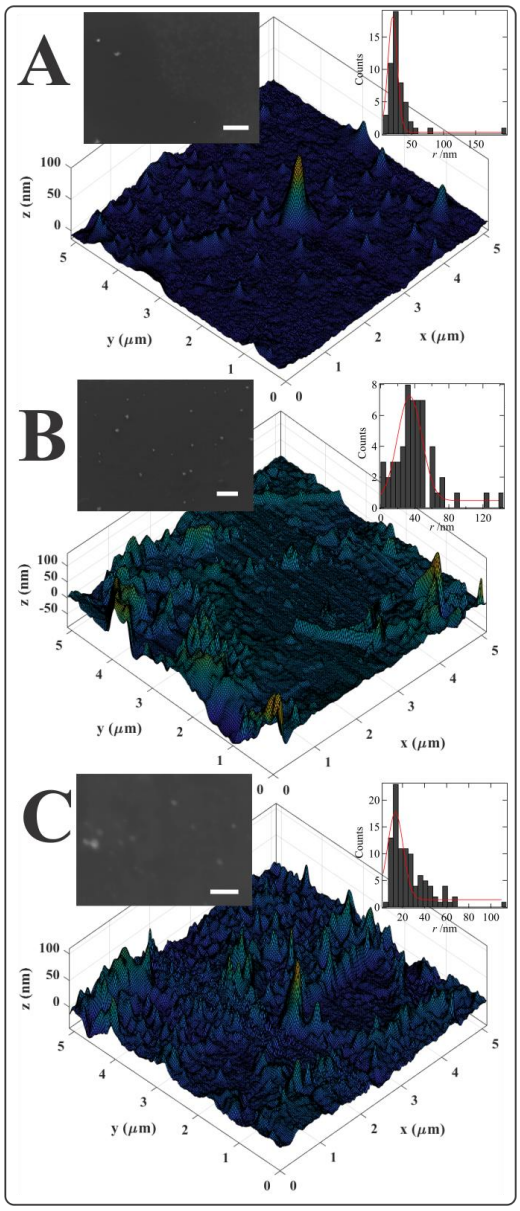

Figure 4-5 AFM images of NP/poly-TT films grown after 25 scans at a micro-ITIES using Cells 4-1 (A), 4-2 (B), or 4-3 (C) with [TT] DCE = 15 mM and deposited on a silicon wafer. Right-hand inset are histograms for NP radii determined from the associated AFM image. Left-hand inset are respective SEM images where the scale bar is equivalent to 400 nm (A and B) and 100 nm (C).

To estimate the total amount of Au NPs generated, the electron transfer wave in Figure 4-3 was integrated for each cycle and summed. Using Faraday's law and assuming quantitative conversion of the $AuCl_4^-$ salt, 4.9, 4.8, and 9.5 nmol of Au NPs were electrogenerated across the 25 scans for pH's 2, 5.5–6, and 8.5 according to the data presented in Figure 4-3. These data represent the maximum total Au content in the film.

Figure 4-6 shows the Nyquist plots acquired from electrochemical impedance spectroscopy (EIS) measurements using Cells 4-1, 2, and 3 in panels A, B, and C, respectively, while changing the concentration of TT in the DCE phase as indicated inset, with a direct applied voltage of $\Delta_o^w\phi$ ≈ 0.4 V, *i.e.*, above the electron transfer potential for TT electropolymerization. Meanwhile, Figure 4-6D depicts the impedance response without TT added for each Cell/pH range as indicated, for comparison. Each spectra shows a semi-circle at high frequencies (low Z') commonly associated with solution resistance and the double layer structure at the ITIES as well as a tail at low frequencies (high Z') linked to mass transport. Solid/dashed curves in Figure 4-6 were obtained by fitting the experimental impedance spectra with the equivalent circuits (EC) shown in Figure 4-6D using Zview software. EC-2 is a modified Randles circuit which consisted of a solution resistance (R_s) in series with a constant phase element (CPE, CPE1) in parallel with a charge transfer resistance (R_{CT}) component and a second CPE, CPE2. Typically, the faradic impedance, Z_f, is equivalent to a resistor and a Warburg element in series.[53] Faradic impedance for simple ion transfer following semi-infinite diffusion can be defined as a combination of a charge transfer resistance and the Warburg impedance as follows,[54,55]

$$Z_f = R_{CT} + Z_w = \frac{RT}{z^2F^2Ak_fc^*_{i,w}} + (1-\mathrm{j})\sigma\omega^{-1/2} \qquad 4\text{-}4$$

where σ is defined as,

$$\sigma = \frac{RT}{\sqrt{2}z^2F^2A}\left(\frac{1}{D_{i,o}^{1/2}c_{i,o}^{*}} + \frac{1}{D_{i,w}^{1/2}c_{i,w}^{*}}\right) \quad 4\text{-}5$$

and where R is the universal gas constant (8.314 J K^{-1}), T is absolute temperature (298.15 K), F is Faraday's constant (96,485.33 C mol^{-1}), A is the interfacial surface area (490 μm^2), k_f is the standard rate constant (1 cm s^{-1}), ω is the angular frequency, $j = \sqrt{-1}$, and z is the charge of species i or the number of electrons transferred. $D_{i,\alpha}$ and $c_{i,\alpha}^{*}$ are the diffusion coefficient and bulk concentration of species i in phase α (*i.e.*, w or o). For simplicity the Warburg impedance element has been replaced by a CPE in EC-2 and −3 in which n = 0.5 represents the idealized Warburg value (semi-infinite diffusion)[56] and n = 1 a perfect capacitor [57]. Impedance of a CPE is represented by,[57]

$$Z(\omega) \approx \frac{1}{Q}(j\omega)^{-n} \quad 4\text{-}6$$

Where Q is a constant with units of $F\,s^{1-n}$. R_s representing the solution resistance and shown in EC-1 but has been omitted for simplicity from the other two equivalent circuits.

The shape of the first loop in Nyquist plot is heavily influenced by the geometry and capacitance at the interface,[56,58] *i.e.*, its size, position, and shape as well as charging along the capillary walls and micro-channel.[32] The tail at low frequencies is impacted by reactions occurring at the interface, including interfacial ion and electron transfer as well as mass transport/semi-infinite diffusion.[54,56] Our micropipette fabrication method affords robust capillaries with uniform geometries that can be cleaned and used repeatedly, similar to those employed by Silver *et al.*[56] While the tip geometry is often the largest contributor to the overall electrolytic cell impedance, in all cases a capillary tip impedance of ≤1 MΩ was obtained using a single-phase experiment as described by Samec's group.[56] This has been demonstrated to be necessary to resolve all of the

individual circuit elements and distinguish the kinetics of simple ion and electron transfer reactions.[54,56]

For [TT] =0 (Figure 4-6D), Nyquist spectra were fit using the modified Randle's circuit (EC-2). In Cell 4-1 at pH 2, the pronounced tail at low frequencies and lower overall magnitude in the impedance profile is owning to the high diffusion coefficient of protons in the aqueous phase.

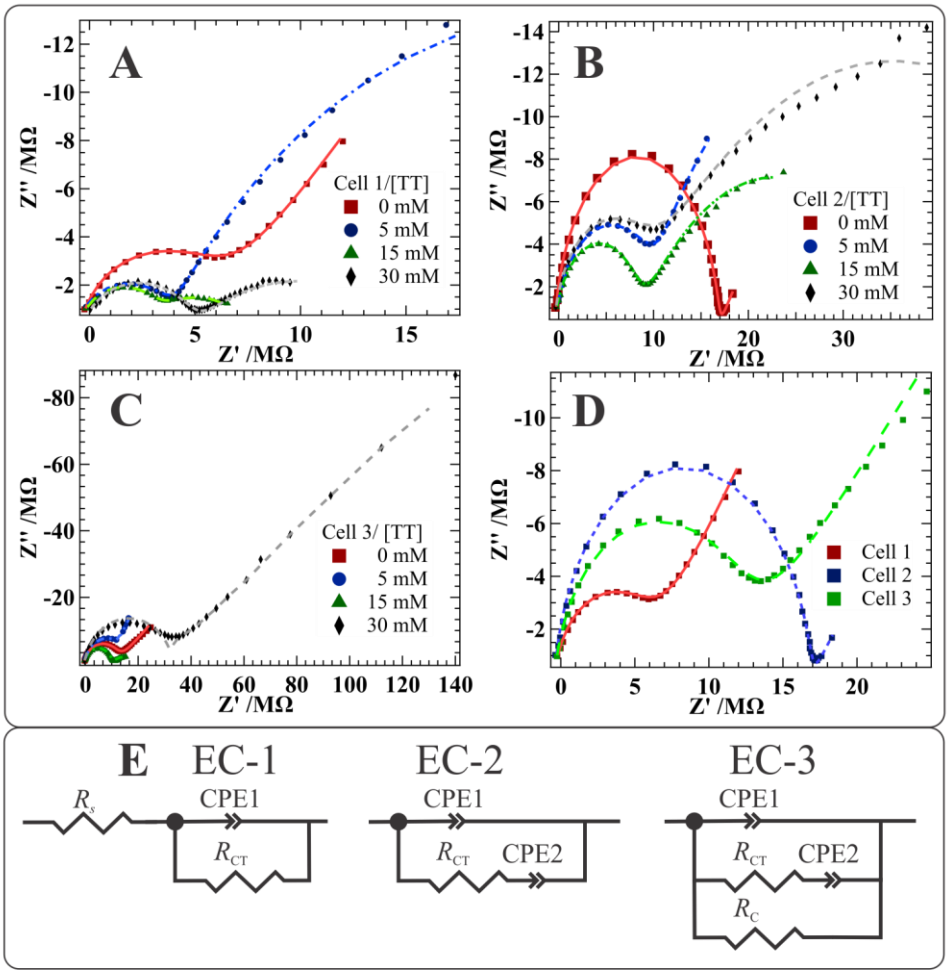

Figure 4-6 Electrochemical Impedance Spectra (EIS) obtained at a 25 µm diameter ITIES using Cells 4-1, 2, and 3 in panels A, B, and C, respectively, with TT added to the DCE phase at the concentrations indicated inset. (D) Depicts spectra recorded without TT added to the DCE phase. Solid and dashed curves were obtained using curve fitting within Zview software with the equivalent circuits (EC) depicted in panel E; the 3 equivalent circuits (EC) employed in which R_s, R_{CT}, and R_C are the solution resistance, charge transfer resistance, and stray resistance, respectively. R_s has been omitted from EC-2 and EC-3 for simplicity.

During electropolymerization in order to record impedance spectra during film growth, three different electrochemical pulse programs were used; (i) in the first approach, a CV has been

performed between each EIS measurement at $\Delta_o^w\phi \approx 0.4$ V, and this loop repeated 10 times; (ii) in the second, 10 consecutive impedance spectra were measured at ~ 0.4 V; (iii) in the last approach, two potential steps, the first at roughly 0.4 V and the second at – 0.2 V were applied for a duration of 15 s before an EIS was recorded. The three programs have been abbreviated CV, EIS, and Pulse, respectively, along the *x*-axis in Figure 4-7. Curve fitting of the Nyquist plots for [TT] >0 were conducted using EC-1 or -3 in Figure 4-6E. The added parallel, stray resistance (R_C) is hypothesized to be owing to the growth of the conductive polymer film across the ITIES which can still mediate electron transfer between $AuCl_4^-$(aq) and TT(org).

Figure 4-7 summarizes the EC curve fitting results from Figure 4-6 across the 3 pH regimes. CPE1 represents the usual capacitance at the ITIES and remains relatively constant throughout the changes in pH and [TT]. Similarly, n_{CPE1} >0.9 in most cases, representing an almost perfect capacitor. The low result at pH = 8.5 and *x* = 5 mM TT for the pulse sequence is likely owing to the poor performance of the gold wire at high pH employed as the working electrode and immersed in the aqueous phase. Indeed, for the EIS protocol, in which the potential was effectively held at 0.4 V, the impedance recording became unstable owing to an increase in local convection in the vicinity of the interface brought about by the films formation; therefore, no result has been included.

At pH 2 (Cell 4-1), R_C increases concomitantly with increasing [TT] for the EIS protocol, *i.e.*, constant applied potential at 0.4 V. This is likely owing to the growth of a poorly formed film that has limited conductivity. These data agree with TEM images of the nanocomposite film (Figure 4-4). Indeed, in three cases EC-1 was employed at pH = 8.5 and [TT] = 15 or 30 mM for the EIS and Pulse methods where the potential was held at roughly 0.4 V for the duration of the experiment.

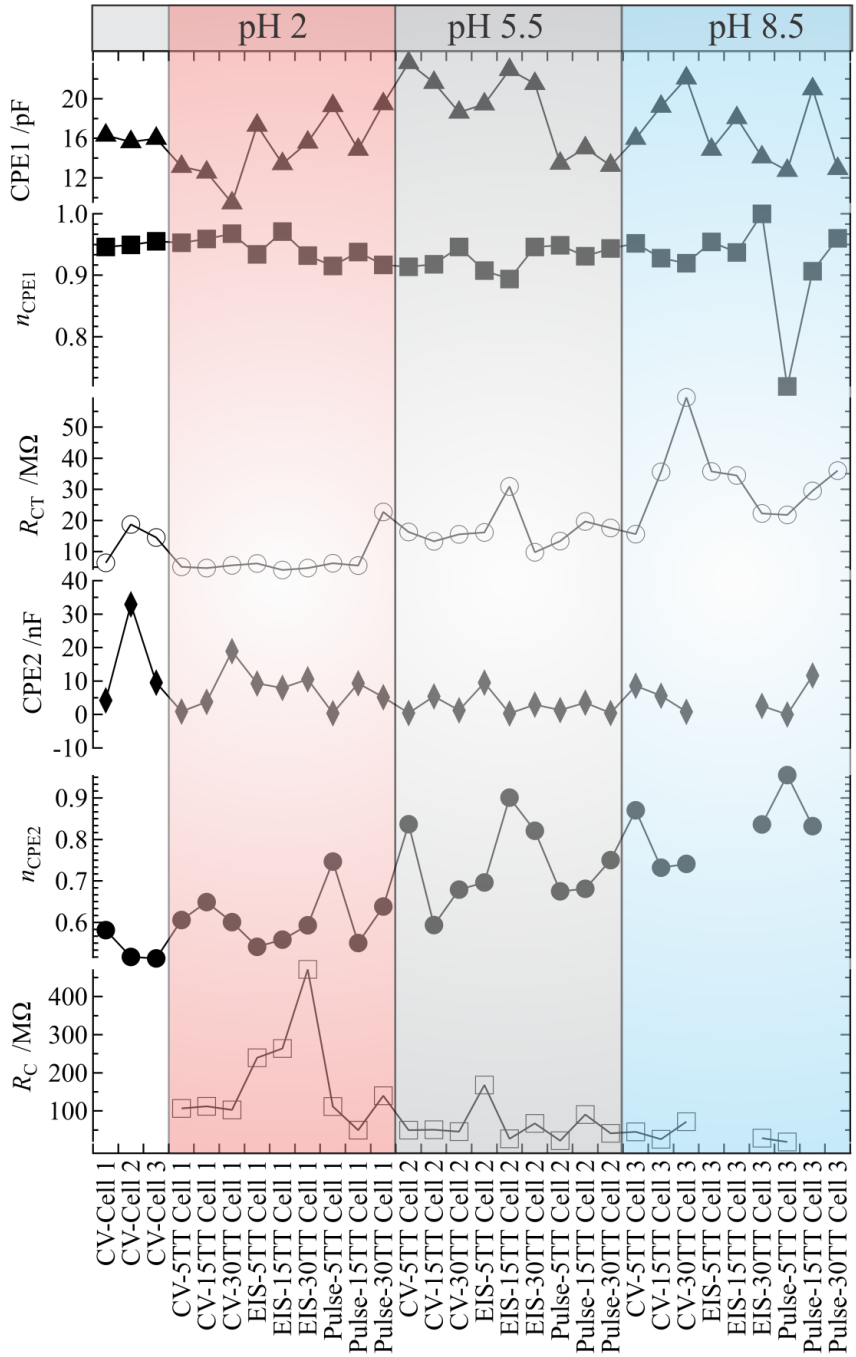

Figure 4-7 Compiled equivalent circuit element results from curve fitting impedance spectra shown in Figure 4-6. Three pulse sequences were employed for electropolymerization are listed on the x-axis and have been abbreviated as, (i) CV = cyclic voltammogram performed between each EIS measurement and repeated 10×; (ii) EIS = 10 consecutive impedance spectra were acquired at ~0.4 V; (iii) Pulse = two potential pulses at 0.4 V, then at – 0.2 V for 15 s were applied before an impedance spectrum was measured at 0.4 V – this sequence was repeated 10×. The final data point in each case has been plotted above. The xTT value in the abbreviation indicates the millimolar concentration of terthiophene (TT) added to the DCE phase; where no TT was added, this term has been omitted.

These curves demonstrated a high degree of noise in the impedance spectra at low frequencies and this is thought to be owing to the poor film formation; however, more investigation, beyond the scope of this work, needs to be performed.

For both the CV and Pulse sequences, R_C remains relatively low across all pH's (<50 MΩ). This is likely owing to ion pairing of the film as it polymerizes with anions in the organic phase. By modulating the interfacial potential between positive and negative regions, this facilitates anion-polymer pairing generating a more cross-linked and conductive film. While more investigations need to be performed concerning the ion pairing mechanism, this is beyond the scope of the present work.

4.5. Conclusions

Au NP/TT nanocomposite thin-films have been electrogenerated at a micro-ITIES formed at the tip of a pulled glass capillary. In this approach, $AuCl_4^-$(aq) accepts electrons through an interfacial electron transfer reaction from TT dissolved in the DCE phase. A combination of TEM and AFM images evidence a growth mechanism in which early Au NPs are small, <2 nm in diameter, and TT acts as a capping agent, that then transitions into a period where the ITIES is covered in the nano-composite material such that TT does not have access to the aqueous phase. In the later stages of electrogeneration, the Au NPs are allowed to grow larger, >10 nm in diameter, since coverage by poly-TT does not impede their growth.

Cyclic voltametric, TEM, and EIS results indicate that a proton acceptor is necessary to facilitate $TT^{+\bullet}$, radical cation coupling; there-fore, neutral to basic pH regimes, >5.5, are needed to enhance electropolymerization at the liquid|liquid interface. AFM contact analysis indicates that after 25 cycles the film is ~0.4 μm thick. SECM and AFM film conductivity investigations are planned for future work.

This method of nanocomposite film generation provides a low overpotential, highly controlled alternative to large-scale film generation that should be of considerable interest in materials chemistry, electrocatalysis, and for the generation of soft electrodes for bioimplantation.

4.6. References

(1) Ibanez, J. G.; Rincón, M. E.; Gutierrez-Granados, S.; Chahma, M.; Jaramillo-Quintero, O. A.; Frontana-Uribe, B. A. Conducting Polymers in the Fields of Energy, Environmental Remediation, and Chemical-Chiral Sensors. *Chem. Rev.* **2018**, *118* (9), 4731–4816. https://doi.org/10.1021/acs.chemrev.7b00482.

(2) Heinze, J.; Frontana-Uribe, B. A.; Ludwigs, S. Electrochemistry of Conducting Polymers-Persistent Models and New Concepts. *Chem. Rev.* **2010**, *110* (8), 4724–4771. https://doi.org/10.1021/cr900226k.

(3) Zotti, G.; Cattarin, S.; Comisso, N. Cyclic Potential Sweep Electropolymerization of Aniline: The Role of Anions in the Polymerization Mechanism. *J. Electroanal. Chem. Interfacial. Electrochem.* **1988**, *239* (1–2), 387–396. https://doi.org/10.1016/0022-0728(88)80293-6

(4) Lin, C. W.; Mak, W. H.; Chen, D.; Wang, H.; Aguilar, S.; Kaner, R. B. Catalytic Effects of Aniline Polymerization Assisted by Oligomers. *ACS. Catal.* **2019**, *9* (8), 6596–6606. https://doi.org/10.1021/acscatal.9b01484.

(5) Sadki, S.; Schottland, P.; Brodie, N.; Sabouraud, G. The Mechanisms of Pyrrole Electropolymerization. *Chem. Soc. Rev.* **2000**, *29* (5), 283–293. https://doi.org/10.1039/a807124a.

(6) Lv, H.; Pan, Q.; Song, Y.; Liu, X. X.; Liu, T. A Review on Nano-/Microstructured Materials Constructed by Electrochemical Technologies for Supercapacitors. *Nano-Micro. Lett.* **2020**. 12, 118. https://doi.org/10.1007/s40820-020-00451-z.

(7) Audebert, P.; Catel, J. M.; le Coustumer, G.; Duchenet, V.; Hapiot, P. Electrochemistry and Polymerization Mechanisms of Thiophene-Pyrrole-Thiopnene Oligomers and Terthiophenes. Experimental and Theoretical Modeling Studies. *J. Phys. Chem. B.* **1998**, *102* (44), 8661–8669. https://doi.org/10.1021/jp9804289.

(8) Audebert, P.; Catel, J.-M.; le Coustumer, G.; Duchenet, V.; Hapiot, P. Electrochemical Oxidation of Five-Unit Heterocycles: A Discussion on the Possible Dimerization Mechanisms; *J. Phys. Chem.* **1995**, 99, 11923-11929. https://pubs.acs.org/sharingguidelines.

(9) Subramanian, V.; Martin, D. C. Direct Observation of Liquid-to-Solid Phase Transformations during the Electrochemical Deposition of Poly(3,4-Ethylenedioxythiophene) (PEDOT) by Liquid-Phase Transmission Electron Microscopy (LPTEM). *Macromolecules.* **2021**, *54* (14), 6956–6967. https://doi.org/10.1021/acs.macromol.1c00404.

(10) Robayo-Molina, I.; Molina-Osorio, A. F.; Guinane, L.; Tofail, S. A. M.; Scanlon, M. D. Pathway Complexity in Supramolecular Porphyrin Self-Assembly at an Immiscible Liquid–Liquid Interface. *J. Am. Chem. Soc.* **2021**, *143*, 9060-9069. https://doi.org/10.1021/jacs.1c02481.

(11) Gamero-Quijano, A.; Dossot, M.; Walcarius, A.; Scanlon, M. D.; Herzog, G. Electrogeneration of a Free-Standing Cytochrome c - Silica Matrix at a Soft Electrified Interface. *Langmuir.* **2021**, *37* (13), 4033–4041. https://doi.org/10.1021/acs.langmuir.1c00409.

(12) Lepková, K.; Clohessy, J.; Cunnane, V. J. Electrodeposition of Metal-Based Nanocomposites at a Liquid-Liquid Interface Controlled via the Interfacial Galvani Potential Difference. *Electrochim. Acta.* **2008**, *53* (21), 6273–6277. https://doi.org/10.1016/j.electacta.2008.04.025.

(13) Lepková, K.; Clohessy, J.; Cunnane, V. J. The PH-Controlled Synthesis of a Gold Nanoparticle/Polymer Matrix via Electrodeposition at a Liquid-Liquid Interface. *J. Phys. Condens. Matter.* **2007**, *19* (37), 375106. https://doi.org/10.1088/0953-8984/19/37/375106.

(14) Vignali, M.; Edwards, R. A. H.; Serantoni, M.; Cunnane, V. J. Electropolymerized Polythiophene Layer Extracted from the Interface between Two Immiscible Electrolyte Solutions: Current-Time Analysis. *J. Electroanal. Chem.* **2006**, *591* (1), 59–68. https://doi.org/10.1016/j.jelechem.2006.03.033.

(15) Vignali, M.; Edwards, R.; Cunnane, V. J. Characterization of Doping and Electropolymerization of Free Standing Films of Polyterthiophene. *J. Electroanal. Chem.* **2006**, *592* (1), 37–45. https://doi.org/10.1016/j.jelechem.2006.04.020.

(16) Knake, R.; Fahmi, A. W.; Tofail, S. A. M.; Clohessy, J.; Mihov, M.; Cunnane, V. J. Electrochemical Nucleation of Gold Nanoparticles in a Polymer Film at a Liquid-Liquid Interface. *Langmuir.* **2005**, *21* (3), 1001–1008. https://doi.org/10.1021/la048277q.

(17) Sarac, S. S.; Evans, U.; Serantoni, M.; Clohessy, J.; Cunnane, V. J. Electrochemical and Morphological Study of the Effect of Polymerization Conditions on Poly(Terthiophene). *Surf Coat. Technol.* **2004**, *182* (1), 7–13. https://doi.org/10.1016/j.surfcoat.2003.08.002.

(18) Evans-Kennedy, U.; Clohessy, J.; Cunnane, V. J. Spectroelectrochemical Study of 2,2′:5′,2″-Terthiophene Polymerization at a Liquid|Liquid Interface Controlled by Potential-Determining Ions. *Macromolecules.* **2004**, *37* (10), 3630–3634. https://doi.org/10.1021/ma0348223.

(19) Johans, C.; Clohessy, J.; Fantini, S.; Kontturi, K.; Cunnane, V. J. Electrosynthesis of Polyphenylpyrrole Coated Silver Particles at a Liquid-Liquid Interface. *Electrochem. Commun.* **2002**, *4* (3), 227–230. https://doi.org/10.1016/S1388-2481(02)00256-4.

(20) Gorgy, K.; Fusalba, F.; Evans, U.; Kontturi, K.; Cunnane, V. J. Electropolymerization of 2,2′:5′,2″ Terthiophene at an Electrified Liquid-Liquid Interface. *Synth. Met.* **2001**, *125* (3), 365–373. https://doi.org/10.1016/S0379-6779(01)00474-X.

(21) Cunnane, V. J.; Evans, U. Formation of Oligomers of Methyl- and Phenyl-Pyrrole at an Electrified Liquid|Liquid Interface. *Chem. Commun.* **1998**, 19, 2163–2164. https://doi.org/10.1039/a806365f.

(22) Scanlon, M. D.; Smirnov, E.; Stockmann, T. J.; Peljo, P. Gold Nanofilms at Liquid-Liquid Interfaces: An Emerging Platform for Redox Electrocatalysis, Nanoplasmonic Sensors, and Electrovariable Optics. *Chem. Rev.* **2018**, *118* (7), 3722–3751. https://doi.org/10.1021/acs.chemrev.7b00595.

(23) Johans, C.; Lahtinen, R.; Kontturi, K.; Schiffrin, D. J. Nucleation at Liquid|liquid Interfaces: Electrodeposition without Electrodes. *J. Electroanal. Chem.* **2000**, *488* (2), 99–109. https://doi.org/10.1016/S0022-0728(00)00185-6.

(24) Trojánek, A.; Langmaier, J.; Samec, Z. Electrocatalysis of the Oxygen Reduction at a Polarised Interface between Two Immiscible Electrolyte Solutions by Electrochemically Generated Pt Particles. *Electrochem. Commun.* **2006**, *8* (3), 475–481. https://doi.org/10.1016/J.ELECOM.2006.01.004.

(25) Su, B.; Abid, J. P.; Fermín, D. J.; Girault, H. H.; Hoffmannová, H.; Krtil, P.; Samec, Z. Reversible Voltage-Induced Assembly of Au Nanoparticles at Liquid|Liquid Interfaces. *J. Am. Chem. Soc.* **2004**, *126* (3), 915–919. https://doi.org/10.1021/ja0386187.

(26) Booth, S. G.; Uehara, A.; Chang, S.-Y.; la Fontaine, C.; Fujii, T.; Okamoto, Y.; Imai, T.; Schroeder, S. L. M.; Dryfe, R. A. W. The Significance of Bromide in the Brust-Schiffrin Synthesis

of Thiol Protected Gold Nanoparticles. *Chem. Sci.* **2017**, *8* (12), 7954–7962. https://doi.org/10.1039/c7sc03266h.

(27) Uehara, A.; Chang, S.-Y.; Booth, S. G.; Schroeder, S. L. M.; Mosselmans, J. F. W.; Dryfe, R. A. W. Redox and Ligand Exchange during the Reaction of Tetrachloroaurate with Hexacyanoferrate(II) at a Liquid-Liquid Interface: Voltammetry and X-Ray Absorption Fine-Structure Studies. *Electrochim. Acta.* **2016**, *190*, 997–1006. https://doi.org/10.1016/j.electacta.2015.12.108.

(28) Uehara, A.; Booth, S. G.; Chang, S. Y.; Schroeder, S. L. M.; Imai, T.; Hashimoto, T.; Mosselmans, J. F. W.; Dryfe, R. A. W. Electrochemical Insight into the Brust-Schiffrin Synthesis of Au Nanoparticles. *J. Am. Chem. Soc.* **2015**, *137* (48), 15135–15144. https://doi.org/10.1021/jacs.5b07825.

(29) Uehara, A.; Hashimoto, T.; Dryfe, R. A. W. Au Electrodeposition at the Liquid-Liquid Interface: Mechanistic Aspects. *Electrochim. Acta.* **2014**, *118*, 26–32. https://doi.org/10.1016/j.electacta.2013.11.162.

(30) Dryfe, R. A. W.; Uehara, A.; Booth, S. G. Metal Deposition at the Liquid-Liquid Interface. *Chem. Rec.* **2014**, *14* (6), 1013–1023. https://doi.org/10.1002/tcr.201402027.

(31) Brust, M.; Walker, M.; Bethell, D.; Schiffrin, D. J.; Whyman, R. Synthesis of Thiol-Derivatised Gold Nanoparticles in a Two-Phase Liquid–Liquid System. *J. Chem. Soc., Chem. Commun.* **1994**, 7, 801–802. https://doi.org/10.1039/C39940000801.

(32) Moshrefi, R.; Suryawanshi, A.; Stockmann, T. J. Electrochemically Controlled Au Nanoparticle Nucleation at a Micro Liquid | Liquid Interface Using Ferrocene as Reducing Agent. *Electrochem. Commun.* **2021**, *122*, 106894. https://doi.org/10.1016/j.elecom.2020.106894.

(33) Nieminen, E.; Murtomäki, L. Kinetics of Cu 2+ Reduction and Nanoparticle Nucleation at Micro-scale 1,2-Dichlorobenzene-water Interface Studied by Cyclic Voltammetry and Square-wave Voltammetry. *Electroanalysis.* **2021**, *33* (9), 2087–2095. https://doi.org/10.1002/elan.202100172.

(34) Barsch, U.; Beck, F. Anodic Overoxidation of Polythiophenes in Wet Acetonitrile Electrolytes. *Electrochim. Acta.* **1996**, *41* (11–12), 1761–1771. https://doi.org/10.1016/0013-4686(95)00493-9.

(35) Stockmann, T. J.; Boyle, P. D.; Ding, Z. Preparation and Crystal Structure of Tetraoctylphosphonium Tetrakis(Pentafluorophenyl)Borate Ionic Liquid for Electrochemistry at Its Interface with Water. *Catal. Today.* **2017**, *295*, 89–94. https://doi.org/10.1016/j.cattod.2017.05.030.

(36) Jiang, Q.; Reader, H. E.; Stockmann, T. J. Electrochemical Characterization of Fe(II) Complexation Reactions at an Electrified Micro Liquid-Liquid Interface. *Chem. Electro. Chem.* **2021**, *8*, 1–9. https://doi.org/10.1002/celc.202100127.

(37) Stockmann, T. J.; Lu, Y.; Zhang, J.; Girault, H. H.; Ding, Z. Interfacial Complexation Reactions of Sr 2+ with Octyl(Phenyl)-n,n-Diisobutylcarbamoylmethylphosphine Oxide for Understanding Its Extraction in Reprocessing Spent Nuclear Fuels. *Chem. Eur. J.* **2011**, *17* (47), 13206–13216. https://doi.org/10.1002/chem.201102491.

(38) Stockmann, T. J.; Ding, Z. Uranyl Ion Extraction with Conventional PUREX/TRUEX Ligands Assessed by Electroanalytical Chemistry at Micro Liquid|Liquid Interfaces. *Anal. Chem.* **2011**, *83* (19), 7542–7549. https://doi.org/10.1021/ac2018684.

(39) Olaya, A. J.; Méndez, M. A.; Cortes-Salazar, F.; Girault, H. H. Voltammetric Determination of Extreme Standard Gibbs Ion Transfer Energy. *J. Electroanal. Chem.* **2010**, *644* (1), 60–66. https://doi.org/10.1016/j.jelechem.2010.03.030.

(40) Stockmann, T. J.; Montgomery, A. M.; Ding, Z. Determination of Alkali Metal Ion Transfers at Liquid|liquid Interfaces Stabilized by a Micropipette. *J. Electroanal. Chem.* **2012**, *684*, 6–12. https://doi.org/10.1016/j.jelechem.2012.08.013.

(41) Stockmann, T. J.; Montgomery, A.-M.; Ding, Z. Formal Transfer Potentials of Strontium and Uranyl Ions at Water|1,2-Dichloroethane Interfaces. *Can. J. Chem.* **2012**, *90* (10), 836–842. https://doi.org/10.1139/v2012-068.

(42) Stockmann, T. J.; Olaya, A. J.; Méndez, M. A.; Girault, H. H.; Ding, Z. Evaluation of Gibbs Energy of Dioxouranium Transfer at an Electrified Liquid|liquid Interface Supported on a Microhole. *Electroanalysis.* **2011**, *23* (11), 2677–2686. https://doi.org/10.1002/elan.201100401.

(43) Zhou, M.; Gan, S.; Zhong, L.; Dong, X.; Ulstrup, J.; Han, D.; Niu, L. Improvement in the Assessment of Direct and Facilitated Ion Transfers by Electrochemically Induced Redox Transformations of Common Molecular Probes. *Phys. Chem. Chem. Phys.* **2012**, *14* (10), 3659–3668. https://doi.org/10.1039/c2cp23184k.

(44) Liu, S.; Li, Q.; Shao, Y. Electrochemistry at Micro- and Nanoscopic Liquid | Liquid Interfaces. *Chem. Soc. Rev.* **2011**, *40* (5), 2236–2253. https://doi.org/10.1039/c0cs00168f.

(45) Stockmann, T. J.; Noël, J.-M.; Abou-Hassan, A.; Combellas, C.; Kanoufi, F. Facilitated Lewis Acid Transfer by Phospholipids at a (Water|CHCl 3) Liquid|Liquid Interface toward Biomimetic and Energy Applications. *J. Phys. Chem. C.* **2016**, *120* (22), 11977–11983. https://doi.org/10.1021/acs.jpcc.6b02354.

(46) Burgoyne, E. D.; Molina-Osorio, A. F.; Moshrefi, R.; Shanahan, R.; McGlacken, G. P.; Stockmann, T. J.; Scanlon, M. D. Detection of Pseudomonas Aeruginosa Quorum Sensing

Molecules at an Electrified Liquid|liquid Micro-Interface through Facilitated Proton Transfer. *Analyst.* **2020**, *145* (21), 7000–7008. https://doi.org/10.1039/D0AN01245A.

(47) Luty-Błocho, M.; Pacławski, K.; Wojnicki, M.; Fitzner, K. The Kinetics of Redox Reaction of Gold(III) Chloride Complex Ions with l-Ascorbic Acid. *Inorg. Chim. Acta.* **2013**, *395*, 189–196. https://doi.org/10.1016/j.ica.2012.10.031.

(48) Mironov, I. v.; Makotchenko, E. v. The Hydrolysis of AuCl 4- And the Stability of Aquachlorohydroxocomplexes of Gold(III) in Aqueous Solution. *J. Solut. Chem.* **2009**, *38* (6), 725–737. https://doi.org/10.1007/s10953-009-9400-9.

(49) Usher, A.; McPhail, D. C.; Brugger, J. A Spectrophotometric Study of Aqueous Au(III) Halide-Hydroxide Complexes at 25-80 °C. *Geochim. Cosmochim. Acta.* **2009**, *73* (11), 3359–3380. https://doi.org/10.1016/j.gca.2009.01.036.

(50) Brasiliense, V.; Clausmeyer, J.; Dauphin, A. L.; Noël, J.-M.; Berto, P.; Tessier, G.; Schuhmann, W.; Kanoufi, F. Optoelektrochemische Opto-electrochemical In Situ Monitoring of the Cathodic Formation of Single Cobalt Nanoparticles. *Angew. Chemie. Int. Ed.* **2017**, *129* (35), 10734–10737. https://doi.org/10.1002/ange.201704394.

(51) Méndez, M. A.; Partovi-Nia, R.; Hatay, I.; Su, B.; Ge, P.; Olaya, A.; Younan, N.; Hojeij, M.; Girault, H. H. Molecular Electrocatalysis at Soft Interfaces. *Phys. Chem. Chem. Phys.* **2010**, *12* (46), 15163–15171. https://doi.org/10.1039/c0cp00590h.

(52) Vanýsek, P.; Haynes, W. M. Electrochemical Series, Ed. CRC Handbook of. Chemistry and Physics, *CRC Press/Taylor*, Boca Raton, FL **2021**, No. 2, 8.20-25.29.

(53) Chen, Q.-Z.; Iwamoto, K.; Senō, M. Kinetic Analysis of Electron Transfer between Hexacyanoferrate(III) in Water and Ferrocene in Nitrobenzene by Ac Impedance Measurements. *Electrochim. Acta.* **1991**, *36* (2), 291–296. https://doi.org/10.1016/0013-4686(91)85251-2.

(54) Cheng, Y.; Schiffrin, D. J. A.C. Impedance Study of Rate Constants for Two-Phase Electron-Transfer Reactions. *J. Chem. Soc., Faraday. Trans.* **1993**, *89* (2), 199. https://doi.org/10.1039/ft9938900199.

(55) Wandlowski, T.; Marecek, V.; Holub, K.; Samec, Z. Ion Transfer across Liquid-Liquid Phase Boundaries: Electrochemical Kinetics by Faradaic Impedance. *J. Phys. Chem.* **1989**, *93* (25), 8204–8212. https://doi.org/10.1021/j100362a013.

(56) Silver, B. R.; Holub, K.; Mareček, V. Ion Transfer Kinetics at the Micro-Interface between Two Immiscible Electrolyte Solutions Investigated by Electrochemical Impedance Spectroscopy and Steady-State Voltammetry. *J. Electroanal. Chem.* **2014**, *731*, 107–111. https://doi.org/10.1016/J.JELECHEM.2014.08.017.

(57) Bisquert, J.; Garcia-Belmonte, G.; Bueno, P.; Longo, E.; Bulhões, L. O. S. Impedance of Constant Phase Element (CPE)-Blocked Diffusion in Film Electrodes, *J. Electroanal. Chem,* **1998,** 452*,* 229-234.

(58) Lhotský, A.; Holub, K.; Neužil, P.; Mareček, V. Ac Impedance Analysis of Tetraethylammonium Ion Transfer at Liquid | Liquid Microinterfaces. *J. Chem. Soc., Faraday Trans.* **1996**, *92* (20), 3851–3857. https://doi.org/10.1039/FT9969203851.

Chapter 5

5. Simultaneous electro-generation/polymerization of Cu nanocluster embedded conductive poly(2,2′:5′,2″-terthiophene) films at micro and macro liquid|liquid interfaces.

5.1. Statement of Co-Authorship

This chapter has been published under the above title in *Scientific Reports* **2023**, 13(1), 1-14. It is presented here in a modified format that includes all contributions for completeness and context.

Authors: Reza Moshrefi, Hanna Przybyła, and Prof. T. Jane Stockmann

This article was a group effort combining the work of co-authors from the research groups of T. Jane Stockmann

Reza Moshrefi (listed in the paper as 1st author): Performed electrochemical experiments, material characterization and contributed to formal analysis, Investigation, writing - review & editing, validation.

Hanna Przybyła: Performed electrochemical experiments, material characterization, writing - review & editing.

Prof. T. Jane Stockmann: Is the principal investigator of this work, who led the project and contributed to conceptualization, methodology, writing - original draft, validation, supervision, project administration, funding acquisition.

5.2. Introduction

Owing to their flexibility[1-3] and biocompatibility,[4] conductive polymeric thin films have seen a significant rise in usage and interest. Motivated to reduce production cost, less expensive and involved preparation methods are being sought. For example, many polymerization methods generate relatively high average molecular weight materials that are robust; however, require electrodeposition onto an anode,[5] often binding the polymer to the electrode surface, or uses specialized bulky methods such as electrospinning.[6] In the case of the former, this likely eliminates the possibility of obtaining a free-standing film/conductive polymer electrode as the polymer is difficult to liberate from the anode and thus can limit the type of applications.

Meanwhile, metal nanoparticles (NPs) form the basis of numerous analytical and electrocatalytic platforms;[7-9] particularly copper (Cu) based NPs which are effective in catalyzing CO_2 reduction.[10-13] Many metal NP preparation methods have emerged; however, the Brust-Schiffrin method, first described in 1994,[14,15] reproducibly generated low dispersity Au NPs by exploiting the interface between two immiscible electrolyte solutions (ITIES), *i.e.*, the liquid|liquid interface. Indeed, the ITIES has recently come under increasing activity in the electrodeless synthesis of both metal NPs[15-27] and conductive polymer films.[4,28-36] Initially, efforts were focused on the immiscible water|oil (w|o) interface;[4,27-36] however, these have recently expanded to the water|ionic liquid (w|IL)[21-26] and oil|ionic liquid (o|IL)[20] ones. In a simple 2-electrode configuration with one electrode immersed in either phase, the Galvani potential difference can be controlled externally via a potentiostat with the potential drop spanning 1-4 nm across the ITIES, $\phi_w - \phi_o = \Delta_o^w \phi$.[8,37]

Johans *et al*.[38] were the first to describe an analytical solution for nucleation of metal NPs at the liquid|liquid interface. In their work, they emphasized the absence of defect sites that are common at a solid/solution interface; thus, there is a large thermodynamic barrier to particle formation at ITIES. Nevertheless, they[38] and others[8,15-18,20,23,24,27,28,39,40] were able to experimentally demonstrate electrochemically controlled metal NP nucleation at w|o interfaces. Interestingly, Nishi's group has suggested that the molecular structure of the liquid|liquid interface is transcribed onto the NP framework.[22] They recently demonstrated that the w|IL interface played an important role mechanistically in the formation of nanostructures. Their IL was modified with a ferrocene (Fc) functional group making it redox active, and was exploited in the formation of Pd nanofiber arrays.[22]

Meanwhile, electropolymerization at liquid|liquid interfaces was initially investigated by Cunnane's group,[36] and more recently by Scanlon's group[4] and ourselves.[28] In these later reports, large, free-standing polymer films were formed. In the case of Lehane *et al*.[4] who generated PEDOT (poly(3,4-ethylenedioxythiophene)) using Ce^{4+} in aqueous and EDOT in *α*,*α*,*α*-trifluorotoluene (TFT), the films were shown to be highly stable and biocompatible. Our work showcased the simultaneous electropolymerization of 2,2′:5′,2″-terthiophene (TT) and electrogeneration of Au NPs at a micro-ITIES (25 μm in diameter),[26] building on Cunnane's study at a large ITIES.[29,30,32] We demonstrated that miniaturization of the ITIES could be used to provide another layer of mechanistic and thermodynamic control towards smaller, low dispersity NPs.

Herein, this is expanded to the simultaneous electrogeneration and electropolymerization of Cu nanocluster incorporated poly(TT) films. Electrochemical impedance spectroscopy was used to monitor film growth, while SEM and TEM imaging were used to compare film/NP morphology at different TT concentrations between the large and micro-ITIES. Two large ITIES platforms

were investigated, including a 1.16 and 10 mm diameter interface. Initial testing of glassy carbon (GC) electrodes modified with the nanocomposite demonstrate excellent electrocatalytic activity towards CO_2 reduction; however, films electrosynthesized at the 25 µm and 1.16 mm interfaces demonstrated poor stability and surface coverage.

5.3. Methods

5.3.1. Chemicals

Copper sulfate ($CuSO_4$, >98%), lithium sulfate (Li_2SO_4, >98%), 1,2-dichloroethane (DCE, ≥99.0%), 1-bromooctane (99%), trioctylphosphine (97%), and 2,2′:5′,2″-terthiophene (TT, 99%) were acquired from Sigma-Aldrich. All reagents were used without additional purification. Ultrapure water from a MilliQ filtration system (>18.2 MΩ cm) was used throughout to generate aqueous solutions. The tetraoctylphosphonium tetrakis(pentafluorophenyl)borate ($P_{8888}TB$) ionic liquid used as an oil phase supporting electrolyte was prepared as detailed previously.[41]

5.3.2. Electrochemistry

Liquid|liquid electrochemical experiments were performed using a PG-618-USB potentiostat (HEKA Electroniks) in four-, three-, and two-electrode configurations at the large and micro-ITIES. In the 4-electrode mode a specialized 10 mm inner diameter cell with two Pt wires annealed into the side of the glass cell were connected to the working (WE) and counter electrode (CE) leads of the potentiostat as shown in Figure 5-1B. The WE was positioned in the aqueous phase, while the CE was in the organic phase. Two references electrodes (RE) were also employed, one in either phase and inserted into Luggin capillaries built into the specialized cell with their tips facing each other ~5 mm apart with the liquid|liquid interface positioned in between them, see Figure 5-1B.

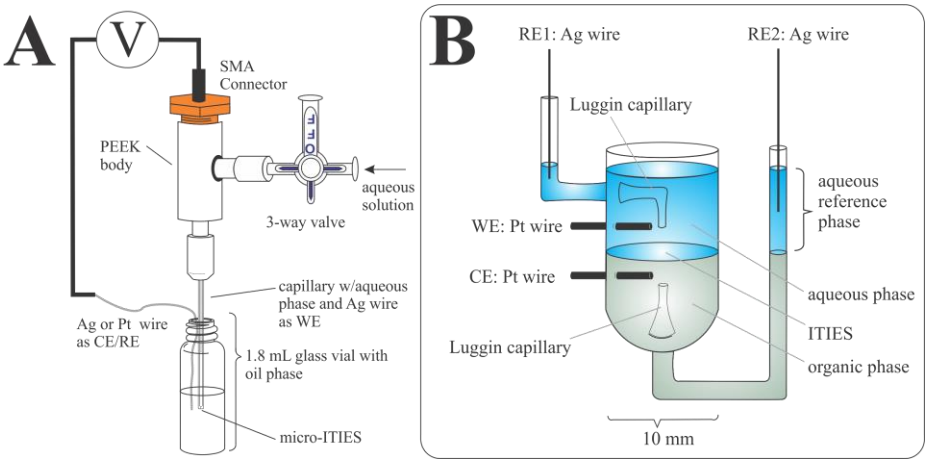

Figure 5-1 Diagram of the specialized (A) micro and (B) large ITIES (interface between two immiscible electrolyte solutions) cell. WE, CE, and RE refer to the working, counter, and reference electrode leads, respectively.

When using the micro-ITIES in two-electrode mode, one Ag wire (Goodfellow Inc.) was integrated into the specialized pipette holder containing the aqueous phase and connected to the WE port of the head-stage, and another Ag wire immersed in the organic phase was connected to the CE/RE port, see Figure 5-1A. The body of the holder was fabricated form poly(ether ether ketone) (PEEK). The pipette was backfilled with the aqueous phase through a syringe attached to a 3-way valve incorporated into the side of the specialized holder, then the tip of the pipette was immersed in the organic phase. The 25 µm diameter ITIES was maintained at the pipette tip using the syringe and monitored using an 18-megapixel CCD camera (AmScope) equipped with a 12× magnifying lens assembly (Navitar). Micropipette fabrication has been described elsewhere.[42] Scheme 5-1 details the electrolytic cells employed. The experimental potential scale was referenced to the Galvani scale by simple SO_4^{2-} transfer, whose formal ion transfer potential $\left(\Delta_o^w \phi'^{\circ}_{SO_4^{2-}}\right)$ was taken to be –0.540 V.[16]

A second large ITIES electrolytic cell (Cell 5-1, general configuration) was created by using the modified holder shown in Figure 5-1A; however, an unmodified borosilicate capillary

(2.0/1.16 mm outer/inner diameter, Sutter Instruments) was used in place of a micropipette. Additionally, a Pt wire counter and Ag wire reference electrodes were used, coupled to the integrated Ag wire as WE in the aqueous phase, in a 3-electrode configuration.

$$\mathrm{Ag}\left|\mathrm{Ag_2SO_4}\right|\begin{matrix}x\text{ mM }\mathrm{CuSO_4}\\5\text{ mM }\mathrm{Li_2SO_4}\\(aq)\end{matrix}\Big\|\begin{matrix}y\text{ mM TT}\\5\text{ mM }\mathrm{P_{8888}TB}\\(DCE)\end{matrix}\Big|\mathrm{AgTB}\left|\mathrm{Ag}\right. \qquad \text{[Cell 5-1]}$$

$$\mathrm{Ag}\left|\mathrm{Ag_2SO_4}\right|\begin{matrix}x\text{ mM }\mathrm{CuSO_4}\\5\text{ mM }\mathrm{Li_2SO_4}\\(aq)\end{matrix}\Big\|\begin{matrix}y\text{ mM TT}\\5\text{ mM }\mathrm{P_{8888}TB}\\(DCE)\end{matrix}\Big|\begin{matrix}5\text{ mM }\mathrm{Li_2SO_4}\\\mathrm{LiTB}\\(aq\sim ref)\end{matrix}\Big|\mathrm{Ag_2SO_4}\left|\mathrm{Ag}\right. \qquad \text{[Cell 5-2]}$$

Scheme 5-1 Electrolytic cells used where x mM of $CuSO_4$ was added to the aqueous phase and y mM the electron donor, 2,2':5',2''-terthiophene (TT), was added to the DCE phase in Cells 5-1 and 5-2, while 5 mM of the ionic liquid $P_{8888}TB$ (tetraoctylphosphonium tetrakis(pentafluorophenyl)borate) was employed as supporting electrolyte in the organic phase. The double bars indicate the polarizable potential w|DCE interface, with diameters of 25 µm in the case of the ITIES maintained at the tip of the micropipette, as well as 1 or 10 mm for the two large electrolytic cells, see Figure 5-1.

Electrochemical impedance spectroscopy (EIS) measurements were performed with a frequency range between 10 and 20 kHz, as well as a 20 mV peak-to-peak perturbation. EIS was only measured using Cell 5-1 at a 25 µm ITIES in a 2-electrode configuration.

Before or in-between experiments, electrolytic cells/capillaries were cleaned using the procedure outlined in the Appendix D.

Electrocatalysis studies were performed using a 3-electrode cell connected to a CH Instruments potentiostat (model# CHI602E) with a glassy carbon (GC, Pine Research) WE (~4 mm in diameter) coupled with Ag/AgCl reference (Dek Research) and Pt wire counter electrodes.

5.3.3. Transmission Electron Microscopy

All transmission electron microscopy (TEM) images were taken using the Tecnai Spirit transmission electron microscope with samples prepared on 200 Mesh Cu ultrathin/lacey carbon or 2 µm holey Au grids (Electron Microscopy Sciences).

5.3.4. Scanning Electron Microscopy (SEM)

SEM imaging was performed using a JEOL JSM 7100 F equipped with energy dispersive X-ray (EDX) which were analyzed via DTSA II software provided by the National Institute of Standards and Technology (NIST) in the US, see https://www.nist.gov/services-resources/software/nist-dtsa-ii.

5.4. Results and discussion

The black, dashed curves shown in Figures 5-2(A-C) illustrate cyclic voltammograms (CVs) recorded using Cells 5-1 and 5-2 at the micro (25 µm diameter), 1.16 mm, and ~10 mm diameter ITIES, respectively, without TT added, but with 5 mM of $CuSO_4$ in the aqueous phase. In each case, the polarizable potential window (PPW) is limited by the transfer of the supporting electrolyte ions. The large positive current increase at positive potentials is owing to the transfer of Li^+/Cu^{2+} from water to oil (w→o) or TB^- from o→w, while the sharp negative increase in current towards negative potentials is owing to the transfer of SO_4^{2-} from w→o and P_{8888}^+ from o→w.[8,43]

The red, solid trace shows the initial *i-V* cycle at the micro-ITIES (Figure 5-2A), after addition of 20 mM of TT to DCE. A positive peak-shaped wave was observed during the forward scan, towards positive potentials, with a peak potential (E_p) at roughly 0.52 V. During the reverse scan, towards negative potentials, a sigmoidal wave was observed with a half-wave potential $\left(\Delta_o^w\phi_{1/2}\right)$ at ~0.515 V. Since the interface was maintained at the tip of a pulled micropipette, the diffusion regime inside and outside the pipette is asymmetric. The former behaves under linear diffusion owing to geometric confinement within the micropipette, while the latter is hemispherical with responses similar to an inlaid disc ultramicroelectrode (UME).[44] Thus, this signal is consistent with the transfer of negative charge from o→w during the forward scan, such that the process is

diffusion limited by a species in the aqueous phase. Therefore, it was hypothesized that this signal is owing to electron transfer from TT in DCE across the ITIES to Cu^{2+} in water; whereby, Cu^{2+} is reduced to Cu^0 and forms nanoparticles, while TT is oxidized and electropolymerized.

To investigate this, the system was cycled a total of 25 times with these *i-V* curves overlaid in Figure 5-2A; the dashed, purple arrow indicates how the peak current (i_p) signal evolves with each consecutive scan. There is only a small change in i_p that may be owing to a localized consumption at the interface, or the formation of a nanoparticle incorporated polymer film at the ITIES. The latter would fundamentally alter the effective surface area of the interface as well as its charge transfer characteristics; both would impact the magnitude of i_p. Cell 5-1 was also tested using [$CuSO_4$] = 0 mM and [TT] = 20 mM; however, no peak-shaped signal was recorded (data not shown). Thus, it is likely that Li^+ does not interact with TT and is a good electro-inactive supporting electrolyte. However, when [TT] was decreased to 10 and 5 mM in DCE, no electron transfer wave was recorded voltammetrically (data not shown).

In all cases at the micro-ITIES, an aqueous droplet was ejected onto a TEM grid for imaging using the syringe equipped on the back of the modified holder. Even at 5 and 10 mM TT, a film-like deposit was visible on the substrate under an optical microscope. Therefore, despite no observable electron transfer wave, cycling at the PPW edge-of-scan can induce electrogeneration of the nanocomposite film. These results agree well with our recent work at the w|DCE micro-interface using $KAuCl_4$(aq) and TT(org);[28] whereby, a thin conductive polymer film, with embedded Au NPs was formed. Lehane *et al*.[4] also recently employed a large w|DCE interface in the electropolymerization of PEDOT with Ce^{4+} as oxidant/electron acceptor in the aqueous phase. Moreover, electrodeposition of Cu, Au, Pd, and Pt NPs at large[16,30,38,40,45] and micro[27,39] interfaces have been demonstrated previously using metallocenes as electron donors dissolved in oil.

An ITIES with a diameter of 1.16 mm using a 3-electrode configuration was also tested voltammetrically, see Figure 5-2B. The overall CV profile is similar to the one at a ~10 mm ITIES (see below) with a signal at ~0.7 V which is likely the electron transfer wave; however, two negative current peaks were recorded at roughly 0.4 and 0.15 V during the scan from positive to negative potentials. These may be the re-oxidation of Cu^0 or anion adsorption waves. Future work will focus on *in situ* spectroscopic methods to evaluate these two curve features.

Next, film generation was investigated at a 10 mm diameter ITIES using Cell 5-2 (see Figure 5-2C). When scanning from negative to positive potentials, two peak-shaped waves were observed at –0.22 and 0.66 V, while on the reverse scan towards negative potentials, two peak signals were recorded at 0.09 and –0.26 V. The two peaks towards the negative end of the PPW form a reversible signal with a $\Delta_o^w\phi_{1/2}$ of –0.240 V which may be the result of the adsorption of anions at the surface of the growing composite film. Indeed, this agrees well with the results of Lehane *et al*.[4] The two signals at the positive end of the PPW are irreversible electron transfer similar to the result observed at the micro-ITIES in this potential region. With repeated sweeps of the potential, the irreversible electron transfer wave shifts to more negative potentials indicating a reduction in the required overpotential. As mentioned above, the liquid|liquid interface is initially free of nucleation sites which increases the amount of applied driving force necessary to achieve NP nucleation/polymerization[38] versus at a solid/electrolyte one. However, once the film begins forming, the population of viable sites increases which is reflected in the concomitant decrease in peak potential of the electron transfer wave. Simultaneously, the signal decreases in current intensity which is likely owing to the consumption of material in the vicinity of the ITIES. The nanocomposite film formed in the large ITIES cell was thick, brittle, and difficult to extract from

the cell. However, pieces were deposited onto glass substrates for SEM imaging and onto a GC electrode for electrocatalytic testing (see below).

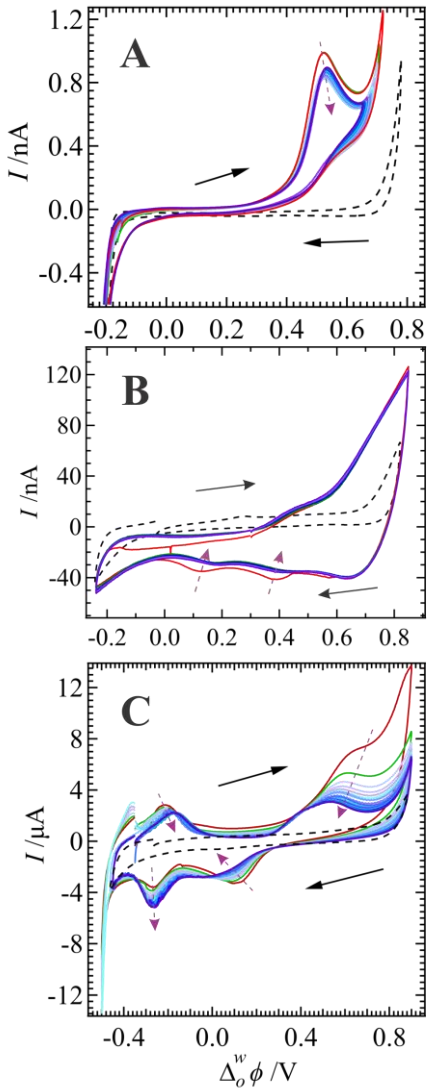

Figure 5-2 i-V curves recorded at 0.020 V s^{-1} using Cell 5-1 (A and B) and 2 (C), or the 25 µm, 1.16 mm, and 10 mm ITIES, respectively, with [TT] = 20 mM and [$CuSO_4$] = 5 mM, while the black, dashed traces show the system without TT added, i.e., blank curves. DCE was used as the organic solvent in all cases. Cyclic voltammograms have been scanned consecutively 25 times and overlaid such that the red and dark purple traces are the first and last scans, respectively; dashed, purple arrows indicate the evolution of the current signals with successive scans. Black arrows indicate scan direction.

The voltammetric negative peak during the reverse scan in Figure 5-2C with a $\Delta_o^w\phi_{1/2}$ at – 0.240 V may be owing to the reorganization of the electric double layer (EDL) and adsorption of supporting electrolyte anions on either side of the forming liquid|solid|liquid interface.[4] As shown by Scanlon's group,[4] supporting electrolyte anions from both phases stabilize film growth through adsorption; however, due to the size and shielded negative charge on $B(C_6F_5)_4^-$, it is likely a minor contributor and most anion adsorption comes from SO_4^{2-} on the aqueous side. Moreover, SO_4^{2-} is molecularly smaller with exposed dense negative charge on the oxygens, doping the film with sulfate is more efficient in stabilizing and neutralizing the film as it forms. However, during the later stages of film growth, diffusion of anions through the film is inhibited making doping/de-doping a slow process and causing voltammetric peak broadening.[46] Regardless, the film will likely be p-doped.

Both micro and large ITIES experiments were also performed at open circuit potential (OCP), *i.e.*, without an applied external potential. In both cases, no film or NPs were observed. Thus, an applied potential is required to induce nanocomposite film formation.

Using the syringe affixed to the back of the pipette holder, a droplet of the aqueous phase was ejected from the tip of the micropipette after 25 consecutive CV scans using Cell 5-1 with 5 mM of $CuSO_4$ paired with 5 or 20 mM of TT in DCE and deposited on a holey-Au TEM grid. Next, the TEM grids were imaged using both TEM and SEM (see Figure 5-3). TEM micrographs in Figure 5-3A and 3B show the low dispersity spherical Cu NPs electrogenerated and embedded within the poly-TT film with average sizes of 5.3 and 1.7 nm at [TT] equal to 5 and 20 mM, respectively. NP sizes were measured using ImageJ software and collated into histograms plotted inset in Figure 5-3; average NP sizes were determined by curve fitting the histograms with a Gaussian distribution. Figure D1 of the Appendix D shows the histogram of Cu NP sizes with the

poly-TT film formed using Cell 5-1 with 10 mM of TT in DCE. With increasing [TT] the NP size decreased such that at TT = 10 or 20 mM, Cu particles are in the range of nanoclusters, *i.e.*, 1.3 or 1.7 nm in diameter, respectively.[47,48] In this case, with higher [TT] the thermodynamics and kinetics of the heterogeneous electron transfer reaction are enhanced facilitating faster electropolymerization, which in turn likely limits the size of the Cu nanoclusters.

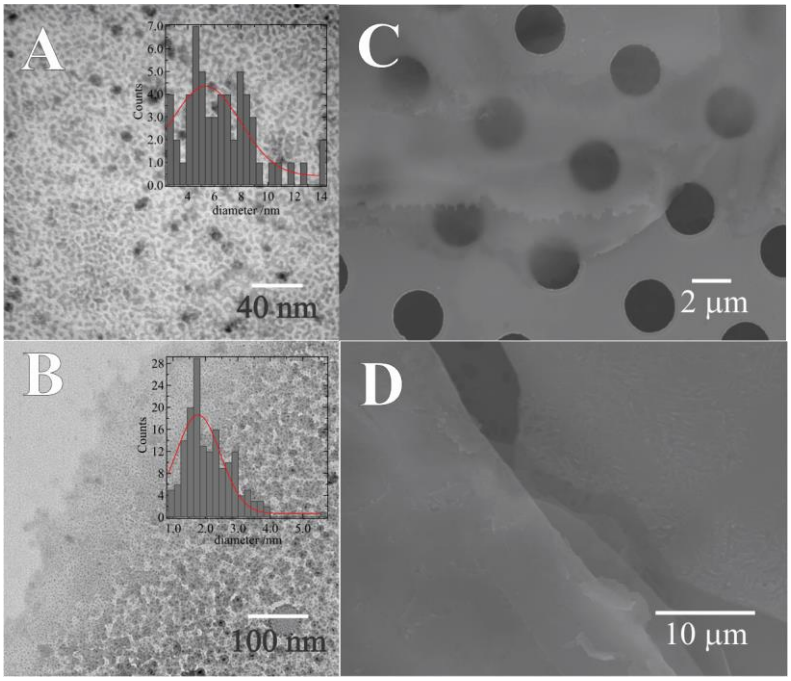

Figure 5-3 TEM micrographs obtained for aqueous phase samples after 25 consecutive CV scans using Cell 5-1 at a w|DCE interface with [$CuSO_4$] = 5 mM, as well as 5 (A) and 20 mM (B) of TT in DCE and deposited on a 2 µm diameter holey Au TEM grid; inset are histograms of Cu NP/nanocluster sizes. (C) SEM micrograph of the sample shown in B. (D) SEM image of the film generated at a large ITIES using Cell 5-2 with 5 mM of $CuSO_4$(aq) and 20 mM of TT(org).

TEM micrographs were also obtained for films electrogenerated at the 1.16 and 10 mm interfaces and deposited onto 200 mesh Au lacey carbon TEM grids. Figure D-3 of the Appendix D shows the TEM micrographs along with histograms for the analysis of the Cu NP sizes performed using ImageJ software. Cu NPs at 1.16 and 10 mm ITIES demonstrate a high dispersity despite Gaussian curve fitting showing peaks at 2.2 and 4.1 nm. Errors shown inset in Figure D-3 are for the Gaussian peak position/fitting. Figure D-4 shows a photograph of the aqueous droplet

suspended from the unmodified capillary (1.16 mm in diameter) post Cu NP/poly-TT electrogeneration and after removal from the oil phase. A thin-film can be observed spread across the droplet surface.

Figure 5-3C depicts the SEM micrograph of the nanocomposite Cu NP/poly-TT film deposited on a holey-Au TEM grid. The film was dense, compact, and smooth; however, it was also quite fragile and broke apart easily. Relatively large sections can be seen covering the TEM grid and occluding several of the 2 μm holes. These images agree well with the reported morphology for electropolymerized terthiophene in low current densities[49,50] and are similar to the PEDOT film electropolymerized at a large ITIES reported by Scanlon's group.[4] Cu NPs were confirmed by energy dispersive X-ray (EDX) spectroscopy performed during SEM imaging (data not shown). 24-hour shake-flask experiments performed in a 2 mL vial (large ITIES) using the same electrolyte compositions and TT concentrations as Cell 5-2 revealed no observable thin film or Cu NPs. Therefore, while not strictly observable voltammetrically at [TT] = 5 mM, by probing the positive edge of the PPW one can initiate Cu NP/poly-TT electrodeposition at relatively low [TT]. Moreover, this can be achieved without the use of extreme overpotentials that risk over-oxidizing the film.[31,51]

Figure 5-3D shows the film generated at the large ITIES with [$CuSO_4$] = 5 mM and [TT] = 20 mM after 1000 CV cycles. The film is smooth; however, the Cu NPs cannot be resolved with SEM. Figure D-2A in the Appendix D shows the CVs recorded during Cu NP/poly-TT electrosynthesis with [$CuSO_4$] = 1 mM and [TT] = 5 mM. The first and every subsequent fifth scan was plotted. The Cu^{2+}/TT reduction/oxidation and Cu re-oxidation waves are visible at roughly 0.85 and 0.55 V, respectively. The Cu NP/poly-TT film was extracted from the cell and deposited on a glass slide, then imaged in the SEM. Figure D-2B shows the SEM micrograph, while Figures

D-2C and D-2D contain plots of the EDX spectra obtained at the two points indicated in Figure D-2B. In Figure D-2B, the EDX spectra show that point C is rich in Cu and likely an agglomeration of Cu NPs, while point D is the polymer film itself containing sulphur and carbon.

The stepwise nucleation, oligomerization, and elongation of complex polymer/composite materials at liquid|liquid interfaces has been described by Vignali *et al*.,[31] Robayo-Molina *et al.*,[52] and recently by us.[28] The early stages of TT electropolymerization via heterogeneous electron transfer and electrodeposition can be described generally by the following,

$$Cu^{2+}(aq) + H\text{-}TT(org) \rightarrow Cu^{+} + H\text{-}TT^{+\bullet}(org) \qquad 5\text{-}1$$

$$Cu^{+}(aq) + H\text{-}TT(org) \rightarrow Cu^{0} + H\text{-}TT^{+\bullet}(org) \qquad 5\text{-}2$$

$$2H\text{-}TT^{+\bullet}(org) \rightarrow H\text{-}TT^{+}\text{-}TT^{+}\text{-}H(org) \qquad 5\text{-}3$$

$$H\text{-}TT^{+}\text{-}TT^{+}\text{-}H(org) + 2OH^{+}(aq) \rightarrow TT_2(s) + H_2O(l) \qquad 5\text{-}4$$

Where H-TT is the terthiophene molecule emphasizing the proton at the α- or β-carbon position on one of the terminal thiophene units, $TT^{+\bullet}$ is the radical cation, and TT_2 is the dimer. This initial stage is likely thermodynamically prohibitive at the liquid|liquid interface since it lacks nucleation sites.[38] However, once seeded with Cu^0 nuclei and the positively doped TT oligomers as capping agents, the thermodynamics likely greatly improve, as mentioned above. It should be emphasized that the glass walls of the micropipette likely behave as nucleation sites; this would also apply to the walls of large glass ITIES electrolytic cells. Using equations 5-1 to 5-4 as a basis, an overall reaction can be composed,

$$Cu^{2+}(aq) + 2H\text{-}TT(org) + 2OH^{-}(aq) \rightarrow Cu^{0}(s) + TT_2(s) + H_2O(l) \qquad 5\text{-}5$$

The overall electron transfer potential $\left(\Delta_o^w\phi_{ET}\right)$ for equation 5-5 can be written as,[27,28,38]

$$\Delta_o^w\phi_{ET} \approx E^{o',DCE}_{TT^{+\bullet}/TT} - E^{o',H_2O}_{Cu(II)/Cu} + (0.059\ V)(14 - pH) \quad 5\text{-}6$$

Where $E^{o',DCE}_{TT^{+\bullet}/TT}$ and $E^{o',H_2O}_{Cu(II)/Cu}$ are the standard redox potentials for $TT^{+\bullet}$/TT and Cu^{2+}/Cu^0 and were taken to be 1.20[28] and 0.342 V,[53] respectively. In this way, $\Delta_o^w\phi_{ET}$ was calculated to be 1.57, 1.36, and 1.18 V for pH's 2, 5.5-6, and 8.5, respectively; since $\Delta G = nF\Delta_o^w\phi_{ET}$,[54] this leads to $\Delta G >> 0$ that nevertheless decreases with increasing pH. These values are much higher than the experimentally determined values at pH ~5.5-6; thus, the difference is likely the thermodynamic contribution of the glass walls. However, silanization of the inside of the micropipette resulted in no observable change in the film produced (data not shown).

Next, electrochemical impedance spectroscopy (EIS) was employed during electrosynthesis at the micro-ITIES to elucidate the underlying physical and electrochemical dynamics of film formation. The sinusoidal applied potential waveform (V_{AC}) can be described by,[55]

$$V_{AC}(\omega t) = V_{DC} + V_0\sin(\omega t) \quad 5\text{-}7$$

Where V_{DC} and V_0 are the applied DC voltage and AC voltage amplitude (0.020 V peak-to-peak), respectively, while ω (= $2\pi f$) is the angular frequency and t is time. In each case, V_{DC} of roughly 0.7 V was applied (*vs.* $\Delta_o^w\phi^{o'}_{SO_4^{2-}}$) and a CV was performed between each impedance measurement at a scan rate of 0.020 V s^{-1}. In this way, the Nyquist diagrams in Figure 5-4(A-C) were recorded using Cell 5-1 at a 25 μm diameter interface with [TT] equal to 0, 5, and 20 mM in DCE, respectively. The semi-circle at high-frequency and partial semi-circle at low-frequencies describe the two typical branches of impedance spectra that are associated with electrical and electrochemical dynamics (*i.e.*, mass transport), respectively.[55] In the case of the liquid|liquid interface, the high-frequency region is often associated with the capacitance of the back-to-back EDLs found in either phase, while the low frequency region is influenced by ion diffusion and

electron transfer reactions.[55-57] These two features give rise to two "time constants" ($\tau = R_{\S}C_{\perp\!\!\!=}$),[55] so called since they are often modelled in equivalent circuits using a resistor ($R_{\S}$) and capacitor ($C_{\perp\!\!\!=}$) in parallel.

Equivalent electric circuits (EECs) used to model the impedance data have been drawn in Figure 5-4D, which include constant phase elements (CPEs) in place of simple capacitors, in parallel with resistors added to model charge transfer reactions (R_{CT}) and kinetic resistance (R_C). As is common, a resistor was added in series to account for the total solution resistance (R_s). EEC1, a Randles-like equivalent circuit, and EEC2 feature the two terminals at either end for the WE and CE/RE employed experimentally. The 2-electrode configuration limits parasitic impedance artifacts from cabling and/or the CE and RE that are often observed at 3- and 4-electrode cells.[57,58] Operating at the micro-ITIES has added benefits and is able to resolve the charge transfer resistance over the solution electrolyte resistance; moreover, by repeatedly using the same micropipette, one can greatly enhance reproducibility.

EIS offers avenues to valuable physical insight into charge transfer processes at the liquid|liquid interface. The geometric capacitance (C_{geo}), recently modeled by von Hauff and Klotz[55] in the context of perovskite solar cells, may be considered analogous to the structural parasitic coupling elements proposed and modelled by Trojánek *et al*.[57] for a 4-electrode cell, which they modelled using a 4-terminal EEC. In either case, C_{geo} is normally modelled in parallel with all the other circuit elements. If it exceeded the individual capacitive circuit elements, *i.e.*, CPE1 and CPE2 in Figure 5-4D, then the high-frequency semi-circle would become enlarged and dominate the impedance spectrum. However, by operating in the 2-electrode mode, and ensuring that the overall impedance of the micropipette was <1 MΩ during single phase experiments, then individual circuit

elements can be resolved.[59] Thus, C_{geo}/parasitic coupling elements can be ignored, greatly simplifying EEC modelling.[57,60,61] The faradaic impedance (Z_f) is described by,[57]

$$Z_f = R_{CT} + Z_w = \frac{RT}{z^2F^2Ak_fc^*_{i,w}} + (1-j)\sigma\omega^{-1/2} \qquad 5\text{-}8$$

where k_f is the apparent rate of charge transfer, A is the surface area of the interface, F is Faraday's constant (96485.33 C mol^{-1}), R is the gas constant (8.314 J mol^{-1} K^{-1}), T is the absolute temperature (298.15 K), z is the number of electrons transferred, and Z_W is a Warburg impedance, within which, $j^2 = -1$, and σ is defined as,[57]

$$\sigma = \frac{RT}{\sqrt{2}z^2F^2A}\left(\frac{1}{D^{1/2}_{i,o}c^*_{i,o}} + \frac{1}{D^{1/2}_{i,w}c^*_{i,w}}\right) \qquad 5\text{-}9$$

Here, $D_{i,o}$ and $c^*_{i,o}$ are the diffusion coefficient and bulk concentration of species i in the oil (o) phase, while subscript w indicates their values in the water phase. CPEs were used to account for the dynamic nature of the interface and facilitate the evolving properties of the growing polymer-NP network. CPE impedance can be written generally as,[62]

$$Z(\omega) \approx \frac{1}{Q}(j\omega)^{-n} \qquad 5\text{-}10$$

In which Q (F s^{1-n}) is a constant and when n = 1 the element is a perfect capacitor, while n = 0.5 is in line with a typical Warburg element for semi-infinite diffusion.

At a freshly cleaned micro-ITIES a CV was performed followed by impedance measurement using a V_{DC} = 0.7 V; whereby the CV-EIS pulse sequence was performed a total of 11 times. Figure 5-4A shows the impedance spectra using Cell 5-1 with [TT] = 0 and [$CuSO_4$] = 5 mM, *i.e.*, a blank spectrum. The pronounced low-frequency tail is likely owing to the relatively high V_{DC} close to the edge of the PPW where supporting electrolyte ions will undergo transfer, *e.g.*, Li^+ w→o. This

spectrum agrees well with one shown recently by Mareček's group[59] which was associated with simple tetraethylammonium ion transfer at a micro-ITIES.

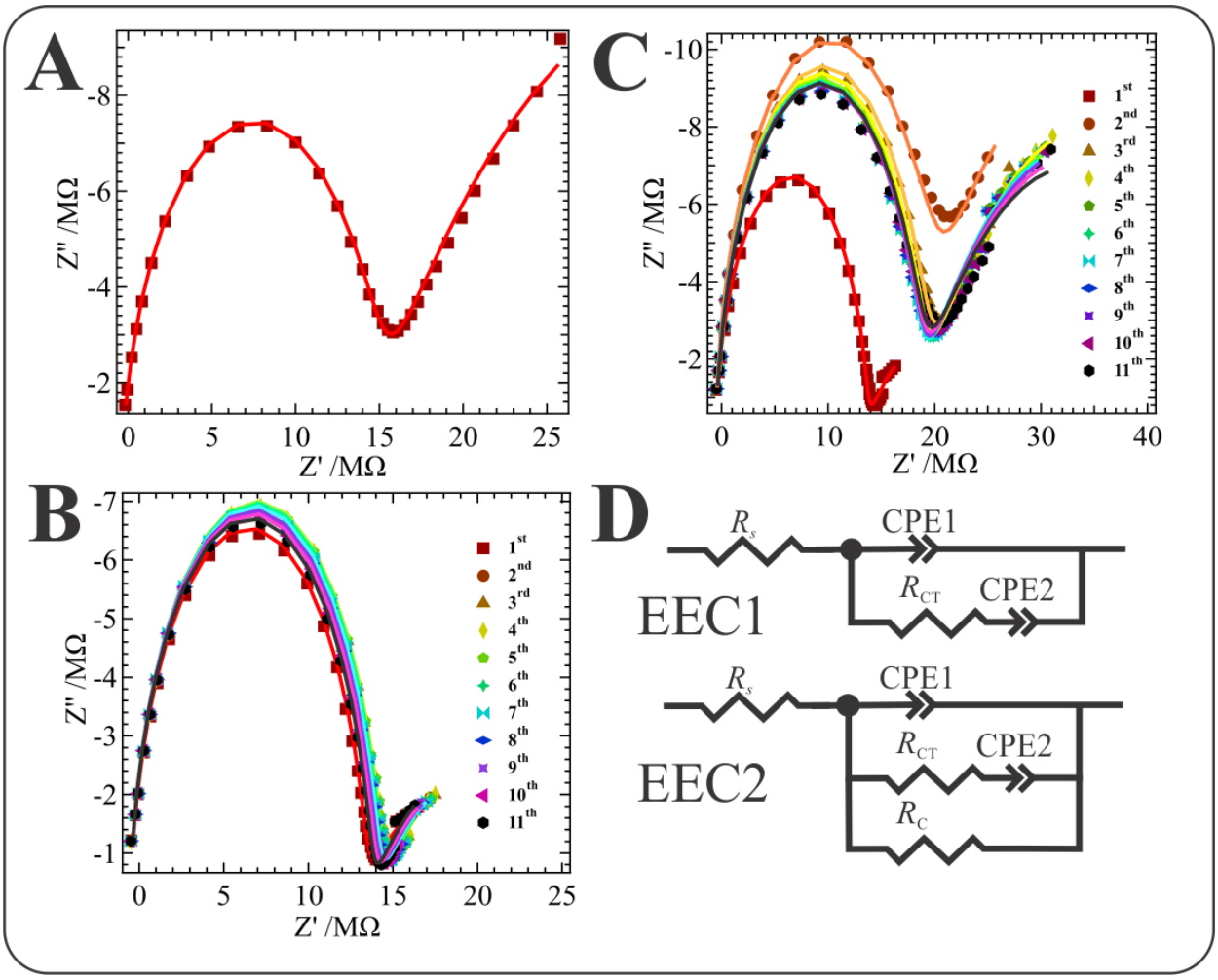

Figure 5-4 The measured (markers) and the fitted (solid line) Nyquist diagrams acquired using Cell 5-1 with 0 (A), 5 (B), and 20 mM (C) of TT added to the DCE phase as well as 5 mM of $CuSO_4$(aq). Spectra were obtained with a direct applied potential (VDC) of ~0.7 V after performing one CV cycle using the potential range shown in Figure 2 with $\nu = 0.020\ V\ s^{-1}$; similarly, in-between each spectrum in B and C a CV pulse was applied. (D) equivalent electric circuits (EEC) for a simple ion transfer (EEC1) or coupled electron and ion transfer during electro-generation (EEC2) of the thin film at an ITIES, such that R_S, R_{CT}, and R_C, are the solution, charge transfer, and kinetic resistance, while CPE1 and CPE2 are constant phase elements.

At low [TT] (Figure 5-4B) the impedance profile does not undergo significant change; however, the tail in the low-frequency region is greatly suppressed relative to the blank spectra performed in the absence of TT (Figure 5-4A). This may indicate that the film has formed after

the first CV-EIS sequence and is blocking, or at least inhibiting simple ion transfer of the supporting electrolyte.

Figure 5-4C shows the response at high [TT] in which the high frequency region of the EIS increases by 50% between the first and second CV-EIS pulse sequence. There is then a small decrease in the high frequency branch, which stabilizes across the 3rd to 11th iteration. Meanwhile, the low-frequency branch at high [TT] becomes more pronounced with each iteration. Based on the CV results (Figure 5-2A), the film forms immediately generating a liquid|solid|liquid interface and, thus, the low-frequency branch is then associated with mediated electron transfer between Cu^{2+}(aq) and TT(org) rather than simple ion transfer. Thus, as the film grows the electron transfer properties change (see below).

Nevertheless, these data indicate a change in the nature of the interface brought about by the development of a liquid|solid|liquid system that occurs immediately upon application of the CV-EIS. It has been shown that forming a barrier at the interface mainly affects the low-frequency region.[28] However, as the film develops, and likely due to the build up of local micro-convections in this domain,[63] it was found that by pushing the impedance measurement to lower and lower frequencies the interface becomes unstable. This either lead to a higher noise level or the interface itself physically broke down, erupting into the organic phase as an electrophoretically induced droplet. Thus, it was not possible to carry out EIS measurements below 10 Hz.

EEC2 (Figure 5-4D) was employed during thin film growth in the presence of $CuSO_4$(aq) and TT(org), while EEC1 was used in the absence of TT, see the blue, solid curves in Figure 5-5. Figure 5-5 shows the changes in the six EEC parameters after each CV-EIS iteration. With 5 mM of TT in the system, orange filled circle(●) curves, CPE1 shows little deviation from the initial value of ~12.0 pF with only a slight decrease over the 11 CV-EIS pulse sequences before finally

stabilizing at ~11.7 pF. As mentioned above, this circuit element is typically associated with the liquid|liquid back-to-back EDLs and these small changes in capacitance may be owing to ion rearrangement on either side of the interface during thin film electrogeneration or changes in the surface morphology at either side of the liquid|solid|liquid junction. At [TT] = 20 mM, yellow filled square (■) traces in Figure 5-5, there is a sudden decrease in CPE1 until the 4th CV-EIS pulse sequence, after which the element recovers and increases to a final value of 12.1 pF. In both cases, *n* varies between roughly 0.96 and 0.98, indicative of a conventional capacitor with likely an inhomogeneity in ion distribution at the interface.

The *n* value for CPE2, R_{CT}, and R_C increase slightly with [TT] = 5 mM and each CV-EIS pulse iteration, while all three parameters show a much larger increase at [TT] = 20 mM. R_{CT} and R_C are ½ and 2× as high, respectively, when [TT] = 20 mM versus 5 mM. This agrees well with impeded electron transfer or ion diffusion through the growing polymer/NP network. The limited diffusion within the nanocomposite structure likely results in limited anion exchange to neutralize individual TT units contributing to its p-doped nature and accumulation of negative charge on the surface of the Cu NP/poly-TT composite. These values agree with those recently reported by us for Au NP/poly-TT nanocomposites electrogenerated at a micro-ITIES[28] after multiple CV-EIS pulses were performed. Herein, the interface was monitored *in situ* using a CCD camera equipped with a 12× zoom lens assembly with a 10-12 cm working distance; however, unlike the Au NP/polyTT film grown previously,[28] the Cu NP/polyTT nanocomposite film was clear/colourless and, therefore, no observable change was observed optically.

Preliminary electrocatalysis results were obtained by modifying the surface of a glassy carbon (GC) electrode with a layer of Cu NP/poly-TT film and using 0.1 M $NaHCO_3$(aq) as

supporting electrolyte. Figure 5-6 shows CVs recorded at a bare and modified electrode; whereby, the solution was purged with either N_2 or CO_2 gas for ~15 min prior to polarization.

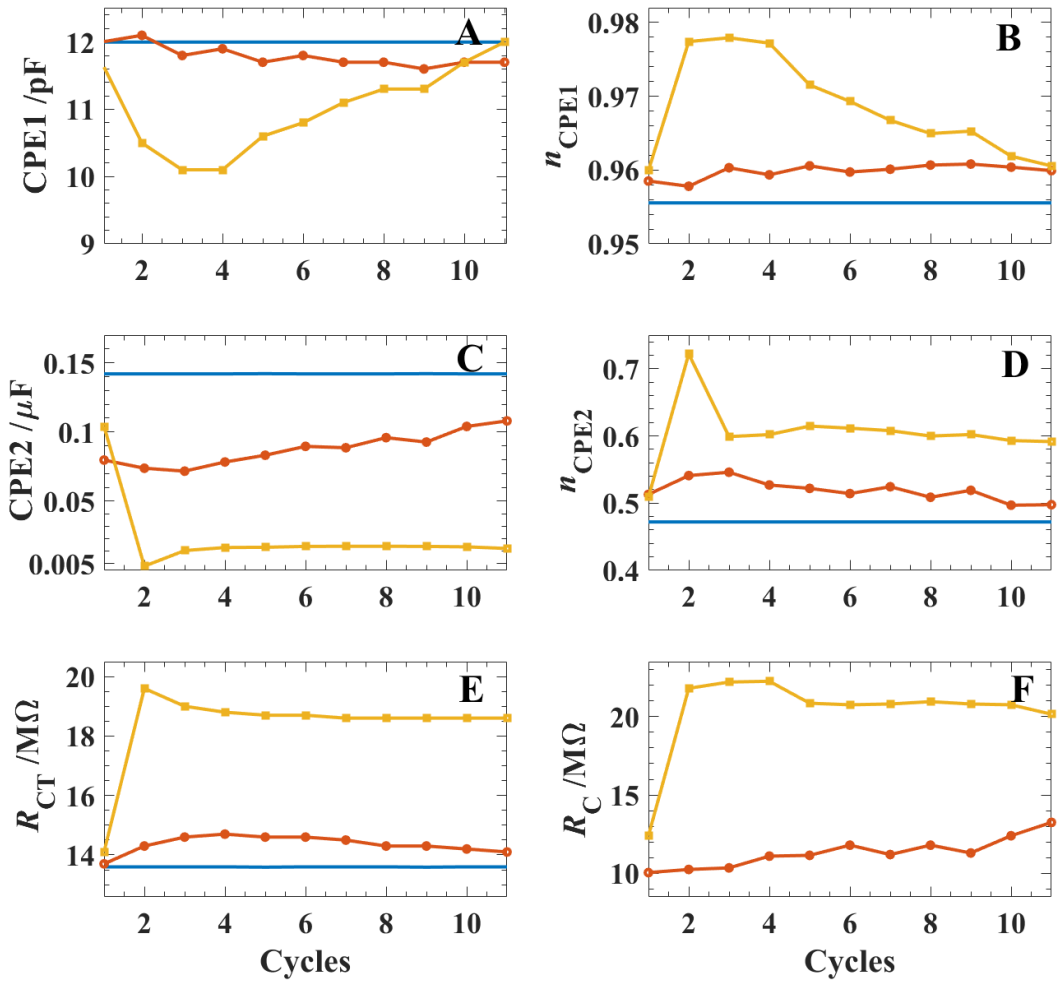

Figure 5-5 Equivalent electric circuit (EEC) parameter values obtained from fitting experimental impedance spectra from Figure 5-4(A-C) using EEC2 depicted in Figure 5-4D, with the orange, ● and yellow, ■, curves derived from curve fitting impedance data obtained from Cell 5-1 with [TT] = 5 and 20 mM, respectively. The blue trace was determined using Cell 5-1 with [TT] = 0 mM.

At a bare GC electrode, and in the N_2 saturated case, the cathodic peak at roughly –0.45 V (*vs.* Ag/AgCl) is likely H^+ reduction. However, this cathodic signal experiences a shift in the onset potential to –0.57 V when purged with CO_2 but maintains the same current intensity. The GC electrode modified with the Cu NP/poly-TT film electrosynthesized at a 1.16 mm ITIES shows a greater than 2× CO_2 reduction current at 0.75 V (*vs.* Ag/AgCl). To modify the GC electrode with

a Cu NP/poly-TT composite at a 10 mm ITIES, the GC plug was dipped into the electrolytic cell after the 25 CV cycles were performed. Afterwards, the *i-V* response shown in Figure 5-6, yellow trace, demonstrated a further shift in the overpotential towards more negative potentials with no increase in the peak current; thus, electrocatalysis is likely suppressed in this instance. Modification of the interface with a single deposit from the 25 µm diameter interface resulted in no significant change relative to the bare GC electrode (data not shown).

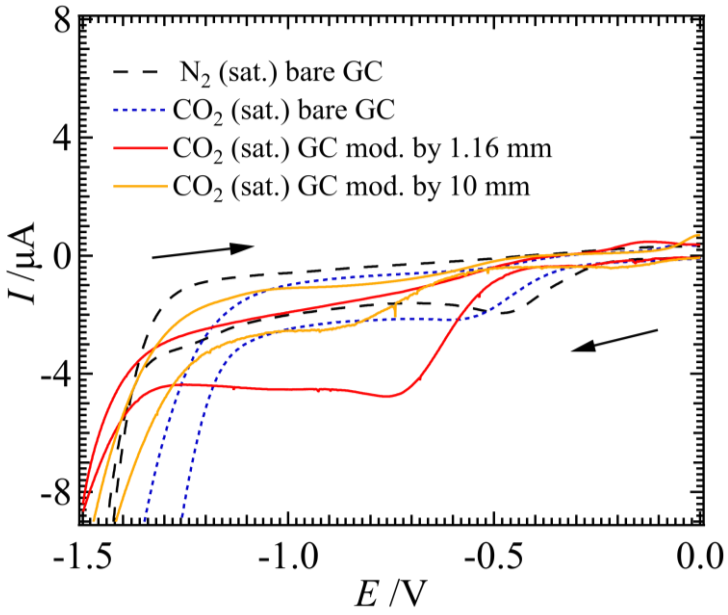

Figure 5-6 CVs recorded at a ~4 mm glassy carbon (GC) electrode immersed in a 0.1 M $NaHCO_3$ aqueous solution without (bare) and with (modified) a layer of Cu NP/poly-TT film deposited on the surface. Films were electrogenerated at the 1.16 or 10 mm ITIES using Cells 5-1 or 5-2, as indicated inset, with [TT] = 20 mM and [$CuSO_4$] = 5 mM, after 25 CV cycles at v = 0.050 V s^{-1}. CVs were recorded in 3-electrode mode using a Ag/AgCl reference (Dek Research) and Pt wire counter electrode.

Figure 5-7 depicts SEM images of the GC electrode surface modified with films generated at the 25 µm (A, D), 1.16 mm (B, E), and 10 mm (C, F) diameter interfaces before (left-hand side) and after (right-hand side) one CV cycle; additionally, using ImageJ software the GC surface coverage was estimated to be 0.3, 9.9, and 62.5%, respectively. The film electrosynthesized at the 25 µm ITIES is smooth and shows evidence of folding with Cu NPs distributed along creases in the film. It is hypothesized that the film quickly occludes the ITIES and new polymeric growth

pushes the film into the aqueous side of the interface generating these folds. The Cu NP are likely concentrated towards the bottom of these folds, adjacent to the ITIES. Advanced, high-resolution optical methods will be needed to monitor film growth at the micro-ITIES in situ; however, this will be the focus of future work.

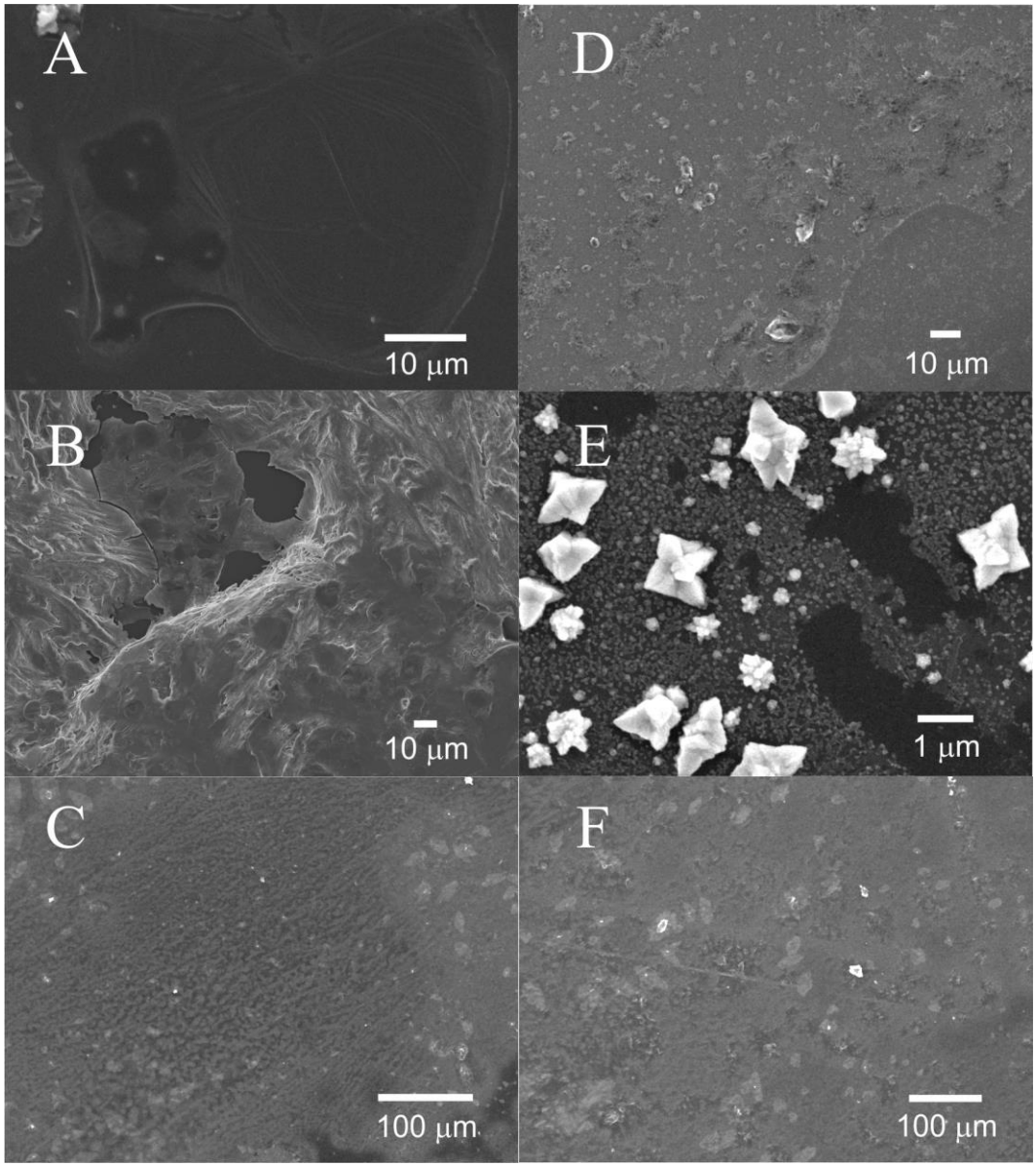

Figure 5-7 SEM micrographs of Cu NP/poly(TT) film deposited on a glassy carbon (GC) electrode before (left-hand side) and after (right-hand side) CV electrocatalysis as shown in Figure 5-6. The top (A, D), middle (B, E), and bottom (C, F) rows were films generated at a 25 μm, 1.16 mm, and 10 mm diameter ITIES, respectively. Scale is indicated inset.

Films developed at the two large ITIES were smooth with a relatively even distribution of Cu NPs and no evidence of folding. Therefore, this phenomenon is likely owing to geometric confinement of the growing polymer film within the micropipette tip.

After electrocatalysis, the Cu NPs in the films generated at the 25 μm and 1.16 mm interfaces showed large changes in NP morphology which have grown by orders of magnitude; therefore, the thin, polymer network in these cases is insufficient to protect them against aggregation/agglomeration. The film created at the 10 mm ITIES showed little change; however, further experimentation is required.

While preliminary, these results are promising. Future work will focus on controlling Cu NP and polymer film morphology while tracking any changes the nanocomposite experiences during electrocatalysis, as well as detailed product analysis.

5.5. Conclusions

The successful application of a micro-ITIES towards electrodeless synthesis of Cu NP/poly-TT has been demonstrated and compared to films generated at a large (mm scale) ITIES. At [TT] = 20 mM a well resolved electron transfer wave was observed at the micro-ITIES. However, the large interfaces showed a more complex CV profile with an irreversible electron transfer wave at high, positive potentials and a reversible signal towards the negative end. The latter is likely anion adsorption/exchange at the liquid|solid|liquid interfaces and agrees well with recent results by Scanlon's group.[4] Impedance data confirm that the nanocomposite film forms early through large changes in R_{CT} and R_C; moreover, increasing [TT] improves film formation while decreasing the median Cu NP size to <2 nm.

Interestingly, while no electron transfer signal was observed at the micro-ITIES a low [TT], a film was electrogenerated and imaged using SEM. These data show that simply by probing the edge of the PPW one can facilitate electrodeless synthesis of the nanocomposite and avoid overoxidation of the polymer network.

Preliminary voltammetric results at a GC electrode modified with the Cu NP/poly-TT film electrogenerated at a 1.16 mm diameter interface elicited a >2× enhancement in the electrocatalytic CO_2 reduction current versus an unmodified electrode. However, this film underwent large changes in NP morphology. While a tentative first step, these results are indicators that these films are promising alternative electrode materials for carbon capture; however, more optimization of nanocomposite electrosynthesis is necessary.

5.6. References

(1) Cheng, H. W.; Zhang, S.; Michalek, L.; Ji, X.; Luo, S.; Cooper, C. B.; Gong, H.; Nikzad, S.; Chiong, J. A.; Wu, Y.; Zheng, Y.; Liu, Q.; Zhong, D.; Lei, Y.; Tomo, Y.; Wei, K. H.; Zhou, D.; Tok, J. B. H.; Bao, Z. Realizing Intrinsically Stretchable Semiconducting Polymer Films by Nontoxic Additives. *ACS. Mater. Lett*. **2022**, 4 (11), 2328–2336. https://doi.org/10.1021/acsmaterialslett.2c00749.

(2) Zhang, Q. An Elastic Autonomous Self-Healing Capacitive Sensor Based on a Dynamic Dual Crosslinked Chemical System. *Adv. Mater.* **2018**, 30, 1801435. https://doi.org/10.1002/adma.201801435.

(3) Wang, S.; Oh, J. Y.; Xu, J.; Tran, H.; Bao, Z. Skin-Inspired Electronics: An Emerging Paradigm. *Acc. Chem. Res.* **2018**, 51 (5), 1033–1045. https://doi.org/10.1021/acs.accounts.8b00015.

(4) Lehane, R. A.; Gamero-Quijano, A.; Malijauskaite, S.; Holzinger, A.; Conroy, M.; Laffir, F.; Kumar, A.; Bangert, U.; McGourty, K.; Scanlon, M. D. Electrosynthesis of Biocompatible Free-Standing PEDOT Thin Films at a Polarized Liquid|Liquid Interface. *J. Am. Chem. Soc.* **2022**, 144 (11), 4853–4862. https://doi.org/10.1021/jacs.1c12373.

(5) Nezakati, T.; Seifalian, A.; Tan, A.; Seifalian, A. M. Conductive Polymers: Opportunities and Challenges in Biomedical Applications. *Chem. Rev*. **2018**, 118 (14), 6766–6843. https://doi.org/10.1021/acs.chemrev.6b00275.

(6) Guo, Y.; Thérien-Aubin, H. Nanofibrous Photocatalytic Membranes Based on Tailored Anisotropic Gold/Ceria Nanoparticles. *ACS. Appl. Mater. Interfaces*. **2021**, 13 (31), 37578–37588. https://doi.org/10.1021/acsami.1c11954.

(7) Roy, D.; Pal, A.; Pal, T. Electrochemical Aspects of Coinage Metal Nanoparticles for Catalysis and Spectroscopy. *RSC. Adv.* **2022**, 12, 12116–12135. https://doi.org/10.1039/D2RA00403H.

(8) Scanlon, M. D.; Smirnov, E.; Stockmann, T. J.; Peljo, P. Gold Nanofilms at Liquid–Liquid Interfaces: An Emerging Platform for Redox Electrocatalysis, Nanoplasmonic Sensors, and Electrovariable Optics. *Chem. Rev*. **2018**, 118 (7), 3722–3751. https://doi.org/10.1021/acs.chemrev.7b00595.

(9) Ben Aissa, M. A.; Tremblay, B.; Andrieux-Ledier, A.; Maisonhaute, E.; Raouafi, N.; Courty, A. Copper Nanoparticles of Well-Controlled Size and Shape: A New Advance in Synthesis and Self-Organization. *Nanoscale*, **2015**, 7 (7), 3189–3195. https://doi.org/10.1039/c4nr06893a.

(10) Kim, D.; Kley, C. S.; Li, Y.; Yang, P. Copper Nanoparticle Ensembles for Selective Electroreduction of CO2 to C2–C3 Products. *Proc. Natl. Acad. Sci.* **2017**. https://doi.org/10.1073/pnas.1711493114%JProceedingsoftheNationalAcademyofSciences.

(11) Song, Y.; Peng, R.; Hensley, D. K.; Bonnesen, P. V.; Liang, L.; Wu, Z.; Meyer, H. M.; Chi, M.; Ma, C.; Sumpter, B. G.; Rondinone, A. J. High-Selectivity Electrochemical Conversion of CO_2 to Ethanol Using a Copper Nanoparticle/N-Doped Graphene Electrode. *ChemistrySelect.* **2016**, 1 (19), 6055–6061. https://doi.org/10.1002/slct.201601169.

(12) Nguyen, T. N.; Chen, Z.; Zeraati, A. S.; Shiran, H. S.; Sadaf, S. M.; Kibria, M. G.; Sargent, E. H.; Dinh, C. T. Catalyst Regeneration via Chemical Oxidation Enables Long-Term Electrochemical Carbon Dioxide Reduction. *J. Am. Chem. Soc.* **2022**, 144 (29), 13254–13265. https://doi.org/10.1021/jacs.2c04081.

(13) Zahid, A.; Shah, A.; Shah, I. Oxide Derived Copper for Electrochemical Reduction of CO_2 to C_2^+ Products. *Nanomaterials.* **2022**, 12 (8), 1380. https://doi.org/10.3390/nano12081380.

(14) Brust, M.; Walker, M.; Bethell, D.; Schiffrin, D. J.; Whyman, R. Synthesis of Thiol-Derivatised Gold Nanoparticles in a Two-Phase Liquid-Liquid System. *J. Chem. Soc. Chem. Commun*. **1994**, 7, 801–802. https://doi.org/10.1039/C39940000801.

(15) Uehara, A.; Booth, S. G.; Chang, S. Y.; Schroeder, S. L. M.; Imai, T.; Hashimoto, T.; Mosselmans, J. F. W.; Dryfe, R. A. W. Electrochemical Insight into the Brust–Schiffrin Synthesis of Au Nanoparticles. *J. Am. Chem. Soc*. **2015**, 137 (48), 15135–15144. https://doi.org/10.1021/jacs.5b07825.

(16) Aslan, E.; Patir, I. H.; Ersoz, M. Cu Nanoparticles Electrodeposited at Liquid–Liquid Interfaces: A Highly Efficient Catalyst for the Hydrogen Evolution Reaction. *Chem. Eur. J.* **2015**, 21 (12), 4585–4589. https://doi.org/10.1002/chem.201406615

(17) Uehara, A.; Hashimoto, T.; Dryfe, R. A. W. Au Electrodeposition at the Liquid-Liquid Interface: Mechanistic Aspects. *Electrochim. Acta*. **2014**, 118, 26–32. https://doi.org/10.1016/j.electacta.2013.11.162.

(18) Dryfe, R. A. W.; Uehara, A.; Booth, S. G. Metal Deposition at the Liquid–Liquid Interface. The *Chem. Rec.* **2014**, 14 (6), 1013–1023. https://doi.org/10.1002/tcr.201402027

(19) Booth, S. G.; Uehara, A.; Chang, S. Y.; La Fontaine, C.; Fujii, T.; Okamoto, Y.; Imai, T.; Schroeder, S. L. M.; Dryfe, R. A. W. The Significance of Bromide in the Brust-Schiffrin Synthesis of Thiol Protected Gold Nanoparticles. *Chem. Sci*. **2017**, 8 (12), 7954–7962. https://doi.org/10.1039/c7sc03266h.

(20) Kuroyama, Y.; Nishi, N.; Sakka, T. Electrochemical Liquid-Liquid Interface between Oil and Ionic Liquid for Reductive Deposition of Metal Nanostructures. *J. Electroanal. Chem.* **2021**, 881. https://doi.org/10.1016/j.jelechem.2020.114959.

(21) Katakura, S.; Amano, K. I.; Sakka, T.; Bu, W.; Lin, B.; Schlossman, M. L.; Nishi, N. Evolution and Reversible Polarity of Multilayering at the Ionic Liquid|Water Interface. *J. Phys. Chem. B.* **2020**, 124 (29), 6412–6419. https://doi.org/10.1021/acs.jpcb.0c03711.

(22) Zhang, Y.; Nishi, N.; Sakka, T. Template-Free and Spontaneous Formation of Vertically Aligned Pd Nanofiber Arrays at the Liquid-Liquid Interface between Redox-Active Ionic Liquid and

Water. *ACS. Appl. Mater. Interfaces.* **2019**, 11 (26), 23731–23740. https://doi.org/10.1021/acsami.9b05255.

(23) Zhang, Y.; Nishi, N.; Amano, K. ichi; Sakka, T. One-Dimensional Pt Nanofibers Formed by the Redox Reaction at the Ionic Liquid|water Interface. *Electrochim. Acta.* **2018**, 282, 886–891. https://doi.org/10.1016/j.electacta.2018.06.024.

(24) Nishi, N.; Yajima, I.; Amano, K. I.; Sakka, T. Janus-Type Gold/Polythiophene Composites Formed via Redox Reaction at the Ionic Liquid|Water Interface. *Langmuir.* **2018**, 34 (7), 2441–2447. https://doi.org/10.1021/acs.langmuir.7b03792.

(25) Nishi, N.; Kakinami, T.; Sakka, T. Dendritic Nanofibers of Gold Formed by the Electron Transfer at the Interface between Water and a Highly Hydrophobic Ionic Liquid. *Chem. Commun.* **2015**, 51 (71), 13638–13641. https://doi.org/10.1039/c5cc05476a.

(26) Moshrefi, R.; Stockmann, T. J. Electrodeless Synthesis of Low Dispersity Au Nanoparticles and Nanoclusters at an Immiscible Micro Water | Ionic Liquid Interface. *Nanomaterials.* **2022**, 12 (16), 2748. https://doi.org/10.3390/nano12162748.

(27) Moshrefi, R.; Suryawanshi, A.; Stockmann, T. J. Electrochemically Controlled Au Nanoparticle Nucleation at a Micro Liquid | Liquid Interface Using Ferrocene as Reducing Agent. *Electrochem. Commun.* **2021**, 122, 106894. https://doi.org/10.1016/j.elecom.2020.106894.

(28) Moshrefi, R.; P. Connors, E.; Merschrod, E.; Stockmann, T. J. Simultaneous Electropolymerization/Au Nanoparticle Generation at an Electrified Liquid | Liquid Micro-Interface. *Electrochim. Acta.* **2022**, 426, 140749. https://doi.org/10.1016/j.electacta.2022.140749.

(29) Lepková, K.; Clohessy, J.; Cunnane, V. J. Electrodeposition of Metal-Based Nanocomposites at a Liquid–Liquid Interface Controlled via the Interfacial Galvani Potential Difference. *Electrochim. Acta.* **2008**, 53. https://doi.org/10.1016/j.electacta.2008.04.025.

(30) Lepková, K.; Clohessy, J.; Cunnane, V. J. The pH-Controlled Synthesis of a Gold Nanoparticle/Polymer Matrix via Electrodeposition at a Liquid-Liquid Interface. *J Phys.* **2007**, 19 (37), 6273–6277. https://doi.org/10.1088/0953-8984/19/37/375106.

(31) Vignali, M.; Edwards, R.; Cunnane, V. J. Characterization of Doping and Electropolymerization of Free Standing Films of Polyterthiophene. *J Electroanal Chem.* **2006**, 592 (1), 37–45. https://doi.org/10.1016/j.jelechem.2006.04.020.

(32) Knake, R.; Fahmi, A. W.; Tofail, S. A. M.; Clohessy, J.; Mihov, M.; Cunnane, V. J. Electrochemical Nucleation of Gold Nanoparticles in a Polymer Film at a Liquid−Liquid Interface. *Langmuir.* **2005**, 21 (3), 1001–1008. https://doi.org/10.1021/la048277q.

(33) Sarac, S. S.; Evans, U.; Serantoni, M.; Clohessy, J.; Cunnane, V. J. Electrochemical and Morphological Study of the Effect of Polymerization Conditions on Poly(Terthiophene). *Surf Coat. Technol*. **2004**, 182 (1), 7–13. https://doi.org/10.1016/j.surfcoat.2003.08.002.

(34) Evans-Kennedy, U.; Clohessy, J.; Cunnane, V. J. Spectroelectrochemical Study of 2,2′:5′,2″-Terthiophene Polymerization at a Liquid | Liquid Interface Controlled by Potential-Determining Ions. *Macromolecules.* **2004**, 37 (10), 3630–3634. https://doi.org/10.1021/ma0348223.

(35) Johans, C.; Clohessy, J.; Fantini, S.; Kontturi, K.; Cunnane, V. J. Electrosynthesis of Polyphenylpyrrole Coated Silver Particles at a Liquid-Liquid Interface. *Electrochem. Commun.* **2002**, 4 (3), 227–230. https://doi.org/10.1016/S1388-2481(02)00256-4.

(36) Gorgy, K.; Fusalba, F.; Evans, U.; Kontturi, K.; Cunnane, V. J. Electropolymerization of 2,2′:5′,2″ Terthiophene at an Electrified Liquid–Liquid Interface. *Synth. Met.* **2001**, 125. https://doi.org/10.1016/S0379-6779(01)00474-X.

(37) Samec, Z. Z.; Langmaier, J.; Kakiuchi, T. Charge-Transfer Processes at the Interface between Hydrophobic Ionic Liquid and Water. *Pure. Appl. Chem.* **2009**, 81 (8), 1473–1488. https://doi.org/10.1351/PAC-CON-08-08-36.

(38) Johans, C.; Lahtinen, R.; Kontturi, K.; Schiffrin, D. J. Nucleation at Liquid|liquid Interfaces: Electrodeposition without Electrodes. *J. Electroanal. Chem.* **2000**, 488 (2), 99–109. https://doi.org/10.1016/S0022-0728(00)00185-6.

(39) Nieminen, E.; Murtomäki, L. Kinetics of Cu^{2+} Reduction and Nanoparticle Nucleation at Micro-Scale 1,2-Dichlorobenzene-Water Interface Studied by Cyclic Voltammetry and Square-Wave Voltammetry. *Electroanalysis.* **2021**, 33 (9), 2087–2095. https://doi.org/10.1002/elan.202100172.

(40) Cheng, Y.; Schiffrin, D. J. Electrodeposition of Metallic Gold Clusters at the Water | 1,2-Dichloroethane *Interface. J. Chem. Soc. - Faraday Trans.* **1996**, 92 (20), 3865–3871. https://doi.org/10.1039/ft9969203865.

(41) Stockmann, T. J.; Boyle, P. D.; Ding, Z. Preparation and Crystal Structure of Tetraoctylphosphonium Tetrakis(Pentafluorophenyl)Borate Ionic Liquid for Electrochemistry at Its Interface with Water. *Catal. Today.* **2017**, 295, 89–94. https://doi.org/10.1016/j.cattod.2017.05.030.

(42) Stockmann, T. J.; Lu, Y.; Zhang, J.; Girault, H. H.; Ding, Z. Interfacial Complexation Reactions of Sr^{2+} with Octyl(Phenyl)-*N, N*-Diisobutylcarbamoylmethylphosphine Oxide for Understanding

Its Extraction in Reprocessing Spent Nuclear Fuels. *Chem. Eur. J.* **2011**, 17. https://doi.org/10.1002/chem.201102491.

(43) Stockmann, T. J.; Guterman, R.; Ragogna, P. J.; Ding, Z. Trends in Hydrophilicity/Lipophilicity of Phosphonium Ionic Liquids As Determined by Ion-Transfer Electrochemistry. *Langmuir*. **2016**, 32 (49), 12966–12974. https://doi.org/10.1021/acs.langmuir.6b03031.

(44) Liu, S.; Li, Q.; Shao, Y. Electrochemistry at Micro- and Nanoscopic Liquid | Liquid Interfaces. *Chem. Soc. Rev.* **2011**, 40 (5), 2236–2253. https://doi.org/10.1039/c0cs00168f.

(45) Nieminen, J. J.; Hatay, I.; Ge, P.; Méndez, M. A.; Murtomäki, L.; Girault, H. H. Hydrogen Evolution Catalyzed by Electrodeposited Nanoparticles at the Liquid | Liquid Interface. *ChemComm.* **2011**, 47 (19), 5548–5550. https://doi.org/10.1039/c1cc10637f.

(46) Wei, Y.; Chan, C. C.; Tian, J.; Jang, G. W.; Hsueh, K. F. Electrochemical Polymerization of Thiophenes in the Presence of Bithiophene or Terthiophene: Kinetics and Mechanism of the Polymerization. Chemistry of Materials. *Chem. Mater.* **1991**, 3 (5), 888–897. https://doi.org/10.1021/cm00017a026.

(47) Jorabchi, M. N.; Abbaspour, M.; Goharshadi, E. K.; Wohlrab, S. Ag, Au, Pt, and Au-Pt Nanoclusters in [N1114][C1SO3] Ionic Liquid: A Molecular Dynamics Study. *J. Mol. Liq.* **2022**, 360. https://doi.org/10.1016/j.molliq.2022.119447.

(48) Baletto, F.; Ferrando, R. Structural Properties of Nanoclusters: Energetic, Thermodynamic, and Kinetic Effects, *Rev. Mod. Phys.* **2005**, 77, 371-423.

(49) Wakeham, D. L.; Donne, S. W.; Belcher, W. J.; Dastoor, P. C. Electrochemical and Morphological Characterization of Electrodeposited Poly(2,2′:5′,2″-Terthiophene) for Photovoltaic Applications. *Synth. Met.* **2008**, 158 (16), 661–669. https://doi.org/10.1016/j.synthmet.2008.04.022.

(50) Harris, C. J.; Belcher, W. J.; Dastoor, P. C. Effect of Film Thickness and Morphology on the Performance of Photoelectrochemical Cells Based on Poly(Terthiophene). *Sol. Energy. Mater. Sol. Cells.* **2007**, 91 (12), 1127–1136. https://doi.org/10.1016/j.solmat.2007.03.018.

(51) Barsch, U.; Beck, F. Anodic Overoxidation of Polythiophenes in Wet Acetonitrile Electrolytes. *Electrochim. Acta.* **1996**, 41 (11–12), 1761–1771. https://doi.org/10.1016/0013-4686(95)00493-9.

(52) Robayo-Molina, I.; Molina-Osorio, A. F.; Guinane, L.; Tofail, S. A. M.; Scanlon, M. D. Pathway Complexity in Supramolecular Porphyrin Self-Assembly at an Immiscible Liquid–Liquid Interface. *J. Am. Chem. Soc.* **2021**, jacs.1c02481. https://doi.org/10.1021/jacs.1c02481.

(53) Vanýsek, P. CRC Handbook of Chemistry and Physics; CRC Press/Taylor, **2021,** 8.20-28.29.

(54) Méndez, M. A.; Partovi-Nia, R.; Hatay, I.; Su, B.; Ge, P.; Olaya, A.; Younan, N.; Hojeij, M.; Girault, H. H. Molecular Electrocatalysis at Soft Interfaces. *Phys. Chem. Chem. Phys.* **2010**, 12 (46), 15163–15171. https://doi.org/10.1039/c0cp00590h.

(55) Von Hauff, E.; Klotz, D. Impedance Spectroscopy for Perovskite Solar Cells: Characterisation, Analysis, and Diagnosis. *J. Mater. Chem. C.* **2022**, 10 (2), 742–761. https://doi.org/10.1039/d1tc04727b.

(56) Suárez-Herrera, M. F.; Cazade, P. A.; Thompson, D.; Scanlon, M. D. Monitoring Transient Changes in the Structure of Water at a Polarised Liquid-Liquid Interface Using Electrocapillary

Curves. *Electrochem. Commun.* **2019**, 109, 106564. https://doi.org/10.1016/j.elecom.2019.106564.

(57) Trojánek, A.; Mareček, V.; Samec, Z. Some Aspects of Impedance Measurements at the Interface between Two Immiscible Electrolyte Solutions in the Four-Electrode Cell. *Electrochim. Acta.* **2015**, 179, 3–8. https://doi.org/10.1016/j.electacta.2014.12.013.

(58) Tuan Tran, A.; Huet, F.; Ngo, K.; Rousseau, P.; Tran, A.; Huet, F.; Ngo, K.; Rousseau, P. Artefacts in Electrochemical Impedance Measurement in Electrolytic Solutions Due to the Reference Electrode. *Electrochim. Acta.* **2011**, 56 (23), 8034–8039. https://doi.org/10.1016/j.electacta.2010.12.088ï.

(59) Silver, B. R.; Holub, K.; Mareček, V. Ion Transfer Kinetics at the Micro-Interface between Two Immiscible Electrolyte Solutions Investigated by Electrochemical Impedance Spectroscopy and Steady-State Voltammetry. *J. Electroanal. Chem.* **2014**, 731, 107–111. https://doi.org/10.1016/j.jelechem.2014.08.017.

(60) Trojánek, A.; Mareček, V.; Samec, Z. Temperature Effect in the Ion Transfer Kinetics at the Micro-Interface between Two Immiscible Electrolyte Solutions. *Electrochim. Acta*. **2015**, 180, 366–372. https://doi.org/10.1016/j.electacta.2015.08.110.

(61) Josypčuk, O.; Holub, K.; Mareček, V. Noise and Ac Impedance Analysis of Ion Transfer Kinetics at the Micro Liquid | Liquid Interface. *Electrochem. Commun.* **2015**, 56, 43–45. https://doi.org/10.1016/j.elecom.2015.04.006.

(62) Bisquert, J.; Garcia-Belmonte, G.; Bueno, P.; Longo, E.; Bulhões, L. O. S. Impedance of Constant Phase Element (CPE)-Blocked Diffusion in Film Electrodes. *J. Electroanal. Chem.* **1998**, 452, 229-234. https://doi.org/10.1016/S0022-0728(98)00115-6.

(63) Lhotský, A.; Holub, K.; Neužil, P.; Mareček, V. Ac Impedance Analysis of Tetraethylammonium Ion Transfer at Liquid | Liquid Microinterfaces. *J. Chem. Soc., Faraday Trans.* **1996**, 92 (20), 3851–3857. https://doi.org/10.1039/FT9969203851.

Chapter 6

6. Electrosynthesis of Au nanocluster embedded conductive polymer films at soft interfaces using dithiafulvenyl-functionalized pyrene

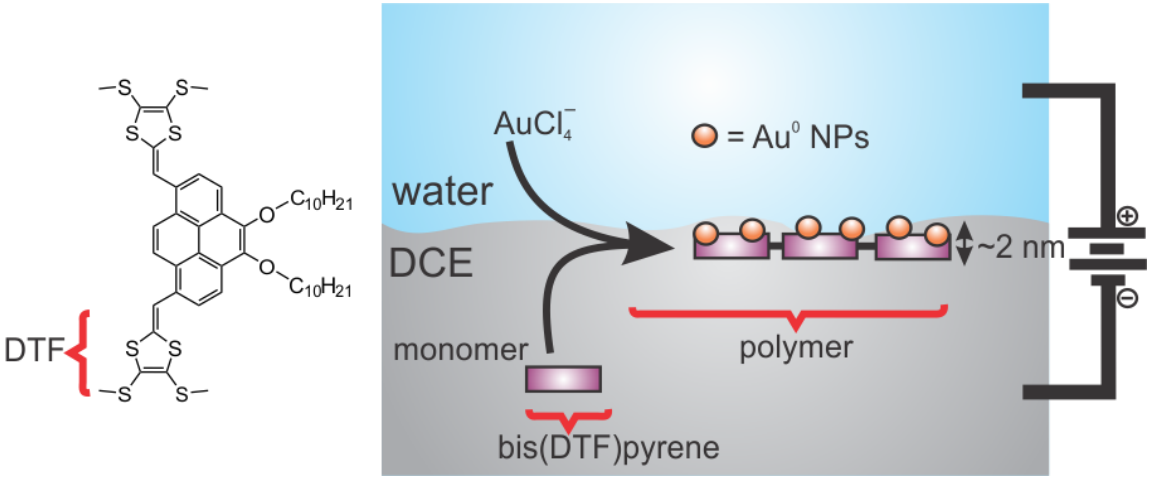

6.1. Statement of Co-Authorship

This chapter has been published under the above title in *Nanoscale* **2023**, 15(12), 5834-5842. It is presented here in a modified format that includes all contributions for completeness and context.

Authors: Reza Moshrefi, Katelyn Ryan, Evan P. Connors, Joshua C. Walsh, Erika Merschrod, Graham J. Bodwell, and Talia Jane Stockmann

This article was a group effort combining the work of graduate and undergraduate student co-authors from the research groups of Erika Merschrod, Graham J. Bodwell, and T. Jane Stockmann

Reza Moshrefi (listed in the paper as 1st author): Performed electrochemical experiments, material characterization and contributed to formal analysis, investigation, writing - review & editing, validation.

Katelyn Ryan: Performed electrochemical experiments, material characterization, writing - review & editing.

Evan P. Connors and Erika Merschrod: Contributed to the collection and interpretation of Atomic (AFM) and Kelvin probe force microscopies (KPFM) data

Joshua C. Walsh and Graham J. Bodwell: Contributed to work and prepared compound 1 shown below in Figure 6.1.

Prof. T. Jane Stockmann: Is the principal investigator of this work, who led the project and contributed to conceptualization, methodology, writing - original draft, validation, supervision, project administration, funding acquisition.

6.2. Introduction

The ITIES, *i.e.*, the liquid|liquid or soft interface, has come under increasing interest as a platform for the growth/synthesis of 2D and 3D molecular[1,2] and nano-structures,[3–7] as well as for electrosynthesis of electrocatalytic materials and conductive polymers[8,9] The Galvani potential difference, *e.g.*, between water|oil (w|o), $\phi_w - \phi_o = \Delta_o^w \phi$, is localized across the interface and controlled with electrodes immersed in either phase positioned relatively far away; thus, this approach is often referred to as 'electrodeless' since electrodes are only indirectly involved. Since the electrodes are not physically or chemically engaged in the electrosynthetic process, one can exploit the pristine, molecularly smooth, defect-free features of the liquid|liquid interface, that lends itself to a high degree of experimental reproducibility. This is advantageous since solid/solution interfaces often carry the risk that morphological features from the solid substrate will be transcribed onto the synthesized

material which can inhibit their ultimate functionality; moreover, the material is often covalently bound to the solid surface complicating its removal and application as a free-standing material. These materials, whether nanoparticle[3,5–7,10] or molecular assemblies[1,2] as well as polymer films,[8,9] have potential use in biomedical, electrocatalytic, and separation science applications.

Early work in externally controlled electropolymerization reactions at liquid|liquid interfaces was performed by Cunnane's group and focused on monomers/electron donors such as 2,2′:5′,2″-terthiophene (TT),[11–14] and functionalized pyrroles.[15] Meanwhile, Mareček's group tested three different modified pyrroles.[16] Similarly, Dryfe's group electrogenerated polypyrrole in the presence of single-walled carbon nanotubes (SWCNTs), which were physically deposited at the liquid|liquid interface, generating a SWCNT/polymer composite material. During this time, electrogeneration of metal nanoparticles (NPs) at soft interfaces was also being explored by Johans *et al.*,[17–20] while Knake *et al.*[21] demonstrated the feasibility of simultaneous Au NP generation and tyramine polymerization at a large ITIES electrosynthesizing a nanocomposite material.

More recently, however, Lehane *et al.*[8] demonstrated the electrosynthesis of poly(3,4-dioxyethylene)thiophene (PEDOT) at a macro liquid|liquid interface (cm scale) between water|*α*,*α*,*α*-trifluorotoluene (w|TFT), using Ce^{4+} as an electron acceptor in the aqueous phase with EDOT dissolved in TFT. They were able to reproducibly electrogenerate films <50 nm thick that could be extracted from the interface, stored for long-term use, and were shown to be biocompatible. Then, our group demonstrated further synthetic control through miniaturization of the ITIES and building on the works for Cunnane and others with simultaneous Au[9] and Cu[22] NP generation and TT electropolymerization. This approach relied on performing the electrosynthesis at a micro-ITIES (25 μm in diameter), while installing the metal salt (e.g., $KAuCl_4$) in the aqueous

phase and TT in 1,2-dichloroethane (DCE). In this way, the large overpotentials thought necessary by Cunnane could be avoided,[14] limiting overoxidation of the film.[23]

Herein, a pyrene skeleton has been functionalized with two dithiafulvenyl (DTF) substituents to create a highly electron-donating molecule, 4,5-didecoxy-1,8-bis(dithiafulven-6-yl)pyrene (**1**, Figure 6-1). Pyrene has become ubiquitous in synthetic, macromolecular, and supramolecular chemistry as a framework on which one can build a wide variety of materials.[24–26] This is enhanced further due to its ready availability industrially as well as owing to its electronic properties. The latter, combined with it being a chromophore have led to pyrenes being active components in organic light emitting diodes (OLEDs) and other organic electronic devices.[26] Similarly, the DTF dimerization mechanism through the formation of a radical cation species is well known and has been employed in the preparation of π-conjugated conductive polymers[27,28] as well as metal NPs.[29] Khadem *et al*.[30] showed that a molecule similar to the bis(DTF)pyrene **1** (see Figure 6-1) was extremely resistant to oxidative coupling despite having two relatively low oxidation potentials at 0.57 and 0.72 V (*vs.* Ag/AgCl) which were attributed to the successive oxidation of the two DTF moieties.

Nevertheless, low dispersity Au nanoclusters (~1.7 nm in diameter) embedded in polymer films were electrosynthesized at a polarizable micro w|DCE interface (25 μm in diameter) through application of **1** as an electron donor dissolved in the DCE phase and $KAuCl_4$ in aqueous. The voltammetric evolution of an electron transfer wave with a concomitant decrease in the signal for $AuCl_4^-$ simple ion transfer with increasing concentration of **1**, c_m, was observed. Films were then ejected from the tip of the micropipette using a syringe attached to the back of the specialized holder and deposited

on Au and glass substrates. Atomic force microscopy (AFM) and Kelvin probe force microscopy (KPFM) were used to image the topography of the nanocomposite film and estimate the film thickness, as well as the change in work function across the material, which is linked to the distribution of Au nanoclusters.

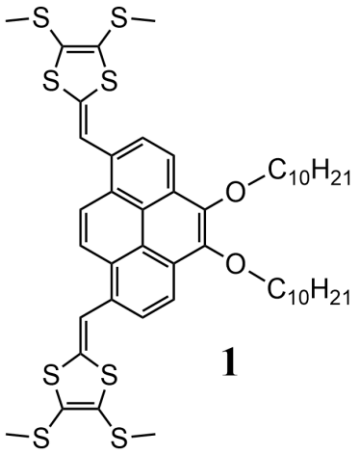

*Figure 6-1 Chemical structure of 4,5-didecoxy-1,8-bis(dithiafulven-6-yl)pyrene (**1**).*

6.3. Experimental

All chemicals were used as received without purification. Potassium tetrachloroaurate ($KAuCl_4$, >98%), hydrochloric acid solution (HCl, >37%), 1,2-dichloroethane (DCE, >98%), trioctylphosphine (97%), trihexyltetradecylphosphonium bromide ($P_{66614}Br$, >95%), and bromooctane (99%) were purchased from Sigma-Aldrich/Merck. Lithium tetrakis(pentafluorophenyl)borate etherate (LiTB, ≥99%) was sourced from Boulder Scientific. The organic phase supporting electrolyte tetraoctylphosphonium tetrakis(pentafluorophenyl)borate ($P_{8888}TB$) and $P_{66614}TB$ (trihexyltetradecylphosphonium tetrakis(pentafluorophenyl)borate) were prepared as described elsewhere.[7,31] Similarly, the preparation of bis(DTF)pyrene **1** has also been reported.[30]

A PG-618-USB potentiostat (Heka Electroniks) was employed to record all electrochemical measurements. The aqueous phase was injected into a micropipette held

inside a specialized holder. The holder was equipped with an integrated Au wire which was immersed in the aqueous phase and connected externally using an SMA connector to the head-stage of the potentiostat serving as the working electrode. The counter/reference electrode was a Pt wire also connected to the head-stage and immersed in the organic phase. The interface between two immiscible electrolyte solutions (ITIES) with a diameter of 25 μm was maintained at the micropipette tip and monitored by a CCD camera (AmScope) attached to a magnifying lens assembly (Navitar). Micropipettes composed of borosilicate glass (Goodfellow Inc.) and modified holder have been described in detail in earlier reports as well as briefly in the Supplementary Information (SI).[32] The electrolytic cells employed throughout have been drawn in Scheme 6-1 and all experiments were performed in a 2-electrode configuration unless indicated otherwise.

$$\mathrm{Au}\left|\mathrm{AuCl_3}\right|\begin{matrix}10\text{ mM HCl}\\ x\text{ mM KAuCl}_4\\ (aq)\end{matrix}\Big\|\begin{matrix}y\text{ mM }\mathbf{1}\\ 5\text{ mM P}_{8888}\text{TB}\\ (DCE)\end{matrix}\Big|\mathrm{PtTB}\Big|\mathrm{Pt} \qquad \text{[Cell 6-1]}$$

$$\mathrm{Au}\left|\mathrm{AuCl_3}\right|\begin{matrix}x\text{ mM KAuCl}_4\\ (aq)\end{matrix}\Big\|\begin{matrix}y\text{ mM }\mathbf{1}\\ 5\text{ mM P}_{8888}\text{TB}\\ (DCE)\end{matrix}\Big|\mathrm{PtTB}\Big|\mathrm{Pt} \qquad \text{[Cell 6-2]}$$

$$\mathrm{Au}\left|\mathrm{AuCl_3}\right|\begin{matrix}5\text{ mM KCl}\\ (aq)\end{matrix}\Big\|\begin{matrix}y\text{ mM }\mathbf{1}\\ 5\text{ mM P}_{8888}\text{TB}\\ (DCE)\end{matrix}\Big|\mathrm{PtTB}\Big|\mathrm{Pt} \qquad \text{[Cell 6-3]}$$

Scheme 6-1 Electrolytic cells where y mM of 1 as the electron donor (see Figure 6-1) was added to the organic phase. Meanwhile, x mM of $KAuCl_4$ (aq) was added to the aqueous phase in Cells 6-1 and 6-2. Tetraoctylphosphonium tetrakis(pentafluorophenyl)borate ($P_{8888}TB$) ionic liquid was employed as the organic phase supporting electrolyte. The double-bars indicate the 25 μm diameter polarizable liquid/liquid interface.

The experimental potential scale was referenced to the Galvani scale using the simple Cl^- transfer, using the formal Cl^- transfer potential $\left(\Delta_o^w\phi_{Cl^-}^{o'}\right)$, –0.479 V, described by Zhou *et al.*[33]

A Tecnai Spirit Transmission Electron Microscope (TEM) was employed to image nanocomposite samples deposited on 2 μm holey Au and 200 mesh Cu TEM grids (Electron Microscopy Sciences). After samples were deposited onto a TEM grid, they were dried under a flow of N_2 gas.

The topography and work function maps were taken using the MFP-3D (AFM/KPFM) from Asylum research equipped with NSC/Pt or NSC35/AL BS tips (MikroMasch) operating at a scan rate of 0.25 Hz for KPFM or AFM topography/scratch test, respectively. The platinum tips' work function was determined using HOPG as a standard.

6.4. Result and discussion

Cyclic voltammograms (CVs) shown in Figure 6-2 were recorded using Cells 6-1, 2, and 3 for the red, black, and blue, dashed traces, respectively, with y = 0 mM in the DCE phase, *i.e.*, no bis(DTF)pyrene **1** added, while 5 mM of $KAuCl_4$ was added to the aqueous phase for Cells 6-1 and 6-2. In each case, the limit of the polarizable potential window (PPW) is described by the large increase in the magnitude of the current at roughly 0.5 and – 0.5 V; whereby, the respective K^+/H^+ and Cl^- supporting electrolyte ions undergo simple ion transfer from water to oil (w→o) and back.[4] The organic phase supporting electrolyte ions, P_{8888}^+ and TB^-, are minor contributors to the PPW limiting signal.[34] The blue, dashed curve depicts the response without $KAuCl_4$ added to the aqueous phase and represents a blank trace. At pH ~5.5 using Cell 6-2 with 5 mM of $KAuCl_4$(aq) (black curve in Figure 6-2), the peak-shaped waves at 0.126 V and – 0.013 V when scanning from positive to negative potentials are due to the simple ion transfer of $AuCl_4^-$ and $AuCl_{(4-\gamma)}(OH)_\gamma^-$ from w→o, respectively. It is recognized that $AuCl_4^-$ undergoes ligand speciation at moderate to high pH forming $AuCl_{(4-\gamma)}(OH)_\gamma^-$ in which γ chlorides have been replaced by hydroxide ligands;

thus, these data are in good agreement with recent reports.[9,10,35–37] The two steady-state waves with half-wave potentials $\left(\Delta_o^w\phi_{1/2}\right)$ at roughly – 0.009 and 0.177 V present during the reverse scan using Cell 6-2 correspond to the respective transfers of $AuCl_{(4-\gamma)}(OH)_\gamma^-$ and $AuCl_4^-$ back from o→w.

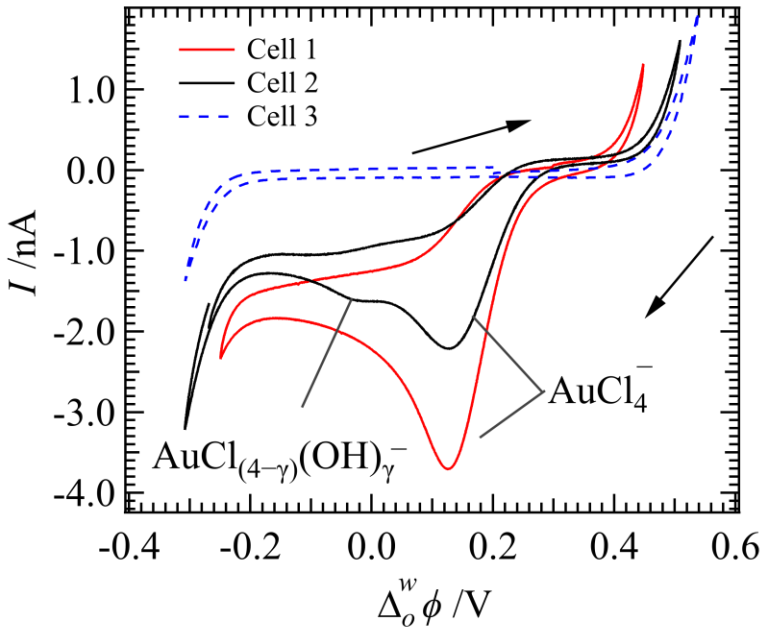

Figure 6-2 Cyclic voltammograms (CVs) recorded using Cells 6-1, 2, and 3 as indicated inset at 0.020 V s^{-1} with 1 = 0 mM in DCE and 5 mM $KAuCl_4$ (aq) in Cells 6-1 and 6-2. Solid black arrows indicate scan direction. Each peak-shaped wave is labeled with the ion undergoing transfer across the ITIES from w⟶o.

At pH 2 in the aqueous phase (red curve in Figure 6-2), only one signal corresponding to $AuCl_4^-$ transfer was observed. The asymmetric *i-V* response between the forward and reverse scan directions is owing to geometric confinement within the micropipette leading to linear and hemispherical diffusion inside and outside of the pipette, respectively; this agrees well with previous studies.[7,38]

Figure 6-3 shows the *i-V* responses for Cells 6-1 and 6-2 with increasing concentrations of **1** (c_m) in DCE and $KAuCl_4$ in the aqueous phase. Only a small amount of **1** added to the DCE phase changes the voltammetric response resulting in a positive peak-shaped wave at potentials greater

than the ion transfer potential for $AuCl_4^-$. For example, in Figure 6-3C using Cell 6-1 with [$KAuCl_4$] = 5 mM, and with increasing c_m, there is a concomitant decrease in the peak intensity for $AuCl_4^-$ ion transfer signal from w→o and the development of a new signal at ~0.35 V. At modest c_m with a [$KAuCl_4$]:[bis(DTF)pyrene] ratio of less than 1:1, but greater than 1:0.5, the *i-V* signal is sigmoidal; however, a ratio of 1:2 results in a peak-shaped wave. The DTF and pyrene core of **1** are both good electron donors; therefore, it is proposed that this is interfacial electron transfer from **1** in oil to $AuCl_4^-/AuCl_{(4-\gamma)}(OH)_\gamma^-$ in water, *i.e.*, a negative charge being transferred from o→w. This agrees well with the transition from sigmoidal to peak-shaped wave, since at low c_m electron transfer would be diffusion limited by **1** in the organic phase; whereby, the electron donor is operating under a hemispherical diffusion regime.[38] Compound **1** is presumably very hydrophobic so unlikely to partition into the aqueous phase. Owing to the high redox potential of $AuCl_4^-$, $E^{o'}_{AuCl_4^-/Au}$ = 1.002 V,[39] the Au salt is likely reduced to Au^0 generating metal nanoparticles (NPs). This agrees well with our recent reports using ferrocene (Fc)[7] and TT[9,22] as organic phase electron donors, as well as Bai *et al.*'s electrosynthesis of Ag wire at a nanopipette interface.[40]

The oxidation potential of **1** was determined by dissolving ~1 mM of the monomer in DCE and recording the CV at a Pt inlaid disc ultramicroelectrode (UME), with a radius of 12.5 μm, and with the potential referenced to the ferrocene redox couple (Fc^+/Fc) as described previously,[41] with $E^{o'}_{Fc^+/Fc}$= 0.64 V (*vs.* SHE).[41] Thus, $E^{o'}_{\mathbf{1}^+/\mathbf{1}}$ was determined to be ~1.6 V (*vs.* SHE). The heterogeneous electron transfer mechanism can be described generally by the following two equations for the system at pH 2 and 5.5-6, respectively,

$$AuCl_4^-(aq) + 3D(org) \rightarrow Au(s) + 3D^{+\bullet}(org) + 4Cl^-(aq) \quad 6\text{-}1$$

$$AuCl_{(4-\gamma)}(OH)_\gamma^-(aq) + \gamma H^+(aq) + 3D(org) \rightarrow Au(s) + 3D^{+\bullet}(org) + (4-\gamma)Cl^-(aq) + \gamma H_2O \quad 6\text{-}2$$

in which, *D* is the electron donor, **1**. Using established analytical solutions[4,42] the approximate electron transfer potential $\left(\Delta_{o}^{w}\phi_{ET}\right)$ can be formulated as,

$$\Delta_{o}^{w}\phi_{ET} \approx E_{\mathbf{1}^{+}/\mathbf{1}}^{o',DCE} - E_{Au(III)/Au}^{o',H_2O} - \frac{(0.059\ V)}{3}\log\left(\left[H^{+}\right]^{\gamma}\right) \qquad 6\text{-}3$$

Since there is no $AuCl_4^-$ speciation at pH 2, the logarithmic term on the right-hand side is ignored in that case. Thus, $\Delta_{o}^{w}\phi_{ET}$ was calculated to be 0.67 and 0.56 V at pH 2 and 5.5-6, respectively, meaning a lower applied potential is needed at moderate pH, which agrees with the voltammetric results and the improved film formation (see below) using Cell 6-2.

To investigate the formation of NPs, aqueous droplets were ejected out of the micropipette after performing 25 consecutive CV cycles, deposited onto a 2 μm holey Au TEM grid, dried with N_2 gas, and imaged (Figure 6-4). Figure 6-4A shows the Au NP/poly-bis(DTF)pyrene composite obtained at pH ~5.5 with [$KAuCl_4$] and c_m equal to 5 and 1 mM, respectively. In this case, the film completely occludes the 2 μm hole in the TEM grid. At pH 2 under otherwise similar conditions, the film was poorly formed (Figure 6-4B). Figure 6-4C shows a magnified section of the image from Figure 6-4A in which the Au nanoclusters can be distinguished; however, these are at the limit of our TEM's resolution. Interestingly, Au nanoclusters are not evenly distributed throughout the film, but rather there are regions with a high density of particles interspersed with areas with few to no particles. It is possible that smaller nanoclusters that are not resolved by our instrument are present in these polymer rich domains; however, this will be the focus of future work.

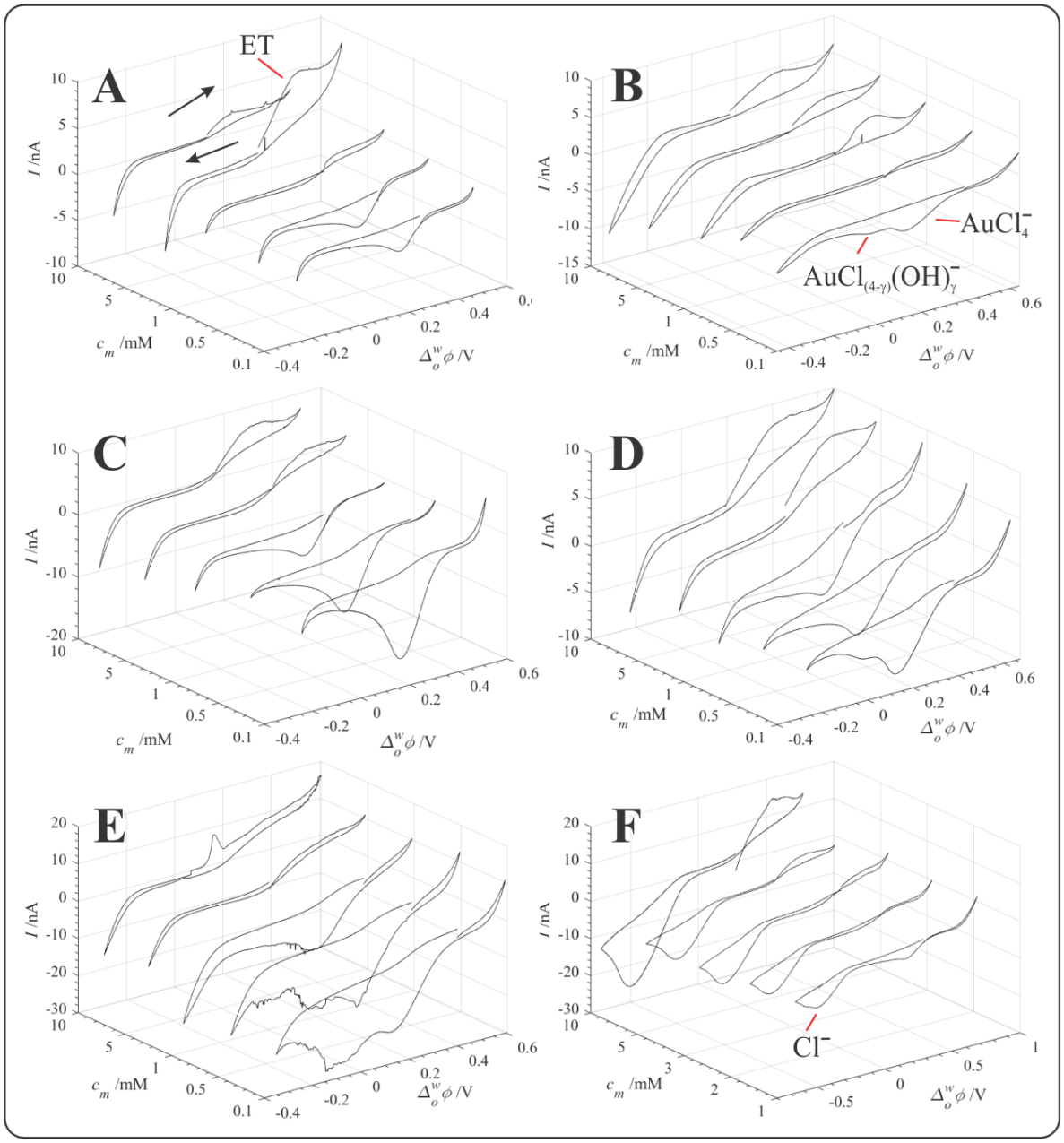

Figure 6-3 Overlay of CVs obtained at a 25 µm diameter micro-ITIES using Cells 6-1 and 6-2 for the left and right-hand columns, with [KAuCl4] or x = 1, 5, and 10 mM for the top, middle, and bottom panels, respectively. While cm was the concentration of 1 (see Figure 6-1) added to the DCE phase. Arrows indicate scan direction, and the CV was swept at a rate of 0.020 V s^{-1}. ET = electron transfer wave; the simple ion transfer signals have been labelled with their associated ions inset.

Moving forward, a shake-flask experiment was used in which a 10 mM solution of $KAuCl_4$ in 500 µL of aqueous phase was combined and mixed with 500 µL of DCE containing 10 mM of **1** and $P_{66614}TB$) in a 2 mL vial, *i.e.*, a large ITIES. Immediately after

shaking, the yellow colour of the $KAuCl_4$ containing aqueous phase disappeared, and the organic phase turned from colourless to black. A 200 mesh Cu TEM grid was immersed and stirred in the solution, then dried and imaged. Figure 6-4D shows the TEM micrograph obtained, in which long polymer strands with embedded Au NPs can be observed. Differentiating individual NPs was difficult and a proper size analysis was not possible; however, they appear to be in the range of 10-20 nm in diameter. These observations, combined with the intermediate hydrophobicity of $AuCl_4^-/AuCl_{(4-\gamma)}(OH)_\gamma^-$, suggest that the Au salt likely partitions into the DCE phase and undergoes homogeneous electron transfer to generate these Au NP coated polymer strands. This mechanism agrees with our recent work at the w|DCE micro interface in which a large negative current offset was observed in the presence of TT, indicating spontaneous $AuCl_4^-/AuCl_{(4-\gamma)}(OH)_\gamma^-$ transfer.[9] Even without mixing, Au NP/poly-bis(DTF)pyrene strands formed in <5 min, suggesting that the bulk, homogeneous organic phase reaction at a large ITIES is rapid and spontaneous. However, these results indicate that by restricting the size of the ITIES and rapidly controlling the potential difference across the interface, one can restrict the reaction to a heterogeneous process and control nanocluster/polymer film formation.

TEM imaged nanoclusters were sized using ImageJ software with data compiled into histograms shown in Figure 6-5(A-F) which were fit using a Gaussian function (red traces). The peak from the Gaussian fitting was taken to be the average nanocluster size and Figure 6-5G depicts a plot of the average diameter with respect to c_m. As c_m increases, there is a concomitant decrease in nanocluster diameter. This is likely owing to an increase in the overall rate of the reaction which in turn likely means faster envelopment of the nanclusters in polymer matrix, limiting their final size.

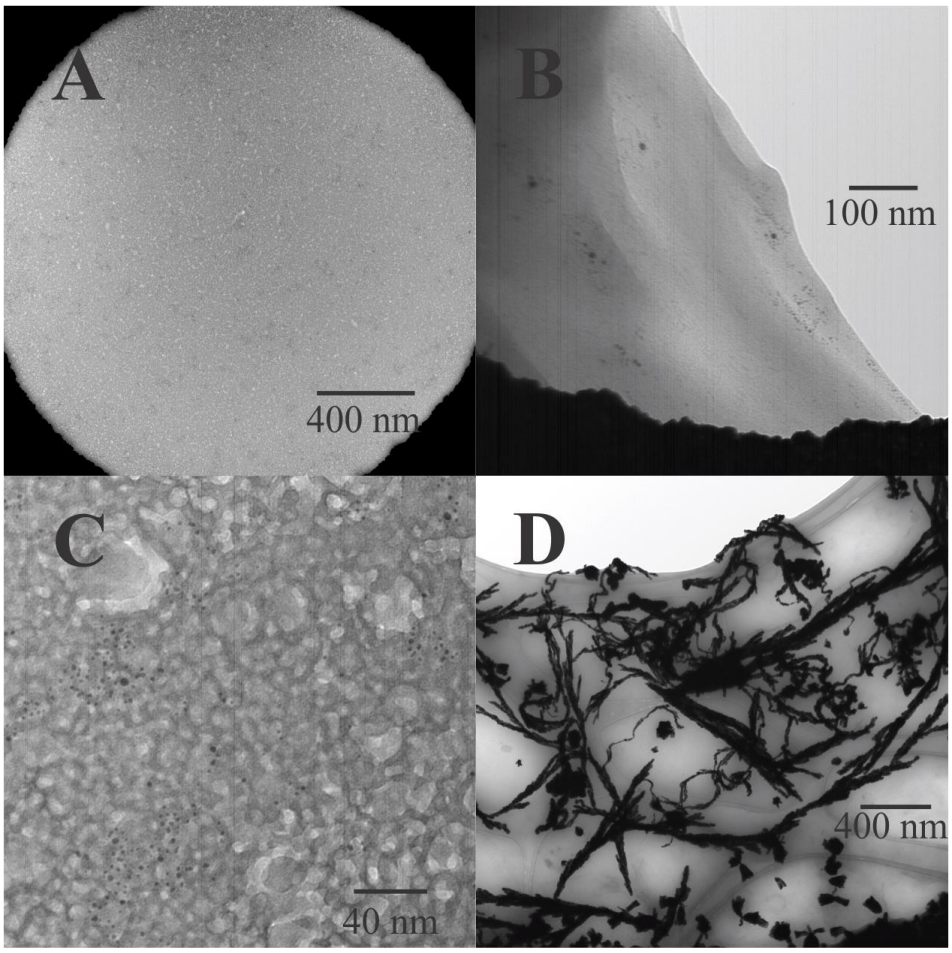

Figure 6-4 TEM micrographs of nanocomposite material generated deposited on 2 µm diameter holey Au TEM grids using Cells 6-2 (left-hand side, A and C) or Cell 6-1 (B), with [$KAuCl_4$] = 5 mM and cm = 1 mM, after 25 CV scans at 0.020 V s^{-1}. (D) Nanocomposite material sampled onto a lacey-carbon 200 mesh Cu TEM grid after a ~5 min shake-flask experiment with 10 mM $KAuCl_4$(aq) combined with a DCE phase containing 10 mM of 1 and 10 mM of $P_{66614}TB$.

Next, Au nanocluster/poly-bis(DTF)pyrene films were similarly prepared and deposited onto glass substrates, then imaged using SEM. A low and high magnification SEM micrograph of the film obtained using Cell 6-1 with [$KAuCl_4$] = 5 mM, c_m = 10 mM, with an aqueous pH = 2, and after performing 25 CV cycles is shown in Figure 6-6A and 6-6B, respectively. The spherical particles dispersed evenly across the films surface are larger Au NPs. Figure 6-6C shows a histogram of the Au NP diameter with a median value of 50 nm. Since the droplet was ejected from the micropipette, the upward facing side of

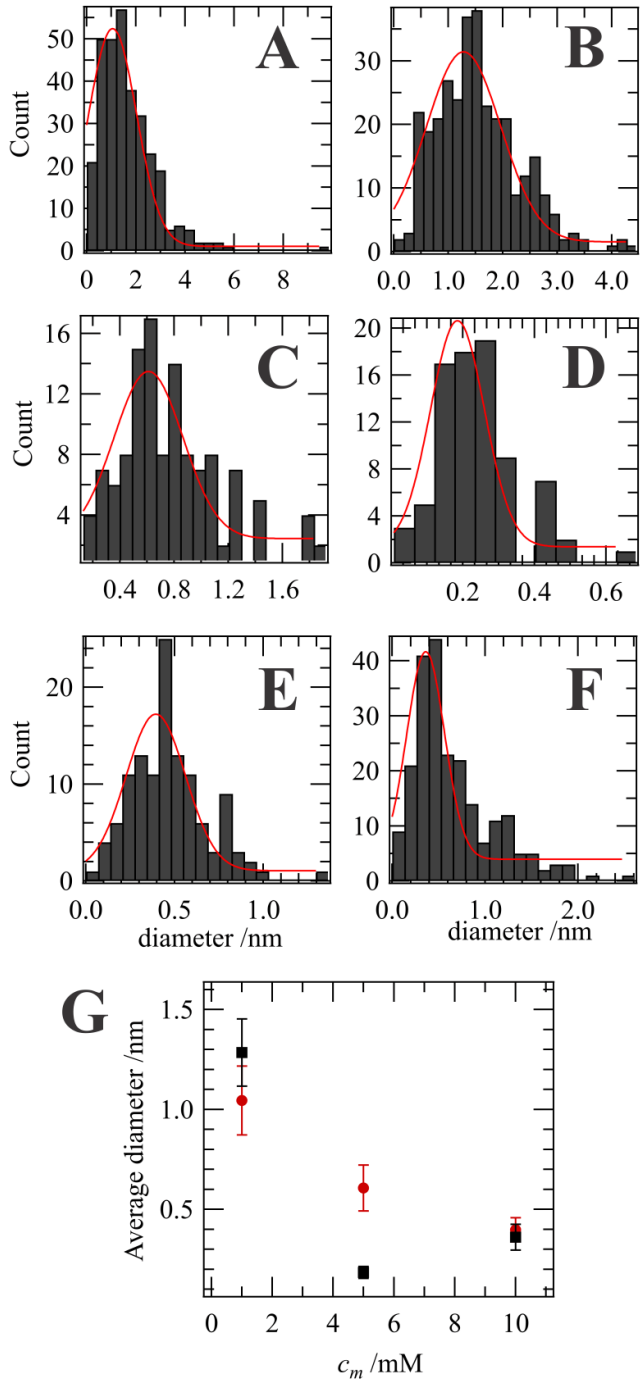

Figure 6-5 Histograms of nanoparticle (NP) diameters obtained from TEM micrographs (see Figure 6-4) using Cell 6-1 (left-hand side) and Cell 6-2 (right-hand side) while increasing cm to 1 (A, B) , 5 (C, D), and 10 mM (E, F); red curves are Gaussian fittings. (G) Trend in the average nanocluster diameter at pH 2 (●) and 5.5-6 (■) with increasing cm; error bars are based on 3 standard deviations.

the Au NP/poly-bis(DTF)pyrene film would be towards the aqueous solution phase. These data are similar to our recent Au NP/poly-TT nanocomposite films;[9] whereby, the NP electrogeneration/electropolymerization process was proposed to occur in stages. Initially, the Au salt and monomer interact directly across the ITIES and the oxidized monomer can act as a capping agent. However, as the polymer film occludes the interface and the film thickness increases, the oxidized monomer no longer has access to the forming NPs. Nevertheless, the polymer is conductive and can mediate electron transfer between the organic and aqueous phases. Thus, Au NPs continue to be generated on the aqueous side; however, since diffusive access of the monomer/capping agent is likely limited by the growing film, these particles are larger on the aqueous side than on the organic one.

When deposited on the glass substrate the film was ~1 mm in diameter and circular. This is several orders of magnitude larger than the ITIES (25 μm in diameter). During electrogeneration, the ITIES was monitored continuously using a CCD camera attached to a magnifying lens assembly and a black film was observed to grow into the aqueous side, up the microchannel. Based on these observations, it is likely that the film folds as it grows and has projections into the water side the interface. This may be owing to the low solubility of the polymer in the aqueous phase and relatively higher solubility in the DCE phase.

Subsequently, films were deposited on conductive Au substrates and analyzed using atomic force microscopy (AFM) as well as in the Kelvin probe force microscopy configuration (KPFM) to measure the topography and surface potential/local work function of the films. In dual-pass, amplitude modulation KPFM mode, the electrostatic force (F_{es}) between the AFM tip and the substrate is related to the externally applied or direct voltage (V_{DC}) and the alternating voltage ($V_{AC}(\omega,t) = V_0\sin(\omega,t)$) by the following relation,[43–45]

$$F_{es}(z,t) = -\frac{1}{2}\frac{\partial C(z)}{\partial z}[(V_{CPD} \pm V_{DC}) + V_0 sin(\omega.t)]^2 \quad 6\text{-}4$$

in which ω is the alternating voltage angular frequency, V_0 is the amplitude of the alternating voltage wavefunction, t is time, and $\partial C(z)/\partial z$ is the capacitance gradient between the tip and sample surface.[43–45] V_{CPD} is the contact potential difference as defined by,

$$V_{CPD} = \frac{\phi_{\text{tip}} - \phi_{\text{sample}}}{-\text{e}_0} \quad 6\text{-}5$$

whereby, ϕ_{tip} and ϕ_{sample} are the work functions of the tip and sample, while e_0 is the elementary electronic charge (1.601×10^{-19} C). Equation 6-4 can be separated into 3 components,[43–45]

$$F_{DC} = -\frac{\partial C(z)}{\partial z}\left[\frac{1}{2}(V_{DC} \pm V_{CPD})^2\right] \quad 6\text{-}6$$

$$F_{\omega} = -\frac{\partial C(z)}{\partial z}(V_{DC} \pm V_{CPD})V_0 sin(\omega, t) \quad 6\text{-}7$$

$$F_{2\omega} = \frac{\partial C(z)}{\partial z}\frac{1}{4}{V_0}^2[cos(2\omega t) - 1] \quad 6\text{-}8$$

F_ω is the relationship employed to measure V_{CPD} in which V_{DC} and V_{AC} are controlled to nullify the affects of the mechanical AFM tip or electrical force oscillations, such that F_ω is a function of only V_{CPD} and V_{AC}; thus, the surface potential or work function values can be extracted.

Figure 6-7 shows KPFM images for Au NP/poly-bis(DTF)pyrene films deposited on Au substrates with work functions varying between 5.03 to 5.34 eV. Average bulk, metallic Au has a work function of ~5.2 eV,[46] while most thiophene incorporated conductive polymer films, *e.g.*, PEDOT:PSS, are in the 4.8-5.6 eV range, which has been shown to be highly dependent on water content and polymer annealing.[47] Khoa *et al*.[48] recently showed a size dependence of Au NPs towards their work function; Au NPs deposited on graphene

oxide demonstrated a decrease in work function from 5.73 to 5.35 eV when transitioning from 40 to 5 nm in size. Thus, the low work function regions within the KPFM images in Figure 6-7, likely correspond to areas dense in Au nanoclusters.

AFM was used to measure the thickness of films deposited on glass slides. A roughly 1 μm × 1 μm area was excavated by the AFM tip to reveal the glass substrate and the area surrounding it scanned. Figure 6-8B shows an example AFM image of a nanocomposite film electrogenerated at the micropipette interface after 25 CV scans and using Cell 6-2 with [$KAuCl_4$] = 5 mM and [TT] 1 mM; whereby, the area labelled 'Well' corresponds to the section physically removed by the AFM tip. Figure 6-8A shows a single line scan moving along the *x*-direction and corresponding to the blue trace in Figure 6-8B. Root-mean-square (RMS) analysis of the noise reveals a sensitivity of ±0.9 nm assuming three standard deviations, while the average distance from the top to the bottom of the Well was considered to be the film thickness. At moderate pH, films were well formed and averaged 3.0 nm thick. However, at pH 2 they were not and only two were successfully sampled. Using Cell 6-1 with [$KAuCl_4$] = 5 mM and [TT] = 1 or 5 mM films were measured to be 139.4 and 1.6 nm, respectively. For the former, it is likely the film was folded in on itself complicating the analysis. The deposition of films onto other substrates, including metal and glassy-carbon electrodes, is ongoing, as well as their spread-ability/wet-ability on different materials; however, this is the focus of future work. Nevertheless, these results are compelling and indicate that extremely thin films with highly accessible nanoclusters are possible with this approach.

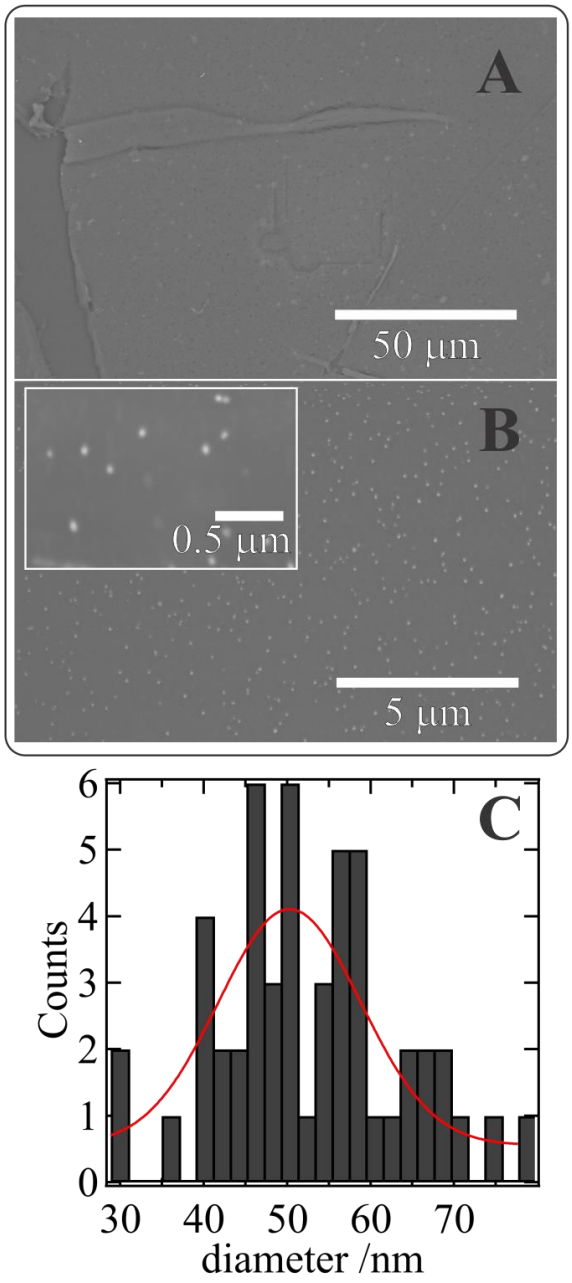

Figure 6-6 SEM image of nanocomposite thin film deposited on a glass slide. Film was electrosynthesized using 25 CV cycles at a micro-ITIES using Cell 6-1 with 5 mM $KAuCl_4$ (aq) and 10 mM 1 (DCE). (B) Magnified section from (A) with, inset, a further increase in the order of magnification. (C) Histogram of Au NP diameters measured from the images shown in panels A and B; red trace is the product of Gaussian curve fitting.

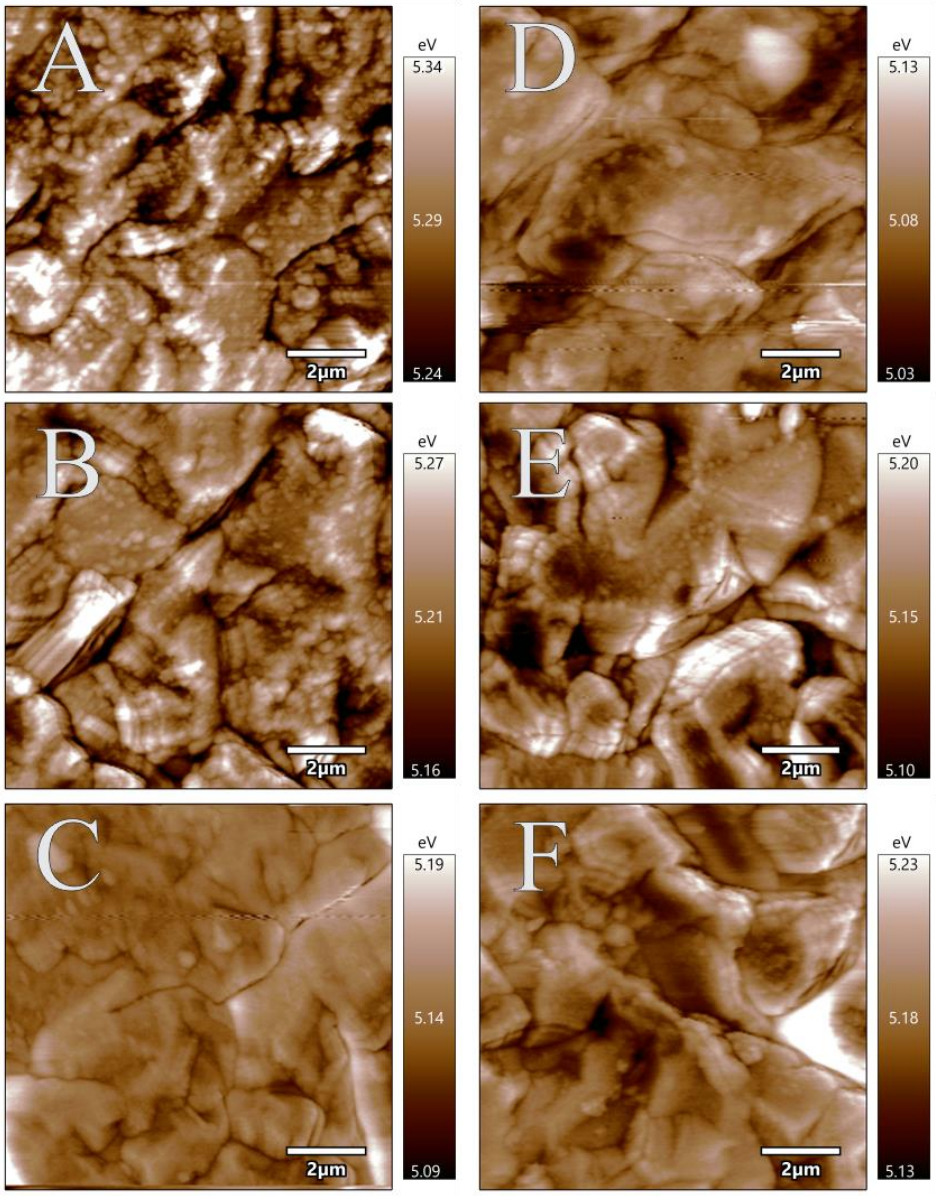

Figure 6-7 Kelvin Probe Force Microscopy (KPFM) images obtained from films developed at a micro-ITIES after 25 CV scans and deposited on a gold substrate using Cells 6-1 (A-C) and 6-2 (D-F) with cm = 1, 5, and 10 mM in DCE for the top, middle, and bottom rows, respectively. Scale bars are in eV.

These results also point to two other phenomena. First, the large area and extremely thin characteristics of the final Au NP/poly-bis(DTF)pyrene film suggest that the film folds into the aqueous side owing to geometric confinement within the microchannel at the pipette tip. Visual observations made using the 12× zoom lens and CCD camera support this in that a dark area extending 25-50 µm up the microchannel was observed. Secondly, since the film is readily broken

apart by ejection from the pipette, the inner glass walls of the microchannel likely act as nucleation sites with the nanocomposite film growing on the walls of the microchannel and along the ITIES, *i.e.*, the film is attached to the glass walls. Thus, this lowers the thermodynamic driving force needed to initiate Au NP generation/electropolymerization, hence the lower observed $\Delta_o^w\phi_{ET}$ versus the calculated value. Herein, we refer to this as the 'frozen pond' mechanism.

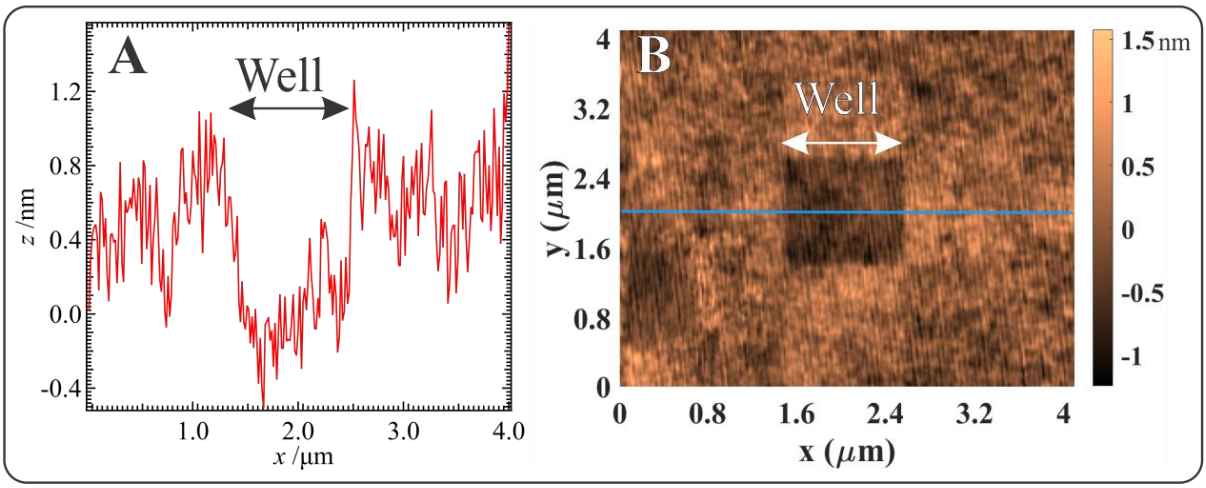

Figure 6-8 (A) Cross-section of AFM topography obtain at a Au NP/poly-bis(DTF)pyrene film electrogenerated at a micro-ITIES after 25 CV cycles using Cell 6-2 with x and y equal to 5 and 1 mM and deposited on a glass substrate. (B) 2-dimensional image of the film in which the blue line corresponds to the line trace from A. The area marked 'Well' was a section of the film excavated by the AFM tip to determine its thickness. The cross-section in A has been baseline corrected to the bottom of the 'Well' for emphasis.

To measure the conductivity of the film, a Pt UME with a radius of 12.5 μm fixed above a 3-axis piezo-motor controlled stage, was brought into contact with Au coated slide with and without film deposited on the surface; Figure 9A and B show the respective *i*–V curves recorded. The film was generated using Cell 6-2 with 5 mM of KCl and $KAuCl_4$ in the aqueous phase and5mMof1in DCE. The CV curve in Figure 9A shows a typical response for a highly conductive material like Au with an ohmic response at roughly− 0.9 V, i.e., $V = iR$. Inverting the axes and using a linear fit of the current between the two plateau regions, one obtains a resistance of ~6Ω. Next, the Au substrate coated with the Au nanocluster/poly-bis(DTF)pyrene composite shows a different *i*–V response which

demonstrates negative resistance that resembles organic tunnel diodes as shown recently for organic semiconductors.[49–52] Nevertheless, performing the ohmic linear curve fitting one obtains a resistance of ~72Ω. Based on this initial *i*–V profile, the film is likely an organic semiconductor; however, more work beyond the scope presented here needs to be done to characterize this property.

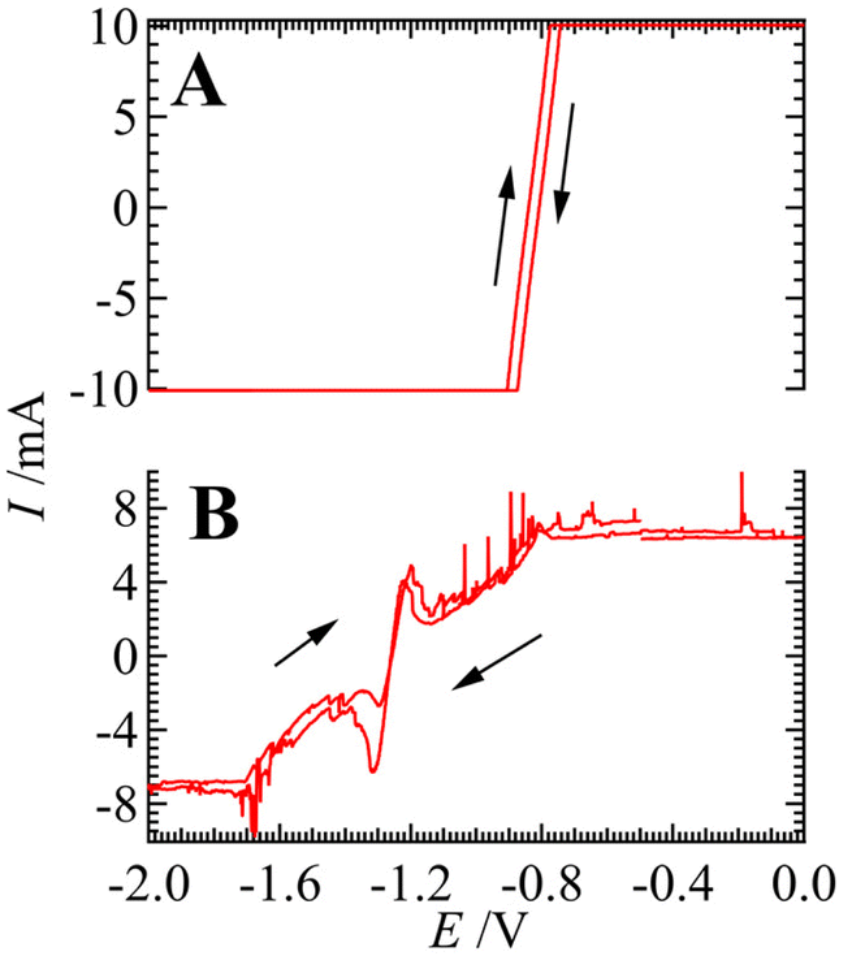

Figure 6-9 i–V response curves for a 25 µm diameter Pt UME in contact with an unmodified Au coated silicon slide (A) and a slide modified withthe Au nanocluster/poly-bis(DTF)pyrenefilm generated using Cell 6-2 (see Scheme 6-1) with 5 mM $KAuCl_4$(aq) and 5 mM 1(DCE) (B).

6.5. Conclusions

Herein, simultaneous, electrochemically controlled Au nanocluster electrogeneration and polymerization of a dithiafulvenyl- substituted pyrene molecule at a micro liquid|liquid interface has been demonstrated. Miniaturization of the ITIES facilitates external electrolytic control of the nanocluster-embedded film that would otherwise proceed via a spontaneous homogeneous reaction in the bulk organic phase. Moreover, the combination of the specialized bis(DTF)pyrene molecule with the micro-ITIES platform permits electrodeless generation of extremely small (<1.7 nm) Au clusters. Altering the pH of the aqueous phase resulted in relatively poor film formation at low pH, while improved film at moderate pH, which agrees with thermodynamic calculations of $\Delta_o^w \phi_{ET}$.

Based on AFM and visual observations the film experiences nucleation at the glass surface along the inner walls of the micropipette and grows across the ITIES surface, similar to ice freezing on a pond. Additionally, the film likely continues to grow even after covering the ITIES, folding up and into the aqueous phase.

The as-prepared films offer a facile strategy for generating low dispersity Au nanocluster embedded conductive polymer films that can be used to modify a variety of substrates for surface enhanced Raman spectroscopy (SERS) or electrocatalysis, as well as a variety of other applications.

6.6. References

(1) Molina-Osorio, A. F.; Yamamoto, S.; Robayo-Molina, I.; Gamero-Quijano, A.; Nagatani, H.; Scanlon, M. D. A Soft on/off Switch Based on the Electrochemically Reversible H-J Interconversion of a Floating Porphyrin Membrane. *Chem. Sci.* **2021**, *12* (30), 10227–10232. https://doi.org/10.1039/d0sc05786j.

(2) Molina-Osorio, A. F.; Manzanares, J. A.; Gamero-Quijano, A.; Scanlon, M. D. Electrochemically Controlled Ion Dynamics in Porphyrin Nanostructures. *J. Phys. Chem. C.* **2020**, *124* (33), 18346–18355. https://doi.org/10.1021/acs.jpcc.0c04976.

(3) al Nasser, H. A.; Kim, C.; Li, Q.; Bissett, M. A.; Haigh, S. J.; Dryfe, R. A. W. The Modified Liquid | Liquid Interface: An Electrochemical Route for the Electrode-Less Synthesis of MoS2 Metal Composite Thin Films. *Electrochim. Acta.* **2022**, *424*, 140609. https://doi.org/10.1016/j.electacta.2022.140609.

(4) Scanlon, M. D.; Smirnov, E.; Stockmann, T. J.; Peljo, P. Gold Nanofilms at Liquid-Liquid Interfaces: An Emerging Platform for Redox Electrocatalysis, Nanoplasmonic Sensors, and Electrovariable Optics. *Chem. Rev.* **2018**, *118* (7), 3722–3751. https://doi.org/10.1021/acs.chemrev.7b00595.

(5) Smirnov, E.; Peljo, P.; Scanlon, M. D.; Girault, H. H. Interfacial Redox Catalysis on Gold Nanofilms at Soft Interfaces. *ACS. Nano.* **2015**, *9* (6), 6565–6575. https://doi.org/10.1021/acsnano.5b02547.

(6) Smirnov, E.; Scanlon, M. D.; Momotenko, D.; Vrubel, H.; Méndez, M. A.; Brevet, P. F.; Girault, H. H. Gold Metal Liquid-like Droplets. *ACS. Nano.* **2014**, *8* (9), 9471–9481. https://doi.org/10.1021/nn503644v.

(7) Moshrefi, R.; Suryawanshi, A.; Stockmann, T. J. Electrochemically Controlled Au Nanoparticle Nucleation at a Micro Liquid | Liquid Interface Using Ferrocene as Reducing Agent. *Electrochem. Commun.* **2021**, *122*, 106894. https://doi.org/10.1016/j.elecom.2020.106894.

(8) Lehane, R. A.; Gamero-Quijano, A.; Malijauskaite, S.; Holzinger, A.; Conroy, M.; Laffir, F.; Kumar, A.; Bangert, U.; McGourty, K.; Scanlon, M. D. Electrosynthesis of Biocompatible Free-

Standing PEDOT Thin Films at a Polarized Liquid|Liquid Interface. *J. Am. Chem. Soc.* **2022**, *144* (11), 4853–4862. https://doi.org/10.1021/jacs.1c12373.

(9) Moshrefi, R.; P. Connors, E.; Merschrod, E.; Stockmann, T. J. Simultaneous Electropolymerization/Au Nanoparticle Generation at an Electrified Liquid | Liquid Micro-Interface. *Electrochim. Acta.* **2022**, *426*, 140749. https://doi.org/10.1016/j.electacta.2022.140749.

(10) Uehara, A.; Booth, S. G.; Chang, S. Y.; Schroeder, S. L. M.; Imai, T.; Hashimoto, T.; Mosselmans, J. F. W.; Dryfe, R. A. W. Electrochemical Insight into the Brust-Schiffrin Synthesis of Au Nanoparticles. *J. Am. Chem. Soc.* **2015**, *137* (48), 15135–15144. https://doi.org/10.1021/jacs.5b07825.

(11) Evans-Kennedy, U.; Clohessy, J.; Cunnane, V. J. Spectroelectrochemical Study of 2,2′:5′,2″-Terthiophene Polymerization at a Liquid | Liquid Interface Controlled by Potential-Determining Ions. *Macromolecules.* **2004**, *37* (10), 3630–3634. https://doi.org/10.1021/ma0348223.

(12) Gorgy, K.; Fusalba, F.; Evans, U.; Kontturi, K.; Cunnane, V. J. Electropolymerization of 2,2′:5′,2″ Terthiophene at an Electrified Liquid-Liquid Interface. *Synth. Met.* **2001**, *125* (3), 365–373. https://doi.org/10.1016/S0379-6779(01)00474-X.

(13) Vignali, M.; Edwards, R.; Cunnane, V. J. Characterization of Doping and Electropolymerization of Free Standing Films of Polyterthiophene. *J. Electroanal. Chem.* **2006**, *592* (1), 37–45. https://doi.org/10.1016/j.jelechem.2006.04.020.

(14) Vignali, M.; Edwards, R. A. H.; Serantoni, M.; Cunnane, V. J. Electropolymerized Polythiophene Layer Extracted from the Interface between Two Immiscible Electrolyte Solutions: Current–Time Analysis. *J. Electroanal. Chem.* **2006**, *591* (1), 59–68. https://doi.org/10.1016/j.jelechem.2006.03.033.

(15) Cunnane, V. J.; Evans, U. Formation of Oligomers of Methyl- and Phenyl-Pyrrole at an Electrified Liquid | Liquid Interface. *Chem. Commun.* **1998**, No. 19, 2163–2164. https://doi.org/10.1039/a806365f.

(16) Maeda, K.; Jänchenová, H.; Lhotský, A.; Stibor, I.; Budka, J.; Mareček, V. Formation of a Polymer Layer from Monomers Adsorbed at a Liquid | Liquid Interface. *J. Electroanal. Chem.* **2001**, *516* (1–2), 103–109. https://doi.org/10.1016/S0022-0728(01)00658-1.

(17) Johans, C.; Liljeroth, P.; Kontturi, K. Electrodeposition at Polarisable Liquid|liquid Interfaces: The Role of Interfacial Tension on Nucleation Kinetics. In *Phys. Chem. Chem. Phys.* **2002**. 4, 1067–1071. https://doi.org/10.1039/b110182j.

(18) Johans, C.; Kontturi, K.; Schiffrin, D. J. Nucleation at Liquid \ Liquid Interfaces: Galvanostatic Study. *J. Electroanal. Chem.* **2002**, *526* (1–2), 29–35. https://doi.org/10.1016/S0022-0728(02)00763-5.

(19) Johans, C.; Clohessy, J.; Fantini, S.; Kontturi, K.; Cunnane, V. J. Electrosynthesis of Polyphenylpyrrole Coated Silver Particles at a Liquid-Liquid Interface. *Electrochem. Commun.* **2002**, *4* (3), 227–230. https://doi.org/10.1016/S1388-2481(02)00256-4.

(20) Johans, C.; Lahtinen, R.; Kontturi, K.; Schiffrin, D. J. Nucleation at Liquid|liquid Interfaces: Electrodeposition without Electrodes. *J. Electroanal. Chem.* **2000**, *488* (2), 99–109. https://doi.org/10.1016/S0022-0728(00)00185-6.

(21) Knake, R.; Fahmi, A. W.; Tofail, S. A. M.; Clohessy, J.; Mihov, M.; Cunnane, V. J. Electrochemical Nucleation of Gold Nanoparticles in a Polymer Film at a Liquid-Liquid Interface. *Langmuir.* **2005**, *21* (3), 1001–1008. https://doi.org/10.1021/la048277q.

(22) Moshrefi, R.; Przybyła, H.; Stockmann, T. J. Simultaneous Electro-Generation/Polymerization of Cu Nanocluster Embedded Conductive Poly(2,2′:5′,2″-Terthiophene) Films at Micro and Macro Liquid | Liquid Interfaces. *Sci. Rep.* **2023**, *13* (1), 1201. https://doi.org/10.1038/s41598-023-28391-9.

(23) Barsch, U.; Beck, F. Anodic Overoxidation of Polythiophenes in Wet Acetonitrile Electrolytes. *Electrochim. Acta.* **1996**, *41* (11–12), 1761–1771. https://doi.org/10.1016/0013-4686(95)00493-9.

(24) Ghasemabadi, P. G.; Yao, T.; Bodwell, G. J. Cyclophanes Containing Large Polycyclic Aromatic Hydrocarbons. *Chem. Soc. Rev.,* **2015**, 44, 6494–6518. https://doi.org/10.1039/c5cs00274e.

(25) Mateo-Alonso, A. Pyrene-Fused Pyrazaacenes: From Small Molecules to Nanoribbons. *Chem. Soc. Rev*. **2014**, 43, 6311–6324. https://doi.org/10.1039/c4cs00119b.

(26) Figueira-Duarte, T. M.; Müllen, K. Pyrene-Based Materials for Organic Electronics. *Chem. Rev*., **2011**, 111, 7260–7314. https://doi.org/10.1021/cr100428a.

(27) Khadem, M.; Zhao, Y. Tetrathiafulvalene Vinylogue-Fluorene Co-Oligomers: Synthesis, Properties, and Supramoleclar Interactions with Carbon Nanotubes. *J. Org. Chem.* **2015**, *80* (15), 7419–7429. https://doi.org/10.1021/acs.joc.5b00792.

(28) Liang, S.; Zhao, Y.; Adronov, A. Selective and Reversible Noncovalent Functionalization of Single-Walled Carbon Nanotubes by a PH-Responsive Vinylogous Tetrathiafulvalene-Fluorene Copolymer. *J. Am. Chem. Soc.* **2014**, *136* (3), 970–977. https://doi.org/10.1021/ja409918n.

(29) Adows, H.; Zhao, Y. Redox Interactions of Au(III) with Carboxylated Dithiafulvenes and Tetrathiafulvalene Analogues in Polar Organic Media. *Chem. Commun.* **2016**, *52* (89), 13101–13104. https://doi.org/10.1039/c6cc07769b.

(30) Khadem, M.; Walsh, J. C.; Bodwell, G. J.; Zhao, Y. A Macrocyclization of 1,8-Bis(Dithiafulvenyl)Pyrenes. *Org. Lett.* **2016**, *18* (10), 2403–2406. https://doi.org/10.1021/acs.orglett.6b00894.

(31) Stockmann, T. J.; Ding, Z. Tetraoctylphosphonium Tetrakis(Pentafluorophenyl)Borate Room Temperature Ionic Liquid toward Enhanced Physicochemical Properties for Electrochemistry. *J. Phys. Chem. B.* **2012**, *116* (42), 12826–12834. https://doi.org/10.1021/jp3081832.

(32) Stockmann, T. J.; Montgomery, A.-M.; Ding, Z. Formal Transfer Potentials of Strontium and Uranyl Ions at Water|1,2-Dichloroethane Interfaces. *Can. J. Chem.* **2012**, *90* (10), 836–842. https://doi.org/10.1139/v2012-068.

(33) Zhou, M.; Gan, S.; Zhong, L.; Dong, X.; Ulstrup, J.; Han, D.; Niu, L. Improvement in the Assessment of Direct and Facilitated Ion Transfers by Electrochemically Induced Redox Transformations of Common Molecular Probes. *Phys. Chem. Chem. Phys.* **2012**, *14* (10), 3659–3668. https://doi.org/10.1039/c2cp23184k.

(34) Stockmann, T. J.; Guterman, R.; Ragogna, P. J.; Ding, Z. Trends in Hydrophilicity/Lipophilicity of Phosphonium Ionic Liquids As Determined by Ion-Transfer Electrochemistry. *Langmuir.* **2016**, *32* (49), 12966–12974. https://doi.org/10.1021/acs.langmuir.6b03031.

(35) Luty-Błocho, M.; Pacławski, K.; Wojnicki, M.; Fitzner, K. The Kinetics of Redox Reaction of Gold(III) Chloride Complex Ions with l-Ascorbic Acid. *Inorg. Chim. Acta.* **2013**, *395*, 189–196. https://doi.org/10.1016/j.ica.2012.10.031.

(36) Luty-Błocho, M.; Wojnicki, M.; Fitzner, K. Gold Nanoparticles Formation via Au(III) Complex Ions Reduction with l-Ascorbic Acid. *Int. J. Chem. Kinet.* **2017**, *49* (11), 789–797. https://doi.org/10.1002/kin.21115.

(37) Uehara, A.; Chang, S.-Y.; Booth, S. G.; Schroeder, S. L. M.; Mosselmans, J. F. W.; Dryfe, R. A. W. Redox and Ligand Exchange during the Reaction of Tetrachloroaurate with Hexacyanoferrate(II) at a Liquid-Liquid Interface: Voltammetry and X-Ray Absorption Fine-Structure Studies. *Electrochim. Acta.* **2016**, *190*, 997–1006. https://doi.org/10.1016/j.electacta.2015.12.108.

(38) Liu, S.; Li, Q.; Shao, Y. Electrochemistry at Micro- and Nanoscopic Liquid | Liquid Interfaces. *Chem. Soc. Rev.* **2011**, *40* (5), 2236–2253. https://doi.org/10.1039/c0cs00168f.

(39) Vanýsek, P.; Haynes, W. M. Electrochemical Series, Ed. CRC Handbook of. Chemistry and Physics, *CRC Press/Taylor,* Boca Raton, FL **2021**, No. 2, 8.20-25.29.

(40) Bai, S.; Liu, C.; Wang, L. Confined Synthesis of Silver Wire at the Nanopipette-Liquid | Liquid Interface. *Langmuir.* **2021**, *37* (36), 10741–10749. https://doi.org/10.1021/acs.langmuir.1c01394.

(41) Moshrefi, R.; Stockmann, T. J. Electrodeless Synthesis of Low Dispersity Au Nanoparticles and Nanoclusters at an Immiscible Micro Water | Ionic Liquid Interface. *Nanomaterials.* **2022**, *12* (16), 2748. https://doi.org/10.3390/nano12162748.

(42) Méndez, M. A.; Partovi-Nia, R.; Hatay, I.; Su, B.; Ge, P.; Olaya, A.; Younan, N.; Hojeij, M.; Girault, H. H. Molecular Electrocatalysis at Soft Interfaces. *Phys. Chem. Chem. Phys.* **2010**, *12* (46), 15163–15171. https://doi.org/10.1039/c0cp00590h.

(43) Melitz, W.; Shen, J.; Kummel, A. C.; Lee, S. Kelvin Probe Force Microscopy and Its Application. *Surf. Sci. Rep*. **2011**, 66, 1–27. https://doi.org/10.1016/j.surfrep.2010.10.001.

(44) Panchal, V.; Pearce, R.; Yakimova, R.; Tzalenchuk, A.; Kazakova, O. Standardization of Surface Potential Measurements of Graphene Domains. *Sci. Rep.* **2013**, *3*, 2597. https://doi.org/10.1038/srep02597.

(45) Liu, L.; Li, G. Electrical Characterization of Single-Walled Carbon Nanotubes in Organic Solar Cells by Kelvin Probe Force Microscopy. *Appl. Phys. Lett.* **2010**, *96* (8), 083302. https://doi.org/10.1063/1.3332489.

(46) J. R. Rumble. CRC Handbook of Chemistry and Physics; *CRC Press/Taylor & Francis*: Boca Raton, FL, 2022.

(47) Koch, N.; Vollmer, A.; Elschner, A. Influence of Water on the Work Function of Conducting Poly(3,4- Ethylenedioxythiophene)/Poly(Styrenesulfonate). *Appl. Phys. Lett.* **2007**, *90* (4), 043512. https://doi.org/10.1063/1.2435350.

(48) Khoa, N. T.; Kim, S. W.; Yoo, D. H.; Kim, E. J.; Hahn, S. H. Size-Dependent Work Function and Catalytic Performance of Gold Nanoparticles Decorated Graphene Oxide Sheets. *Appl. Catal. A,* **2014**, *469*, 159–164. https://doi.org/10.1016/j.apcata.2013.08.046.

(49) S, R.; Dhar, R.; Dutta, S.; Ray, D. Intra-Device Gating Effect in Graphene Electrode-Based Organic Diodes. *Org. Electron.* **2022**, *101*, 106399. https://doi.org/10.1016/j.orgel.2021.106399.

(50) Conti, S.; Martínez-Domingo, C.; Lay, M.; Terés, L.; Vilaseca, F.; Ramon, E. Nanopaper-Based Organic Inkjet-Printed Diodes. *Adv. Mater. Technol.* **2020**, *5* (6), 1900773. https://doi.org/10.1002/admt.201900773.

(51) Cao, M.; Hyun, W. J.; Francis, L. F.; Frisbie, C. D. Inkjet-Printed, Self-Aligned Organic Schottky Diodes on Imprinted Plastic Substrates. *Flexible and Printed Electronics* **2020**, *5* (1), 015006. https://doi.org/10.1088/2058-8585/ab670a.

(52) Viola, F. A.; Brigante, B.; Colpani, P.; Dell'Erba, G.; Mattoli, V.; Natali, D.; Caironi, M. A 13.56 MHz Rectifier Based on Fully Inkjet Printed Organic Diodes. *Adv. Mater.* **2020**, *32* (33). https://doi.org/10.1002/adma.202002329.

Chapter 7

7. Conclusions and Perspectives

The objective of this thesis was to investigate heterogeneous electropolymerization at an immiscible liquid|liquid micro-interface and generate a free-standing, thin film by dissolving a monomer as electron donor in an organic phase and a metal salt as an electron acceptor in an aqueous phase. The research program aimed to comprehend the HET (heterogeneous electron transfer) mechanisms at the interface that lead to the development of oligomers and nanoparticles, as well as investigate the mass transport processes that support HET. Additionally, the research sought to examine the alterations of the ITIES (interface between two immiscible electrolyte solutions) characteristics as oligomers and nanoparticles deposit at the interface.

In the first phase, we sought to fine-tune the size, shape, and uniformity of the nanoparticles formed at an electrified interface. This was achieved through the use of ferrocene (Fc) as an electron donor in the organic phase, and $KAuCl_4$ dissolved in the aqueous phase, as detailed in Chapter 2. The calculation for HET potential between Fc and $KAuCl_4$ revealed that it was not spontaneous, indicating the need for an external electrical field to induce the reaction. Interestingly, the pH of the solution was identified as a crucial factor in controlling the size and shape of the resulting NPs by influencing the interaction between Fc and hydroxide anions, with ferrocenium acting as a capping agent during NP formation. As the ferrocenium cations get shielded at higher pH values, leading to reduced stabilization of the forming Au NPs and an increase in their size. In addition, the results revealed that the partition of ferrocene into the aqueous phase, which is thermodynamically favored, constitutes a competing reaction pathway in

the absence of an external electrical field. This mechanism resulted in the formation of particles with random shapes and sizes.

To minimize the partitioning of the electron donor into the aqueous phase during the reaction between Fc and $KAuCl_4$, a ferrocenyl moiety that was linked to the phosphonium core by an acyl chain was used instead of the Fc in the system, as discussed in Chapter 3. This allowed the investigation of the efficacy of a more hydrophobic electron donor. Electrochemical analyses demonstrated that, while the modified ferrocene prevented the partitioning of the electron donor, it also drew tetrachloroaurate into the organic phase, creating an alternative reaction pathway. To limit electron transfer only to HET-type, DCE was substituted with an ionic liquid (IL), which also took advantage of the supramolecular fluidic microenvironment of the IL. TEM images of droplets extracted from the aqueous phase revealed that such conditions lead to favoring the formation of Au nanoclusters with a diameter of less than 1.7 nm.

The next step involved the use of terthiophene (TT) as the electron donor and monomer for the formation of a nanocomposite thin film at the w|DCE interface, as discussed in Chapter 4. Cyclic voltammograms showed a HET wave in positive potentials, but calculations demonstrated that the HET reaction between TT and tetrachloroaurate was not spontaneous. TEM and AFM images provided evidence of a growth mechanism in which early Au NPs were small, <2 nm in diameter, and TT acted as a capping agent that then transitioned into a period where the ITIES was covered in the nanocomposite material, such that TT did not have access to the aqueous phase. In the later stages of electrogeneration, the Au NPs were allowed to grow larger, >10 nm in diameter, since coverage by poly-TT did not impede their growth. Cyclic voltammetric, TEM, and EIS results indicated that a proton acceptor was necessary to facilitate $TT^{+\bullet}$, radical cation coupling; therefore, neutral to basic pH regimes, >5.5, were needed to enhance electropolymerization at the

liquid|liquid interface. AFM contact analysis indicated that after 25 cycles, the film was ~0.4 μm thick.

As a further step, the feasibility of using a metal with a lower oxidation potential to form a nanocomposite thin film at an ITIES was investigated, in this case Cu. Furthermore, the impact of the size of the interface on the properties of the resulting nanocomposite films was investigated. In Chapter 5, it was reported that the micro-ITIES displayed a well-resolved electron transfer wave when the concentration of TT was 20 mM, due to lower uncompensated IR-drop when using the micro-interface, while the large-ITIES exhibited a more complex CV profile that included anionic doping and de-doping of the forming films at ITIES. The calculated or theoretical HET potential at various monomer concentrations indicated that increasing the monomer concentration would decrease the applied potential required, which was ultimately supported experimentally. Impedance data confirmed that a 2D film covered most of the interface in less than 6 minutes at 20 mM of terthiophene, which later acts as a bipolar electrode facilitating HET at the interface and 3D growth of the film in organic and aqueous side of the ITIES follows. Preliminary voltammetric results on a GC electrode modified with the Cu NP/poly-TT film electrogenerated at a 1.16 mm diameter interface showed a more than 2-fold increase in the electrocatalytic CO_2 reduction current compared to an unmodified electrode. However, a more comprehensive study is required to completely understand the performance of the formed film at different sizes while keeping the surface coverage and film deposition parameters optimized and comparable. Additionally, the morphology of the nanocomposite film underwent significant changes for films formed at 25 μm and 1.16 mm diameter interfaces, which may indicate that further optimization of nanocomposite electrosynthesis is necessary, or the films were overloaded due to an improper balance between the size of the films and the applied potential.

In the final phase, described in Chapter 6, the impact of monomer chemistry was examined. Specifically, a larger conjugated monomer was employed in the DCE phase to enable creating a free-standing thin film through the simultaneous electrogeneration of Au nanoclusters and polymerization of a dithiafulvenyl-substituted pyrene molecule (bis(DTF)pyrene) at a micro liquid|liquid interface. Using bis(DTF)pyrene with the micro-ITIES platform, we were able to generate extremely small Au clusters (<1.7 nm), indicating rapid polymerization and subsequent fast deposition of the formed oligomers at the ITIES. The nanocomposite films exhibited highly conductive properties and displayed negative resistance behavior within the range of –1.4 V to –1.1 V, opening up exciting new research avenues with many potential applications in electronic technology.

Controlling mass transfer is essential for manipulating the properties of forming nanocomposite thin films.[1–3] Our research confirms that using a micro-interface in combination with an external electrical field provides superior control over mass transfer.[4–8] This is due to the small uncompensated IR drop in a micro-interface, which enables more efficient potential control. Additionally, micro-interfaces provide greater insight into the mechanisms of reactions at an electrified interface than previous studies at larger interfaces.[2,9–11] Our work has revealed that the kinetics of polymerization reactions are significantly affected by the pH of the aqueous medium, with high pH promoting faster reaction rates; while most previous studies relied on the use of the ceric(IV)/cerous(III) sulfate redox couple in the aqueous phase, that requires an extremely low pH to ensure this salt is solubilized.[1,10,12–14] By adjusting the external electrical field, reactant concentration, and aqueous phase pH, a specific polymerization reaction pathway can be favored, and the mechanism of film formation can be directed towards either gradual or instantaneous deposition. Furthermore, the nature of the non-aqueous phase strongly affects the film deposition

mechanism and limiting reaction pathway at the interface, as shown in our preliminary results. To fully understand the effect of the non-aqueous phase, further studies are necessary. EIS studies shed more light on how the double layer structure changes at an electrified interface as the film begins to form at the interface, and it can be used as a powerful tool for monitoring film growth at an ITIES. While our preliminary results suggest that film formation is faster at the interface when the solubility of forming oligomers is limited in the non-aqueous phase, and the reaction pathway is limited to HET when the solubility of reactants is limited in the opposite phase, more research is needed to draw definitive conclusions about the effect of non-aqueous phases on the polymerization process at an electrified interface.

This work presents valuable physical insights into the fundamental principles of electrodeless synthesis of materials and introduces a novel approach to controlling the formation and morphology of nanocomposite thin films. The controllable reaction conditions and reproducibility of the method make it highly suitable for industrial applications. The ability to manipulate the electrical and mechanical properties of nanocomposite thin films is crucial for their extensive use in biomedical and catalytic fields. However, the findings presented herein also indicate the potential challenge of achieving uniform film formation using this approach. As the film grows and covers the interface, the mobility of monomers and metal ions decreases, and the film will evolve into a 3D Janus-type film. To prevent such issues, channels can be created in the film structure, by employing charged particles that can be pushed and pulled based on applied external potential, thus promoting the formation of a uniform film.

Future research will likely be anticipated to employ the chronoamperometry technique[15] to investigate the influence of applied potential on the characteristics of the developing film, including molecular structure, molar mass distribution, tacticity, and chain topology. Exploring

the manipulation of monomer chemistry to decrease oxidation potential,[8,16] incorporating functional groups to enhance the film's selectivity and sensitivity towards specific analytes,[17] and utilizing functional groups to enhance the film's mechanical stability through crosslinking[18] are promising avenues for exploration. Furthermore, the copolymerization of diverse monomers with precise monomer sequence control, particularly in the case of condensative chain-growth, may be feasible by applying positive and negative potentials to oxidize and reduce electroactive monomers,[19,20] as highlighted in the introduction with regard to organic thin film transistors.

The polymerization process can be influenced by the characteristics of non-aqueous solvents,[15,21] as the interaction between molecules and solvents governs molecular mobility and thereby affects reaction kinetics. Moreover, the nature of the interface formed between the aqueous and non-aqueous phases plays a direct role in determining the reaction mechanism by favoring specific pathways and reducing associated activation barriers. The presence of supporting electrolytes stabilizes intermediate products, and it will be crucial for future research to evaluate their impact on the overall electropolymerization process.[15]

Preliminary studies have revealed the potential inclusion of platinum and iron oxide nanoparticles, as well as copper and gold nanoparticles, within nanocomposite thin films. Platinum NPs are highly interesting due to their exceptional electrocatalytic properties. They exhibit excellent catalytic activity for various important reactions, such as oxygen reduction,[22] hydrogen evolution,[23] and carbon monoxide oxidation.[24] Iron oxide nanoparticles, on the other hand, offer distinct magnetic properties and exhibit excellent biocompatibility, making them particularly valuable for biomedical applications.[25] Their surface can be modified with diverse molecules to enhance stability, biocompatibility, and targeted functionality, rendering them suitable for use in biocompatible electrodes for Parkinson's disease treatment. Furthermore, iron oxide nanoparticles

possess catalytic properties relevant to environmental remediation, including CO_2 reduction,[26] water treatment[27] and pollutant degradation.[28] In addition to exploring the chemistry of individual metals, alloy deposition of metal nanoparticles at ITIES[29] has demonstrated feasibility and represents a means to finely adjust and optimize the properties of nanocomposite thin films for specific purposes.

Gaining a comprehensive understanding of the fundamental physical and chemical processes involved in interfacial polymerization is crucial for advancing the field. Therefore, the incorporation of microscopic and spectroscopic tools to effectively analyze reaction products and potentially intermediates, ideally with atomic resolution, becomes imperative. Moreover, the integration of in-situ spectroscopic techniques in conjunction with electrochemical methods, particularly electrochemical impedance spectroscopy (EIS), will be essential for a thorough investigation of reaction kinetics and a deeper comprehension of the mechanisms governing the formation of nanocomposite thin films. A key aspect will involve the adjustment of monomer and metal salt concentrations, as well as the inclusion of other additives, to precisely tailor the properties of the films to meet specific requirements. The technique's notable feature lies in the potential for continuous feeding of initial reactants and continuous removal of final products.

7.1. References

(1) Evans-Kennedy, U.; Clohessy, J.; Cunnane, V. J. Spectroelectrochemical Study of 2,2′:5′,2″-Terthiophene Polymerization at a Liquid/Liquid Interface Controlled by Potential-Determining Ions. *Macromolecules.* **2004**, *37* (10), 3630–3634. https://doi.org/10.1021/ma0348223.

(2) Cunnane, V. J.; Evans, U. Formation of Oligomers of Methyl- and Phenyl-Pyrrole at an Electrified Liquid|Liquid Interface. *ChemComm.* **1998**, *19*, 2163–2164. https://doi.org/10.1039/a806365f.

(3) Robayo-Molina, I.; Molina-Osorio, A. F.; Guinane, L.; Tofail, S. A. M.; Scanlon, M. D. Pathway Complexity in Supramolecular Porphyrin Self-Assembly at an Immiscible Liquid–Liquid Interface. *J. Am. Chem. Soc.* **2021**, *70(4)*, 1640-1644. https://doi.org/10.1021/jacs.1c02481.

(4) Moshrefi, R.; Stockmann, T. J. Electrodeless Synthesis of Low Dispersity Au Nanoparticles and Nanoclusters at an Immiscible Micro Water/Ionic Liquid Interface. *Nanomater.* **2022**, *12(16)*, 2748. https://doi.org/10.3390/nano12162748.

(5) Moshrefi, R.; Suryawanshi, A.; Stockmann, T. J. Electrochemically Controlled Au Nanoparticle Nucleation at a Micro Liquid/Liquid Interface Using Ferrocene as Reducing Agent. *Electrochem. Commun.* **2021**, *122*, 106894. https://doi.org/10.1016/j.elecom.2020.106894.

(6) Moshrefi, R.; P. Connors, E.; Merschrod, E.; Stockmann, T. J. Simultaneous Electropolymerization/Au Nanoparticle Generation at an Electrified Liquid|Liquid Micro-Interface. *Electrochim. Acta.* **2022**, 426, 140749. https://doi.org/10.1016/j.electacta.2022.140749.

(7) Moshrefi, R.; Przybyła, H.; Stockmann, T. J. Simultaneous Electro-Generation/Polymerization of Cu Nanocluster Embedded Conductive Poly(2,2′:5′,2″-Terthiophene) Films at Micro and Macro Liquid|Liquid Interfaces. *Sci. Rep.* **2023**, 13 (1), 1201. https://doi.org/10.1038/s41598-023-28391-9.

(8) Moshrefi, R.; Ryan, K.; Connors, E. P.; Walsh, J. C.; Merschrod, E.; Bodwell, G. J.; Stockmann, T. J. Electrosynthesis of Au Nanocluster Embedded Conductive Polymer Films at Soft Interfaces Using Dithiafulvenyl-Functionalized Pyrene. *Nanoscale.* **2023**, 15 (12), 5834–5842. https://doi.org/10.1039/D2NR06519C.

(9) Lepková, K.; Clohessy, J.; Cunnane, V. J. Electrodeposition of Metal-Based Nanocomposites at a Liquid-Liquid Interface Controlled via the Interfacial Galvani Potential Difference. *Electrochim. Acta.* **2008**, 53 (21), 6273–6277. https://doi.org/10.1016/j.electacta.2008.04.025.

(10) Vignali, M.; Edwards, R.; Cunnane, V. J. Characterization of Doping and Electropolymerization of Free-Standing Films of Polyterthiophene. *J. Electroanal. Chem.* **2006**, 592 (1), 37–45. https://doi.org/10.1016/j.jelechem.2006.04.020.

(11) Lepková, K.; Clohessy, J.; Cunnane, V. J. The PH-Controlled Synthesis of a Gold Nanoparticle/Polymer Matrix via Electrodeposition at a Liquid–Liquid Interface. *J. Condens. Matter Phys.* **2007**, *19(37)*, 375106. https://doi.org/10.1088/0953-8984/19/37/375106.

(12) Gorgy, K.; Fusalba, F.; Evans, U.; Kontturi, K.; Cunnane, V. J. Electropolymerization of 2,2′:5′,2″ Terthiophene at an Electrified Liquid-Liquid Interface. *Synth. Met.* **2001**, *125* (3), 365–373. https://doi.org/10.1016/S0379-6779(01)00474-X.

(13) Maeda, K.; Jänchenová, H.; Lhotský, A.; Stibor, I.; Budka, J.; Mareček, V. Formation of a Polymer Layer from Monomers Adsorbed at a Liquid | Liquid Interface. *J. Electroanal. Chem.* **2001**, 516 (1–2), 103–109. https://doi.org/10.1016/S0022-0728(01)00658-1.

(14) Lehane, R. A.; Gamero-Quijano, A.; Malijauskaite, S.; Holzinger, A.; Conroy, M.; Laffir, F.; Kumar, A.; Bangert, U.; McGourty, K.; Scanlon, M. D. Electrosynthesis of Biocompatible Free-Standing PEDOT Thin Films at a Polarized Liquid|Liquid Interface. *J. Am. Chem. Soc.* **2022**, 144 (11), 4853–4862. https://doi.org/10.1021/jacs.1c12373.

(15) Lehane, R. A. Electrosynthesis of Biocompatible Free-Standing PEDOT Thin Films at a Polarized Liquid|liquid Interface. *J. Am. Chem. Soc.* **2022**, *144(11)*, 4853-4862. https://doi.org/10.1021/jacs.1c12373.

(16) Mareček, V.; Jänchenová, H.; Stibor, I.; Budka, J. Compact Poly-Pyrrole Layers Formed at a Liquid|liquid Interface. *J. Electroanal. Chem.* **2005**, *575* (2), 293–299. https://doi.org/10.1016/j.jelechem.2004.09.021.

(17) Çorman, M. E.; Ozcelikay, G.; Cetinkaya, A.; Kaya, S. I.; Armutcu, C.; Özgür, E.; Uzun, L.; Ozkan, S. A. Metal-Organic Frameworks as an Alternative Smart Sensing Platform for Designing Molecularly Imprinted Electrochemical Sensors. *TrAC. Trends in Anal. Chem.*, **2022**, *150*, 116573. https://doi.org/10.1016/j.trac.2022.116573.

(18) Kamyab, H.; Chelliapan, S.; Tavakkoli, O.; Mesbah, M.; Bhutto, J. K.; Khademi, T.; Kirpichnikova, I.; Ahmad, A.; ALJohani, A. A. A Review on Carbon-Based Molecularly-Imprinted Polymers (CBMIP) for Detection of Hazardous Pollutants in Aqueous Solutions. *Chemosphere* **2022**, *308*, 136471. https://doi.org/10.1016/j.chemosphere.2022.136471.

(19) Liu, Y.; Cui, X.; Lee, Y. I.; Liu, H. G. Self-Assembly of Polystyrene- b-Poly(2-Vinylpyridine)/Chloroauric Acid at the Liquid/Liquid Interface. *Langmuir* **2022**, *38* (15), 4589–4598. https://doi.org/10.1021/acs.langmuir.1c03338.

(20) Zhou, Y. N.; Li, J. J.; Wu, Y. Y.; Luo, Z. H. Role of External Field in Polymerization: Mechanism and Kinetics. *Chem. Rev.*, **2020**, 120(5), 2950–3048. https://doi.org/10.1021/acs.chemrev.9b00744.

(21) Nishi, N.; Yajima, I.; Amano, K. I.; Sakka, T. Janus-Type Gold/Polythiophene Composites Formed via Redox Reaction at the Ionic Liquid|Water Interface. *Langmuir* **2018**, *34* (7), 2441–2447. https://doi.org/10.1021/acs.langmuir.7b03792.

(22) Li, Z.; Zou, J.; Xi, X.; Fan, P.; Zhang, Y.; Peng, Y.; Banham, D.; Yang, D.; Dong, A. Native Ligand Carbonization Renders Common Platinum Nanoparticles Highly Durable for

Electrocatalytic Oxygen Reduction: Annealing Temperature Matters. *Adv. Mater.,* **2022**, *34* (26), 2202743. https://doi.org/10.1002/adma.202202743.

(23) Yang, Y.; Dai, Q.; Shi, L.; Liu, Y.; Isimjan, T. T.; Yang, X. Electronic Modulation of Pt Nanoparticles on Ni3N-Mo2C by Support-Induced Strategy for Accelerating Hydrogen Oxidation and Evolution. *J. Phys. Chem.* **2022**, *13* (9), 2107–2116. https://doi.org/10.1021/acs.jpclett.2c00021.

(24) Kovalskii, A. M.; Volkov, I. N.; Evdokimenko, N. D.; Tkachenko, O. P.; Leybo, D. V.; Chepkasov, I. V.; Popov, Z. I.; Matveev, A. T.; Manakhov, A.; Permyakova, E. S.; Konopatsky, A. S.; Kustov, A. L.; Golberg, D. V.; Shtansky, D. V. Hexagonal BN- and BNO-Supported Au and Pt Nanocatalysts in Carbon Monoxide Oxidation and Carbon Dioxide Hydrogenation Reactions. *Appl. Catal. B.* **2022**, *303*, 120891. https://doi.org/10.1016/j.apcatb.2021.120891.

(25) Tadic, M.; Lazovic, J.; Panjan, M.; Kralj, S. Hierarchical Iron Oxide Nanocomposite: Bundle-like Morphology, Magnetic Properties and Potential Biomedical Application. *Ceram Int.,* **2022**, *48* (11), 16015–16022. https://doi.org/10.1016/j.ceramint.2022.02.145.

(26) Suppiah DD, Daud WM, Johan MR. Supported Metal Oxide Catalysts for CO2 Fischer–Tropsch Conversion to Liquid Fuels ─ A Review. *Energ. Fuel*., **2021**, *35(21)*, 17261-78. https://doi.org/10.1021/acs.energyfuels.1c02406

(27) Jabbar, K. Q.; Barzinjy, A. A.; Hamad, S. M. Iron Oxide Nanoparticles: Preparation Methods, Functions, Adsorption and Coagulation/Flocculation in Wastewater Treatment. *Environ. Nanotechnol. Monit. Manag.*, **2022**, *17,* 100661. https://doi.org/10.1016/j.enmm.2022.100661.

(28) Mahlaule-Glory, L. M.; Mapetla, S.; Makofane, A.; Mathipa, M. M.; Hintsho-Mbita, N. C. Biosynthesis of Iron Oxide Nanoparticles for the Degradation of Methylene Blue Dye,

Sulfisoxazole Antibiotic and Removal of Bacteria from Real Water. *Heliyon,* **2022**, *8* (9), e10536. https://doi.org/10.1016/j.heliyon.2022.e10536.

(29) Booth, S. G.; Dryfe, R. A. W. Assembly of Nanoscale Objects at the Liquid/Liquid Interface. *J. Phys. Chem. C,* **2015**, *119* (41), 23295–23309. https://doi.org/10.1021/acs.jpcc.5b07733.

Appendix A

A. Supporting Information for Chapter 2

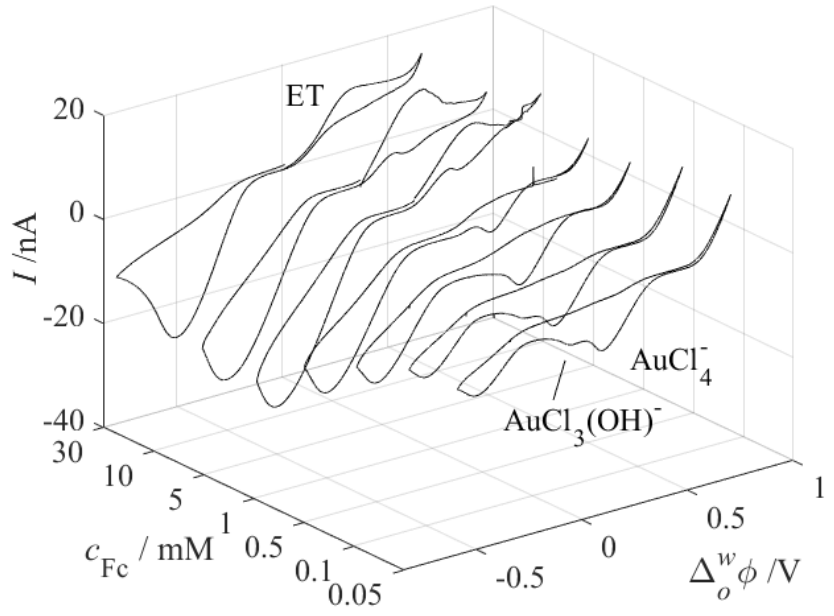

Figure 0-1 CVs obtained using Cell 2-3 with pH ≈ 8.5, dissolved [$KAuCl_4$] = 10 mM, and varying c_{Fc} from 0.1 to 30 mM. All other parameters are the same as those given in Figure 2-2 of the main text.

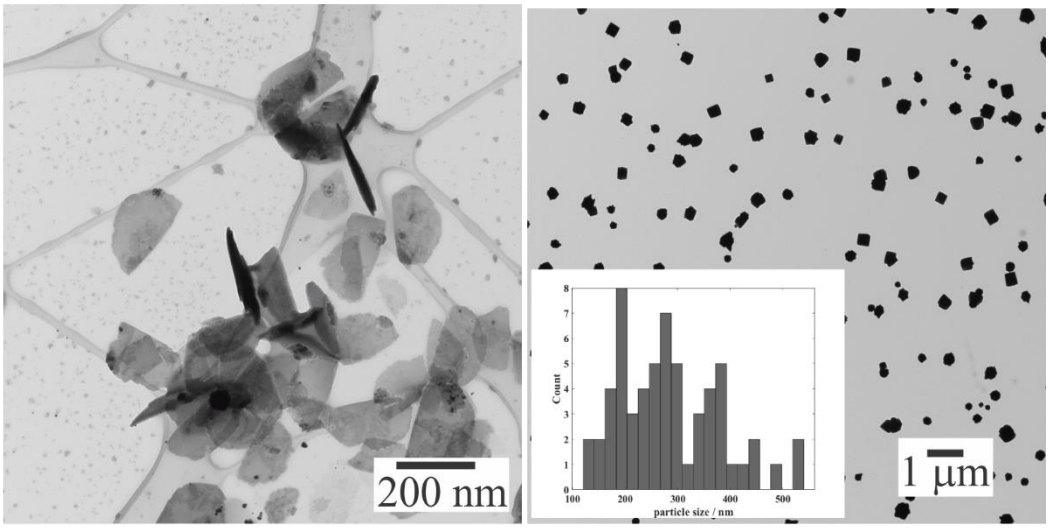

Figure A-2 TEM micrographs obtained from aqueous phase droplet samples taken directly from the micropipette after 20 s immersion (A) and after 30 s applied potential at 500 mV (B), using Cell 2-2 with 1 mM $KAuCl_4$ and 10 mM HCl in the aqueous phase as well as 3 mM of Fc in the organic phase. Histogram of Au NP size is shown inset in B.

Appendix B

B. Supporting Information for Chapter 3

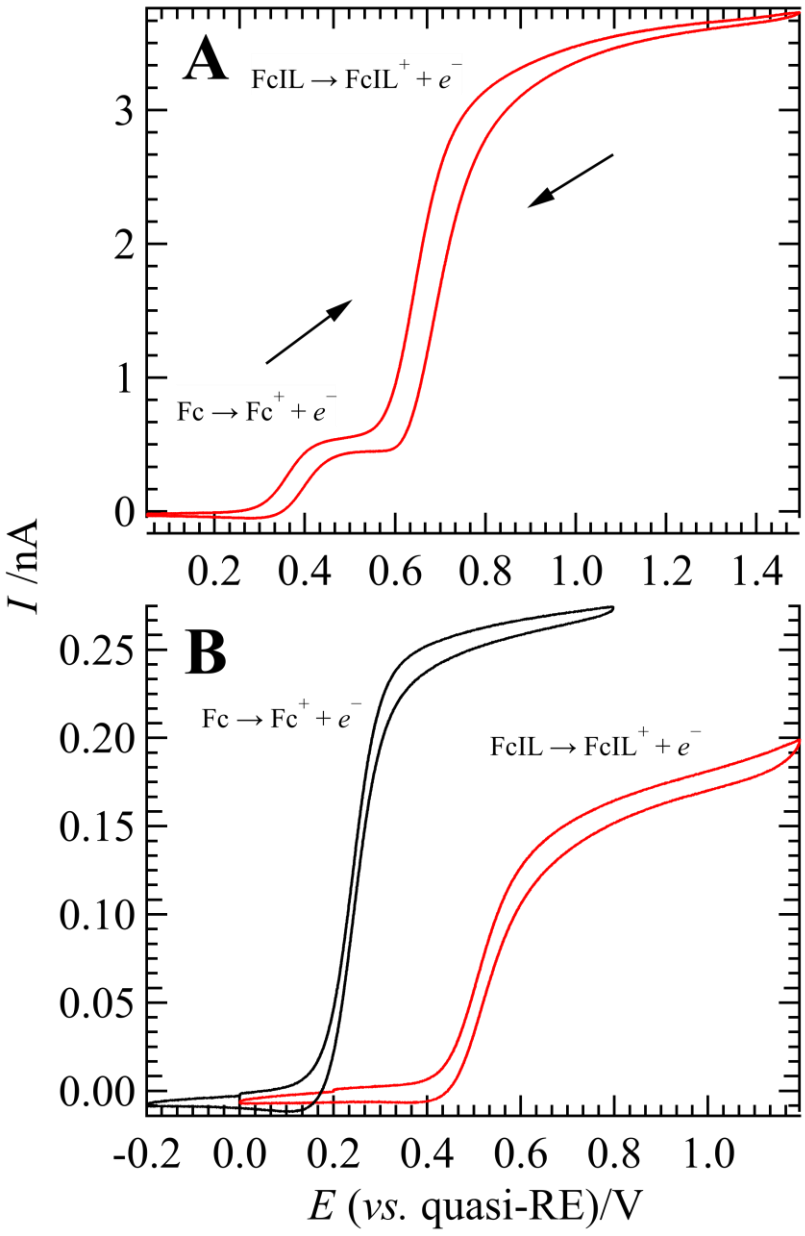

Figure B-1 CVs obtained at a 25 µm diameter inlaid disc Pt ultramicroelectrode (UME) immersed in a DCE solution of (A) 0.1 mM Fc and 1 mM 1 (see Figure 3-1 of the main text) or (B) individual 50 µM solutions of Fc or 1. All solutions also contained 5 mM $P_{8888}TB$ as supporting electrolyte, employed a Ag wire as counter/quasi-reference electrode, and were swept at a rate of 50 mV s^{-1}.

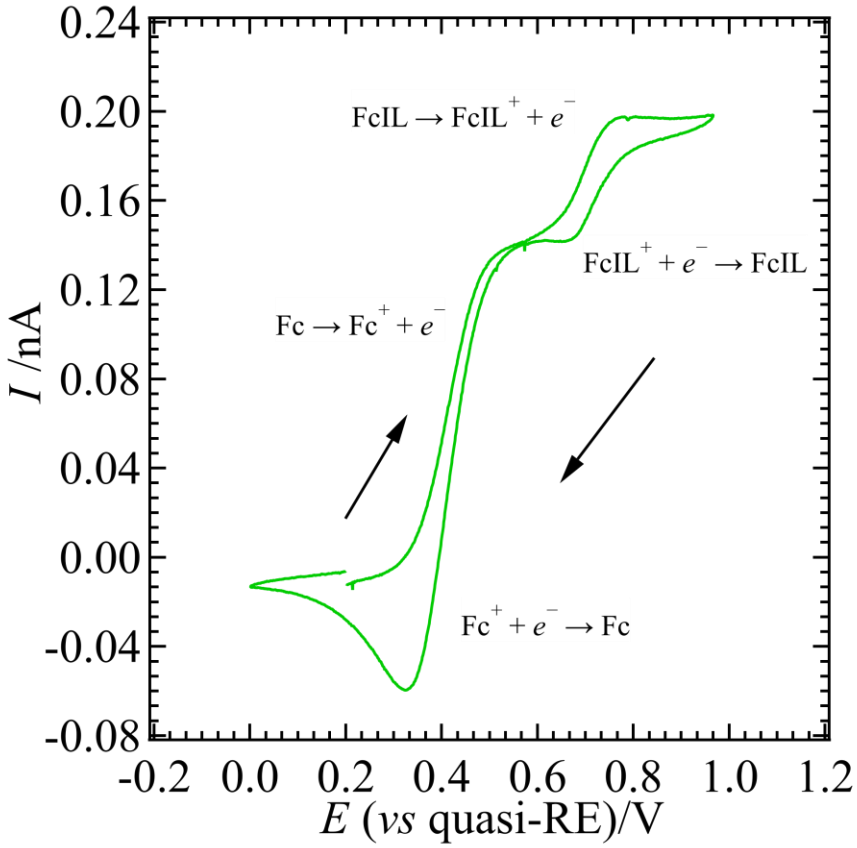

Figure B-2 Voltammetric response at a 7 µm diameter inlaid disc carbon fiber UME immersed in $P_{8888}TB$ containing 100 mM of Fc and 1 (FcIL, see Figure 3-1 of the main text) performed at a rate of 50 mV s^{-1} and ~60°C, while using an Ag wire as a counter/quasi-reference electrode.

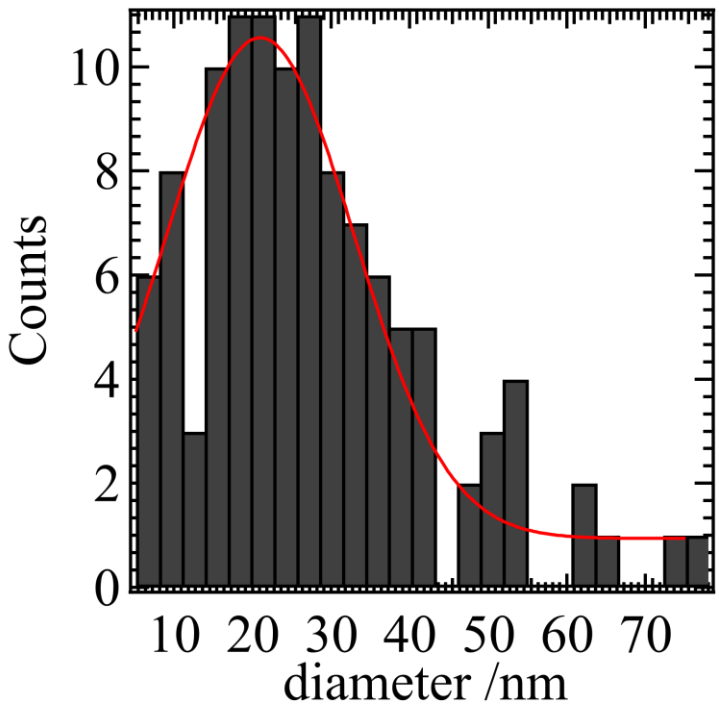

Figure B-3 Histogram of Au NP diameters measured from TEM micrographs of aqueous phase sample taken after one i-V scan using Cell 3-3b with 1 mM $KAuCl_4$ and 500 mM of 1 in $P_{8888}TB$.

Appendix C

C. Supporting Information for Chapter 4

C.1. Micropipette Fabrication

For micropipette fabrication, a borosilicate glass capillary (1.16 mm/2.0mm internal/external diameter) was fixed in an electric puller (PC-100-CA, Narishige, Japan). The capillary was centered within the pullers heating coil and pulled gravimetrically using a weight fixed to the bottom; whereby, two tapered tips were generated. A hand torch was then used to seal the tapered ends of the capillaries. Approximately 1.5 cm of Pt-wire (25 µm in diameter, Goodfellow Inc.) was loaded into the capillary through the open end and pushed into place in the other tapered end using a ~1 mm diameter copper wire. Under vacuum (a small hose was attached to the open end of the capillary), the Pt-wire was annealed in place using the electric puller and suspending the tapered end inside the heating coil. Next, by using increasingly fine grinding/polishing pads, including 12, 4 and 3 µm FibrMet aluminum oxide Abrasive discs (Buehler), a smooth cross-section of the capillary was achieved and confirmed *via* visual inspection using an optical microscope. Polishing was also used to achieve an $R_g > 50$ ($R_g=r_g/a$), where r_g is the outer glass radius and a is the Pt disc radius. The Pt-wire was then etched *via* immersion in aqua regia (3:1 ratio of HCl:HNO_3) for up to 7 days generating a 25 µm diameter microchannel.[1,2]

C.2. Terthiophene Electropolymerization Mechanism

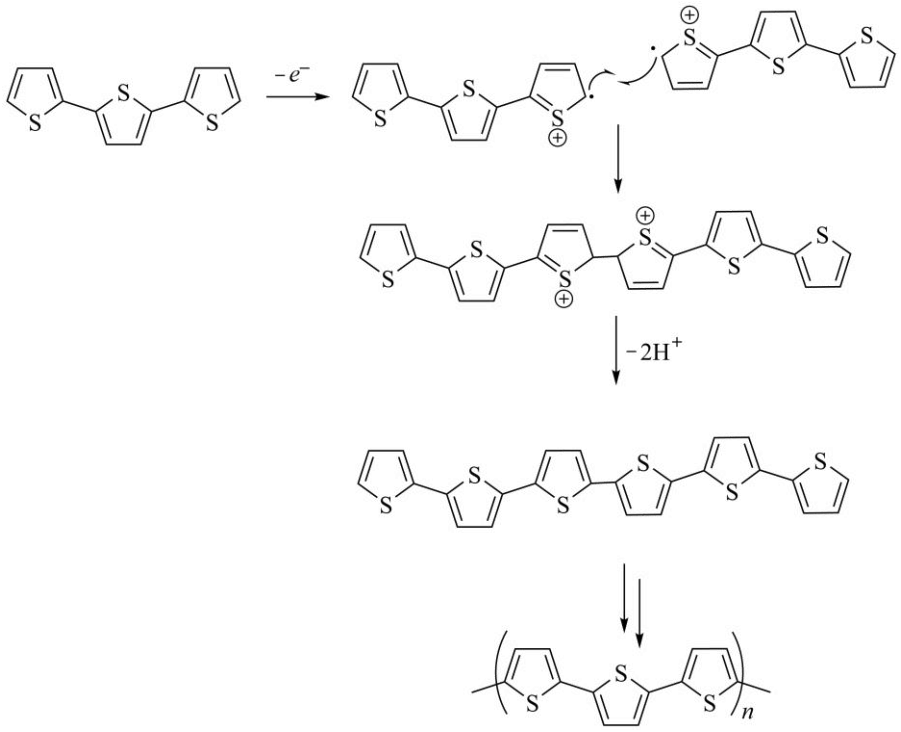

Figure C-1 General electropolymerization mechanism of terthiophene through the formation of a cation-radical and subsequent substitution at the α-carbon.

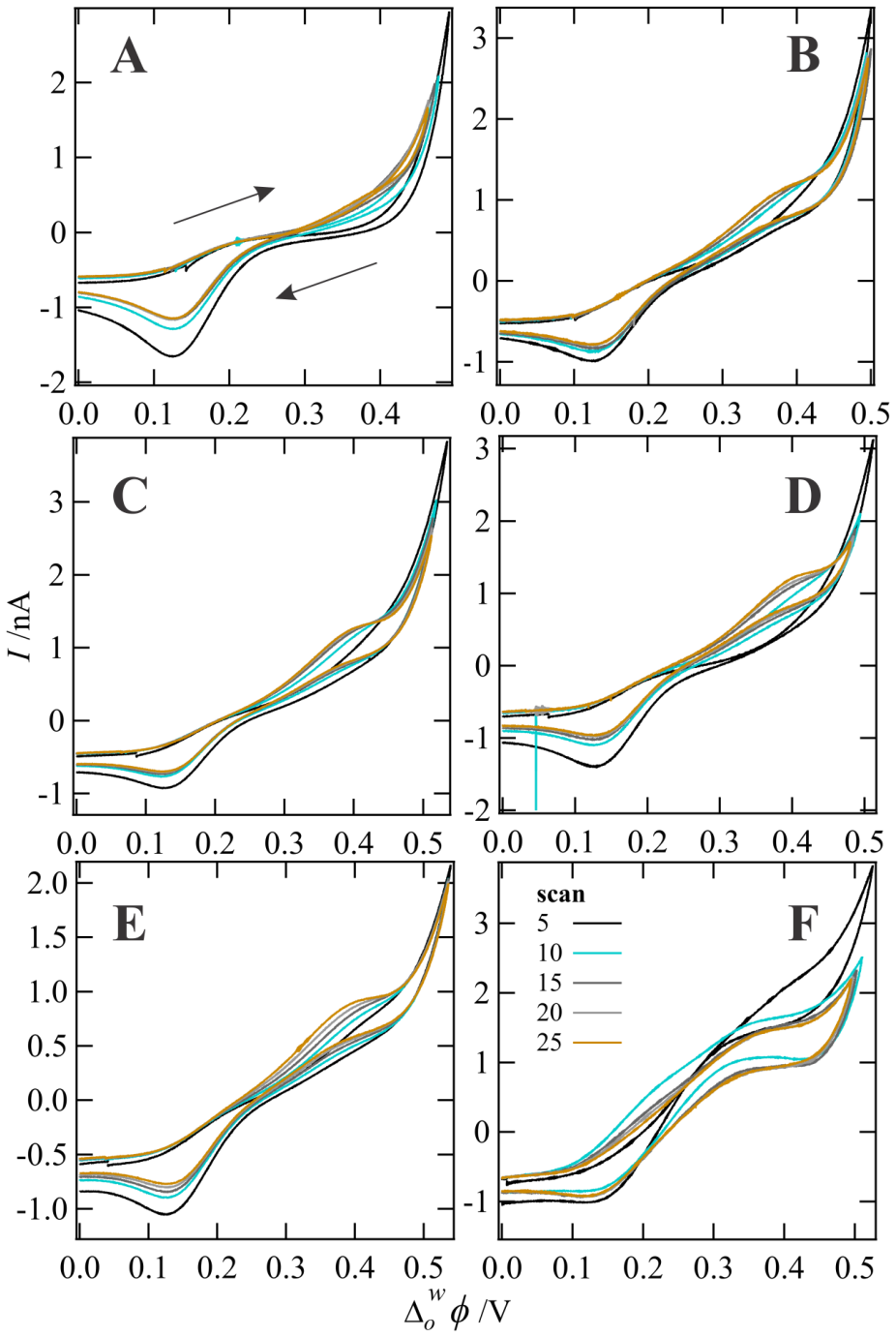

Figure C-2 CVs obtained using Cells 4-1 (A, B), 4-2, (C, D), and 4-3 (E, F) in which the [TT] was 5 and 15 mM in DCE for the left- and right-hand panels, respectively. Arrows indicate scan direction. All other instrumental parameters were the same as indicated for Figure 4-2 of the main text.

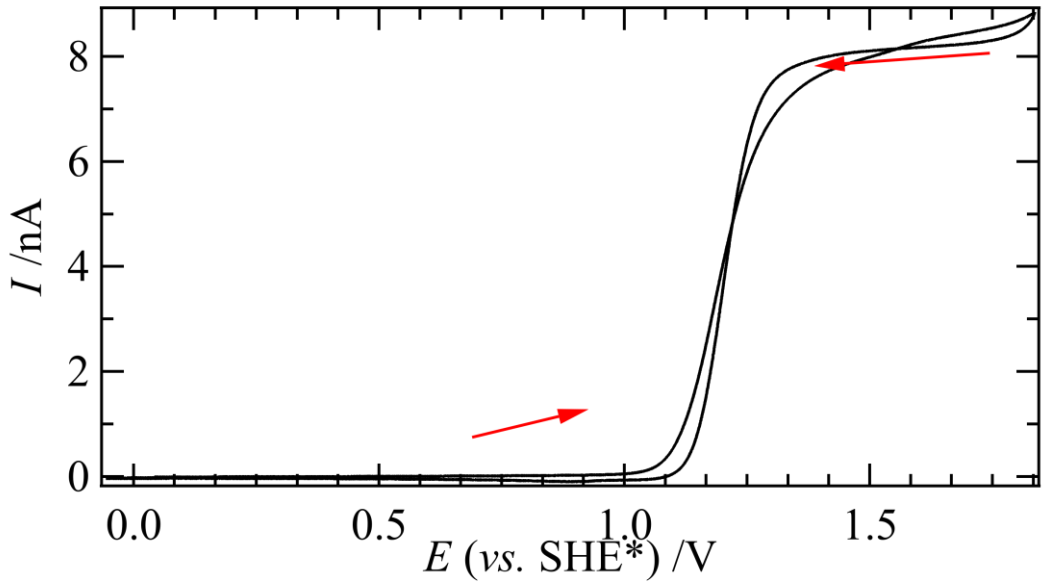

Figure C-3 plot of the CV showing the oxidation of TT in DCE at a carbon fibre ultramicroelectrode (7 μm in diameter). The potential scale has been referenced towards SHE using ferrocene and assuming $\left[E^{o'}_{Fc^+/Fc}\right]^{DCE}_{SHE} = 0.64 \pm 0.05$ V.[3]

C.3. Heterogeneous Electron Transfer ~ basic aqueous phase

For the heterogeneous, liquid|liquid electron transfer, one begins with a modified version of the Nernst equation,[3,4]

$$\Delta^{w}_{o}\phi_{ET} = E^{o',\,DCE}_{TT^{+\cdot}/TT} - E^{o',\,H_2O}_{Au(III)/Au} + \frac{RT}{n_{TT^{+\cdot}/TT}\, n_{Au(III)/Au}\, F} \log\left(\frac{[Cl^-]^{(4-\gamma)}}{\left[AuCl_{(4-y)}(OH)^-_{\gamma}\right][H_2\text{-}TT]^3[OH^-]^{(6-\gamma)}}\right)$$

$$\Delta^{w}_{o}\phi_{ET} = E^{o',\,DCE}_{TT^{+\cdot}/TT} - E^{o',\,H_2O}_{Au(III)/Au} + \frac{RT}{6F} \ln\left[\left(\frac{[Cl^-]^{(4-\gamma)}}{\left[AuCl_{(4-y)}(OH)^-_{\gamma}\right][H_2-TT]^3}\right) - log[OH^-]^{(6-\gamma)}\right]$$

$$\Delta^{w}_{o}\phi_{ET} = E^{o',\,DCE}_{TT^{+\cdot}/TT} - E^{o',\,H_2O}_{Au(III)/Au} + \frac{RT}{6F} \ln\left(\frac{[Cl^-]^{(4-\gamma)}}{\left[AuCl_{(4-y)}(OH)^-_{\gamma}\right][H_2-TT]^3}\right) - \frac{RT}{3F} log[OH^-]^{(6-\gamma)}$$

[C1]

Neglecting the 3rd term on the right-hand side for simplicity, one arrives at,

$$\Delta_{\mathrm{o}}^{\mathrm{w}}\phi_{ET} \approx E^{o',\,\mathrm{DCE}}_{\mathrm{TT}^{+\cdot}/\mathrm{TT}} - E^{o',\,\mathrm{H_2O}}_{\mathrm{Au(III)}/\mathrm{Au}} - \frac{(0.059\ \mathrm{V})}{6} log[OH^-]^{(6-\gamma)}$$

$$\Delta_{\mathrm{o}}^{\mathrm{w}}\phi_{ET} \approx E^{o',\,\mathrm{DCE}}_{\mathrm{TT}^{+\cdot}/\mathrm{TT}} - E^{o',\,\mathrm{H_2O}}_{\mathrm{Au(III)}/\mathrm{Au}} - \frac{(0.059\ \mathrm{V})(6-\gamma)}{6} \log[OH^-]$$

$$\Delta_o^w\phi_{ET} \approx E^{o\prime.DCE}_{TT^{+\cdot}/TT} - E^{o\prime.H_2O}_{Au(III)/Au} - \frac{(0{,}059\ V)(6-\gamma)}{6}\ \mathrm{pOH} \qquad [C2]$$

$$\Delta_o^w\phi_{ET} \approx E^{o\prime.DCE}_{TT^{+\cdot}/TT} - E^{o\prime.H_2O}_{Au(III)/Au} - \frac{(0{,}059\ V)(6-\gamma)}{6}\ (14-\mathrm{pH})$$

C.4. References

1. Moshrefi, R.; Suryawanshi, A.; Stockmann, T. J. *Electrochem. Commun.* **2021**, *122*, 106894.

2. Jiang, Q.; Reader, H. E.; Stockmann, T. J. *ChemElectroChem* **2021**, *8*, 1580-1587.

3. Méndez, M. A.; Partovi-Nia, R.; Hatay, I.; Su, B.; Ge, P. Y.; Olaya, A.; Younan, N.; Hojeij, M.; Girault, H. H. *Phys. Chem. Chem. Phys.* **2010**, *12*, 15163-15171.

4. Johans, C.; Lahtinen, R.; Kontturi, K.; Schiffrin, D. J. *J. Electroanal. Chem.* **2000**, *488*, 99-109.

Appendix D

D. Supporting Information for Chapter 5

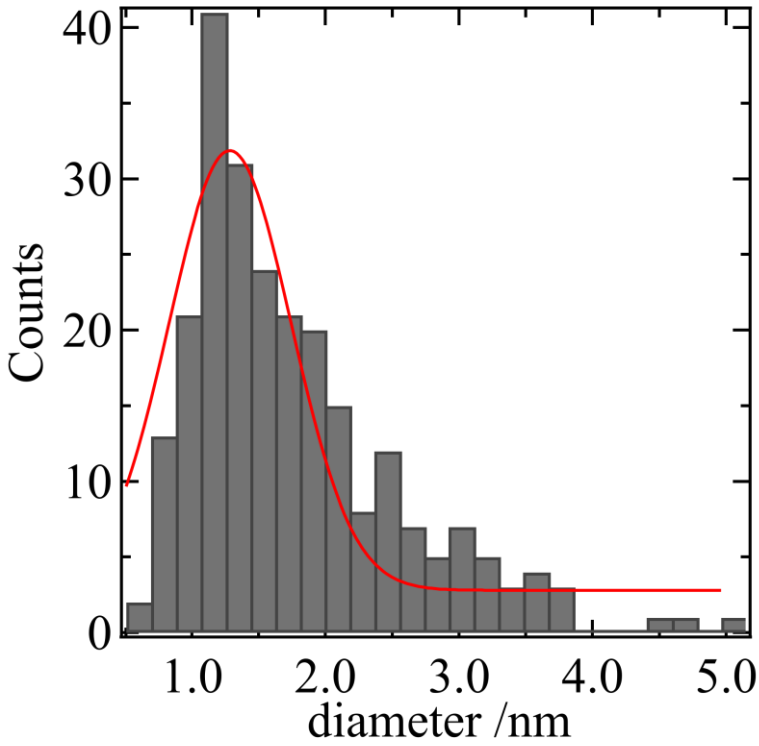

Figure D-1 Histogram of Cu NPs sizes embedded in poly-TT after 25 CV scans using Cell 5-1 with [TT] = 10 mM in DCE.

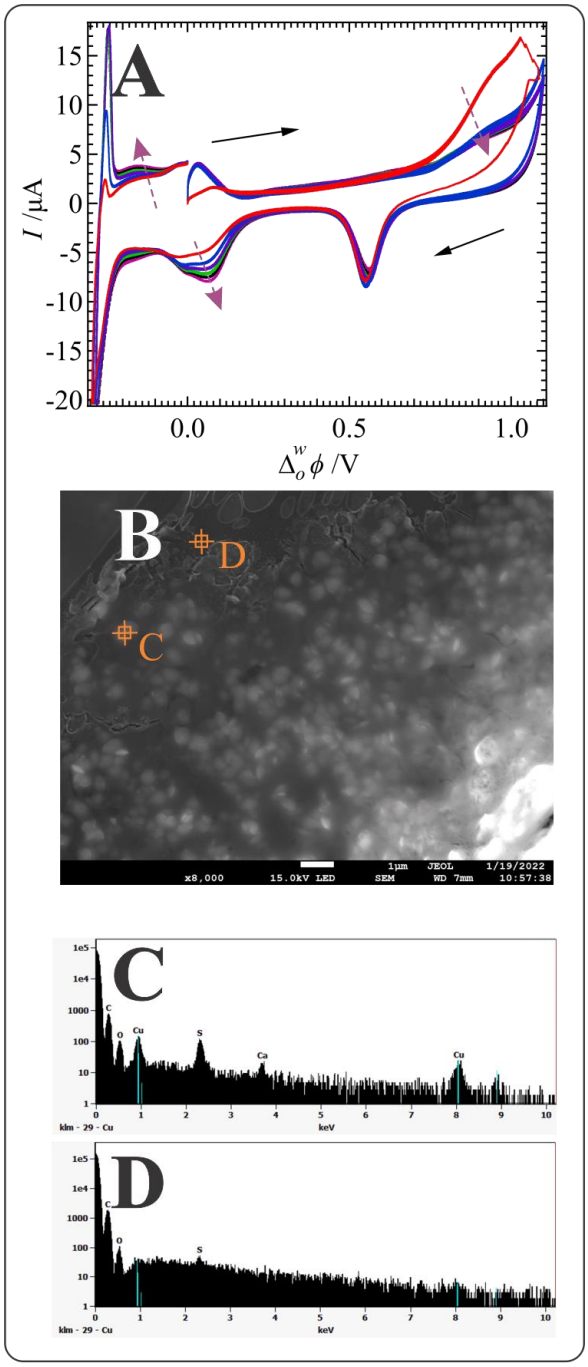

Figure D-2 (A) 25 CVs recorded in succession using Cell 5-2 at a large, 10 mm diameter ITIES with [$CuSO_4$] = 1 mM, [TT] = 5 mM, and a scan rate of 0.020 V s^{-1}. The first and every subsequent 5th scan are displayed. Black arrows indicate scan direction, while dashed, purple arrows the evolution of current signals with each CV cycle. (B) SEM micrograph of the Cu NP/poly-TT film extracted from the large ITIES cell after the CV experiments shown in A and deposited on a glass slide. (C) and (D) are energy dispersive X-ray (EDX) spectra of the corresponding points indicated in B.

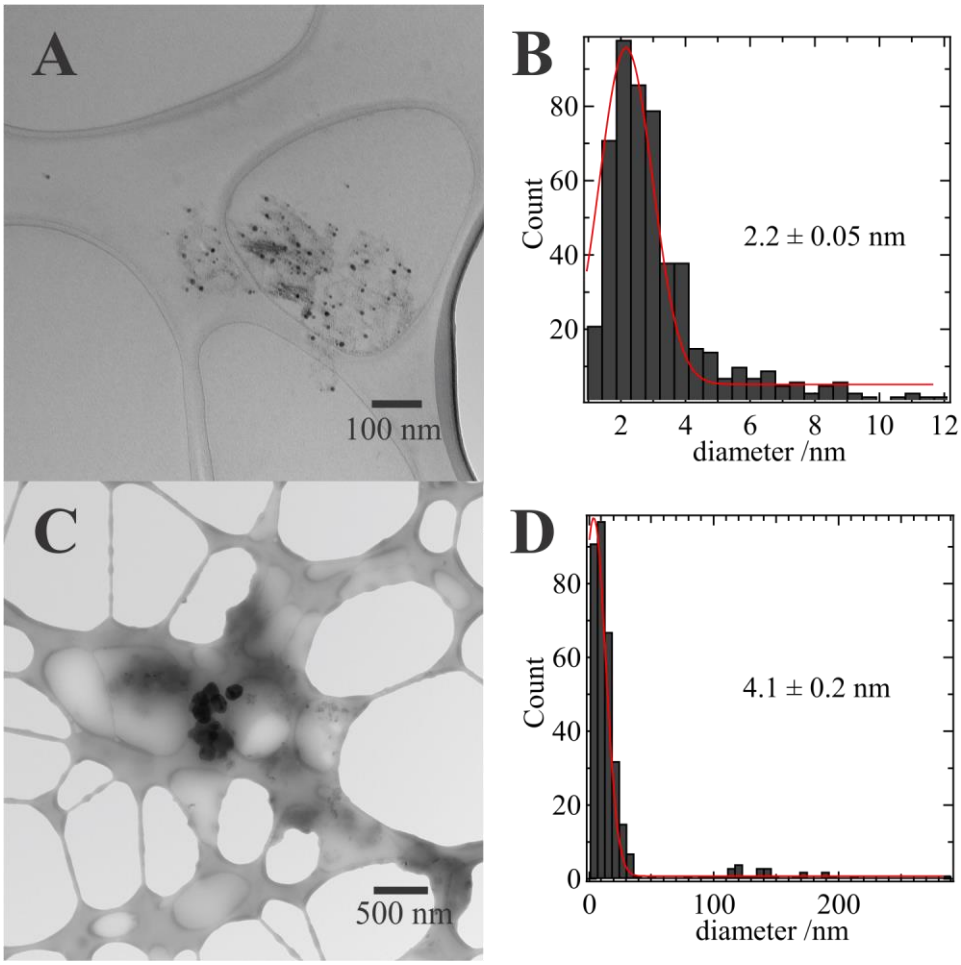

Figure D-3 TEM micrographs and histrgrams of Cu NP sizes taken of Cu NP/poly-TT film electrogenerated at a 1.16 (A, B) and 10 mm (C, D) deposited on Au 200 mesh lacy carbon/ultra-thin film TEM grids. Cu NP sizes were measured using ImageJ software.

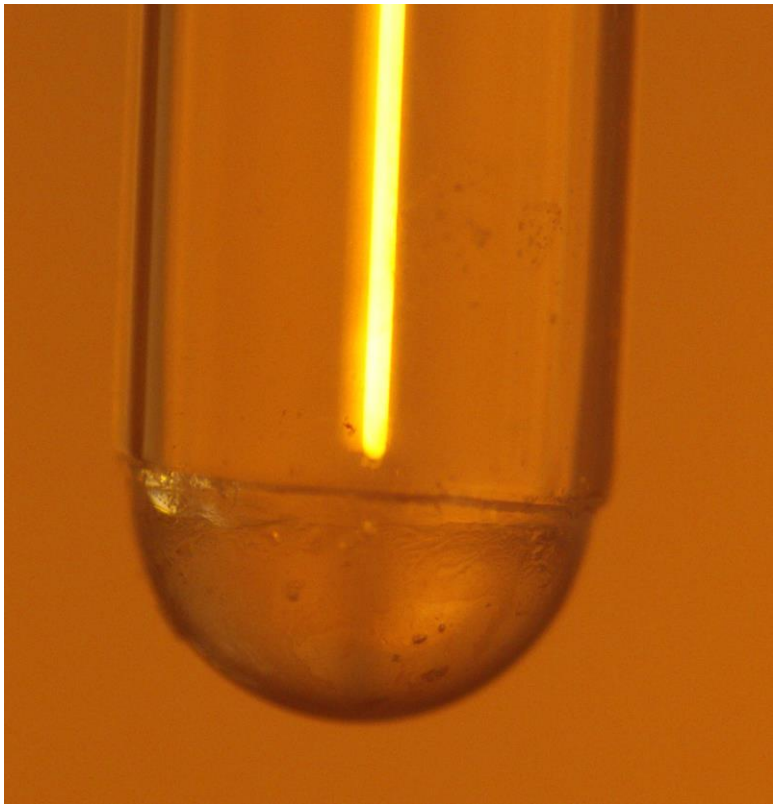

Figure D-4 Photograph taken after the 1.16 mm diameter ITIES capillary was carefully removed from the organic phase. The thin, nanocomposite film can be seen covering the surface of the aqueous droplet.

D.1. Thermodynamics of Interfacial Electron Transfer

Using the fundamental equations for heterogeneous electron transfer at liquid|liquid interfaces described by Johans *et al.*[1] and others,[2] one can develop the following from general chemical reaction given in equation 5-5 of the main text as follows,

$$\Delta_{\mathrm{o}}^{\mathrm{w}}\phi_{ET} = E^{o',\,\mathrm{DCE}}_{\mathrm{TT}^{+\cdot}/\mathrm{TT}} - E^{o',\,\mathrm{H_2O}}_{\mathrm{Cu(II)}/Cu} - \frac{RT}{n_{\mathrm{TT}^{+\cdot}/\mathrm{TT}}\, n_{\mathrm{Cu(II)}/Cu}\, F}\ln([Cu^{2+}][\mathrm{H_2\text{-}TT}]^2[\mathrm{OH^-}]^2)$$

$$\Delta_{\mathrm{o}}^{\mathrm{w}}\phi_{ET} = E^{o',\,\mathrm{DCE}}_{\mathrm{TT}^{+\cdot}/\mathrm{TT}} - E^{o',\,\mathrm{H_2O}}_{\mathrm{Cu(II)}/Cu} - \frac{RT}{2F}\ln([Cu^{2+}][\mathrm{H_2\text{-}TT}]^2) - \frac{RT}{2F}log[\mathrm{OH^-}]^2 \qquad [D1]$$

$$\Delta_{\mathrm{o}}^{\mathrm{w}}\phi_{ET} = E^{o',\,\mathrm{DCE}}_{\mathrm{TT}^{+\cdot}/\mathrm{TT}} - E^{o',\,\mathrm{H_2O}}_{\mathrm{Cu(II)}/Cu} - \frac{RT}{2F}\ln([Cu^{2+}][\mathrm{H_2\text{-}TT}]^2) - \frac{RT}{F}log[\mathrm{OH^-}]^2$$

Neglecting the 3rd term on the right-hand side for simplicity, one arrives at,

$$\Delta_o^w\phi_{ET} = E^{o',\,DCE}_{TT^{+\cdot}/TT} - E^{o',\,H_2O}_{Cu(II)/Cu} - \frac{RT}{F} log[OH^-]$$

$$\Delta_o^w\phi_{ET} = E^{o',\,DCE}_{TT^{+\cdot}/TT} - E^{o',\,H_2O}_{Cu(II)/Cu} - (0.059\ V)\ \log[OH^-]$$

$$\Delta_o^w\phi_{ET} = E^{o',\,DCE}_{TT^{+\cdot}/TT} - E^{o',\,H_2O}_{Cu(II)/Cu} - (0.059\ V)\ pOH \qquad [D2]$$

$$\Delta_o^w\phi_{ET} = E^{o',\,DCE}_{TT^{+\cdot}/TT} - E^{o',\,H_2O}_{Cu(II)/Cu} - (0.059\ V)\ (14 - pH)$$

D.2. Micropipette/Cell cleaning procedure

All capillaries and glass electrolytic cells were cleaned extensively before use to prevent contamination between experiments. The cleaning procedure was as follows:

1. Rinse the capillary (or electrochemical cell) with DI water.

   Note: capillaries were rinsed using a syringe equipped with a flexible needle (MicroFil 28G, World Precision Instruments) and the inner solution was removed from the capillary using a small diameter tubing with one end attached to the house-air or N_2 line and the other affixed by hand to the micropipette end of the capillary, while holding a Kim-wipe at the open end of the capillary to catch the cleaning solution. Use caution as only a weak air/N_2 flow is needed. During sonication, capillaries were suspended in a 20 mL scintillation vial filled with DI water by drilling a hole in the plastic cap large enough to hold the capillary in place. Multiple holes were drilled in the cap and several capillaries were suspended in this way, in one scintillation vial at a time.
2. Fill the rinsed capillary/cell with a solution of 0.1 M $KMnO_4$ in 0.2 M H_2SO_4 and leave it to stand overnight.
3. Empty the washing solution and rinse with DI water to remove any remaining $KMnO_4$ solution left inside.

4. Fill the capillary/cell with a cleaning solution composed of 1 mL H_2O_2 (30%), 1 mL H_2SO_4 (95%) in 500 mL of DI water (piranha solution) and sonicate for 10-20 min. It is important not to exceed 20 min of sonication when cleaning the large ITIES electrochemical cells, as the solution can etch the glass and cause leaking around the Pt embedded electrodes.
5. Dispose of the cleaning solution in an appropriate container and rinse the capillary with DI water using the syringe with flexible needle and compressed air/N_2.
6. Next, fill the capillary with DI water and sonicate for 20 mins.
7. Finally, rinse the cell with DI water and it is ready to use.

D.3. References

1. Johans, C., Lahtinen, R., Kontturi, K. & Schiffrin, D. J. Nucleation at liquid|liquid interfaces: electrodeposition without electrodes. *J. Electroanal. Chem.* **488**, 99-109, doi:https://doi.org/10.1016/S0022-0728(00)00185-6 (2000).

2. Méndez, M. A. *et al.* Molecular electrocatalysis at soft interfaces. *Phys. Chem. Chem. Phys.* **12**, 15163-15171, doi:10.1039/c0cp00590h (2010).

Appendix E

E. Supporting Information for Chapter 6

E.1. Modified Pipette Holder:

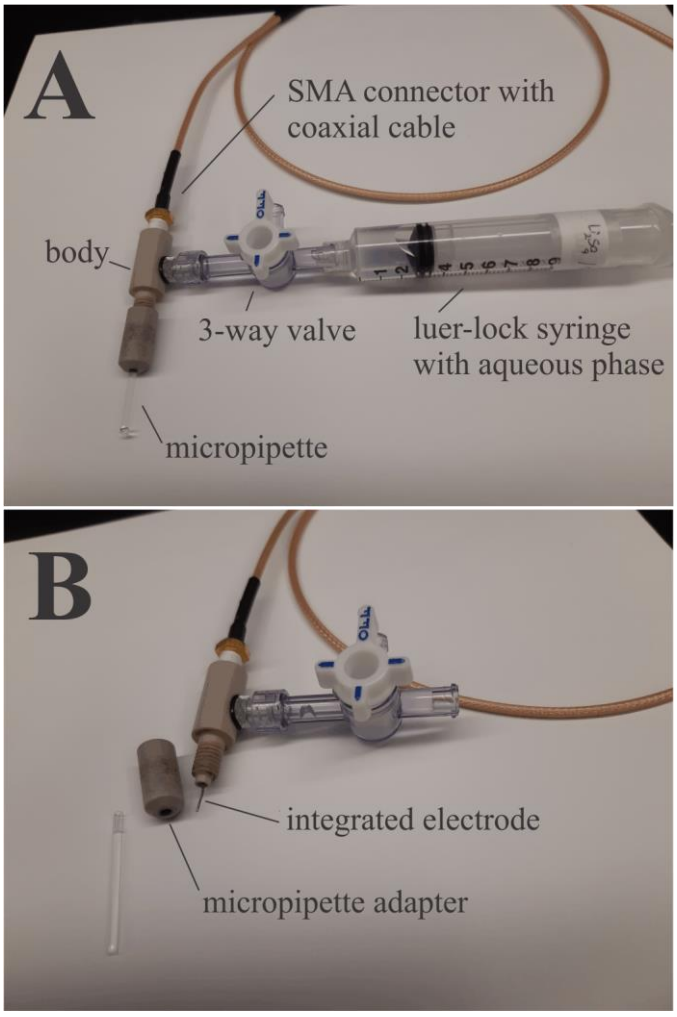

Figure 0-1 Photographs of the assembled (A) and partially disassembled (B) micropipette holder with integrated working electrode connected to an SMA adapter and shielded coaxial cable which is connected to the head-stage (not pictured) of the HEKA potentiostat. The body of the holder was fabricated from PEEK, i.e., poly(ether ether ketone), by Memorial University's Technical Services Department.

E.2. Micropipette fabrication

Micropipettes were fabricated from a single borosilicate glass capillary (1.16 mm/2.0mm internal/external diameter, Sutter Instruments). The capillary was installed inside of an electric puller (PC-100-CA, Narishige, Japan) with the heating coil situated towards its middle and pulled by a weight affixed to the bottom end. In this way, two tapered tips were generated. Next, a hand torch was used to seal the tapered ends of the capillaries. A ~1.5 cm long segment of Pt-wire (25 μm in diameter, Goodfellow Inc.) fed into the open end of the capillary and pushed down into the tapered end using a ~1 mm diameter copper wire. A vacuum line was attached to the open end of the capillary which was held inside the electric puller. The capillary was place under vacuum for ~5 min, and then the Pt-wire was annealed in place using the electric puller and suspending the tapered end inside the heating coil. Next, by using increasingly fine grinding/polishing pads, including 12, 4 and 3 μm FibrMet aluminum oxide Abrasive discs (Buehler), a smooth cross-section of the capillary was achieved and confirmed *via* visual inspection using an optical microscope (AmScope). Polishing was also used to achieve an $R_g > 50$ ($R_g = r_g/a$), where r_g is the outer glass radius and a is the Pt disc radius. The Pt-wire was then etched *via* immersion in aqua regia (3:1 ratio of HCl:HNO_3) for up to 7 days generating a 25 μm diameter microchannel.[1-3]

E.3. References

1. R. Moshrefi, A. Suryawanshi and T. J. Stockmann, *Electrochem. Commun.*, 2021, **122**, 106894.

2. Q. Jiang, H. E. Reader and T. J. Stockmann, *ChemElectroChem*, 2021, **8**, 1580-1587.

3. R. Moshrefi, E. P. Connors, E. Merschrod and T. J. Stockmann, *Electrochim. Acta*, 2022, **426**, 140749.